MICROFLUIDIC AND 3D PRINTING TECHNOLOGIES FOR THE DEVELOPMENT OF AN *IN VITRO* THROMBUS MIMIC

By

Bethany Gross

A DISSERTATION

Submitted to
Michigan State University
in partial fulfillment of the requirements
for the degree of

Chemistry - Doctor of Philosophy

2016

ABSTRACT

MICROFLUIDIC AND 3D PRINTING TECHNOLOGIES FOR THE DEVELOPMENT OF AN *IN VITRO* THROMBUS MIMIC

By

Bethany Gross

Platelets from individuals with diabetes, cystic fibrosis, multiple sclerosis, hypertension, and sickle cell anemia are hyperactive or more likely to aggregate and form a blood clot or thrombus. Furthermore, each of these diseases exhibits abnormal red blood cell (RBC) adenosine triphosphate (ATP) release, an agonist of platelet activation. RBC-derived ATP release is also a proven factor in the regulation of vascular tone through a signal cascade that results in nitric oxide release from endothelial cells and relaxation of smooth muscle cells. This relaxation leads to vessel dilation and a localized increase in blood flow. The presence of hyperactive platelets in conjunction with altered RBC-derived ATP release results in an impaired ability to dilate local resistance vessels, and ultimately puts individuals with these diseases at higher risk for deleterious thrombus formation.

The work detailed in this dissertation outlines the development of microfluidic and 3D printed *in vitro* models of *in vivo* circulation, capable of inducing an injury to a localized region of the endothelium. Specifically, chemical and electrical lysis of endothelial cells will be demonstrated through the use of embedded or removable electrodes or with laser irradiation of a photochemical dye. The fabricated devices mimic flow seen in blood vessels, facilitate the study of platelet adhesion to sub-endothelial collagen, and allow for the study of thrombus formation in stored blood samples showing altered ATP release from RBCs. With a more rapid fabrication process, reusability of the final device, and possibility of standardization via open software sharing, 3D printing offers a more

attractive method to develop and utilize an *in vitro* thrombus mimic compared to more widely employed soft lithographic techniques.

Channels of 3D printed devices featured a stenosis region (0.8 mm height, 2 mm length, and 1 mm width) and wide regions (device 1: 5; device 2: 3.83 mm width). Surface modification of channels with either polydimethylsiloxane (PDMS) or polystyrene (PS) was necessary to promote endothelial cell adherence. Thicknesses of PDMS and PS channel coatings were determined using scanning electron microscopy. The PDMS coating varied in thickness from 3 μm to 100 μm. Multiple PS coatings were required to form a 100 μm thick coating. Cells remained viable on the devices for five days (98% viable), though cell coverage decreased after day four with static media delivery. Optimal lysis conditions (applied electrical potential and duration) were determined for the two different geometries of the 3D printed devices to ensure localized endothelial cell clearance. Selective cell lysis was achieved with efficiencies of 94% (device 1) and 96% (device 2).

FDA approved blood storage solutions expose RBCs to hyperglycemic amounts of glucose. As seen with RBCs from individuals with diabetes, ATP release from stored RBCs is significantly decreased compared to control RBCs. The effect of this decreased ATP release on thrombus formation was evaluated when hyper and normoglycemic stored RBCs were reincorporated with platelet rich plasma by measuring percent transmittance through the device, where increased thrombus coverage corresponded to a decrease in transmittance. Within the same storage period, RBCs stored in hyper and normoglycemic conditions showed no significant difference in hemoglobin absorption indicative of cell adherence. However, a significant decrease in cell adherence between day 1 and week 3 hyper and normoglycemic samples was observed (normo: $p = 0.005$, $n \geq 3$; hyper: $p < 0.003$, $n \geq 3$).

“Why, sometimes I’ve believed as many as six impossible things before breakfast.”

Lewis Carroll

ACKNOWLEDGMENTS

I would like to thank the funding sources that have supported my research including the College of Natural Science and the Graduate School at Michigan State University, and the National Institutes of Health. Funding to attend conferences throughout my graduate career was facilitated by support from the Department of Chemistry, the College of Natural Science, and the Society for Laboratory Automation and Screening.

I thank my committee members, Merlin Bruening, Gary Blanchard, and Rémi Beaulac for critical insight into my research at various stages of my graduate career. I also acknowledge Brian Wright from the Department of Electrical and Computer Engineering for his assistance printing 3D devices, and Per Askeland from the Department of Engineering for his expertise in acquiring SEM images.

I would like to acknowledge members of the Spence group from 2010 – 2015 that I worked alongside. Suzanne Summers, Kari Anderson, Sarah O'Brien, and Jayda Meisel were instrumental in helping me learn the ways of the Spence group by passing on their knowledge and were always willing to discuss research ideas. I owe much to the Spence group members including Chengpeng Chen and Yueli Liu, as well as other graduate students in the department: John Mcllroy, Christine Hay, Sujana Pradhan, Chen Zhang, Afrand Kamali, and Li Ciu for their support and friendship in and out of the lab. I would also like to thank the current Spence group members: Kristen Entwistle, Ruipeng Mu, Tiffany Bell, Cody Pinger, Hamideh Keshavarz, and Andrew Heller. Many of my fellow graduate students and my undergraduate assistant Megan McNitt were instrumental in the acquisition of some of the data presented in this dissertation. I am grateful for the

friendships that I formed with these individuals and thank them for making my experience at Michigan State University memorable.

I would like to thank my chemistry coach, Dana Spence, for fostering a research environment that provided guidance while allowing me to explore my own ideas. I have learned much about the scientific process and life from Dr. Spence through his devotion to his work and family. I thank him for taking a chance on a free agent. I will be forever grateful for the opportunity.

I am grateful to Peavey and Nymeria for their companionship. I thank my family, friends, and loved ones for their support during grad school and for embracing the ridiculous with me. I would like to thank my parents, William and Tina Gross, who have never faltered in their commitment to my education. There were many red shells on the race track that was my journey through graduate school, but with the support of family and friends, I now find myself successfully across the finish line.

TABLE OF CONTENTS

LIST OF TABLES

LIST OF FIGURES

KEY TO ABBREVIATIONS

RBCs: Red blood cells

GP: Glycoprotein

vWF: von Willebrand factor

ATP: Adenosine triphosphate

ADP: Adenosine diphosphate

ECM: Extra cellular matrix

NO: Nitric oxide

GPCRs: G-protein coupled receptors

cAMP: Cyclic adenosine monophosphate

TF: Tissue factor

PT: Prothrombin

T: Thrombin

FB: Fibrinogen

F: Fibrin

TXA2: Thromboxane A2

EDRF: Endothelium derived relaxing factor

NOS: Nitric oxide synthase

CF: Cystic fibrosis

CFTR: Cystic fibrosis transmembrane conductance regulator

SCA: Sickle cell anemia

MS: Multiple sclerosis

PDMS: Polydimethylsiloxane

SDS: Sodium dodecyl sulfate

PDT: Photodynamic therapy

CAD: Computer aided design

STL: Standard tessellation language

3D: Three dimensional

2D: Two dimensional

SLA: Stereolithography

SLS: Selective laser sintering

FDM: Fused deposition modeling

LOM: Laminate object manufacturing

DMD: Digital mirror device

ROS: Reactive oxygen species

dsDNA: Double stranded deoxyribonucleic acid

ssDNA: Single stranded deoxyribonucleic acid

OH: Hydroxide

PBS: Phosphate buffered saline

μTAS: μ total analysis system

FIA: Flow injection analysis

MEM: Microelectromechanical

ABS: Acrylonitrile butadiene styrene

PS: Polystyrene

IPA: Isopropyl alcohol

bPAECs: Bovine pulmonary artery endothelial cells

EGM: Endothelial growth media

DMEM: Dulbecco's modified eagle's medium

ACD: Acid citrate dextrose

MTB: Modified Tyrode's buffer

CN: Collagen

FN: Fibronectin

DMSO: Dimethylsulfoxide

PRP: Platelet rich plasma

PPP: Platelet poor plasma

CMFDA: Cell tracker green 5-chloromethylfluorescein diacetate

SEM: Scanning electron microscopy

bioMEMS: Biomedical microelectromechanical systems

CPD: Citrate phosphate dextrose

AS: Additive solution

CP2D: Citrate phosphate double dextrose

GLUT1: Glucose transporter protein 1

NAD: Nicotinamide adenine dinucleotide

FDA: Food and drug administration

PVC: Polyvinyl chloride

DEHP: Di(ethylhexyl)-phthalate

SMCs: Smooth muscle cells

GTP: Guanosine triphosphate

cGMP: Cyclic guanosine monophosphate

AC: Adenyl cyclase

sGC: Soluble guanylyl cyclase

CVD: Cardio vascular disease

TRALI: Transfusion-related acute lung injury

Hbt: Total hemoglobin

Hbf: Hemoglobin in the supernatant

EC_{50}: Half maximal effective concentration

CMTPX: Cell tracker red

CD31: Cluster of differentiation 31

ISTH: International society on thrombosis and hemostasis

CLIP: Continuous liquid interface production

CHAPTER 1

INTRODUCTION

1.1 Platelet Biology

Platelets, also referred to as thrombocytes, are the key cell type responsible for the regulation of hemostasis, or normal blood flow, in the event of an injury. The primary mechanism by which platelets achieve hemostasis is by arresting blood loss and reforming an impaired vessel wall after injury through thrombus or blood clot formation. Platelets are the second most prominent cell type in whole blood, after red blood cells (RBCs; 5×10^{12} RBCs per liter of whole blood), numbering $150\text{-}450 \times 10^{9}$ platelets per liter.[1,2]

1.1.1 Origin and Death

Platelets are primarily produced from megakaryocytes (hematopoietic stem cells also responsible for the production of RBCs) in the bone marrow,[3,4] but can also form in the bloodstream and lungs as a consequence of megakaryocyte migration into the bloodstream.[5] In total, megakaryocytes produce 100 billion platelets per day and can produce even more depending on demand.[6] Platelets have a lifespan in the blood stream of 7-10 days, in comparison to the typical RBC lifespan of ~ 120 days.[3] Older platelets have an impaired ability to respond to agonists and are filtered from the bloodstream primarily by macrophages in the liver and spleen, but also in the lung, to a lesser extent.[7]

1.1.2 Structure

Platelets are disc-shaped anucleated cells measuring 2-5 μm in diameter. The surface of the platelet is covered in minute folds that most likely serve to increase the surface area of the platelet during adhesion. Glycoprotein (GP) receptors necessary for

platelet activation and adhesion events cover the surface. A subsurface membrane filament system, cytoskeletal microtubule coils, and actomyosin filament system enable the platelet to elongate during injury and retract afterwards.[8] Of note, platelets contain mitochondria (for energy metabolism), lysosomes, α granules, dense bodies (γ granules), and glycogen (for energy storage). α granules are the most prominent organelle in the platelet (40 to over 100 per platelet) and contain von Willebrand factor (vWF), coagulation factor V, thrombospondin, P-selectin, and fibrinogen – all factors that release upon platelet activation and play a role in thrombus formation.[7,9] The contents of the dense bodies (4 to 8 per platelet) are released upon platelet activation to aid in recruitment and activation of neighboring platelets and include adenosine triphosphate (ATP), adenosine diphosphate (ADP), and calcium.[9]

1.2 Platelet Function

Maintaining hemostasis after vascular damage involves the formation of a thrombus that is initiated by platelet adhesion to exposed sub-endothelium collagen in the extra cellular matrix (ECM), and is primarily composed of RBCs and platelets.[10,11,12] However, white blood cells and plasma proteins are also present in the clot. Collagen activates platelets, causing a shape change (Figure 1.1) where protrusions are developed, making them more readily able to adhere to other platelets as well as prompting the release of factors to activate surrounding platelets and recruit them to the site of injury.[10,11] Neighboring activated platelets aggregate and form connections via fibrinogen, a plasma protein. In this manner, platelets serve to form a platelet plug at the site of injury in a process known as primary hemostasis. Components of the thrombus are held together by

membrane proteins on the platelet and importantly through the conversion of fibrinogen to fibrin via the coagulation cascade, resulting in a stable thrombus.[12]

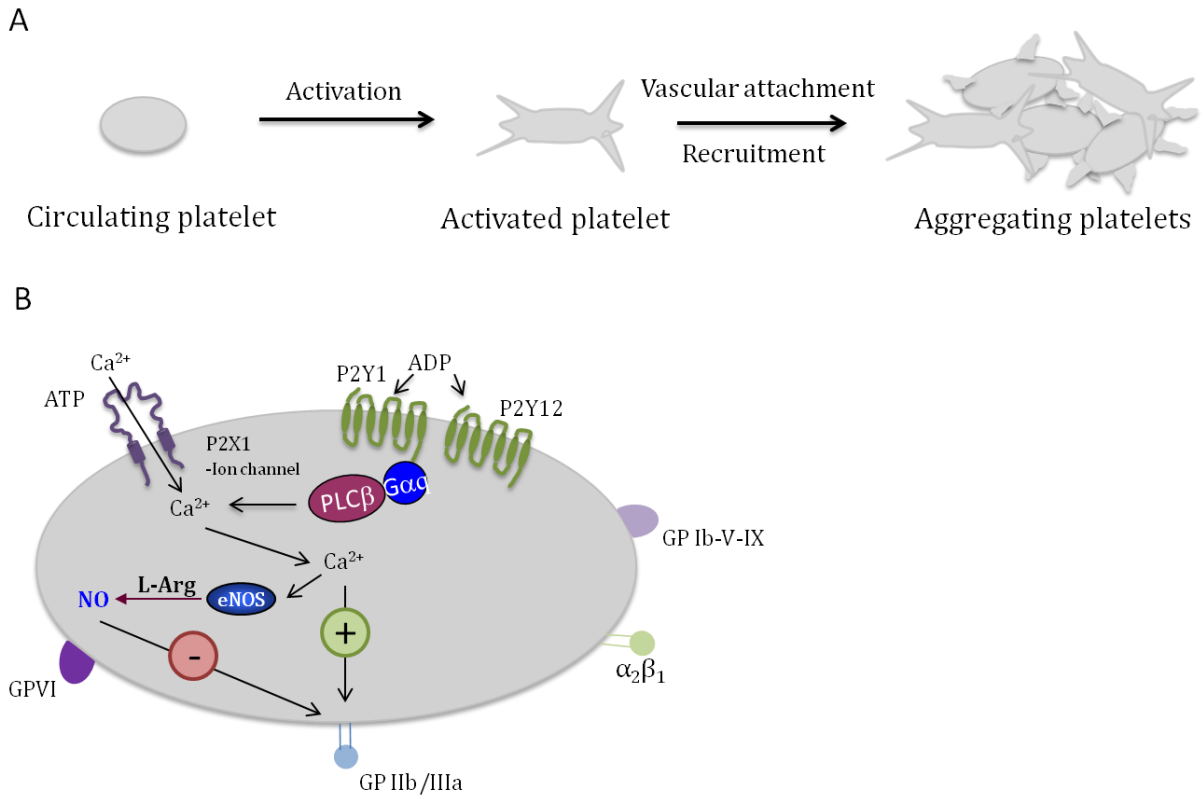

Figure 1.1 Platelet overview. Platelet morphology progression from an inactivated and circulating platelet to aggregated platelets forming a platelet plug. Activation commonly occurs through exposure to the subendothelial layer or via agonists such as ATP and ADP (A). Purinergic and glycoprotein receptors on the platelet surface necessary for platelet activation or aggregation. P2X1, an ion channel activated by ATP, allows for an influx of Ca^{2+} that triggers a shape change in the platelet (B).

1.2.1 Blood Vessel Physiology

The vascular system is comprised of vessels that deliver blood to and from the heart, specifically arteries (6 mm- 1.5 cm diameter) carry oxygenated blood away from the heart and veins (5 mm diameter) carry deoxygenated blood back to the heart. An artery gives rise to a smaller resistance vessel (so named because of the smaller diameter being

somewhat “resistant” to blood flow), an arteriole (10-100 μm diameter), that connect to capillaries (2-10 μm diameter) which give rise to venules (20-100 μm diameter) and finally to veins.[13] Blood vessels are comprised of an inner layer of endothelial cells, that are resistant to the adhesion of flowing platelets.

Surrounding this layer of endothelial cells is the extra cellular matrix (ECM) that contains various adhesive proteins such as collagen, fibronectin, tissue factor, and vWF. Smooth muscle cells adhere to the outside of the ECM and facilitate constriction and dilation of blood vessels for blood flow regulation. Due to their size, RBCs flow in the center of the vessel, pushing the smaller platelets closer to the vessel walls where they can quickly come in contact with an injury site. Flowing blood forms a laminar flow profile, where the velocity of blood at the center of the blood vessel is faster than near the vessel wall due to increased shear stress experienced at the flow/wall boundary. Shear rate is a term used to describe varying flow velocity in the blood vessel as a function of distance from the wall (expressed as $(cm \cdot s^{-1}) \cdot cm^{-1} = s^{-1}$). Under normal, physiological conditions the shear rate ranges between 500 and 5000 s^{-1}, but higher shear rates (in excess of 20,000 s^{-1}) are experienced during injury and serve to aid in platelet activation.[14] Blood is a non-Newtonian fluid meaning that its viscosity is dependent upon its shear rate, and higher shear rates and stress are experienced in smaller resistance vessels where lower hematocrits (percentage by volume of RBCs in whole blood) and viscosities are observed compared to larger vessels.[15]

1.2.2 Activation and Adhesion

Platelet activation in the event of vessel injury is primarily triggered by exposure of integrins on the platelet surface to adhesive proteins in the subendothelial ECM. Integrins

are transmembrane receptors that regulate ECM and cell-cell interactions. Injured or activated endothelial cells release factors to inhibit platelet activation (nitric oxide (NO) and prostaglandin I_2) so that not all platelets passing through the vessel participate in clot formation. Platelets first tether to an injury site when exposed vWF interacts with the platelet surface integrin GPIb-V-IX (25,000 receptors/platelet) which allows for an unstable interaction between the vessel wall and platelet resulting in rolling adhesion of the platelet with the surface. This rolling interaction facilitates GPVI interaction with collagen leading to a conformational change to a high affinity state for integrins on the platelet surface and release of ADP and thromboxane A2 (agonists of receptors that induce platelet activation). ADP is stored in granules in the platelet and thromboxane A2 is synthesized from arachidonic acid released by platelet membrane phospholipids.[16] α2β1 (4000/platelet) interacts with collagen in the ECM and aids in stationary adhesion. With 80,000 receptors on the platelet surface, GP IIb/IIIa is the main receptor for adhesion and aggregation. Ligands for GPIIb/IIIa include fibrinogen, fibronectin, and vWF interacting with collagen. GPIIb/IIIa integrins bind fibrinogen (converted to fibrin at the end of the coagulation cascade to form a platelet plug) between platelets to strengthen the formed thrombus.[17,18]

Purinergic receptors (regulated by nucleotides and adenosines such as ADP) on the platelet surface also facilitate platelet activation. P2Y1 and P2Y12 (ADP receptor) and P2X1 (ATP receptor) are G-protein coupled receptors (GPCRs) and have long been implicated as determinants in platelet activation and aggregation, respectively. Specifically, activation of these receptors leads to the following: Inhibition of adenyl cyclase within the platelet (breaks ATP down to cyclic AMP (cAMP) which is an inhibitor of platelet aggregation),

stimulation of dense granule secretion, mobilization of Ca^{2+} for platelet shape change, and facilitation of fibrinogen binding by making binding sites accessible (platelet-platelet aggregation). The purinergic receptor P2X1 is a ligand-gated cation channel (ATP activated) that allows for Ca^{2+} influx into the platelet, which is necessary for platelet spreading to occur.[19,20,21,22] A depiction of platelet plug formation can be seen in Figure 1.2.

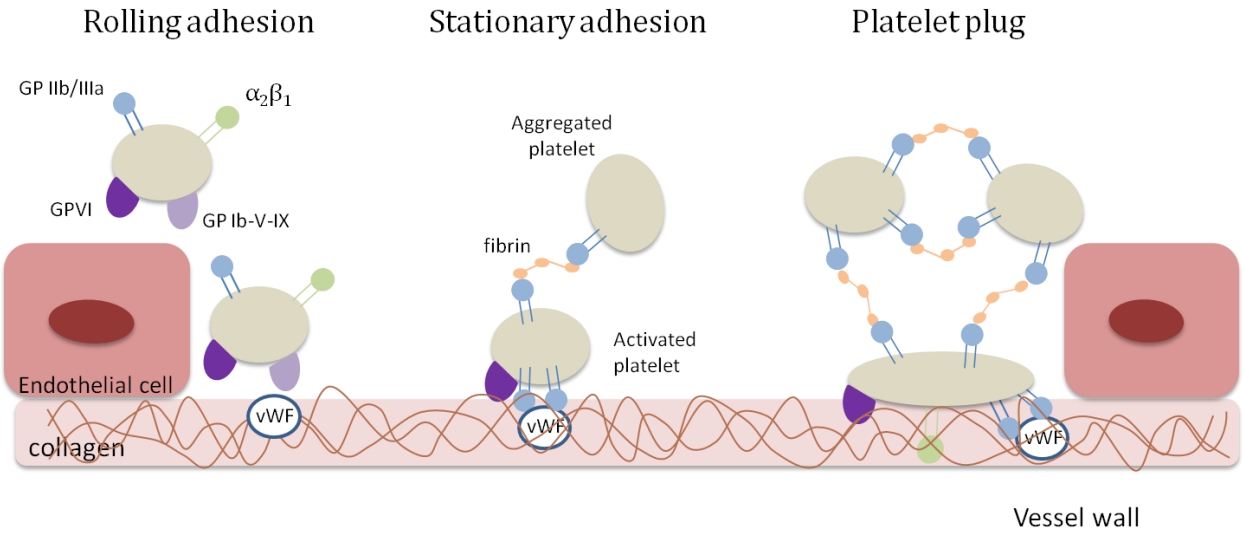

Figure 1.2 Platelet surface glycoproteins involved in platelet plug formation at site of injury. After an injury, components of the subendothelial layer become exposed. Rolling adhesion is initiated by GP lb-V-IX interacting with vWF. These interactions are not permanent, but slow the platelet and allow for stronger connections to be made. Stationary adhesion is brought about by GP IIb/IIIa and vWF bonding as well as GPVI interactions with collagen. Platelet adhesion to neighboring platelets is made through GP IIb/IIIa connections via fibrin. A stable platelet plug is formed when $\alpha_2\beta_1$ secures the platelet to the subendothelium and numerous platelet aggregates are participating in the plug.

1.2.3 Coagulation Cascade

The main function of the coagulation cascade is the formation of fibrin that forms stable bonds between GP IIb/IIIa integrins connecting platelets in a formed thrombus. In short, it results in the conversion of prothrombin to thrombin to facilitate fibrinogen conversion to fibrin. Throughout the cascade, various factors, most of which are inactive enzyme precursors, are converted to their active enzyme forms. Specifically, tissue factor

(TF), expressed by smooth muscle cells and cells in the outer layer of the vessel (fibroblasts), is exposed after vessel injury. TF has a high affinity for factor VII (FVII) that is found circulating in blood, and together TF and FVII form a complex containing the active form of FVII (FVIIa) that activates FIX and FX. FXa then forms a complex with FVa which is responsible for the conversion of prothrombin to thrombin. Thrombin converts the fibrinogen, forms platelet connections in an aggregate, to fibrin. Fibrin converts FXIII to its active form (FXIIIa), which serves to facilitate the cross linking of fibrin monomers.[23] A depiction of the coagulation cascade is shown in Figure 1.3.

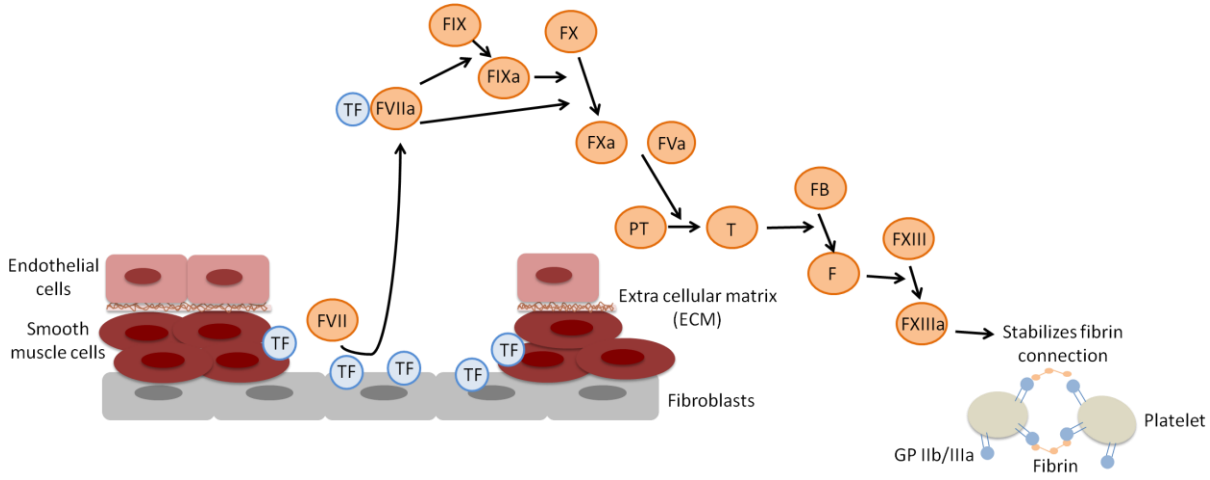

Figure 1.3 Coagulation cascade. Initiation of coagulation begins when tissue factor (TF) is exposed in subendothelial layers (smooth muscle cells and fibroblasts). Exposure of the plasma protein FVII to TF forms a complex that includes the activated form or FVII. Together TF and FVIIa activate FIX to FIXa. FIXa in conjunction with FVIIa converts FX to FXa. FXa and FVa convert prothrombin (PT) to thrombin (T) which converts fibrinogen (FB) to fibrin (F). Fibrin makes up the connections between aggregated platelets and is stabilized by FXIIIa.

1.2.4 Role of Platelets and Red Blood Cells in Blood Flow Regulation

RBCs carry oxygen to demanding tissues via hemoglobin, and platelets are integral for initiating thrombus formation, but beyond these vital abilities, these cells have also been implicated in the regulation of blood flow through the release of ATP and NO.

Furthermore, RBCs clustering around the thrombus often account for the majority of the thrombus mass.[24] RBCs contain millimolar concentrations of ATP,[25] and exposure of RBCs to mechanical deformation (shear stress), reduced oxygen tension, or pharmacological stimuli, results in the cell releasing nanomolar to micromolar concentrations of ATP, which results in the generation of vasodilators in the local endothelium.[26,27] Specifically, RBC-derived ATP release stimulates nitric oxide synthase (NOS) in endothelial cells lining the blood vessel.[28,29]

Binding of extracellular ATP to platelets leads to platelet activation prompting a shape change that makes platelets prone to aggregation with one another, and stimulates NOS in platelets leading to NO production.[30] Moreover, activated platelets release ATP (and other pro-thrombotic molecules) further serving to aid in local regulation of vascular tone.[1] NO, commonly referred to as the endothelium derived relaxing factor (EDRF), is a vasodilator that stimulates the relaxation of the smooth muscle surrounding endothelial cells which results in an increase in local blood flow. NO also serves to inhibit platelet activation and aggregation, potentially preventing a thrombus that can detrimentally occlude a resistance vessel.[31,32] Figure 1.4 shows the fates of RBC-derived ATP and NO in the vasculature. Malfunction of the ability of RBCs and platelets to respond to various stimuli that prompt the release of ATP and NO can contribute to and further propagate complications associated with circulation and the vasculature evident in numerous diseases.[26,31] RBCs from individuals with multiple sclerosis[33,34] and sickle cell anemia[35,36] release higher than normal levels of ATP and RBCs from individuals with diabetes,[37,38] cystic fibrosis,[39,40] and hypertension[41,42] display decreased ATP release.

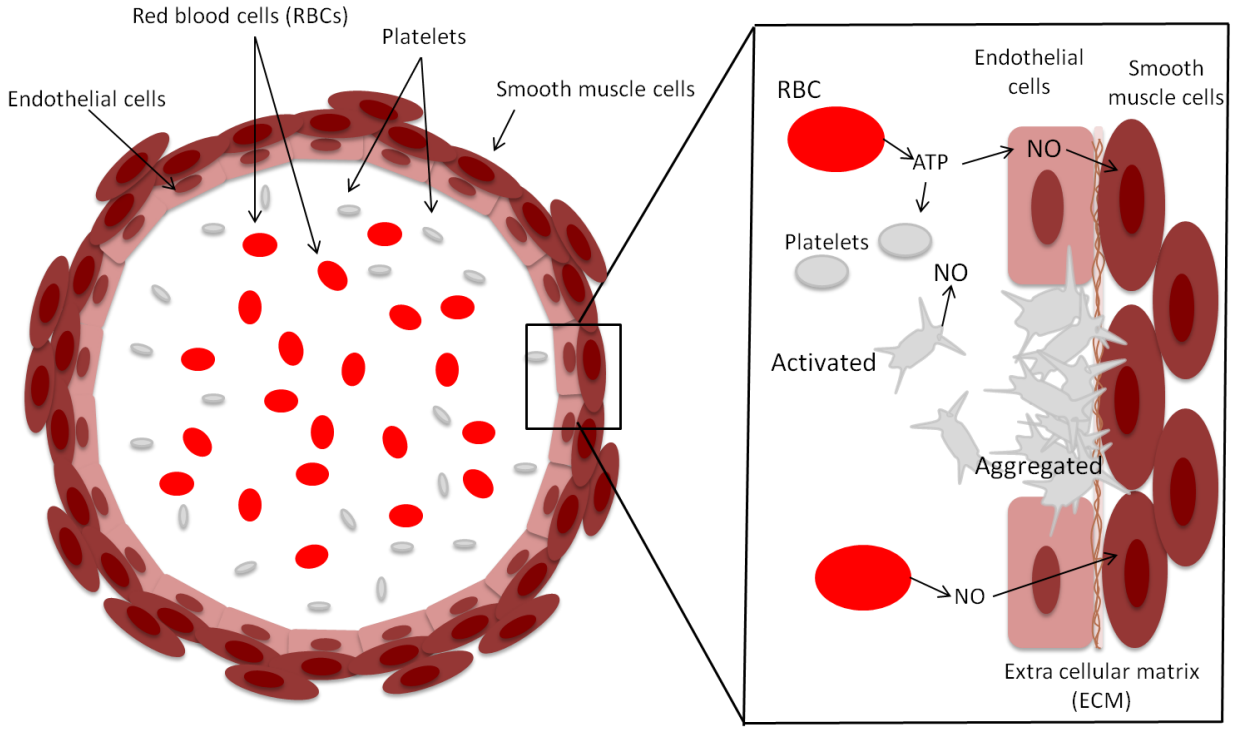

Figure 1.4 Blood vessel physiology. All blood containing vessels are lined with a single layer of endothelial cells surrounded by smooth muscle cells. Inside the vessel RBCs and platelets, the two most prominent blood cells, are shown with platelets occupying the space closest to the vessel wall. Upon various stimuli, the RBC releases nanomolar to micromolar amounts of ATP which stimulate NOS for NO production in the endothelium. NO can then stimulate smooth muscle relaxation allowing for vessel dilation. RBC derived ATP also activates platelets, causing them to undergo a shape change making the platelet more amenable to aggregation. In the event of an injury this process occurs to form a platelet plug over the site of injury to arrest blood loss.

1.3 Hyperactive Platelets and at Risk Diseases for Thrombus Formation

Increased platelet activity (hyperactivity) is a hallmark of a number of diseases that also often have increased atherosclerosis association, or plaque buildup on the vessel wall leading to stenosis (narrowing of the vessel). These diseases include diabetes, cystic fibrosis, hypertension, sickle cell anemia, and multiple sclerosis.[43,39,41,35,34]

1.3.1 Diabetes

Diabetes, a metabolic disease resulting in hyperglycemia due to insulin secretion and action defects, currently affects 20.8 million people in the United States, a number projected to increase to 48.3 million people by 2050.[44,45] Vascular complications associated with diabetes include hypertension, atherosclerosis, heart disease, and increased occurrence of heart attack and stroke.[46] Cardiovascular disease alone contributes to 66% of deaths associated with diabetes.[47] A major health concern is the increasing prevalence of stroke and heart attack resulting from platelet adhesion and thrombus formation after erosion of atherosclerotic plaque,[10] and patients with diabetes are two to three times more likely to develop atherosclerosis and suffer an atherosclerotic stroke or heart attack.[46,48] Furthermore, individuals suffering from diabetes have an increased number of platelets in the circulation that are hyperactive and prone to activation and aggregation.[49,50]

Diabetics are also known to have RBCs that display decreased ATP release compared to healthy individuals, due to decreased RBC deformability.[47,51] Diminished RBC-derived ATP results in less efficient NO synthesis in the endothelium and impaired vasodilation due to a decrease in NO-mediated relaxation of vascular smooth muscle.[29] These defects in components of the circulation may be contributing to the higher incidences of vascular complications in individuals with diabetes, as compared to healthy

controls.[29] The Spence group hypothesizes that the presence of a greater than normal amount of hyperactive platelets in conjunction with a decrease in RBC-derived ATP release results in the impaired ability to dilate local resistance vessels, and ultimately puts individuals with diabetes at higher risk for formation of a thrombus. This is paramount, as thrombus formation is the initial event in the disease process leading to heart attack, stroke, and peripheral vascular disease,[52,46] further exemplifying the importance of RBCs and platelets in regulating perfusion.

1.3.2 Cystic Fibrosis

Cystic fibrosis (CF) is a genetic disease that affects 1 in 2500 births and results in a defect in the cystic fibrosis transmembrane conductance regulator (CFTR) protein, an integral protein for fluid and electrolyte balance via ion transport through epithelial cells. Specifically, defects in the CFTR protein cause decreased chloride secretions for mucous membranes, leading to increased mucous blockages and reduced mucous clearance. For epithelial cells lining the lungs, blockages lead to infection and inflammation and eventually respiratory failure. Interestingly, platelets of individuals with CF have increased platelet aggregability and TXA2 release. Furthermore, there is an increased number of circulating hyperactive (more reactive to platelet activation agonists) platelets in CF patients and increased plasma ATP levels in comparison to healthy individuals.[39,53,54]

1.3.3 Hypertension

Hypertension (hypertensive cardiovascular disease or high blood pressure) is a risk factor for stroke, heart attack, heart failure, and peripheral vascular disease and is commonly affected by diet and exercise regimes.[55] Platelets from individuals with hypertension display increased aggregability compared to normal platelets, and a decrease

in plasma fibrinolytic activity.[56] As such, these individuals are at an increased risk to form clots and these formed clots are less likely to dissolve or disaggregate.

1.3.4 Sickle Cell Anemia

The hereditary blood disease sickle cell anemia (SCA) is characterized by irregularities in hemoglobin within RBCs, which cause the cells to take on a sickle shape instead of a biconcave shape. As hemoglobin is the oxygen-carrying molecule in the RBC, oxygen delivery is impaired in SCA. Furthermore, there is an increased activation and coagulation of platelets under non-duress conditions. Factors necessary for coagulation and platelet activation (factor V, prothrombin, etc.) are also increased in SCA.[35]

1.3.5 Multiple Sclerosis

Multiple sclerosis (MS) in an inflammatory, demylinating disease of the central nervous system (CNS). Over time, the myelin sheath protecting the axon of a nerve cell is degraded leading to a breakdown in CNS communication resulting in mental and physical impairments.[57] In several studies, MS-associated platelets were found to be more adhesive than healthy controls and those with inactive MS.[58,59,60] RBCs of individuals with MS release three times as much ATP compared to healthy controls,[61] which in conjunction with hyperactive platelets poses concerns in the event of vessel injury.

1.3.6 Altered Metabolic States of Stored Red Blood Cells

Current blood storage conditions in the United States immerse RBCs in environments containing 110 mM of glucose. For comparison, a healthy individual's blood glucose level ranges from 4-6 mM, and diabetic levels are classified as amounts > 7 mM.[62] These elevated glucose levels have adverse effects on the ability of RBCs to release ATP, a known agonist of platelet activation. In the event of a transfusion, these RBCs may not be

able to activate platelets as readily as healthy controls, putting the patient at an increased risk for hemorrhage or other deleterious effects such as decreased ability of RBCs to regulate blood flow.[63,64]

1.4 Methods for Monitoring Thrombus Formation and Platelet Activation

Historically, platelet activation and adhesion have been studied using either animal models or *in vitro* platforms ranging from microfluidic devices to specialized equipment. These models have proven invaluable in advancing knowledge on platelet function and their role in hemostasis, as well as characterizing aberrant platelet function in diseases where platelets are affected.

1.4.1 Animal Models

Animal models for thrombus formation include dogs, rabbits, mice, pigs, monkeys, cats, guinea pigs, hamsters, and rats. Benefits of small animal use include decreased costs, increased availability, and ease of thrombus monitoring due to small/often transparent blood vessels. Complex thrombus components including platelets, tissue factor, and fibrin have been imaged in real time in mice.[65] Small animals, such as mice, have also been genetically modified to result in atherosclerotic plaque buildup in vessels so that plaque injury can be studied. Large primates offer the best comparative model as platelet function and coagulation processes are the most similar to humans, however slight differences in the thrombolytic pathway do exist. Dogs and pigs have more differences from humans including differing levels of coagulation cascade factors (pig) and increased roles of platelets in the formed thrombus and RBCs that do not release ATP (dog).[66,67]

1.4.2 *In Vitro* Models

There are a number of commercial and academic based microfluidic *in vitro* models and clinical instrumentation available to study thrombus formation, platelet activation, and platelet adhesion. Aggregometers interrogate the activity of platelets by measuring light transmittance through a vial containing platelet rich plasma. An agonist of platelet activation (most commonly ADP) is added to the vial and the platelets begin to aggregate and create spaces in the suspension allowing more light to pass through. More active platelets will result in greater light transmittance. Flow cytometry has been used in conjunction with fluorescent tags to evaluate surface expression of platelet proteins and secretion mechanisms.[16]

Cellix is a commercial company that fabricates and sells microfluidic devices that feature microfluidic channels in parallel coated with either endothelial cells or collagen as a substrate. Studies monitoring platelet adhesion/thrombus formation on either of these surfaces can be made using purified platelets or whole blood as a sample source. Academic-based microfluidic devices typically feature channels in parallel and utilize either endothelial cells or adhesive proteins like collagen and fibronectin as ECM representatives. Devices designed for determining shear rate effects on platelet activation and adhesion,[68] inhibitors of platelet receptors responsible for platelet activation,[69] and more elaborate devices allowing for agonists/antagonists of platelet activation to be selectively introduced into the channel by incorporating a membrane into the device design have been reported in the literature.[70,71]

1.4.3 Comparison of Animal and *In Vitro* Models

Microfluidic devices are well suited to mimic blood vessels as realistic dimensions and shear stress experienced by blood cells can be recreated, human cells can be incorporated, and cell-cell interactions can be monitored. In a controlled manner, the *in vivo* environment can be selectively mimicked on an *in vitro* platform, allowing for desired agonists/vasculature components to be incorporated to evaluate specific interactions. Microfluidic devices fabricated using conventional soft lithography and etching techniques employing PDMS or glass substrates, respectively, have proven useful when creating environments for cell adhesion.[72,73] However, the development of microfluidic devices that facilitate studies involving an injury to the vessel wall has been limited for a number of possible reasons, including the multiple steps and tasks that must be simultaneously successful prior to analysis. For example, devices fabricated using PDMS and polystyrene require the use of a master for replicate molding,[74,75] and etching employs strong acids for microstructure formation.[76] Cell immobilization then needs to be followed by electrode integration for electrical lysis of cells in the microfluidic channel.

3D printing offers a more streamlined fabrication process compared to conventional techniques while removing the designer from the actual production of the device to be printed. Animal models such as primates are the ideal mimic to study thrombus formation with intent to compare to human processes. However, current thrombus formation studies are performed on animal models whose biology is not an exact match to humans, and using *in vitro* devices fails to incorporate components of the vasculature necessary for physiological thrombus formation.[77] A more accurate mimic of human thrombus formation

requires an *in vitro* model that incorporates elements of a resistance vessel. Namely, an endothelium, RBCs, platelets, white blood cells, plasma and collagen must be included.

1.5 Drug Discovery Implications

Microfluidic devices modeling *in vitro* thrombus formation also have the potential to be utilized in early stages of antithrombotic/thrombolytic drug discovery by providing a high throughput method for testing drug candidates.[78,79] Importantly, microfluidic devices that mimic the dimensions of the vasculature, incorporate blood flow, and integrate appropriate cell types to realistically determine drug efficacy ensure that non-viable drug compounds will not proceed further to animal models, thereby improving the efficacy of the drug testing process.[80,78] Figure 1.5 highlights where such a device could impact the field of drug discovery during *in vitro* testing in the preclinical stage. Currently it takes on average 12.5 years[81] and costs over a billion dollars (1.25 billion in 2005)[82] to bring a drug to market. A possible ten thousand drug candidates are whittled down through various stages of testing, when finally, one candidate makes it through to approval for human use.[78,83] During the drug research phase, possible candidates undergo high-throughput screening, a process that takes 4-6 years and encompasses 10,000 possible drugs. During the preclinical stage (1-2 years long, testing less than 250 compounds) a series of *in vitro* tests for drug potency, selectivity, and functionality are performed. This is followed by primary *in vivo* testing in rodent and rabbit models and secondary efficacy studies in canine, porcine, and nonhuman primate models. If successful during the preclinical stage, an application for drug testing in humans is submitted to the FDA. Only around 5 compounds make it to clinical trials where drug testing on humans in phases I, II, and III occurs over the course of 4-6 years. During phase I 20-100 participants are given the drug

to test for side effects, dosing, and drug efficacy. Phase II (over 200 participants) focuses on random dosing including the use of placebos. Single and double blind studies are performed where either the subject or providers are unaware of whether or not a drug or placebo is administered to further test drug efficacy and safety. Phase III enlists 1000-5000 participants and expands on the efficacy and side effects studies performed in previous phases. If a compound successfully completes phase III clinical trials, it is reviewed by the FDA and if approved, large scale manufacturing commences.[84,85,86]

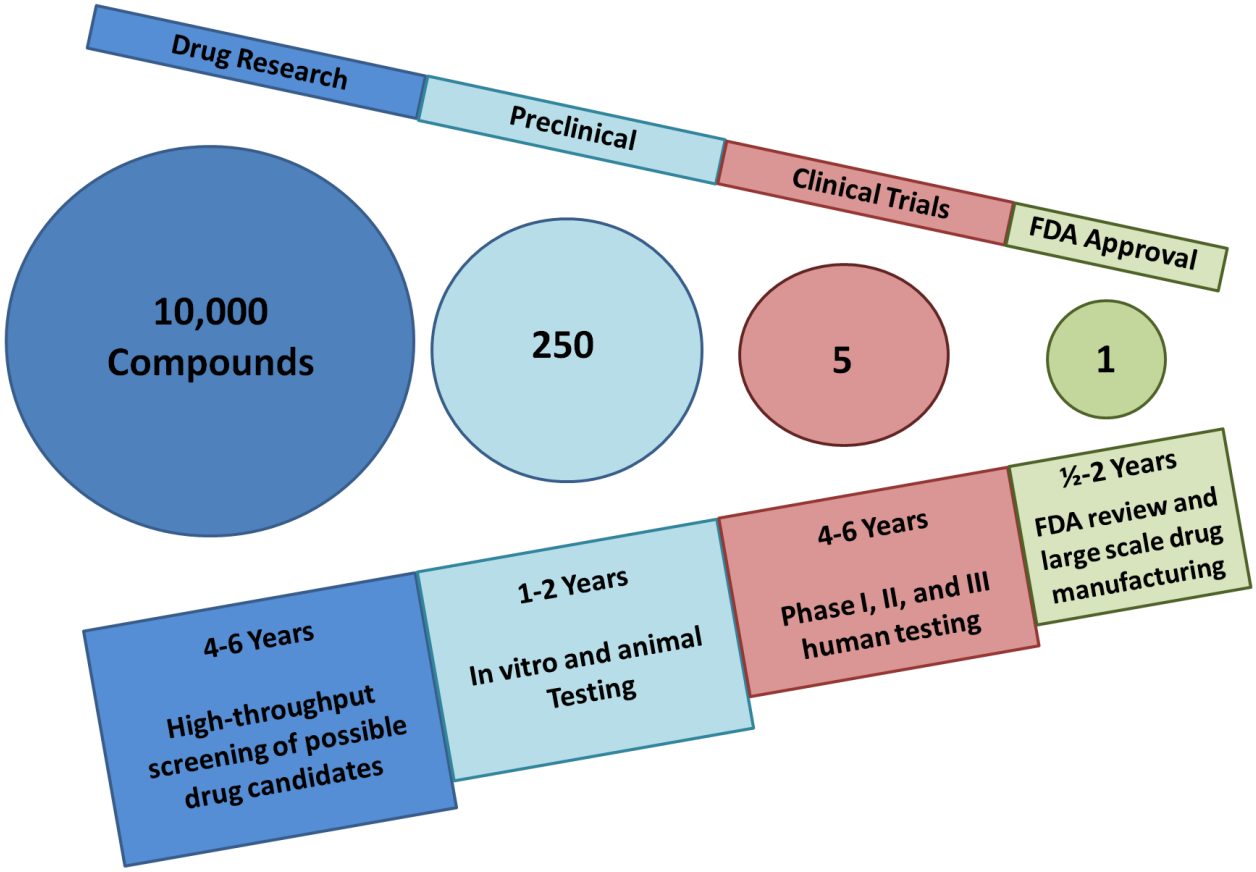

Figure 1.5 Therapeutic target identification and validation process. The drug discovery process begins with high-throughput screening of 10,000 possible drug candidates spanning the course of 4-6 years. During the 1-2 years of the preclinical stage where only 250 candidates remain, *in vitro* testing in isolated systems for potency and functionality occurs as well as primary *in vivo* efficacy testing on rodent and rabbit models followed by secondary studies on canine, porcine, and nonhuman primate models. If these studies are successful then the candidate is an applicant for testing in humans. Around 5 compounds make it to clinical trials with humans. This process spans 4-6 years and encompasses phase I (20-100 participants), II (over 200 participants), and III (1000-5000 participants) testing. Throughout these phases drug efficacy, side effects, and single and double blind studies are carried out to further evaluate the drug candidate. For antithrombotic and thrombolytic drug testing, a microfluidic-based vascular mimic such as that described in this dissertation could be implemented in the preclinical stage during *in vitro* testing to aid in eliminating ineffective drug candidates.[84,78]

1.6 Methods of Cell Lysis for Injury Simulation

Cell lysis, the disruption of the cell membrane resulting in the release of cellular contents, has previously been achieved on microfluidic platforms.[87-92] Cell lysate is typically used for the analysis of cellular components such as DNA. However, cell lysis techniques can prove useful in mimicking vascular injury. Physical, mechanical, chemical, and electrical lysis methods are commonly employed to achieve cell lysis.[89,93,94] When choosing a lysis method suited for vascular injury recreation using a microfluidic device the ease and efficiency of lysis, the ability to scale down to small dimensions, and maintenance of *in vivo* conditions need to be addressed.

1.6.1 Physical Lysis

Thermal cycling[92] and cavitation, the generation and collapse of bubbles produced from ultrasound driven pressure waves,[95,96] have been used to physically lyse cells. *In vivo* methods of physical lysis are typically limited to applying pressure to the blood vessel with blunt instruments, such as forceps, or by simply introducing a wire into the vessel.[67]

1.6.2 Mechanical Lysis

Mechanical lysis has been achieved by introducing cells into a channel lined with nanoscale barbs fabricated using deep reactive ion etching on a silicon wafer substrate,[90] with abrasive action using beads in a microfluidic chamber,[97] and by compression on polydimethylsiloxane (PDMS)-based microfluidic devices.[98]

1.6.3 Chemical Lysis

Lytic agents, such as detergents like sodium dodecyl sulfate (SDS), are commonly used to chemically lyse cells by disrupting the lipid membrane.[91,99] Ferric chloride is a typical chemical used to cause thrombus formation in animal models and is applied to

gauze and placed on an artery.[100,101] Photodynamic therapy (PDT) is an approved chemotherapy treatment in many countries, and relies on the use of chemicals (photosensitizers) that when irradiated with a specific wavelength in the presence of oxygen produce free radicals and singlet oxygen that lead to cell apoptosis, autophagy, and necrosis. PDT results in visible cell swelling, membrane distortion, and disruption of the lipid membrane.[102,103] Direct laser irradiation of vessels without the use of a photochemical has also been used in animal models for thrombosis formation studies.[67]

1.6.4 Electrical Lysis

There are two main avenues for lysis on a microfluidic device when electrodes are involved: electrical lysis or lysis via electrochemically generated hydroxide. Lysing adhered cells by hydroxide generation is difficult to control and exposes cells to chemicals not typically present in the blood stream. Electrical cell lysis requires a transmembrane potential of the cell to be greater than 1V, potentials less than or equal to this lead to poration of the cell membrane. This transient pore formation is reversible if the external electric field is removed and allows for cell fusion or delivery of drugs or DNA into a cell, but will not lead to cell lysis.[104] Electrical lysis on microfluidic devices typically entails applying a large electric field ($kV \cdot cm^{-1}$) with short lysis times (< millisecond) and has been successfully used for cell analysis studies.[87,89,105] Furthermore, electrical lysis employing a low voltage (< 100 V reported in the literature)[93] and a channel geometry featuring a narrow region have resulted in sufficiently large electric fields to lyse cells.[88,93,106]

1.7 3D Printing Principles

3D printing, also known as additive manufacturing, rapid prototyping, or solid freeform technology, was first introduced in the 1980s.[107] The principle of the technique

relies on generating a 3D model using computer aided design (CAD) software and then converting the design into a standard tessellation language (.STL) file which can be interpreted by the 3D printer. The .STL file stores the information of the design in the form of triangulated sections, with coordinates of the vertices defined in a text file. Higher resolution can be obtained by increasing the triangle density that defines a surface so that more data points exist in the text file to define the 3D model's surface. Figure 1.6 is a graphic representation of the information stored in an .STL file for a 3D printed device.

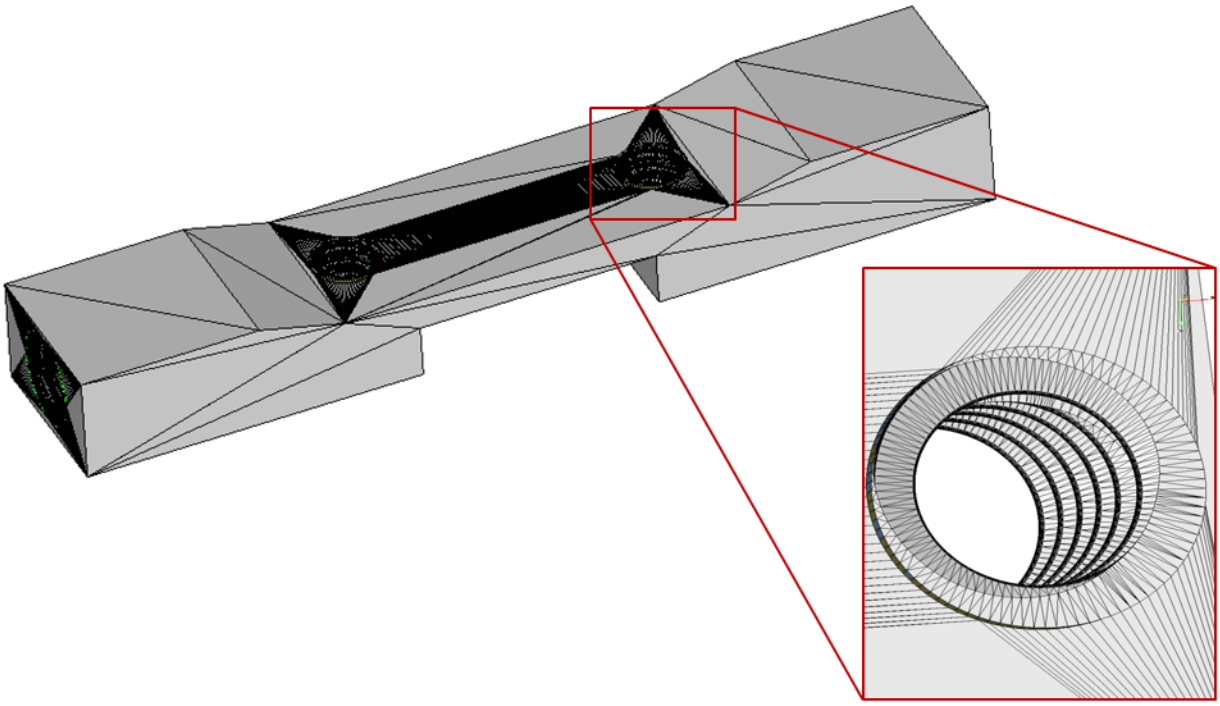

Figure 1.6 Representation of information stored in an .STL file. Models designed using CAD software are converted into .STL files which represent graphic information in the form of triangles. Each vertice of the triangle is a data point that is interpreted by the printer. High density areas of triangles correspond to parts of the device of higher resolution.

The coordinates contained in the .STL file are converted into a G-file via slicer software present in the 3D printer. Specifically, the G-file divides the .STL file into a sequence of two-dimensional (2D) horizontal cross sections, which allows layers of the 3D object to be printed in an additive, consecutive manner from a series of 2D layers. Improving the finished product through the development of better slicing algorithms is an ongoing area of research.

There are five types of 3D printers: stereolithography (SLA), inkjet printing, selective laser sintering (SLS), fused deposition modeling (FDM), and laminate object manufacturing (LOM). Beyond differences in the basic printing techniques between these printers, the material and resolution of formed objects is often different for each.

1.7.1 Stereolithography (SLA)

SLA was the first commercialized additive manufacturing technology developed by Chuck Hull in the early 1980s.[107] The principle of the technique relies on UV-initiated curing of defined photoresist layers. The two approaches for SLA printing are direct/laser writing (Figure 1.7 A) and mask-based writing (Figure 1.7 B, digital light projection).[108,109,110] These techniques are categorized as free surface (Figure 1.7 A, bath configuration) and constrained surface (Figure 1.7 B, layer configuration) depending on the orientation of the laser source. Direct/laser writing encompasses a movable base, liquid resin tank, UV light, and computer interface. Mask-based writing utilizes the movable platform, resin tank, computer, UV beam and a mask or digital mirror device that facilitates layer-by-layer curing. The bath configuration, the oldest technique of SLA, requires UV beam tracing a 2D cross section onto a base submerged in a tank of photoactive liquid resin that polymerizes upon irradiation.[111] Exposure duration, scan speed, power source

intensity, and energy of the UV light all control the thickness of the cured resin layer. After a layer is formed, the base lowers into the resin vat by a predefined distance and UV-curing of the next layer commences. In between curing steps, the surface of the resin is leveled to ensure uniform layers. Vat size limiting the height of the 3D models, resin waste, and extensive cleaning procedures are limitations of the bath configuration.[112,113]

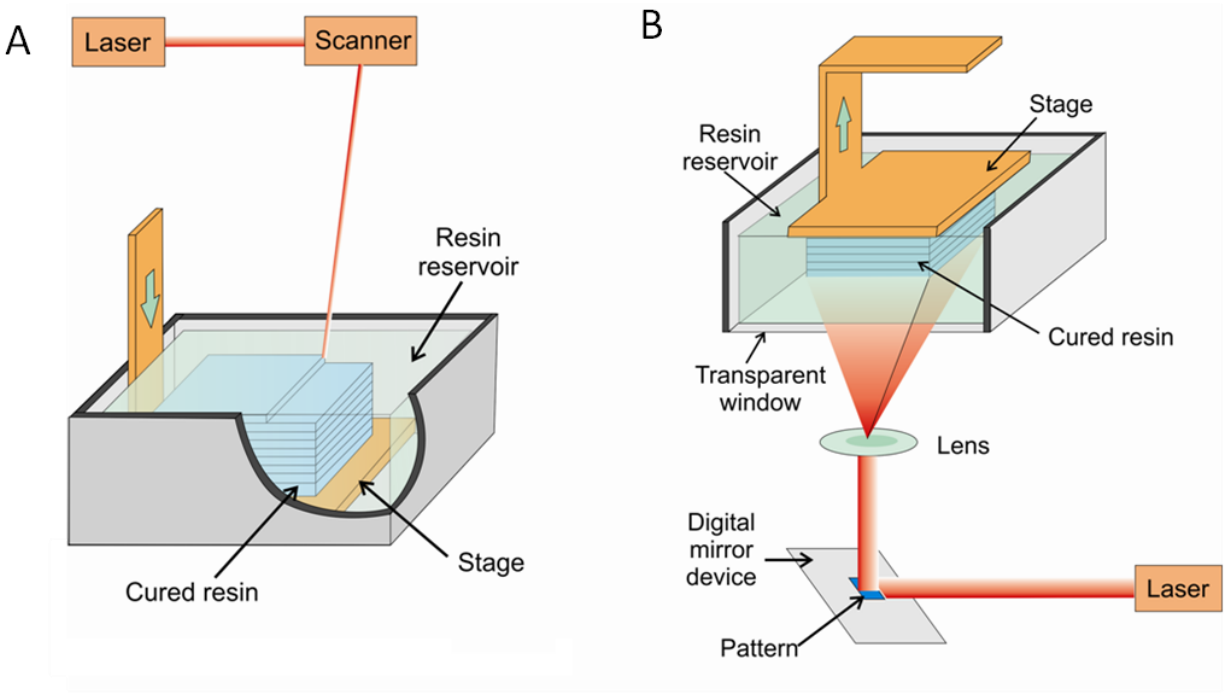

Figure 1.7 SLA 3D printer bath and layer configurations. The bath configuration utilizes a stage just below the surface of the resin and a laser moves along the surface of the resin, until completely curing a layer. The stage then lowers allowing a new layer of resin to cover the build area (A). Layer configuration where the stage is submerged into a reservoir of photopolymer a defined distance. A laser is used to polymerize the resin in defined areas. For projection based curing, a DMD is used for an entire layer of resin to be cured simultaneously. After a layer is finished, the stage is raised a defined distance, exposing uncured resin and the process continues until device completion (B).

For the layer configuration, the movable platform is suspended above the resin reservoir instead of being submerged, and the UV light is positioned beneath the optically clear vat. This allows for lower resin volume and unrestricted part height. During printing, a thin layer of resin fills the reservoir where it meets the movable platform. After curing the

first layer, the platform raises and uncured resin fills the gaps left from the cured layer. This process is repeated until the device is completed.[114,115]

For both configurations, a final step of UV irradiation is performed after fabrication to ensure all reactive groups of the resin are polymerized and to strengthen the bonding of the final object.[116,117] The mask-based approach relies on a digital mirror device (DMD) employing millions of mirrors that allow for an entire layer to be cured at once, reducing layer production time.[110,118] The thickness of the cured layer with this approach can be summarized in equation 1.1:

$$C_D = D_P \ln\left(\frac{E}{E_c}\right) \qquad \text{Equation 1.1}$$

where layer thickness (C_D) is governed by the intensity of the light source (E), the crucial energy of the resin (E_C), and the depth of light penetration (D_P).[119,120] Optimizing layer thickness is a route to increase the curing efficiency. Vertical resolution is dependent on the cured layer thickness (single-digit micrometer) and lateral resolution depends on the diameter of the UV beam (80-250 μm).[110,118,119,120]

Selection of a UV light source depends on the resin, with the HeCd laser (325 nm) and xenon lamp being the most common sources.[110,121,115] For higher resolution applications, two photon polymerization has been utilized.[122] Resin cost, waste, and the fact that only one resin can be used at a time, are all limitations of SLA. The majority of resins are epoxy or acrylic based and often shrink upon polymerization and become brittle.[123,124] SLA printers themselves are typically expensive, but offer high resolutions (70-250 μm in the X/Y plane and 1-10 μm in the Z plane).[125]

1.7.2 Fused Deposition Modeling (FDM)

FDM is one of the cheapest 3D printing technologies due to the simple mechanics of the printer and the low cost of the build materials. Because of this, FDM printers enjoy widespread use and are one of the most common personal printers on the market today. 3D objects are fabricated by heating thermoplastic materials and feeding them through a nozzle that deposits the material onto a movable platform as seen in Figure 1.8. The nozzle traces the design in horizontal cross-sections and semi-molten plastic is deposited and solidified; the stage then lowers and the process continues.[126,127,128] Staircase and chordal effects resulting from the nature of the slicing software and the .STL file format are common in FDM. These effects can be best understood when considering how a channel would be formed with an FDM printer. The printer would start to deposit plastic for the base of the design and to accommodate the channel would offset each layer resulting in an overhang of material. Defects in feed filament diameter and density can result in imperfections in the printed objects.[129] The resolution of FDM printers is the lowest of any other technique (250 μm XY, 50 μm Z direction), but multiple materials can be easily incorporated into an object by simply changing the plastic filament feed. Common materials used with FDM printers are wax blends, polycarbonate, polystyrene, acrylonitrile butadiene styrene (ABS), glass reinforced polymers, metal, ceramics, and bio-resorbable materials.[130,131] Ceramic and metal powders require the addition of a binder so that these materials can be used in filament form.[131]

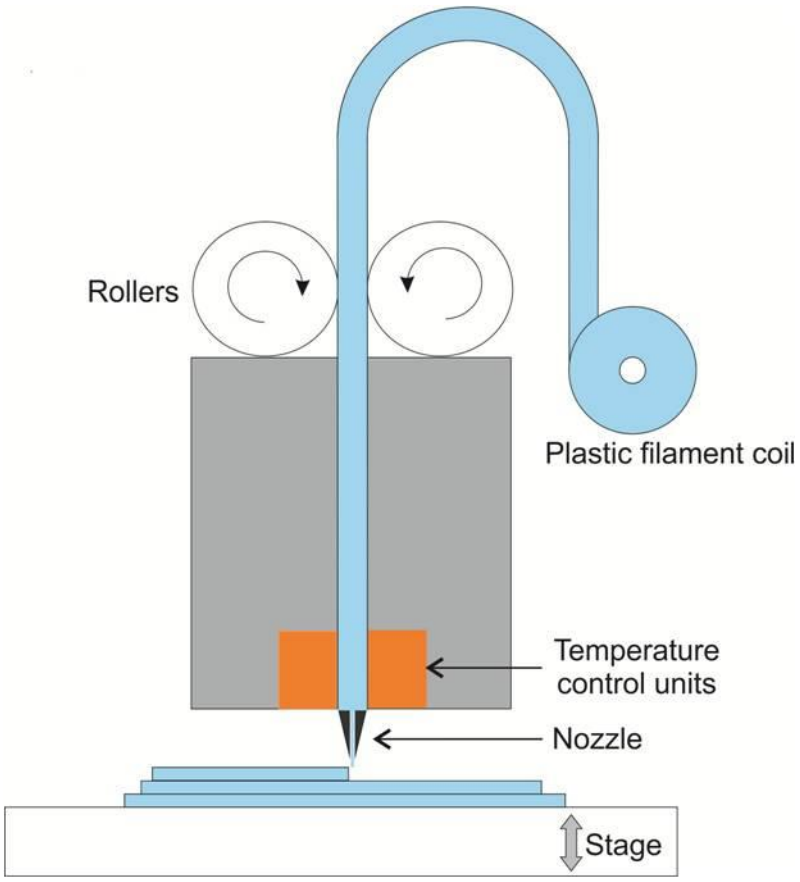

Figure 1.8 FDM 3D printer apparatus. Plastic filament is guided through a heated block where it becomes semi-molted and can be printed through a nozzle onto an adjustable stage. After a layer is deposited, the stage is lowered and subsequent material deposited in an additive fashion to form the final object.

1.7.3 Selective Laser Sintering (SLS)

SLS utilizes a high power laser (e.g. CO_2 and Nd:YAG) to sinter polymer powders to form a 3D model.[132,133] As seen in Figure 1.9, the first layer of powder is evenly distributed onto the build stage via a roller and the powder bed is heated to a temperature below the material's melting point.

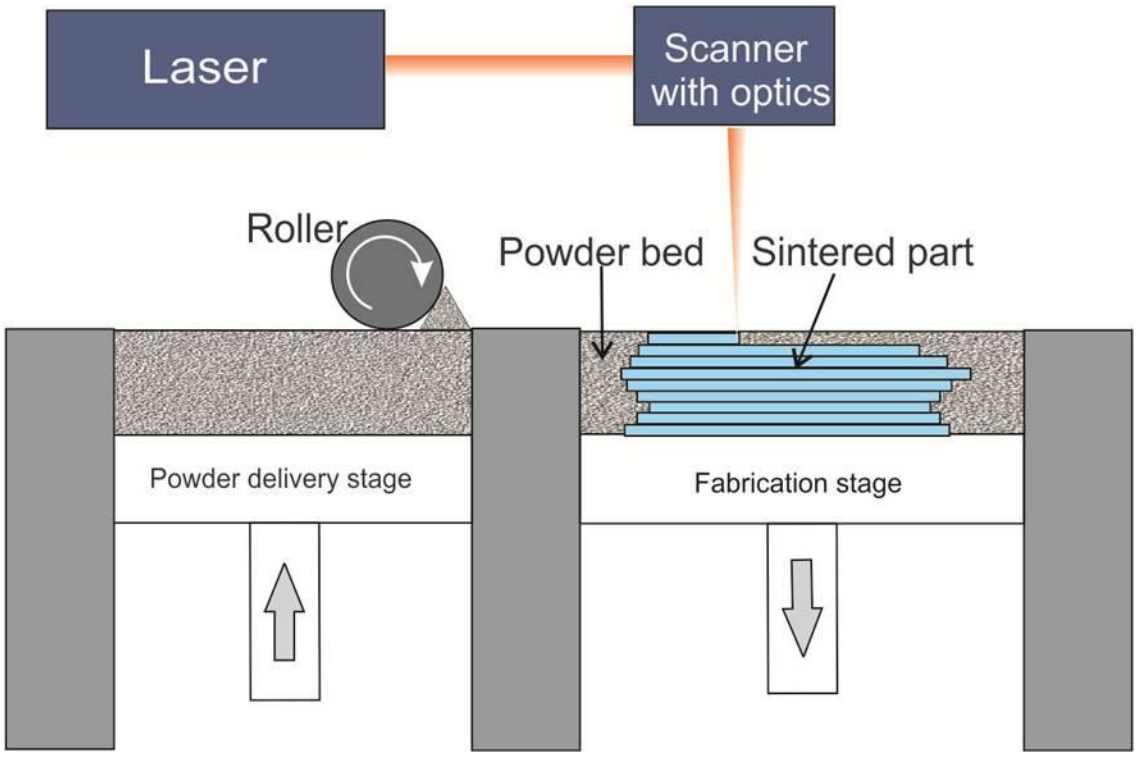

Figure 1.9 SLS 3D printer apparatus. The printing stage for SLS is lowered a defined distance and a roller administers an even layer of powder. A laser is used to polymerize the powder in specific areas. The stage lowers and fresh powder is rolled over the build area, and the process repeated until the device is completed.

Based on the data contained in the .STL file, desired areas are scanned with a laser to raise the temperature above the melting point, fusing particles together. After the base layer is completed, a fresh layer of powder is added and smoothed and the process continues. Unbound powder acts as support material during printing and is removed after fabrication.

This technique can be used with a wide variety of materials including polycarbonate, polyvinyl chloride, acrylonitrile butadiene styrene, nylon, resin, polyester, metal, and ceramic powders.[134,135,136] Thermal heating and subsequent cooling often leads to shrinkage and model deformation.[137] Laser power and focusing along with the size of the powder material all contribute to the 3D object's resolution. Current resolutions for SLS are 50 μm in the XY plane and 1-2 μm in the Z direction.[135,138]

1.7.4 Laminated Object Manufacturing (LOM)

Paper, plastic, and metal sheets are stacked together to form 3D objects using LOM[134] (Figure 1.10). Sheet material is rolled over a movable stage and a laser or razor traces each layer's cross-section to define the pattern.[139,140] New material is then rolled over the stage and the process continues with the stage lowering for subsequent layer deposition. Either the stage or supply roll is heated to adhere layers together.[141] Non-uniform heating can result in defects such as delamination or structural damage.[142] Consecutive layers are joined using adhesives or welding based on the material. Material use with LOM is limited to those that can be made into sheets and bound with adhesive or welding, namely adhesive-coated polymers, paper, cellulose, and metal sheets. This limits the applicability of this technique in some fields as paper or cellulose may not be amenable to certain chemical applications. The resolution of LOM based devices is 10 μm in the XY plane and 100 μm in the Z direction.[126]

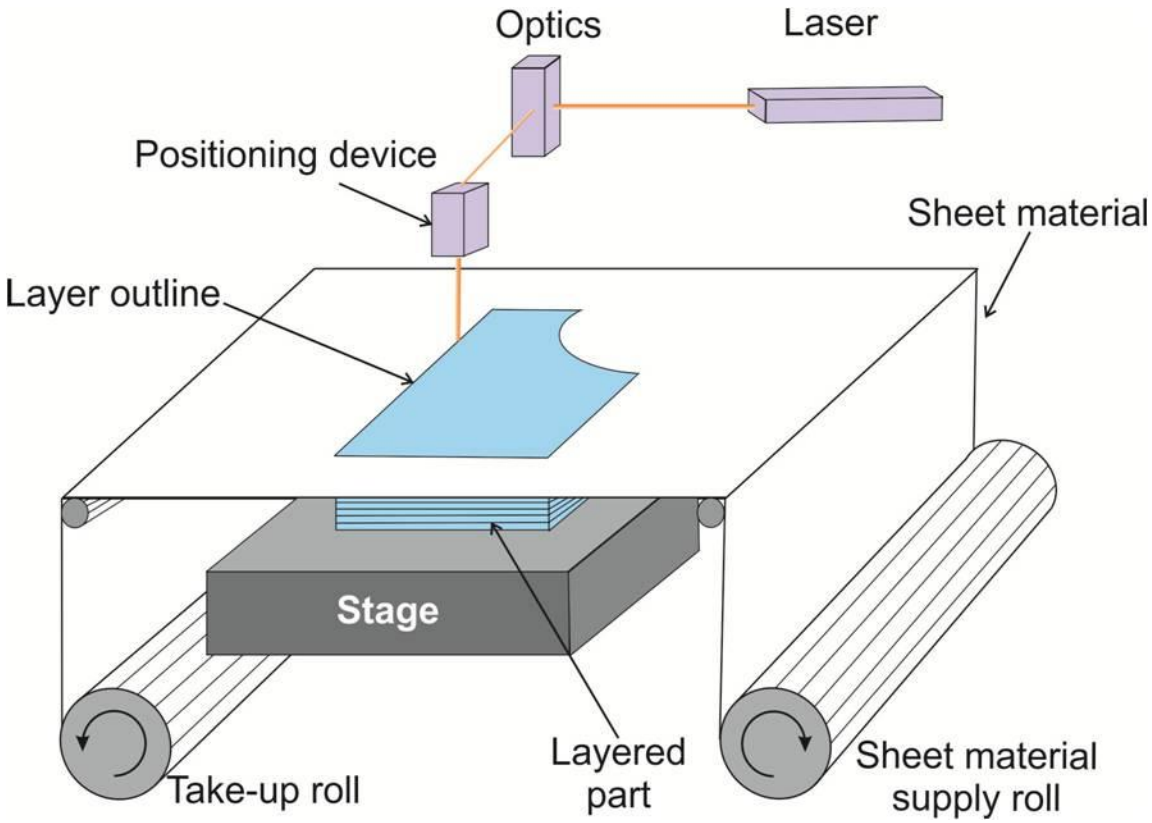

Figure 1.10 LOM 3D printer. A sheet of material is rolled over the build stage and either a laser (shown) or a razor is used to trace the outline of the layer. Excess material is removed, the stage adjusted, and a new layer of material rolled over the stage. Consecutive layers are secured via adhesive (paper material) or by welding (metals).

1.7.5 Inkjet Printing

Inkjet printing is mainly a powder-based method where layers of solid particles (sizes range from 50-100 μm) are bound together by a printed liquid material.[143]

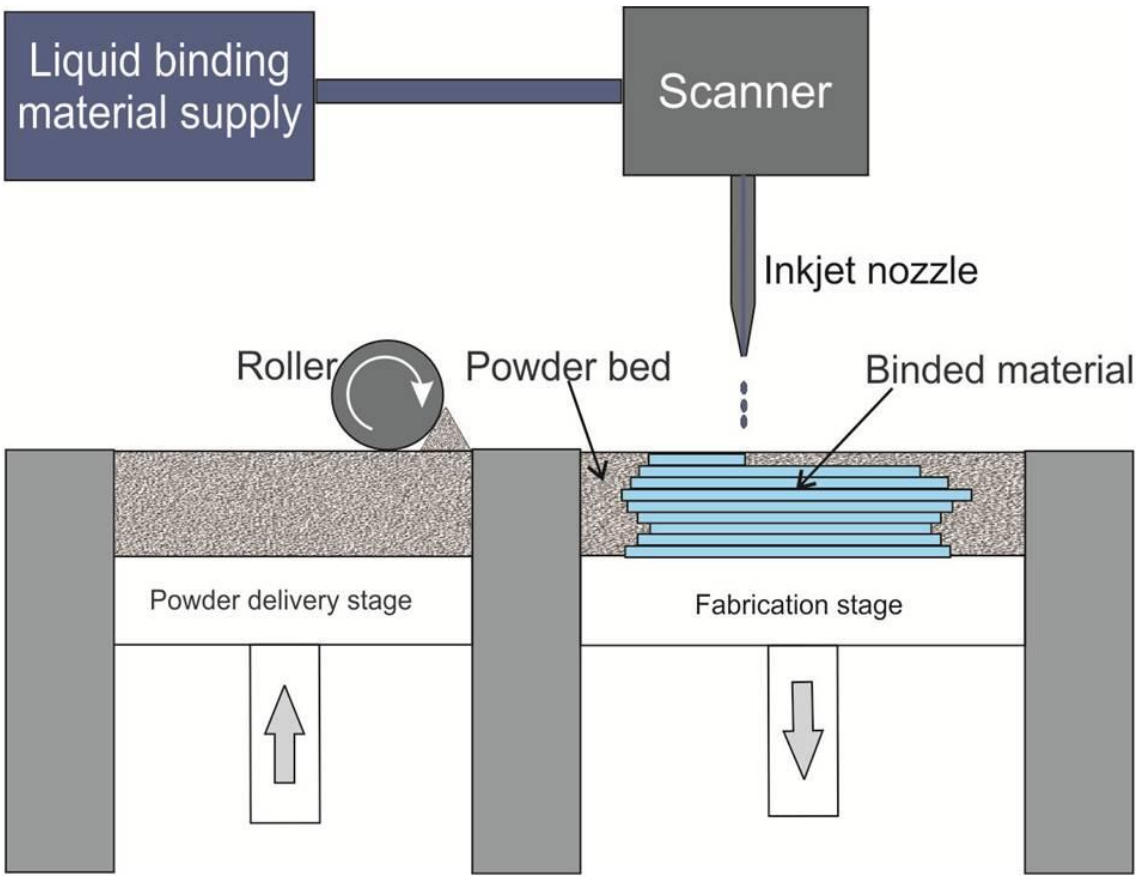

Figure 1.11 Inkjet 3D printer. The build stage is lowered a defined distance and a roller administers an even layer of powder material. A printing head prints liquid binding material onto the powder bed in desired areas. After one layer is complete, the build stage lowers and a new layer of powder is rolled and the process continues.

As seen in Figure 1.11, a layer of powder (polymer, ceramic, or glass based) is distributed on the top of a support stage by a roller and an inkjet printer head prints droplets of liquid binding material onto the powder layer in desired areas. After the first layer, the stage lowers and a second powder layer is distributed and selectively combined with the liquid

bonding material. Heat treatment follows this additive deposition step to enhance binding. Void spaces are supported by unbound powder that can be removed after fabrication.

Inkjet printing has found widespread use in biological scaffolding as it does not require a photopolymerizable materials or liquids with specific viscosities due to powder-based material use. Materials for inkjet printing includes polymer, ceramic, and glass powders combined with a liquid binding agent.[118] Limitations of powder-based inkjet printing arise as the printed liquid's chemical and physical properties dominate the final printed device. Many polymer glues are biologically toxic and therefore unfit for use in tissue scaffold fabrication. Furthermore, the optical transparency of finished devices is often lacking from incomplete binding of liquid with powder particles. The inherent porosity of finished models and surface roughness can also be a disadvantage depending on the application.[144] Inkjet printing offers resolutions of 20-50 μm in the XY plane and 50 μm in the Z plane.[145,] Non-powder based inkjet printers exist, typically employing polymer, and are often referred to as polyjet printers and are a hybrid between SLA and inkjet.

1.7.6 Polyjet Printing

Polyjet 3D printing (Figure 1.12) utilizes photo-curable resins containing a photoinitiator that are deposited from a jetting head and then exposed to UV light to initiate photo-polymerization.[146] For models that contain a void space such as a channel, the printer deposits support material that also contains a photoinitiator.[147] The support material can be removed by physical and chemical means after the model is printed. Even after removal of support material the rough sides remain, posing a possible limitation of fabricating channels with this type of printer. Droplet resolution of polyjet 3D printers is 100 μm in the XY direction and 16 μm in the Z direction.[148] Material use is often limited to

the proprietary photoresins provided by the manufacturer or risk voiding the printer's warranty through custom resin use.

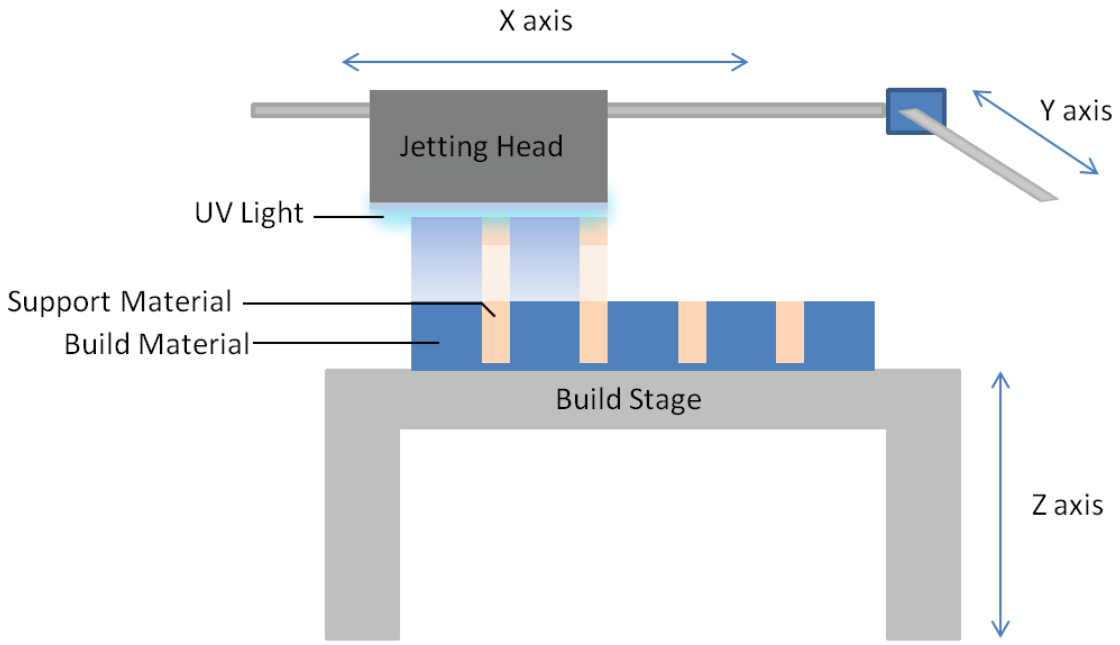

Figure 1.12 Mechanics of a polyjet 3D printer. The jetting head moves over the surface area of the build stage and deposits build material (photocurable resin) or support material (void spaces) in an additive manner. The materials are scanned with UV light to initiate photocuring before the next layer is added. Resolution for the printer used in these studies is 100 μm (X/Y) and 16 μm (Z/height).

1.8 Utility of 3D Printed Devices for Biological Studies

3D printing has found use in biomedical engineering, pharmacokinetics/ pharmacodynamics, forensic science, education, electronics, industry, and customizable labware. However, it is the emergence of the technique for chemical applications in micro/macro-fluidics that has allowed for a more streamlined fabrication process compared to soft lithography. Extensive efforts have been made with 3D environments to control cell patterning using soft lithography, which has proved to be useful for this purpose. However, compared to soft lithographic techniques, 3D printing offers a simpler fabrication process by eliminating the need to use a master for replica molding. 3D printing

has overcome some of the troubles that have plagued traditional replica molding techniques, including a lack of standardization between laboratories and the labor-intensive fabrication process.

One of the first examples of 3D printing technology being applied towards microfluidics was the fabrication of a complex microvascular network composed of 100-300 μm cylindrical channels capable of diffusion-based mixing under laminar flow profiles and mixing from turbulent flow in 2003.[149] Researchers from Stanford 3D printed a bionic ear utilizing silicon scaffold incorporating chondrocytes and silver nanoparticles for cochlea formation interfaced with electronic modalities capable of detecting electromagnetic frequencies produced from a stereo.[150]

Organ-on-chip efforts are another example of how 3D printing has been utilized for tissue engineering applications. The liver in particular is a heavily researched organ-on-chip candidate, and a number of different 3D printing techniques have been used in the fabrication of a scaffold integrated with hepatocytes.[151,152,153] Due to the plethora of diseases that affect the cardiovascular system, a large area of tissue engineering has been applied to vasculature reconstructions. To accomplish this a variety of rapid prototyping techniques and materials have been used resulting in designs as simple as a single channel,[154] to the recreation of complex vascular pathways,[155] and even complex collagen scaffolds.[156]

1.9 Challenges of 3D Printing for Microfluidic Applications Featuring Cells

One of the main challenges that exists and must be overcome for 3D printing to become more applicable to biological sciences involving cells is the development and implementation of materials that are amenable to cell culture. Currently, the material pool

for 3D printers is limited to those that can be made into powder form or have low enough viscosities to be extruded from a printing nozzle. Furthermore, a number of 3D printers require users to utilize only approved resins, whose components are proprietary, or forfeit the warranty on the printer. There are a number of commercially available materials that are medical grade, or compatible with living tissue implantation, and numerous examples of 3D printed prosthetics prove this.[147,157,158] However, examples of these materials comprising *in vitro* devices with adherent cells are lacking from the literature. Post-print processing of printed devices to improve optical clarity is also an area in need of improvement as resolution of these devices is not yet high enough to forego this step and achieve optical resolution on par with traditional soft-lithography based devices. Post-print processing is especially necessary for those printing techniques that require the use of support material to print void spaces. Resolution limitations are constantly improving as the technology advances, but methods to improve optical clarity and material amenability for cell culture in microfluidic channels are needed for 3D printing to find widespread utility in biomedical devices.

1.10 Project Objectives: Soft-Lithography and 3D Printing Technologies for *In Vitro* Fluidic-Based Thrombosis Mimics

Platelets play a major role in regulating hemostasis by arresting blood loss. Platelets in conjunction with RBCs regulate blood flow through the release of ATP and NO. ATP release from RBCs stimulates platelet activation through the purinergic receptor P2X1. ATP stimulates NOS in endothelial cells lining the blood vessel to produce NO which in turn diffuses to the surrounding smooth muscle cells and triggers relaxation of these cells and dilation of the vessel. NO released from endothelial cells prevents platelet adhesion to the

vessel wall and platelet-derived NO release, a consequence of platelet activation, inhibits further platelet recruitment to a formed thrombus.

Current *in vitro* mimics of *in vivo* thrombus formation are often incomplete in that they lack components of the vascular wall and fail to simulate injury. The work presented here is based on the hypothesis that soft-lithography based microfluidic devices and 3D printed fluidic devices can be utilized as *in vitro* models of thrombus formation. As shown in Figure 1.13 (for a 3D printed version relying on electrical lysis), these devices will mimic *in vivo* conditions by encompassing and allowing for the following: incorporation of vascular components, multiple cell type interactions, flow conditions, platelet adhesion/blood clot formation, and injury induction on chip. Specifically, the design and development of devices relying on various lysis techniques for injury simulation and differing fabrication techniques will be discussed and evaluated. Furthermore, the impact of these devices on studying blood flow mechanics in diseases with aberrant platelet function (diabetes, MS, CF, hypertension, and SCA) and the drug discovery process of anti- and thrombolytic drugs will be discussed.

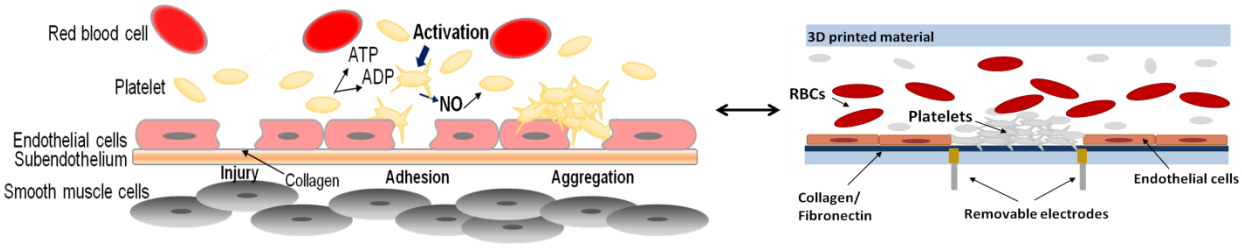

Figure 1.13 Microfluidic technologies for *in vitro* thrombosis mimics. The devices detailed in this dissertation aim to recreate sub-endothelial collagen exposure after blood vessel injury triggering platelet activation and blood clot formation through various lysis techniques leading to endothelium injury (electrical lysis with electrodes shown).

In detail, Chapter 2 of this dissertation describes various means of achieving chemical lysis of adherent endothelial cells on microfluidic devices fabricated using conventional soft-lithography techniques. Chapter 3 outlines the design, fabrication, and characterization of 3D printed devices featuring removable electrodes for electrical lysis of adhered cells. Utilization of the 3D printed device as an *in vitro* platform for thrombus formation is discussed in Chapter 4. Lastly, Chapter 5 summarizes the conclusions of the previous chapters, introduces new techniques for evaluating a formed thrombus, and delineates the future directions of this project.

REFERENCES

REFERENCES

(1) Harrison, P. *Blood Reviews* **2005**, *19*, 111-123.

(2) Klinken, S. P. *The International Journal of Biochemistry & Cell Biology* **2002**, *34*, 1513-1518.

(3) Weiss, H. J. *The New England Journal of Medicine* **1975**, *11*, 531-541.

(4) Ogawa, M. *Blood* **1993**, *81*, 2844-2853.

(5) Italiano, J. E.; Hartwig, J. H. In *Platelets* Michelson, A. D., Ed.; Academic Press: Burlington, MA, 2007, pp 23-44.

(6) Kaushansky, K. *The New England Journal of Medicine* **2006**, *354*, 2034-2045.

(7) Hartley, P. S. *Clinical Laboratory* **2007**, *53*, 157-166.

(8) Escolar, G.; Krumwiede, M.; White, J. G. *The American Journal of Pathology* **1986**, *123*, 86-94.

(9) White, J. G. *Platelet Structure*, Second ed.; Academic Press: Burlington, MA, 2007.

(10) Nieswandt, B.; Watson, S. P. *Blood* **2003**, *102*, 449-461.

(11) Furie, B.; Furie, B. C. *The New England Journal of Medicine* **2008**, *359*, 938-949.

(12) Wootton, D. M.; Ku, D. N. *Annual Review of Biomedical Engineering* **1999**, *1*, 299-329.

(13) Prabhakarpandian, B.; Shen, M.; Pant, K.; Kiani, M. F. *Microvascular Research* **2011**, *82*, 210-220.

(14) Para, A.; Bark, D.; Lin, A.; Ku, D. *Annals of Biomedical Engineering* **2011**, *39*, 1961-1971.

(15) Papaioannou, T. G.; Stefanadis, C. *Hellenic Journal of Cardiology* **2005**, *46*, 9-15.

(16) Brass, L. *Hematology* **2010**, *2010*, 387-396.

(17) Varga-Szabo, D.; Pleines, I.; Nieswandt, B. *Arteriosclerosis, Thrombosis, and Vascular Biology* **2008**, *28*, 403-412.

(18) Davi, G.; Patrono, C. *The New England Journal of Medicine* **2007**, *357*, 2482-2494.

(19) Kunapuli, S. P.; Dorsam, R. T.; Kim, S.; Quinton, T. M. *Current Opinion in Pharmacology* **2003**, *3*, 175-180.

(20) Puri, R. N. *Biochemical Pharmacology* **1999**, *57*, 851-859.

(21) Zieve, P. D.; Greenough III, W. B. *Biochemical and Biophysical Research Communications* **1969**, *35*, 462-466.

(22) Noe, L.; Peeters, K.; Izzi, B.; Van Geet, C.; Freson, K. *Current Medicinal Chemistry* **2010**, *17*, 2897-2905.

(23) Davie, E. W.; Fujikawa, K.; Kisiel, W. *Biochemistry* **1991**, *30*, 10363-10370.

(24) Jackson, S. P. *Nature Medicine* **2011**, *17*, 1423-1436.

(25) Olearczyk, J. J.; Stephenson, A. H.; Lonigro, A. J.; Sprague, R. S. *American Journal of Physiology Heart and Circulatory Physiology* **2004**, *286*, 940-945.

(26) Sprague, R. S.; Ellsworth, M. L. *Microcirculation* **2012**, *19*, 430-439.

(27) Sridharan, M.; Adderley, S. P.; Bowles, E. A.; Egan, T. M.; Stephenson, A. H.; Ellsworth, M. L.; Sprague, R. S. *American Journal of Physiology Heart and Circulatory Physiology* **2010**, *299*, 1146-1152.

(28) Sprague, R. S.; Ellsworth, M. L.; Stephenson, A. H. *American Journal of Physiology* **1996**, *271*, 2717-2722.

(29) Sprague, R. S.; Stephenson, A. H.; Bowles, E.; Stumpf, M.; Ricketts, G.; Lonigro, A. *Hypoxia and Exercise* **2006**, 207-216.

(30) Ku, C.; Karunarathne, W.; Kenyon, S.; Root, P.; Spence, D. *Analytical Chemistry* **2007**, *79*, 2421-2426.

(31) Kotsis, D. H.; Spence, D. M. *Analytical Chemistry* **2003**, *75*, 145-151.

(32) Morrel, C. N.; Matsushita, K.; Chiles, K.; Scharpf, R. B.; Yamakuchi, M.; Mason, R. J. A.; Bergmeier, W.; Mankowski, J. L.; Baldwin III, W. M.; Faraday, N.; Lowenstein, C. J. *PNAS* **2005**, *102*, 3782-3787.

(33) Letourneau, S.; Hernandez, L.; Faris, A. N.; Spence, D. M. *Analytical and Bioanalytical Chemistry* **2010**, *397*, 3369-3375.

(34) Wright, H. P.; Thompson, R. H.; Zilkha, K. J. *Lancet* **1965**, *2*, 1109-1110.

(35) Ataga, K. I.; Orringer, E. P. *The American Journal of Medicine* **2003**, *115*, 721-728.

(36) Francis, R. B. J. *Blood Coagulation & Fibrinolysis* **1991**, *2*, 341-353.

(37) Vinik, A. I.; Erbas, T.; Park, T. S.; Nolan, R.; Pittenger, G. L. *Diabetes Care* **2001**, *24*, 1476-1485.

(38) Carroll, J.; Raththagala, M.; Subasinghe, W.; Baguzis, S.; D'Amico Oblak, T.; Root, P.; Spence, D. *Molecular BioSystems* **2006**, *2*, 305-311.

(39) O'Sullivan, B. P.; Linden, M. D.; Frelinger, A. L.; Barnard, M. R.; Spencer-Manzon, M.; Morris, J. E.; Salem, R. O.; Laposata, M.; Michelson, A. D. *Blood* **2005**, *12*, 4635-4641.

(40) Sprague, R. S.; Ellsworth, M. L.; Stephenson, A. H.; Kleinhenz, M. E.; Lonigro, A. J. *Amercan Journal of Physiology* **1998**, *275*, H1726-32.

(41) Somova, L.; Mufunda, J. *Clinical and Experimental Hypertension* **1993**, *15*, 781-796.

(42) Sprague, R. S.; Stephenson, A. H.; Ellsworth, M. L.; Keller, C.; Lonigro, A. J. *Experimental Biology and Medicine* **2001**, *226*, 434-439.

(43) Tchoepe, D.; Roesen, P.; Esser, J.; Schwippert, B.; Nieuwenhuis, H. K.; Kehrel, B.; Gries, F. A. *Seminars in Thrombosis and Hemostasis* **1991**, *17*, 433-438.

(44) Venkat, N. K.; Boyle, J. P.; Geiss, L. S.; Saaddine, J. B.; Thompson, T. J. *Diabetes Care* **2006**, *29*, 2114-2116.

(45) Ahmad, L. A.; Crandall, J. P. *Clinical Diabetes* **2010**, *28*, 53-59.

(46) Donnelly, R.; Emslie-Smith, A. M.; Gardner, I. D.; Morris, A. D. *British Medical Journal* **2000**, *320*, 1062-1066.

(47) Roach, R. C.; Wagner, P. D.; Hackett, P. H. In *Expression of the heterotrimeric G protein Gi and ATP release are imparied in erythrocytes of humans with diabetes mellitus*, Sprague, R. S.; Stephenson, A. H.; Bowles, E.; Stumpf, M.; Ricketts, G.; Lonigro, A., Eds.; Springer: New York, 2007, pp 207-216.

(48) Davies, M. J. *Circulation* **1996**, *94*, 2013-2020.

(49) Colwell, J. A.; Nesto, R. W. *Diabetes Care* **2003**, *26*, 2181-2188.

(50) Kakouros, N.; Rade, J.; Kourliouros, A.; Resar, J. R. *International Journal Of Endocrinology* **2011**, *2011*, 14.

(51) Sprague, R. S.; Stephenson, A. H.; Bowles, E. A.; Stumpf, M. S.; Lonigro, A. J. *Diabetes* **2006**, *55*, 3588-3593.

(52) Freedman, J. E. *Circulation* **2005**, *112*, 2725-2734.

(53) Stead, R. J.; Barradas, M. A.; Mikhailidis, D. P.; Jeremy, J. Y.; Hodson, M.; Batten, J. C.; Dandona, P. *Prostaglandins Leukotrienes and Medicine* **1987**, *26*, 91-103.

(54) Mikhailidis, D. P.; Stead, R. J.; Barradas, M. A.; Hodson, M. E.; Batten, J. C.; Dandona, P. *Haematologica* **1990**, *75*, 137-140.

(55) Burt, V. L.; Whelton, P.; Roccella, E. J.; Brown, C.; Cutler, J. A.; Higgins, M.; Horan, M. J.; Labarthe, D. *Hypertension* **1995**, *25*, 305-313.

(56) Poplawski, A.; Skorulska, M.; Niewiarowski, S. *Journal of Atherosclerosis Research* **1968**, *4*, 721-723.

(57) Rejdak, K.; Jackson, S.; Giovannoni, G. *British Medical Bulletin* **2010**, *95*, 79-104.

(58) Millar, J. H. D.; Merrett, J. D.; Dalby, A. M. *Journal of Neurology, Neurosurgery & Psychiatary* **1966**, *29*, 187-190.

(59) Caspary, E. A.; Prineas, J.; Miller, H.; Field, E. J. *Ibid* **1965**, *2*, 1108-1109.

(60) Sheremata, W. A.; Jy, W.; Horstman, L. L.; Ahn, Y. S.; Alexander, J. S.; Minagar, A. *Journal of Neuroinflammation* **2008**, *5*, 27-32.

(61) Letourneau, S.; Hernandez, L.; Faris, A. N.; Spence, D. M. *Analytical and Bioanalytical Chemistry* **2010**, *397*, 3369-3375.

(62) Engelgau, M. M.; KNarayan, K. M.; Herman, W. H. *Diabetes Care* **2000**, *23*, 1563-1580.

(63) Hess, J. R. *Transfusion and Apheresis Science* **2010**, *43*, 51-59.

(64) Wang, Y.; Giebink, A.; Spence, D. M. *Integrative Biology* **2014**, *6*, 65-75.

(65) Falati, S.; Gross, P.; Merrill-Skoloff, G.; Furie, B.; Furie, B. *Nature Medicine* **2002**, *8*, 1175-1180.

(66) Vilahur, G.; Padro, T.; Badimon, L. *Journal of Biomedicine and Biotechnology* **2011**, *2011*, 12.

(67) Westrick, R. J.; Winn, M. E.; Eitzman, D. T. *Arteriosclerosis, Thrombosis, and Vascular Biology* **2007**, *27*, 2079-2093.

(68) Conant, C. G.; Schwartz, M. A.; Beecher, J. E.; Rudoff, R. C.; Ionescu-Zanetti, C.; Nevill, J. T. *Biotechnology and Bioengineering* **2011**, *108*, 2978-2987.

(69) Maloney, S. F.; Brass, L. F.; Diamond, S. L. *Integrative Biology* **2010**, *4*, 183-192.

(70) Neeves, K. B.; Diamond, S. L. *Lab Chip* **2008**, *8*, 701-709.

(71) Neeves, K. B.; Illing, D. A. R.; Diamond, S. L. *Biophysical Journal* **2010**, *98*, 1344-1352.

(72) Chiu, D. T.; Jeon, N. L.; Huang, S.; Kane, R. S.; Wargo, C. J.; Choi, I. S.; Ingber, D. E.; Whitesides, G. M. *PNAS* **2000**, *97*, 2408-2413.

(73) van der Meer, A. D.; Poot, A. A.; Duits, M. H. G.; Feijen, J.; Vermes, I. *Journal of Biomedicine and Biotechnology* **2009**, *2009*, 823148.

(74) McDonald, J. C.; Whitesides, G. M. *Accounts of Chemical Research* **2002**, *35*, 491-499.

(75) Johnson, A. S.; Anderson, K. B.; Halpin, S. T.; Kirkpatrick, D. C.; Spence, D. M.; Martin, R. S. *Analyst* **2013**, *138*, 129-136.

(76) Stjernstrom, M.; Roeraade, J. *Journal of Micromechanics and Microengineering* **1998**, *8*, 33-38.

(77) Rumbaut, R. E.; Slaaf, D. W.; Burns, A. R. *Microcirculation* **2005**, *12*, 259-274.

(78) Leadley, R. J.; Chi, L.; Rebello, S. S.; Gagnon, A. *Journal of Pharmacological and Toxicological Methods* **2000**, *43*, 101-116.

(79) Dittrich, P. S.; Manz, A. *Nature Reviews* **2006**, *5*, 210-218.

(80) Tolan, N. V.; Genes, L. I.; Subasinghe, W.; Raththagaia, M.; Spence, D. M. *Analytical Chemistry* **2009**, *81*, 3102-3108.

(81) Kaitin, K. *Clinical Pharmacology and Therapeutics* **2010**, *87*, 356.

(82) Dimasi, J. A.; Grabowski, H. G. *Managerial and Decision Economics* **2007**, *28*, 469-479.

(83) Adams, C. P.; Brantner, V. V. *Health Affairs* **2006**, *25*, 420-428.

(84) Kola, I.; Landis, J. *Nature Reviews Drug Discovery* **2004**, *3*, 711-716.

(85) Golan, D. E.; Tashjian, A. H.; Armstrong, E. J. *Principles of Pharmacology: The Pathophysiologic Basis of Drug Therapy*; Lippincott Williams & Wilkins, 2011.

(86) Levine, R. R.; Walsh, C. T.; Schwartz-Bloom, R. D. *Pharmacology: Drug Actions and Reactions*; CRC Press, 2000.

(87) Lu, H.; Schmidt, M. A.; Jensen, K. F. *Lab Chip* **2005**, *5*, 23-29.

(88) Wang, H.; Bhunia, A. K.; Lu, C. *Biosensors and Bioelectronics* **2006**, *22*, 582-588.

(89) Lee, S.; Tai, Y. *Sensors and Actuators A: Physical* **1999**, *73*, 74-79.

(90) Di Carlo, D.; Jeong, K.; Lee, L. P. *Lab Chip* **2003**, *3*, 287-291.

(91) Irimia, D.; Tompkins, R. G.; Toner, M. *Analytical Chemistry* **2004**, *76*, 6137-6143.

(92) Waters, L. C.; Jacobson, S. C.; Kroutchinina, N.; Khandurina, J.; Foote, R. S.; Ramsey, M. J. *Analytical Chemistry* **1998**, *70*, 158-162.

(93) Lee, D. W.; Cho, Y. *Sensors and Actuators B: Chemical* **2007**, *124*, 84-89.

(94) Huang, Y.; Mather, E. L.; Bell, J. L.; Madou, M. *Analytical and Bioanalytical Chemistry* **2002**, *372*, 49-65.

(95) Ward, M.; Wu, J.; Chiu, J. *The Journal of the Acoustical Society of America* **1999**, *105*, 2951-2957.

(96) Sims, C. E.; Meredith, G. D.; Krasieva, T. B.; Berns, M. W.; Tromberg, B. J.; Allbritton, N. L. *Analytical Chemistry* **1998**, *70*, 4570-4577.

(97) Kim, J.; Jang, S. H.; Jia, G.; Zoval, J. V.; Da Silva, N. A.; Madou, M. J. *Lab Chip* **2004**, *4*, 516-522.

(98) Kim, Y. C.; Kang, J. H.; Park, S. J.; Yoon, E. S.; Park, J. K. *Sensor and Actuators B: Chemical* **2007**, *128*, 108-116.

(99) Schilling, E. A.; Kamholz, A. E.; Yager, P. *Analytical Chemistry* **2002**, *74*, 1798-1804.

(100) Wang, L.; Miller, C.; Swarthout, R. F.; Rao, M.; Mackman, N.; Taubman, M. B. *Blood* **2009**, *113*, 705-713.

(101) Kurz, K. D.; Main, B. W.; Sandusky, G. E. *Thrombosis Research* **1990**, *60*, 269-280.

(102) Dougherty, T. J.; Gomer, C. J.; Henderson, B. W.; Jori, G.; Kessel, D.; Korbelik, M.; Moan, J.; Peng, Q. *Journal of the National Cancer Institute* **1998**, *90*, 889-905.

(103) Yoon, I.; Li, J. Z.; Shim, Y. K. *Clinical Endoscopy* **2013**, *46*, 7-23.

(104) Zimmermann, U. *Trends in Biotechnology* **1983**, *1*, 149-155.

(105) McClain, M. A.; Culbertson, C. T.; Jacobson, S. C.; Albritton, N. L.; Sims, C. E.; Ramsey, M. J. *Analytical Chemistry* **2003**, *75*, 5646-5655.

(106) Wang, H.; Lu, C. *Analytical Chemistry* **2006**, *78*, 5158-5164.

(107) SPIE-Professional. *Chuck Hull: Pioneer in Stereolithography*; http://spie.org/x91418.xml (accessed September 10, 2015).

(108) Melchels, F. P. W.; Feijen, J.; Grijpma, D. W. *Biomaterials* **2010**, *31*, 6121-6130.

(109) Webb, P. A. *Journal of Medical Engineering & Technology* **2000**, *24*, 149-153.

(110) Bertsch, A.; Renaud, P. In *Stereolithography*; Springer, 2011, pp 81-112.

(111) Hull, C.W. *Apparatus for production of three-dimensional objects by stereolithography*. U.S. Patent 4,575,330, March 11, 1986.

(112) Cooke, M. N.; Fisher, J. P.; Dean, D.; Rimnac, C.; Mikos, A. G. *Journal of Biomedical Materials Research Part B: Applied Biomaterials* **2003**, *64*, 65-69.

(113) Lee, J. W.; Lan, P. X.; Kim, B.; Lim, G.; Cho, D.-W. *Microelectronic Engineering* **2007**, *84*, 1702-1705.

(114) Huang, Y. M.; Kuriyama, S.; Jiang, C. P. *Int. J. Adv. Manuf. Technol.* **2004**, *24*, 361-369; Takagi, T.; Nakajima, N. In *Micro Electro Mechanical Systems, 1993, MEMS'93, Proceedings An Investigation of Micro Structures, Sensors, Actuators, Machines and Systems. IEEE.*; IEEE, 1993, pp 173-178.

(115) Ikuta, K.; Hirowatari, K. In *Micro Electro Mechanical Systems, 1993, MEMS'93, Proceedings An Investigation of Micro Structures, Sensors, Actuators, Machines and Systems. IEEE.*; IEEE, 1993, pp 42-47.

(116) Harris, R. A.; Hague, R. J. M.; Dickens, P. M. *International Journal of Machine Tools and Manufacture* **2004**, *44*, 59-64.

(117) Wang, Y.; Balowski, J.; Phillips, C.; Phillips, R.; Sims, C. E.; Allbritton, N. L. *Lab Chip* **2011**, *11*, 3089-3097.

(118) Waldbaur, A.; Rapp, H.; Länge, K.; Rapp, B. E. *Analytical Methods* **2011**, *3*, 2681-2716.

(119) Pan, Y.; Zhou, C.; Chen, Y. In *Proceeding of the 2012 International Manufacturing Science and Engineering Conference*, 2012, pp 4-8.

(120) Choi, J.-W.; Wicker, R.; Lee, S.-H.; Choi, K.-H.; Ha, C.-S.; Chung, I. *Journal of Materials Processing Technology* **2009**, *209*, 5494-5503.

(121) Waldbaur, A.; Rapp, H.; Lange, K.; Rapp, B. E. *Analytical Methods* **2011**, *3*, 2681-2716.

(122) Maruo, S.; Ikuta, K. *Sensors and Actuators A: Physical* **2002**, *100*, 70-76.

(123) Melchels, F. P. W.; Feijen, J.; Grijpma, D. W. *Biomaterials* **2010**, *31*, 6121-6130.

(124) Waterman, N. A.; Dickens, P. *World Class Design to Manufacture* **1994**, *1*, 27-36.

(125) FormLabs. Formlabs-High Resolution Desktop 3D Printer. http://formlabs.com/ (accessed September 21, 2015).

(126) Pham, D. T.; Gault, R. S. *International Journal of Machine Tools and Manufacture* **1998**, *38*, 1257-1287.

(127) Waldbaur, A.; Rapp, H.; Lange, K.; Rapp, B. E. *Analytical Methods* **2011**, *3*, 2681-2716.

(128) Sood, A. K.; Ohdar, R. K.; Mahapatra, S. S. *Materials & Design* **2009**, *30*, 4243-4252.

(129) Van Weeren, R.; Agarwala, M.; Jamalabad, V.; Bandyophadyay, A.; Vaidyanathan, R.; Langrana, N.; Safari, A.; Whalen, P.; Danforth, S.; Ballard, C. In *Proceedings of the Solid Freeform Fabrication Symposium*; ASME, 1995, pp 314-21.

(130) Zhong, W. H.; Li, F.; Zhang, Z. G.; Song, L. L.; Li, Z. M. *Mat Sci Eng a-Struct* **2001**, *301*, 125-130; Wu, G.; A. Langrana, N.; Sadanji, R.; Danforth, S. *Materials & Design* **2002**, *23*, 97-105; Bellini, A. *Fused deposition of ceramics: A comprehensive experimental, analytical and computational study of material behavior, fabrication process and equipment design*. Ph.D., Drexel University, Ann Arbor, 2002; Zein, I.; Hutmacher, D. W.; Tan, K. C.; Teoh, S. H. *Biomaterials* **2002**, *23*, 1169-85.

(131) Agarwala, M.; Van Weeren, R.; Bandyopadhyay, A.; Whalen, P.; Safari, A.; Danforth, S. In *Proceedings of Solid Freeform Fabrication Symposium*; The University of Texas, 1996, pp 385-92.

(132) Kumar, S. *JOM* **2003**, *55*, 43-47.

(133) Kruth, J.-P.; Mercelis, P.; Van Vaerenbergh, J.; Froyen, L.; Rombouts, M. *Rapid Prototyping Journal* **2005**, *11*, 26-36.

(134) Yan, X.; Gu, P. *Computer-Aided Design* **1996**, *28*, 307-318.

(135) Ko, S. H.; Pan, H.; Grigoropoulos, C. P.; Luscombe, C. K.; Fréchet, J. M. J.; Poulikakos, D. *Nanotechnology* **2007**, *18*, 345202.

(136) Tolochko, N. K.; Khlopkov, Y. V.; Mozzharov, S. E.; Ignatiev, M. B.; Laoui, T.; Titov, V. I. *Rapid Prototyping Journal* **2000**, *6*, 155-161.

(137) Wang, R.-J.; Wang, L.; Zhao, L.; Liu, Z. *The International Journal of Advanced Manufacturing Technology* **2006**, *33*, 498-504.

(138) Chung, J.; Ko, S.; Bieri, N. R.; Grigoropoulos, C. P.; Poulikakos, D. *Applied Physics Letters* **2004**, *84*, 801; Chung, J.; Bieri, N. R.; Ko, S.; Grigoropoulos, C. P.; Poulikakos, D. *Applied Physics A* **2004**, *79*.

(139) Klosterman, D.; Chartoff, R.; Graves, G.; Osborne, N.; Priore, B. *Composites Part A: Applied Science and Manufacturing* **1998**, *29*, 1165-1174.

(140) Dutta, D.; Prinz, F. B.; Rosen, D.; Weiss, L. *Journal of Computing and Information Science in Engineering* **2001**, *1*, 60.

(141) Frank, M. C.; Peters, F. E.; Karthikeyan, R. *Twenty Forth Annual International Solid Freeform Fabrication Symposium – An Additive Manufacturing Conference* **2010**.

(142) Flach, L.; Jacobs, M. A.; Klosterman, D. A.; Chartoff, R. In *Solid Freeform Fabrication Symposium Proceedings, University Of Texas At Austin, Austin, TX*, 1998, pp 407-416.

(143) Pfister, A.; Landers, R.; Laib, A.; Hubner, U.; Schmelzeisen, R.; Mulhaupt, R. *Journal of Polymer Science Part A: Polymer Chemistry* **2004**, *42*, 624-638.

(144) Doraiswamy, A.; Dunaway, T. M.; Wilker, J. J.; Narayan, R. J. *Journal of Biomedical Materials Research Part B: Applied Biomaterials* **2009**, *89B*, 28-35.

(145) Calvert, P. *Chemistry of Materials* **2001**, *13*, 3299-3305.

(146) de Gans, B. J.; Duineveld, P. C.; Schubert, U. S. *Advanced Materials* **2004**, *16*, 203-213.

(147) Gross, B. C.; Erkal, J. L.; Lockwood, S. Y.; Chen, C.; Spence, D. M. *Analytical Chemistry* **2014**, *86*, 3240-3253.

(148) 3DSystems. *Polyjet Technology.* http://www.stratasys.com/3d-printers/technology/polyjet-technology (accessed September 25, 2015).

(149) Therriault, D.; White, S. R.; Lewis, J. A. *Nature Materials* **2003**, *2*, 265-271.

(150) Mannoor, M. S.; Jiang, Z.; James, T.; Kong, Y. L.; Malatesta, K. A.; Soboyejo, W. O.; Verma, N.; Gracias, D. H.; McAlpine, M. C. *Nano Letters* **2013**, *13*, 2634-2639.

(151) Wang, X.; Yan, Y.; Pan, Y.; Xiong, Z.; Liu, H.; Cheng, J.; Liu, F.; Lin, F.; Wu, R.; Zhang, R.; Lu, Q. *Tissue Engineering* **2006**, *12*, 83-90.

(152) Liu, H.; Yan, Y.; Wang, X.; Cheng, J.; Lin, F.; Xiong, Z.; Wu, R. *Chinese Science Bulletin* **2006**, *51*, 1830-1835.

(153) Wang, X.; Yan, Y.; Zhang, R. *Trends in Biotechnology* **2007**, *25*, 505-513.

(154) Zhao, L.; Lee, V. K.; Yoo, S.; Dai, G.; Intes, X. *Biomaterials* **2012**, *33*, 5325-5332.

(155) Wu, W.; DeConinck, A.; Lewis, J. A. *Advanced Materials* **2011**, *23*, H178-H183.

(156) Liu, C. Z.; Xia, Z. D.; Han, Z. W.; Hulley, P. A.; Triffitt, J. T.; Czernuszka, J. T. *Journal of Biomedical Material Research Part B: Applied Biomaterials* **2008**, *85B*, 519-528.

(157) Bergmann, C.; Lindner, M.; Zhang, W.; Koczur, K.; Kirsten, A.; Telle, R.; Fischer, H. *Journal of the European Ceramic Society* **2010**, *30*, 2563-2567.

(158) Cuodeau, A.; Sachs, E.; Cadarise, S. *Journal of Biomedical Materials Research* **2000**, *53*, 525-535.

CHAPTER 2

CELL LYSIS ON MICROFLUIDIC DEVICES USING CHEMICAL LYSIS TECHNIQUES

2.1 Introduction

This chapter introduces microfluidic devices fabricated using traditional soft-lithography and replica molding procedures. Lysis of adhered endothelial cells was characterized and optimized for fabricated devices designed for chemical lysis techniques employing irradiation of a chemical and electrochemically generated hydroxide formation. A comparison between the various fabricated microfluidic devices and lysis mechanisms was made with respect to the use of these devices as *in vitro* thrombosis mimics.

2.1.1 Chemical Method of Cell Lysis for Injury Simulation

Chemical lysis of cells encompasses a variety of techniques ranging from the use of surfactants such as sodium dodecyl sulfate (SDS) to the generation of chemicals capable of lysing action through electrochemistry or laser irradiation. For the purpose of injury simulation, flowing SDS over an immobilized layer of cells in a microfluidic channel is a simple, cost effective solution. However, this protocol involves introducing nonnative circulatory components into a device meant to mimic vasculature. Laser irradiation of a photochemical dye to produce a lysing agent is an attractive approach to induce injury as it can be done in a site specific manner. Rose bengal is one such dye that upon irradiation at 514 nm produces an oxygen radical that causes membrane damage. This technique is used heavily to injure vasculature in animal models[1] and has potential for being utilized with *in vitro* platforms.

2.1.2 Photochemical Lysis

Chemicals (sensitizing dyes or molecular oxygen) irradiated by visible light produce the following reactive oxygen species (ROS): $^1O_2$: singlet oxygen, H_2O_2: peroxide

(hydrogen), $O_2^{\cdot-}$: oxygen anion radical, and ·OH: hydroxide radical. These species damage the cell via a photochemical injury mechanism.[2,3,4] An appealing feature of this method is that the injury is confined to the irradiated area, or close it, as the migration of ROSs is limited by their short lifetime (less than 0.04 microseconds and less than 0.02 μm diffusion pathlength for singlet oxygen).[3] Irradiation of rose bengal dye (a photosensitizer) with 16 W/cm^2 using an argon ion laser at 514 nm stimulates the photocatalytic conversion of oxygen molecules to free radicals, leading to cell death by apoptosis, autophagy (to remove damaged cells), or necrosis.[5,6,7] Monitoring cell damage and subsequent thrombus formation using this technique has for the most part been limited to animal models.[8,9] However, rose bengal and other photosensitizers have been approved by the Food and Drug Administration (FDA) for use in the United States as photodynamic therapy for diseased tissue and cancer treatment.[3,7] Figure 2.1 shows a representative image of what cell injury looks like when using this method.

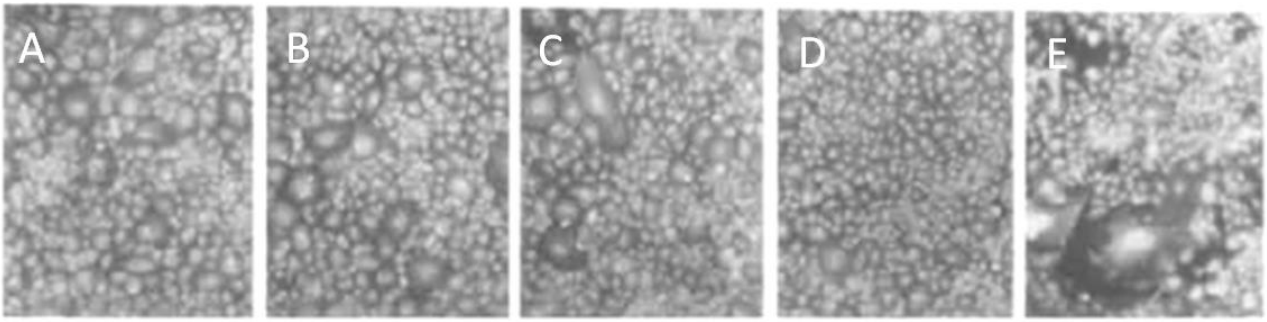

Figure 2.1 Photochemical lysis of cells. Effects of increasing laser irradiation duration on cellular damage of vascular endothelial cells incubated with 5 x 10^{-4} M rose bengal on glass slides. 0.5 min laser exposure (A). 2.5 min (B). 5 min (C). 7.5 min (D). 15 min (E). (Reprinted with permission from reference 6. Copyright ARVO.)

Photochemical cellular damage is characterized by cytoplasm vacuolization, cell and organelle swelling, plasma membrane breakdown, and loss of internal cell components.[7]

2.1.3 Lysis Via Hydroxide Formation

Used in conjunction with SDS, NaOH has long been utilized as a means to lyse cells and harvest DNA. In this method, known as alkaline lysis, cells are suspended in a solution containing SDS and NaOH. The SDS serves to solubilize the cell membrane while NaOH breaks down the cell wall and denatures double stranded DNA (dsDNA) to single stranded (ssDNA). After lysis, the solution is neutralized and the DNA precipitates isolated.[10]

Hydroxide (OH^-) generation from the electrolysis of water lyses cells by cleaving fatty acid–glycerol ester bonds in phospholipids in the lipid membrane of the cell. This results in the production of fatty acid chains and lysophospholipids, and compromises the cell membrane through degradation.[11,12] Specifically, hydroxide is generated from the reduction of water comprising the lysis buffer (e.g. PBS) at the cathode upon potential application to the electrodes, as seen in the following reactions:

Cathode $2H_2O + 2e^- \rightarrow H_{2(g)} + 2OH^-$

Anode $2H_2O \rightarrow 4e^- + 4H^+ + O_{2(g)}$

2.1.4 Techniques for Microfluidic Device Fabrication

The field of microfluidics, also referred to as lab-on-a-chip and μ total analysis system (μTAS), is now commonplace in both academic and industrial settings. This technology encompasses micro-fabricated systems with as low as femtoliter volume capacities, integration of sample preparation, separation, detection, and (in some cases) analysis, all on one device. The advantages of microfluidics include reduced sample volume, waste products, and therefore cost. Because of this, these devices are also well suited for analysis of rare or expensive analytes. Microfluidic technology offers flexibility in

experimental design, as many devices are meant for one time use while others are reusable. Due to their small size, microfluidic devices are portable and can be transported directly to samples for *in situ* testing. Smaller channel dimensions means shorter diffusion distances and analysis times. Furthermore, microfluidic devices are amenable to integration of multiple processes on one platform, namely, labeling, purification, separation, and detection.[13]

2.1.5 History of Microfluidic Devices

In 1979 the first account of microfluidics in the literature was reported by Terry et al. They highlighted the use of a micromachined silicon wafer containing a 1.5 m long column used for gas chromatography separations of gaseous hydrocarbon mixtures in less than 10 seconds, with a thermal conductivity detector mounted onto the separation column.[14] In the early 1980s, Ruzicka and Hansen developed devices for flow injection analysis (FIA). Conventional FIA provides results within 15 seconds, with a minimum throughput of 120 samples per hour, and boasts 30 μL of sample solution and less than 1 mL of reagent use for each analysis. The plastic, e.g. polyvinyl chloride, devices by Ruzicka and Hansen miniaturized the liquid injection and detection onto a device they termed "integrated microchemielectronic devices" which featured engraved or imprinted channels, utilized hydrodynamic injection, and on-device detection using optical fibers.[15,16] While this work did not yield drastic improvements in performance compared to conventional FIA, it did bring all components onto a single, reusable platform for the first time in a device that resembles modern microfluidic devices.

Andreas Manz et al. published work on miniaturization of a total chemical analysis system (TAS), highlighting capillary electrophoresis performed on glass chips in the early

1990s.[17,18,19] The devices were fabricated using micromachining techniques relying on photolithography and etching of a silicon wafer, and initial proof of concept studies focused on the separation of fluorescent dyes. Despite a simplistic design, this device sparked widespread interest in the field of microfluidics. In the mid 1990s microfluidic devices were used for microchip electrophoresis[20] and DNA analysis for the first time.[21] The field had garnered enough interest in 1996 for the first μTAS conference to be held which focused on miniaturized systems for chemistry and life sciences. The year 1998 marked the launch of the first commercially available microchip systems combined with microelectromechanical (MEM) sensor technology (Hewlett-Packard Company and Caliper Technologies Corp). These devices were geared toward biochemical processing, made by etching 80 μm wide and 10 μm deep channels into glass, silicon, quartz, or plastic, and capable of nanoliter per second flow rates.[22] As of 2013, commercial microfluidic systems were widely available from several sources including Abbott, Agilent, Caliper, and Waters.[13] The first journal dedicated solely to microfluidic technologies, *Lab on a Chip*, was launched in 2001 by the Royal Society of Chemistry.

Microfluidic systems were initially comprised of silicon and glass substrates, but with increased demand the material pool spread to include ceramics, polymeric materials (elastomers and thermoplastics), and paper.[13] One of the most widely used elastomeric materials, polydimethylsiloxane (PDMS), was made popular through the development of soft lithography for microfluidic device fabrication by the Whitesides group at Harvard.[23] Soft lithography employing elastomeric materials allows for feature dimensions as small as 30 nm in size, where feature resolution on a finished device is limited to the resolution of the features on the master.[24] The use of soft lithographic techniques for the fabrication of

PDMS based devices integrated with circulation components and amenable to physiological blood flow conditions have been well documented in the literature.[25,26] Moreover, there has been extensive work towards specific cell patterning on such devices including elaborate scaffold materials to support cell culture. [27,28.29] Taken together, this body of literature shows an impressive undertaking in recreating *in vivo* vascular conditions where even minutiae such as the elongated morphology of the cells under constant flow conditions can be recreated.[30]

Polystyrene (PS) is the same material used to make cell culture flasks, and therefore well suited for implementation in PS-based devices for cell culture. A number of examples from the literature highlight the use of microfluidic devices fabricated from PS applied towards *in vitro* vasculature recreation.[31,32] While electrodes have been integrated with PDMS in the past (e.g. carbon ink electrodes), merging the two is often cumbersome.[32] PS offers a more rigid material and less labor intensive process to integrate electrodes with the microfluidic device compared to PDMS. The fabrication of microfluidic devices merging PS and PDMS parts allows for integration of more components into the system, while capitalizing on the most attractive advantages from both materials.

2.2 Methods

2.2.1 Soft Lithography

The PDMS-based microfluidic components and complete devices featured in this chapter were fabricated from a silicon master containing channel features made using photolithography and final PDMS devices using soft lithography techniques.[28,33] To begin, a 4 inch silicon wafer (Silicon, Inc., Boise, ID) was cleaned with acetone and isopropyl alcohol (IPA), and then dried with nitrogen gas. The wafer was then placed on a hotplate set to 200

°C and heated for 15 minutes. After cooling to room temperature, 4 mL of negative SU8-50 photoresist (MicroChem Corp., Newton MA) was pipetted onto the center of the wafer, which was secured via a vacuum seal on a spin coater (Brewer Science, Rolla, MO). The spin program, namely the rotational speed, dictates the thickness of the photoresist deposited on the wafer and determines the subsequent feature height. A spin program set at 500 RPM for 15 seconds followed by 1000 RPM for 30 seconds resulted in a 100 μm thick film. After spin coating, the wafer was pre-baked on a hotplate set to 95 °C for 15 minutes to ensure solvent separation from the photoresist. Channel structures were drawn freehand (Corel Draw 8) and printed onto a transparency (600 dpi resolution) to create a negative mask. The negative transparency mask was then positioned over the wafer, so that after exposure to UV light using a flood source (Newport, 350-450 nm), the resulting features would be upraised on the master. After exposure, the master was post-baked on a hotplate for 5 minutes at 95 °C to further aid in the polymerization of the photoresist. After post-baking, excess photoresist not exposed to UV light was removed with a developing solution (propylene glycol monomethyl ether acetate). The finished master was cleaned by rinsing with acetone followed by IPA, and then dried with nitrogen.

Figure 2.2 depicts the photolithography process for master making and Figure 2.3 shows the process of replica molding using the master. A master with upraised channel features was used to make the PDMS component of the microfluidic device. PDMS was prepared by mixing Sylgard 184 bulk polymer with a curing agent (Dow Corning) and mixing thoroughly before degassing via vacuum. A 20:1 mixture of polymer to curing agent was utilized over the channels and for the surface that would be in contact with PS for sealing purposes. A 5:1 mixture of polymer to curing agent was poured onto the preexisting

20:1 mixture to add rigidity to the device. The chip was heated at 75 °C for 15 minutes after adding each layer of PDMS. Sample inlets were punched into the PDMS using a 20 gauge luer stub adapter, and waste wells and electrode vents were 1/8" diameter wells.

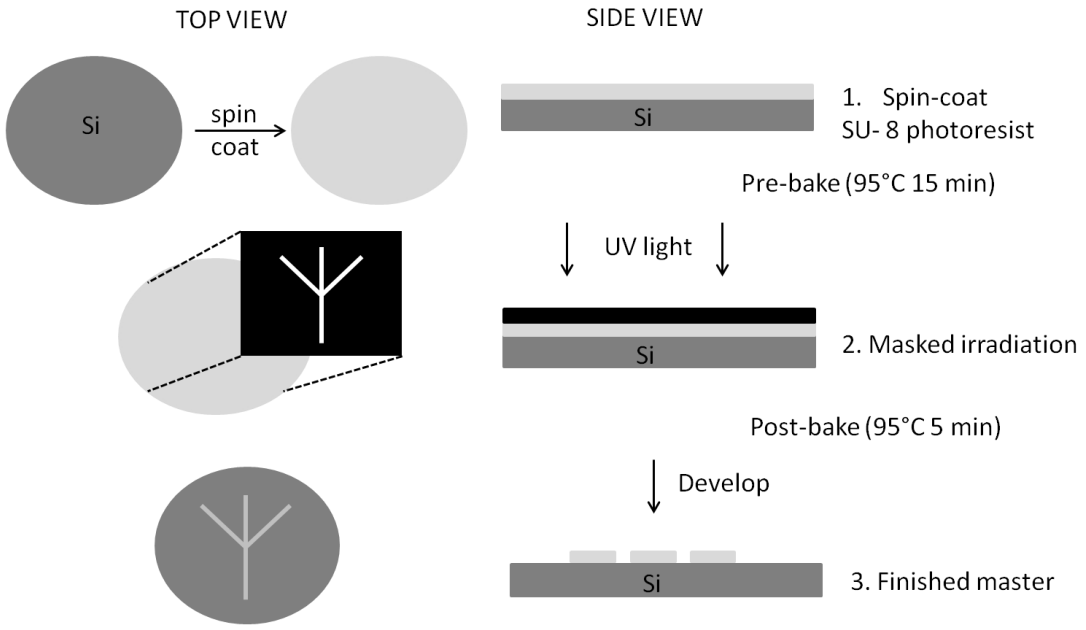

Figure 2.2 Photolithography for master making. A silicon wafer was spin coated with SU-8 photoresist then pre-baked at 95 °C for 15 min. A negative mask made using computer software and printed onto transparency paper was placed on top of the wafer. A UV flood source was used to illuminate exposed areas of SU-8, and initiate curing. The mask was removed and the wafer post-baked at 95 °C for 5 min on a hot plate. The wafer was then placed in a solution of developing solution to remove any uncured photoresist. The finished master was rinsed and then ready for use in replica molding with PDMS.

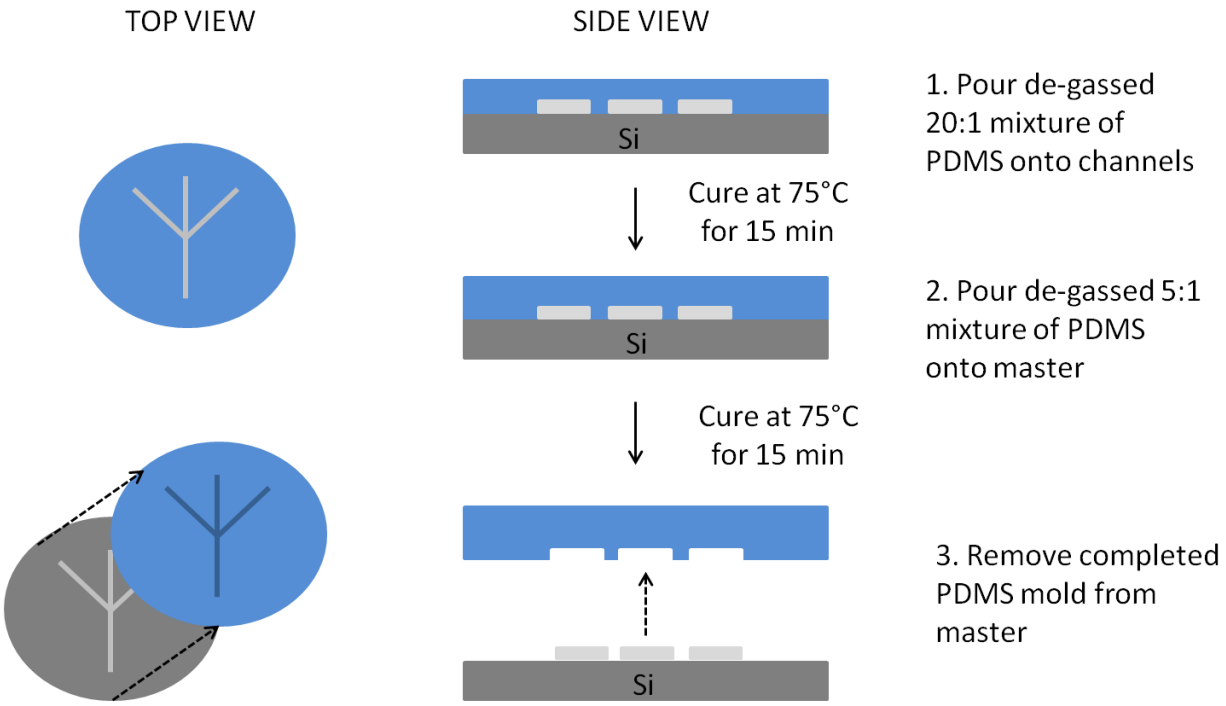

Figure 2.3 Replica Molding for PDMS device fabrication. A de-gassed 20:1 mixture of bulk polymer to curing agent was poured onto a master. The wafer was placed in an oven set at 75 °C for 15 min to cure. A 5:1 mixture of PDMS was then poured over the existing 20:1 layer to add rigidity to the device and placed back into the oven (75 °C for 15 min). After curing, the mold was removed from the silicon master.

2.2.2 Fabrication of a Polystyrene Base with Embedded Electrodes

For devices relying on electrochemically generated hydroxide formation for cell lysis, a PS base with embedded electrodes was fabricated. The procedure for fabricating the polystyrene chip was amended from a paper published by the Spence and Martin groups, as depicted in Figure 2.4.[32]

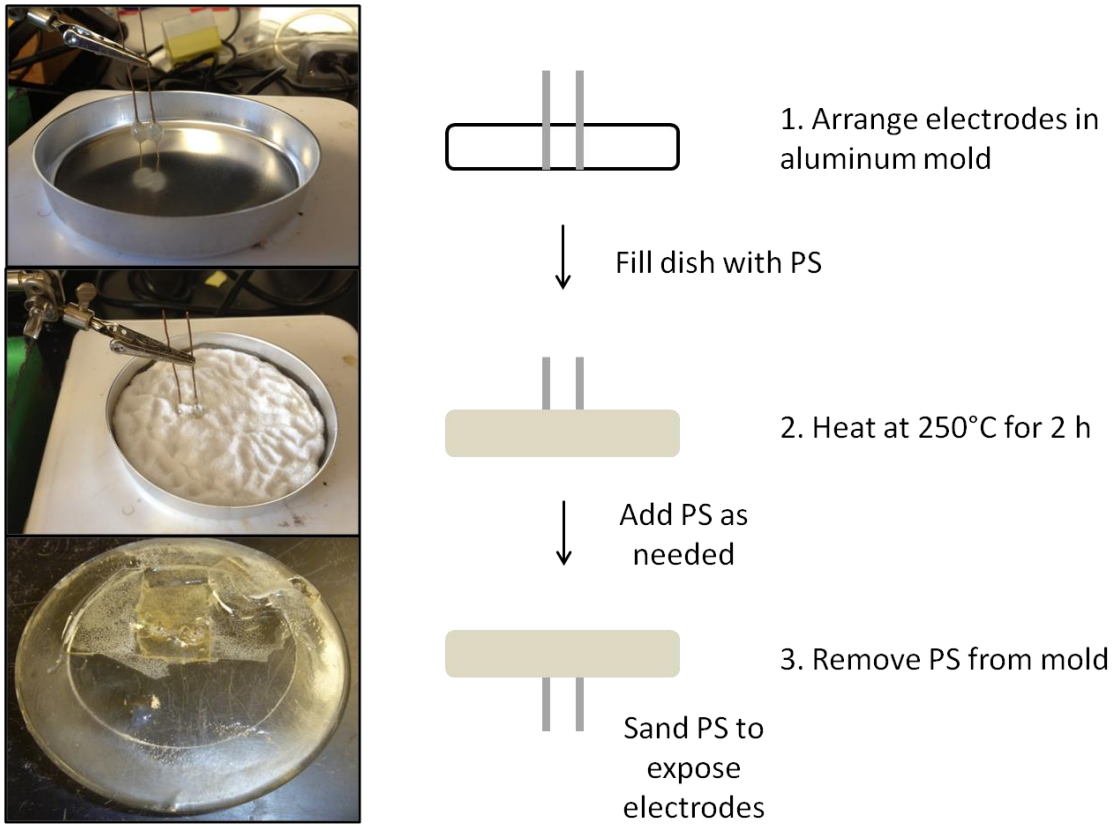

Figure 2.4 Fabrication of the PS base with embedded electrodes. Electrodes were held in place with a clamp and oriented in an aluminum mold. The mold was filled with 250 µm PS beads and placed on a hot plate set to 250 °C to melt the PS over 2 hours. Additional PS was added during this time as needed. The PS was allowed to slowly cool to room temperature and removed from the mold. The surface was polished until electrodes were exposed.

Electrode spacing on the device was 1 cm. The two 1 mm diameter palladium electrodes (Alfa Aesar, Ward Hill, MA) were each connected to copper wire with silver conductive epoxy (MGchemicals) and then reinforced with C-7 Armstrong epoxy (100:6 m/m,

Ellsworth Adhesives, Germantown, WI). The two electrodes were then vertically oriented in a 140 mm diameter aluminum weighing dish (VWR International) placed on top of a hot plate. The electrodes were kept in place using a mold fashioned out of PDMS with holes 1 cm apart for electrode insertion and a clamp attached to a ring stand. PS powder (250 μm particle size, Goodfellow, Oakdale, PA) was poured into the aluminum dish, which was placed on a hot plate set to 250 °C for 2 hours. During this time more PS was added as needed to provide adequate electrode support. Occasionally, bubbles would form in the device while the PS was melting. Any bubbles that could be accessed without disrupting electrode orientation are removed via suction using a syringe. Imperfections from bubbles on the base of the device could be filled with C-7 Armstrong Epoxy.

After the PS powder had completely melted, the device was allowed to equilibrate to room temperature and removed from the metal mold. Thorough sanding of the device was performed to ensure a uniform surface of substrate and electrodes. Rough sanding was carried out using 80 grit sandpaper until the electrodes were visible, then 220 grit followed by 500 grit sandpaper was used. The electrodes were polished using 1 μm, 0.3 μm, and lastly 0.05 μm alumina powder on nylon (1.0 and 0.3 μm) and microcloth (0.05 μm) polishing pads. The device was sonicated in water for 10 minutes prior to moving to finer grit sizes to remove any particulates. The PDMS layer containing channels was reversibly sealed to the PS component by placing the two together and removing any air bubbles trapped under the PDMS. A 20 gauge stainless steel tube connected to Tygon tubing (0.02 inch inner diameter) attached to a syringe with a luer lock was used to administer samples.

2.2.3 Device Design Rationale for Photochemical Lysis Method

Studies employing laser irradiation of a photochemical dye to stimulate oxygen radical production and subsequent cell membrane damage were carried out on either twelve well culture plates containing immobilized endothelial cells grown to confluency or microfluidic devices (Figure 2.5) comprised of PDMS with four or six inlaid parallel channels (100 μm height, 200 μm width, 3 cm length) reversibly sealed onto a petri dish. This design allowed for easy visualization of cells before and after irradiation.

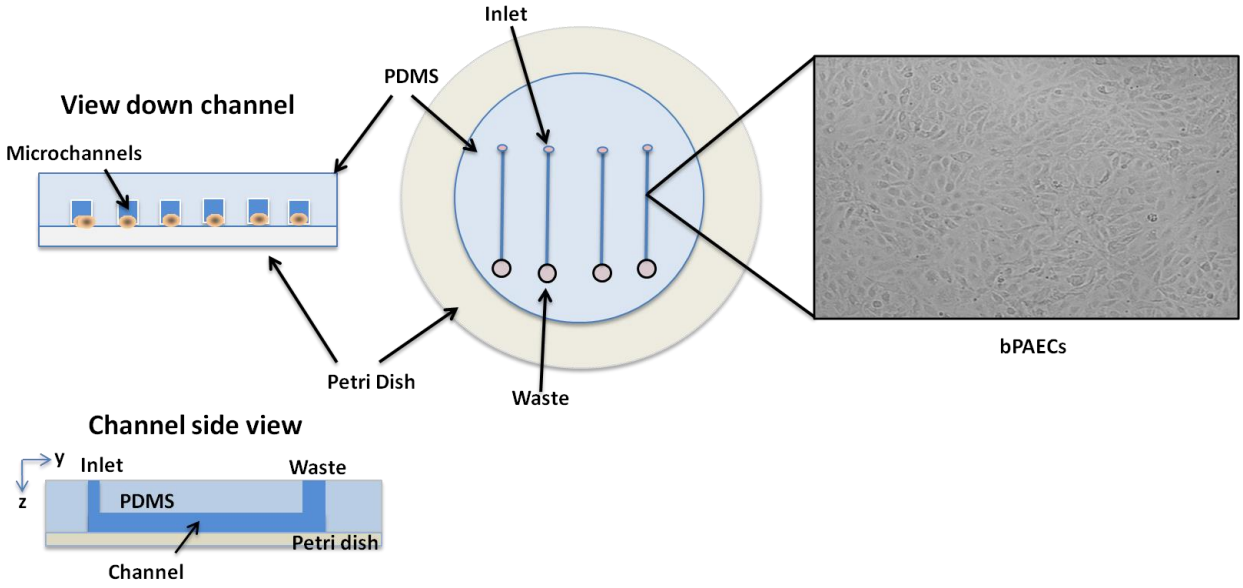

Figure 2.5 Device used for photochemical injury of cells. The device featured a piece of PDMS with parallel channels (100 μm height, 200 μm width, 3 cm length) reversibly sealed to a petri dish base. Endothelial cells are seeded onto the device and grown to confluency.

2.2.4 Device Design Rationale for Hydroxide Generation for Chemical Lysis Method

Iterations of devices relying on hydroxide generation at the cathode for cell degradation and eventual lysis were designed to allow for hydroxide diffusion to a desired lysis region. Initial efforts at integrating electrodes into a microfluidic device featured a single channel placed over the electrodes as seen in Figure 2.6. Because of gas production at the electrodes from the electrolysis of water, vents were incorporated above electrodes

to allow for pressure release. This design failed to allow for selective lysis (area between the two electrodes), and was improved upon in following device iterations.

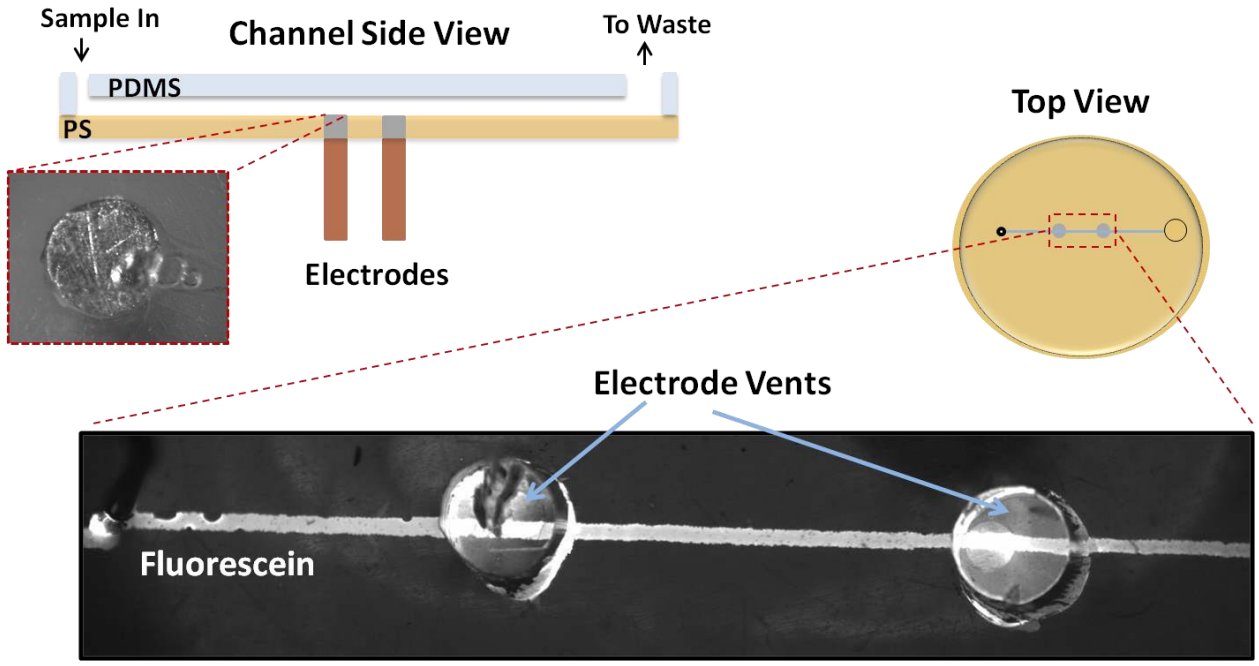

Figure 2.6 Initial microfluidic device with integrated electrodes. Fluorescein highlights the single microfluidic channel (100 µm height, 200 µm width, and 3 cm length) that was placed over two palladium electrodes. Because of gas production at the electrodes from electrolysis of the lysis buffer (PBS), vents were punched over the electrodes to allow for pressure release.

The second device, based off of a Y-shaped channel, was characterized by lysis that was often difficult to control and spread beyond the desired region. For this reason, a device utilizing a strategically placed polycarbonate membrane to better allow for controlled lysis was implemented.

2.2.4.1 Y Channel Design

Cell lysis from hydroxide generation originates from the cathode and spreads towards the desired lysis region as hydroxide diffuses through the microfluidic channel. This iteration of the device utilized a Y shaped channel to allow for selective lysis at the channel intersection, as seen in Figure 2.7.

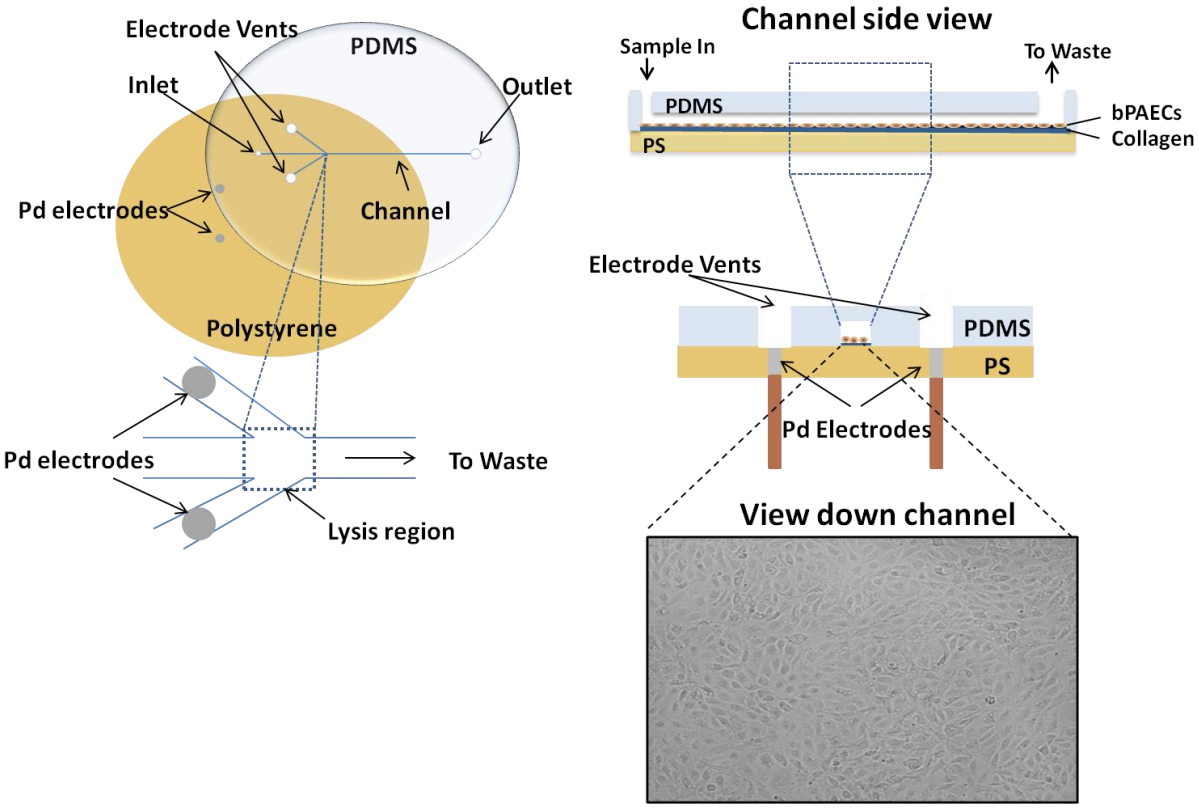

Figure 2.7 Y channel device for electrical lysis of cells. The PDMS component containing the channel features is reversibly sealed feature side down onto the polystyrene substrate housing the palladium (Pd) electrodes. The channel dimensions were 200 µm width x 100 µm height x 3 cm length. The area where the electrode channels intersect the main channel was the desired lysis region (A). Cross section of the channel containing bPAECs over collagen adhered on the PS substrate. The view down the channel shows the electrode vents over the Pd electrodes allowing for gas escape during electrical lysis (B).

Figure 2.8 shows the completed device with channel areas dyed for visual clarity. The dye remains in the channel due to PDMS reversibly sealing to the PS base.

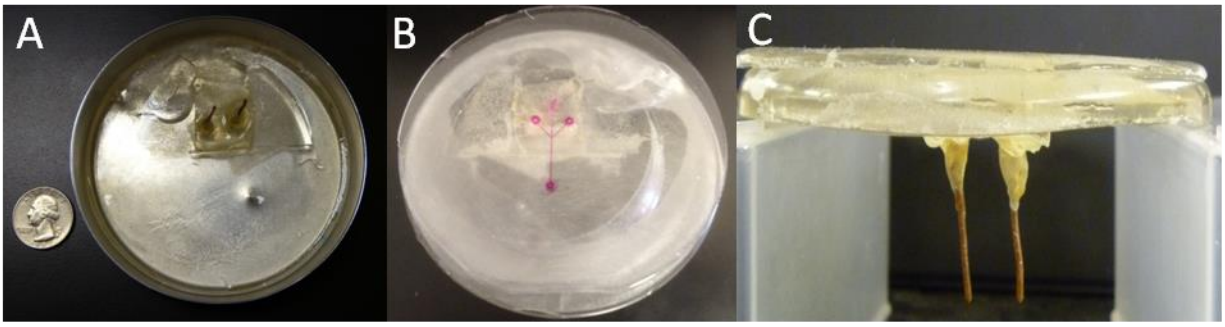

Figure 2.8 Completed device based on a Y channel design with embedded electrodes in a PS base. Size comparison of the PS base with embedded electrodes before removal from the aluminum mold (A). PS microfluidic base with a PDMS top featuring a Y channel with two vent wells over the electrodes and a waste well seen in pink (B). Side view of the PS microfluidic prototype where the electrodes can be seen protruding from the PS base (C).

After cell lysis, the PDMS component was removed and discarded and the PS base was reused after removal of cells and polishing the electrodes. The reusability of the PS component and disposability of PDMS was a significant advantage to using PDMS and PS together in this manner.

2.2.4.2 Polycarbonate Membrane Implementation for Controlled Diffusion Design

In order to have more control over lysis in the desired region, a polycarbonate membrane (0.4 μm pore size) was used to allow better diffusion of hydroxide to specific areas. Figure 2.9 shows the modified device features. This device was more complicated than its predecessor, and relied on two pieces of PDMS placed on top of the PS base with embedded electrodes. From the bottom up, there was the PS base, then a PDMS component with a channel that connects three wells, two that were placed directly over the electrodes and one in the middle of the channel. A piece of polycarbonate membrane was placed over

this middle well and the final PDMS piece was placed on top, which had wells for electrode vents and a 200 μm width x 100 μm height x 3 cm length channel. This arrangement allowed for hydroxide produced at the cathode to diffuse to the middle well of the middle PDMS piece, through the polycarbonate membrane, and to eventually lyse any cells in the channel above the membrane in the top piece of PDMS.

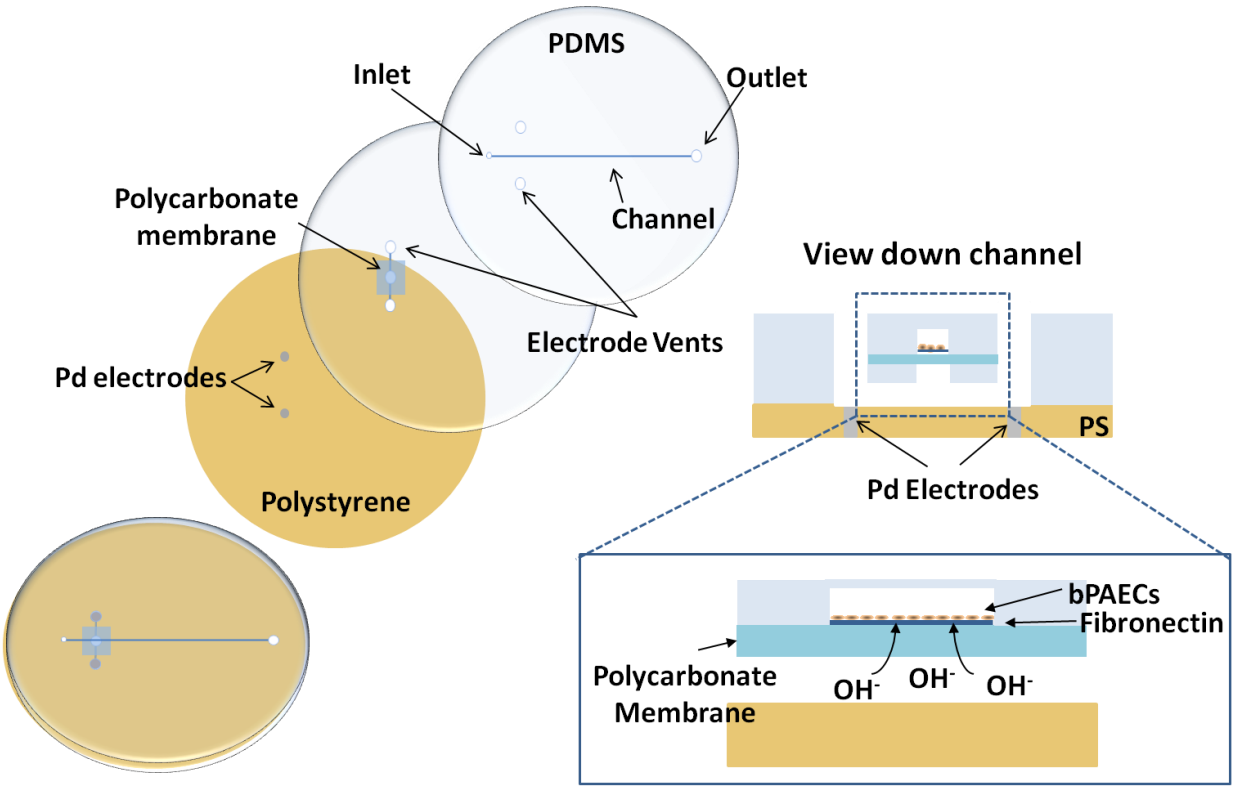

Figure 2.9 Device integrated with polycarbonate membrane for controlled hydroxide diffusion. A PDMS slab with a channel connecting the two palladium electrodes was placed directly onto the PS base. Electrode vents and a well in the middle of the channel were punched. A piece of polycarbonate membrane containing 0.4 μm diameter pores was positioned on top of the channel well to allow for hydroxide diffusion to the region directly above the microfluidic channel contained in the topmost PDMS component. This top PDMS piece contains a channel with inlet and waste wells, and also continued the vents above electrodes. Endothelial cells were seeded onto this top piece.

2.2.5 Preparation of Reagents

All reagents were used as received without further purification unless otherwise noted.

Endothelial Growth Media

Endothelial growth media (EGM) was prepared under sterile conditions from Dulbecco's Modified Eagle's Medium (DMEM, Caisson, North Logan, UT) containing 7.5% fetal bovine serum, 2.5% adult bovine serum, and 2.5% penicillin as an antibiotic solution.

Acid Citrate Dextrose

Acid citrate dextrose (ACD) was prepared in distilled deionized water and contained 38 mM $C_6H_8O_7$ (citric acid), 75 mM $C_6H_5O_7{\cdot}2H_2O{\cdot}3Na$ (sodium citrate dihydrate), and 124 mM $C_6H_{12}O_6{\cdot}H_2O$ (dextrose monohydrate). The resulting solution was sterile filtered once.

Modified Tyrode's Buffer

Modified Tyrode's Buffer (MTB) was prepared in distilled deionized water with the following composition: 12 mM $NaHCO_3$, 0.32 mM NaH_2PO_4, 10 mM HEPES, 137 mM NaCl, 2.7 mM KCl, 0.5 mM $MgCl_2{\cdot}6H_2O$, 5.5 mM glucose, 2 mM $CaCl_2$ (for MTB with calcium, for calcium free MTB this was omitted). The pH of the buffer was adjusted to 7.5 and sterile filtered once.

Phosphate Buffered Saline

Phosphate buffered saline (PBS) was prepared by dissolving 137 mM NaCl, 10 mM Na_2HPO_4, 2 mM KH_2PO_4, and 2.7 mM KCl in 1 L of distilled deionized water. The pH was adjusted to 7.4 with HCl and sterile filtered once.

Collagen

Purified collagen (CN) came as a 3.0 $mg \cdot mL^{-1}$ stock solution (Advanced Biomatrix San Diego, CA). Working solutions of 100 $\mu g \cdot mL^{-1}$ were prepared in distilled deionized water.

Fibronectin

A 1000 $\mu g \cdot mL^{-1}$ stock solution of fibronectin (FN; Sigma Aldrich St Louis, MO) was diluted in distilled deionized water to a working concentration of 100 $\mu g \cdot mL^{-1}$.

Rose Bengal

A 0.005 M stock solution of rose bengal (Sigma Aldrich St. Louis, MO) was prepared in PBS buffer. From this a working solution of 0.5 mM was made and used to incubate with cells.

Hoechst 33342

The nuclear cell stain Hoechst 33342 (Ex: 350 nm, Ex: 461 nm, Invitrogen, Carlsbad, CA) was prepared as a 10 $mg \cdot mL^{-1}$ solution in the PBS buffer described above.

Fluorescein

For studies measuring changes in the fluorescence intensity of fluorescein (fluorescein diacetate $C_{24}H_{16}O_7$, Sigma Aldrich St. Louis, MO) as an indicator of pH change, a 10,000 ppm stock solution was made from dissolving fluorescein in the PBS buffer solution described above. From this stock, a working solution of 10 ppm fluorescein was made.

Cell Tracker Green CMFDA

Cell tracker green CMFDA (5-chloromethylfluorescein diacetate; MW: 464.9 $g \cdot mol^{-1}$; Ex: 492 nm, Em: 517 nm; Invitrogen, Waltham, MA) was dissolved in 20 µL of anhydrous

dimethylsulfoxide (DMSO) to a final concentration of 5.4 mM. The stock solution was diluted into a final working concentration of 10.8 μM when 2 μL of the stock solution was added to a total volume of 1 mL of purified platelet suspensions or whole blood.

2.2.6 Collection and Purification of Human Platelets from Whole Blood

Platelets were purified from whole blood that was collected from consenting donors and used the same day for experiments using a procedure common to the Spence lab.[34] Two tubes or about 20 mL of whole blood was collected into heparinized tubes and centrifuged at 100*g* at 22 °C for 15 minutes. The resulting supernatant was comprised of platelet rich plasma (PRP), and was collected from the centrifuged suspension. Platelets were isolated from the PRP by adding 1 mL of ACD for every 9 mL of PRP and centrifuging at 1500*g* at 37 °C for 10 minutes. Platelets were then harvested and washed twice through centrifugation (1200*g* at 37 °C for 10 minutes) with a solution containing 10% ACD calcium-free MTB. Platelets were resuspended in 1 mL 10% ACD calcium free MTB. Washed platelets were counted using a hemacytometer and adjusted to a concentration of 3.0 x 10^8 platelets per milliliter in one mL of calcium free MTB. Platelets were stained for visualization by incubating with 0.011 mM CMFDA (Ex: 492 nm, Em: 517 nm) for one hour. After incubation, platelets were washed three times (1200*g* at 37 °C for 10 minutes in 10% ACD calcium-free MTB) to remove excess CMFDA.

2.2.7 Culture of Bovine Pulmonary Artery Endothelial Cells (bPAECs)

2.2.7.1 Cell Freezing

In order to preserve cell divisions, bPAECs were frozen during earlier divisions (passages 4-10). The freezing solution was comprised of EGM and 5% dimethyl sulfoxide (DMSO, v/v); 4 mL of freeze solution was prepared for each T-75 culture flask. Cells were

subcultured, removed from the flask with 0.25% trypsin, and resuspended in the freezing media. Cells were distributed in small cryo tubes (1 mL each) and immediately placed into a -80°C freezer for 4-12 hours. After this time, cells were transferred to a liquid nitrogen storage tank.

2.2.7.2 Cell Thawing

Frozen bPAECs stored in cryo tubes were removed from liquid nitrogen storage and thawed in a water bath set to 37 °C. The thawed cell solution was resuspended and added drop wise into a T-75 culture flask containing 10-14 mL of EGM at 37 °C. The flask was placed in a cell incubator (37 °C and 5% CO_2) for 24 hours, whereupon media was changed if the cells had attached as confirmed by microscopy.

2.2.8 Immobilization of Endothelial Cells on Microfluidic Devices

The micro-channels of the devices were sterilized prior to cell seeding by first cleaning both the PDMS slab and the polystyrene substrate with isopropyl alcohol, rinsing with distilled deionized water, and drying with nitrogen. The PDMS was placed channel-side down on the PS substrate, effectively reversibly sealing the two parts together. PS was chosen as the device substrate due to its use in tissue culture flasks and amenability to culture bPAECs among other cell types. Prior to seeding bPAECs, channels were coated with either 100 $\mu g \cdot mL^{-1}$ of FN or 50 $\mu g \cdot mL^{-1}$ of CN prepared in phosphate buffered solution, as optimized by the Spence group (only FN coating previously optimized),[35] as an adhesive substrate protein to which bPAECs can adhere. The adhesion protein was pipetted into the waste well of the device and drawn through the channel via suction. The adhesive protein was allowed to incubate on the device for 45 minutes at 37 °C. The channel was then dried with nitrogen gas and exposed to UV light for 15 minutes to sterilize the device. bPAECs

were cultured in T-75 flasks and resuspended in 1 mL EGM. This concentrated bPAEC solution was loaded into the channels of the device using a syringe. The cells in channels of devices were incubated at 37 °C for 1.5-2 hours until cells had attached, as confirmed via monitoring using an inverted microscope. After this time, cell adhesion was monitored and if needed, more cells were added to the channel. Cell media (EGM) was changed every 1-2 hours after cell attachment to the polystyrene substrate was confirmed.

2.2.9 Cell Lysis on the Microfluidic Devices

Cell lysis protocols differ based on the technique. For devices designed for laser-induced injury of bPAECs, rose bengal, a nucleus and cytoplasm stain, was used to allow visualization of cellular damage to the membrane. Cells in the presence of an electric field form transient membrane pores, therefore a cytoplasmic stain could be expelled from the cell. To confirm lysis via hydroxide generation, a nuclear stain (Hoechst) was used in conjunction with rose bengal or a post-lysis rose bengal staining treatment was done to verify the absence of any cells.

2.2.10 Laser-Induced Injury of bPAECs

Twelve well culture plates containing confluent endothelial cells or microfluidic chips (device in Figure 2.5) with cells grown to confluency in the channels were washed three times with PBS, then incubated with 0.5 mM rose bengal for 5 minutes. After incubation, cells were rinsed two times with PBS to remove excess rose bengal. Cells were irradiated at 514 nm with a pulsed Nd:YAG laser (Opotek, Carlsbad, CA) that delivered 10 shots per seconds, and each shot delivered 21 mJ. The power was set to 8 W/cm^2 and 0.21 W with an irradiated area of 0.0114 cm^2. Cells were re-stained with rose bengal to confirm lysis. Before and after the lysis procedure, bPAECs were imaged using an Olympus inverted

microscope. After laser injury, a 3 x 10^8 platelet per milliliter solution of CMFDA labeled platelets in calcium containing MTB was flowed over the irradiated endothelium for 20 minutes at a flow rate of 2.0 μL per minute using a syringe pump (Harvard Apparatus, Holliston, MA). The device was then incubated for 20 minutes in a cell incubator at 37 °C and 5% CO_2. After this time non-adherent platelets were rinsed away from the channel by flowing MTB for 20 minutes at a flow rate of 2.0 μL per minute. Adhered CMFDA-labeled platelets were visualized with an Olympus inverted microscope.

2.2.11 Electrochemically Produced Hydroxide

Once bPAECs had grown to confluency in a T-75 culture flask, 2 μL of a 10 mg·mL^{-1} stock solution of Hoechst 33342 stain was added to the flask 30 minutes before harvesting to visualize cells during the immobilization and lysis process. After the immobilization process, cells were rinsed with PBS. A PowerPac Universal Power Supply (Bio-Rad, CA) was used as the voltage source for bPAEC lysis. Optimal cell lysis was determined by testing a range of electrical potentials and monitoring cell lysis. Before lysis, bPAECs were imaged using an Olympus MVX10 macroscope (Olympus America, Melville, NY) with an electrothermally cooled charge-coupled device (CCD) camera (Orca, Hamamatsu) and Microsuite software (Olympus America). The macroscope was fitted with a DAPI filter cube (ChromaTechnology Corp.) containing the excitation (325-375nm) and emission (435-485nm) filters. Potentials applied to the device were 40, 60, 80, and 100 V for 1 minute, or for optimized times when specified. For optimized lysis times, potentials were applied until cell clearance in the channel intersection was observed. After electrical lysis, the channels were rinsed with PBS to ensure any non-adherent cells were removed from the channel. After rinsing, the channel was again imaged so that lysis efficiency could be determined.

2.2.12 Cell Damage Image Capture and Analysis

Cell imaging was carried out using either an Olympus MVX10 macroscope (Olympus America, Melville, NY) or an Olympus IX71 inverted microscope (Olympus America, Melville, NY) with electrothermally cooled CCD camera (Orca, Hamamatsu) and Microsuite software (Olympus America, Melville, NY). The macro and inverted microscopes were fitted with appropriate filter cubes to image Hoechst 33342 labeled bPAECs and fluorescein. For fluorescein, the macroscope was fitted with a FITC (fluorescein isothiocyanate) filter cube (ChromaTechnology Corp., Bellows Falls, VT) containing the excitation (460-500 nm) and emission (505-560 nm) filters. When determining lysis efficiency (hydroxide lysis protocol), Hoechst 33342 labeled bPAECs where imaged on a macroscope fitted with a DAPI filter cube (ChromaTechnology Corp., Bellows Falls, VT) containing the excitation (325-375nm) and emission (435-485nm) filters.

2.2.13 Confirmation of Lysis Method

2.2.13.1 Photochemical Lysis

Cell membrane damage via laser irradiation of a photochemical dye (rose bengal) was confirmed through visualization of cells on an inverted microscope before and after injury and compared to cell damage reported in the literature. Cells were incubated with 0.05 mM rose bengal for five minutes, then bPAECs were washed by flowing PBS through microfluidic channels to remove excess dye. Cells were irradiated with a pulsed 514 nm Nd:YAG laser as described under laser-induced injury of bPAECs.

2.2.13.2 Hydroxide Formation

To confirm lysis was caused via hydroxide formation, the origin of lysis and time for cells to lyse was monitored. Cells labeled with Hoechst 33342 were visualized during the lysis process using an inverted microscope. Furthermore, hydroxide generation at the cathode was monitored using fluorescein as a pH indicator. Fluorescein intensity is sensitive to changes in pH 5-9 as seen in the Figure 2.10.

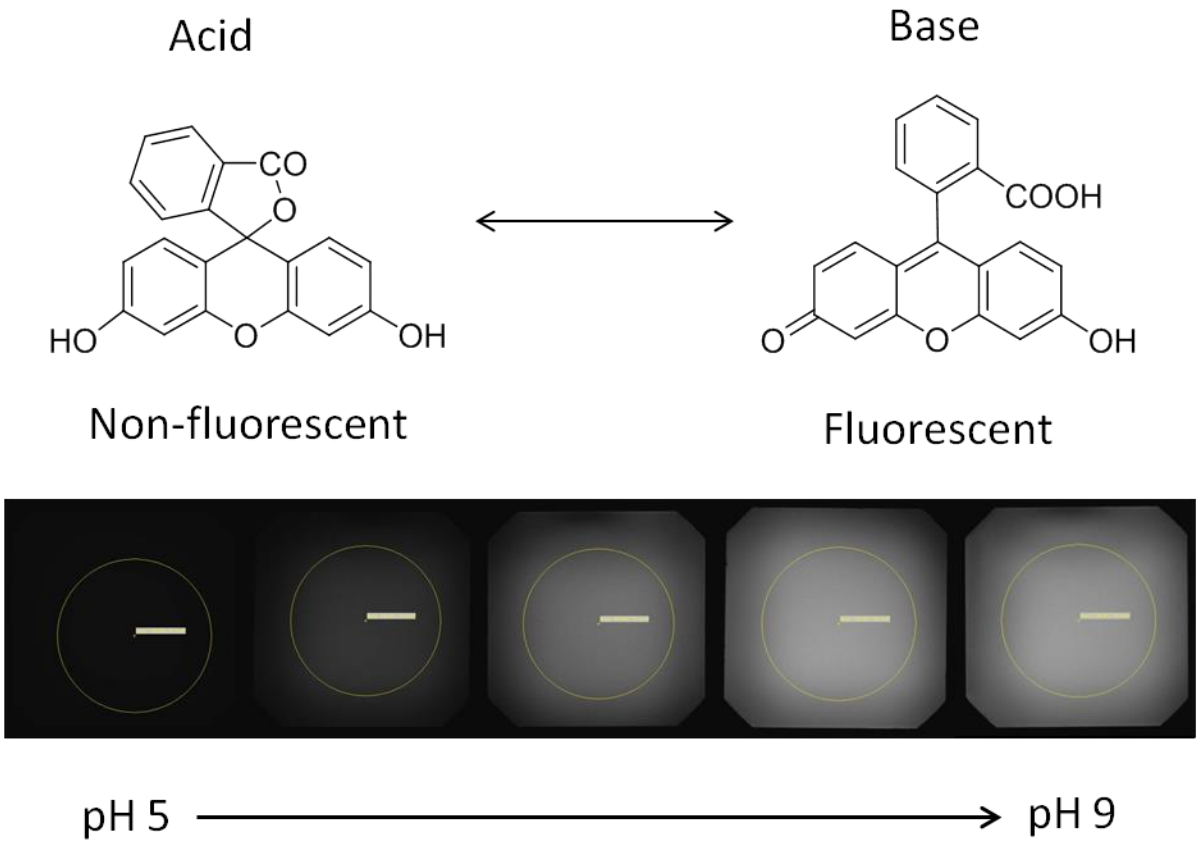

Figure 2.10 Utilization of fluorescein as a means to calculate pH of electrolyzed buffer generated at the cathode. At an acidic pH fluorescein appears colorless, but as the pH becomes more basic, the fluorescence intensity increases. Qualitative images correspond to pH standards 5-9 made from 10 ppm fluorescein in PBS.

2.2.14 Determining Lysis Efficiency

2.2.14.1 Hydroxide Formation

To determine lysis efficiency, cells in the channel intersection (or the desired lysis region) fluorescently labeled with Hoechst 33342 were imaged on an inverted microscope and enumerated before and after lysis as depicted in Figure 2.11.

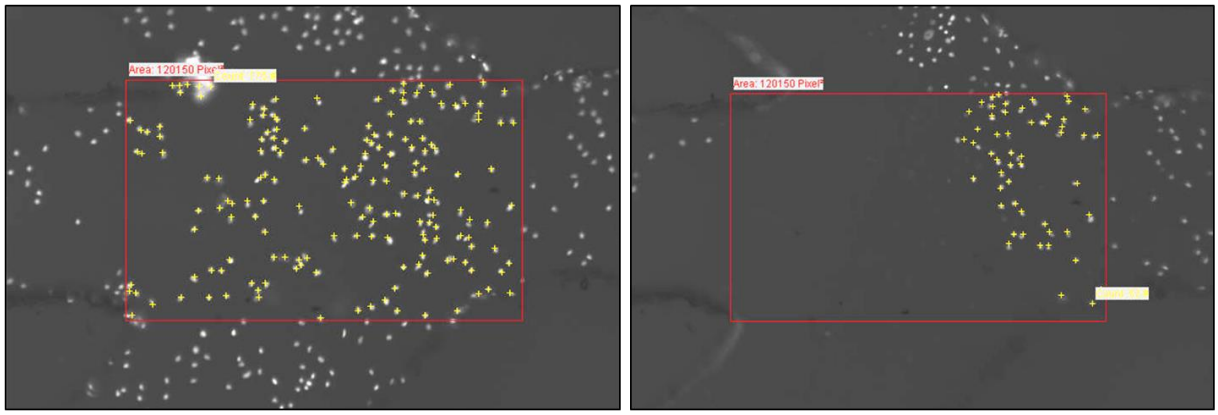

Figure 2.11 Determining cell lysis efficiency. Cells in the intersection region were enumerated before lysis (left, 175 cells) and following lysis (right, 53 cells) to find the number of lysed cells. Using equation 2.1, the cell lysis percent correlating to lysis efficiency was determined. Images correspond to 60 V applied for 78 seconds and a cell lysis efficiency of 70% using the device seen in Figure 2.7.

Cell lysis efficiency was determined using equation 2.1. The percent cell lysis or lysis efficiency was calculated for each potential applied for a given time, and this value was used to express lysis efficiency. The number of cells lysed was determined using Microsuitesoftware to count the number of cells before and after lysis. The number of cells lysed was defined as the difference in the number of cells remaining in the cell lysis region compared to the total number of cells present before lysis.

$$CellLysis\% = \frac{cellslysed}{cellsbefore} * 100 \qquad \text{Equation 2.1}$$

To ensure reproducibility of the cell count, the number of cells in the lysis region before and after lysis for one device were counted four times each to ensure consistent manual counting. The relative standard deviation (RSD) from this study was 10%.

2.2.15 Determining Optimal Lysis Potentials and Durations

Optimal lysis potentials, those which resulted in lysis selective to the desired lysis region for each channel geometry, were found by applying fixed potentials for fixed durations. Optimal potential durations were found by monitoring the lysis region during potential application and noting the time required to achieve cell clearance. A variety of potentials were used for one minute periods (100, 80, 60, and 40 V) or with optimized lysis times (100, 80, and 60 V). Hoechst 33342 stained bPAECs were used to visualize various stages of the lysis process.

2.3 Results

2.3.1 Photochemical Lysis

Laser irradiation of rose bengal labeled bPAECs immobilized on twelve well culture plates resulted in the cell damage seen in Figure 2.12. Culture plates were initially used to determine the optimal laser conditions before moving to a microfluidic platform. It was evident from the resulting images that two to four shots (42-92 mJ) would provide appropriate cell damage for subsequent platelet adhesion studies. Employing the microfluidic devices shown in Figure 2.5, platelet adhesion to the injured endothelium was monitored as seen in Figure 2.13. Increased platelet adherence occurred when the endothelium was injured, and more platelets were adhered when CN was used as the adhesive protein compared to FN.

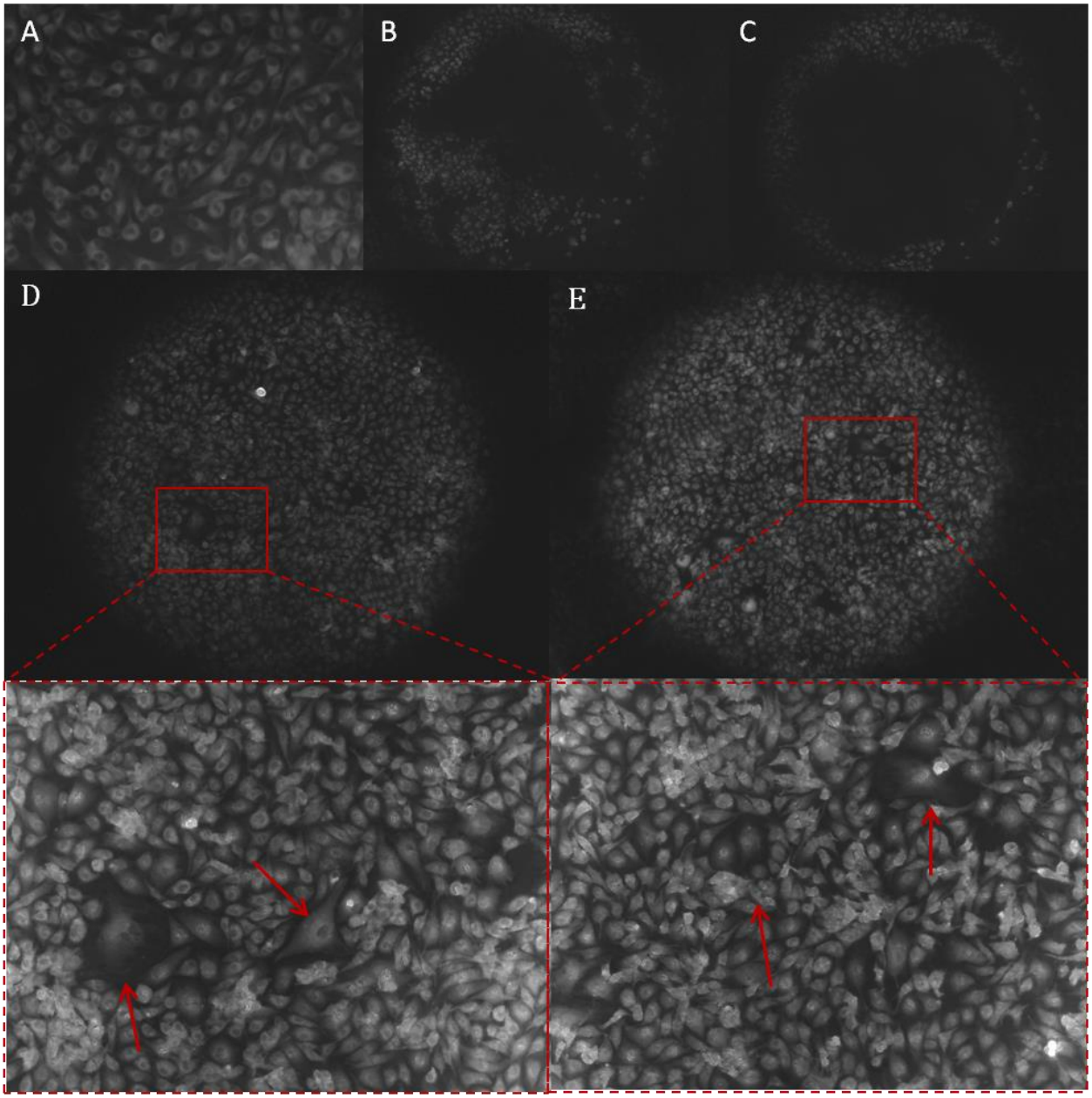

Figure 2.12 Cells injured via laser irradiation of a photochemical. All cell images are shown with cells labeled with 0.05 mM rose bengal. Cells were irradiated with a Nd:YAG laser (514 nm); power of 8 W/cm^2, 0.21 W; irradiated area of 0.0114 cm^2; pulsed laser: 10 shots/second where each shot was 21 mJ. No injury (A). 1 second irradiation (210 mJ) (B). 2 second irradiation (410 mJ) (C). 2 shots of irradiation (42 mJ) and corresponding image of increased magnification showing damaged cells (red arrows) (D). 3 shots of irradiation (63 mJ) and magnified area of damage (E).

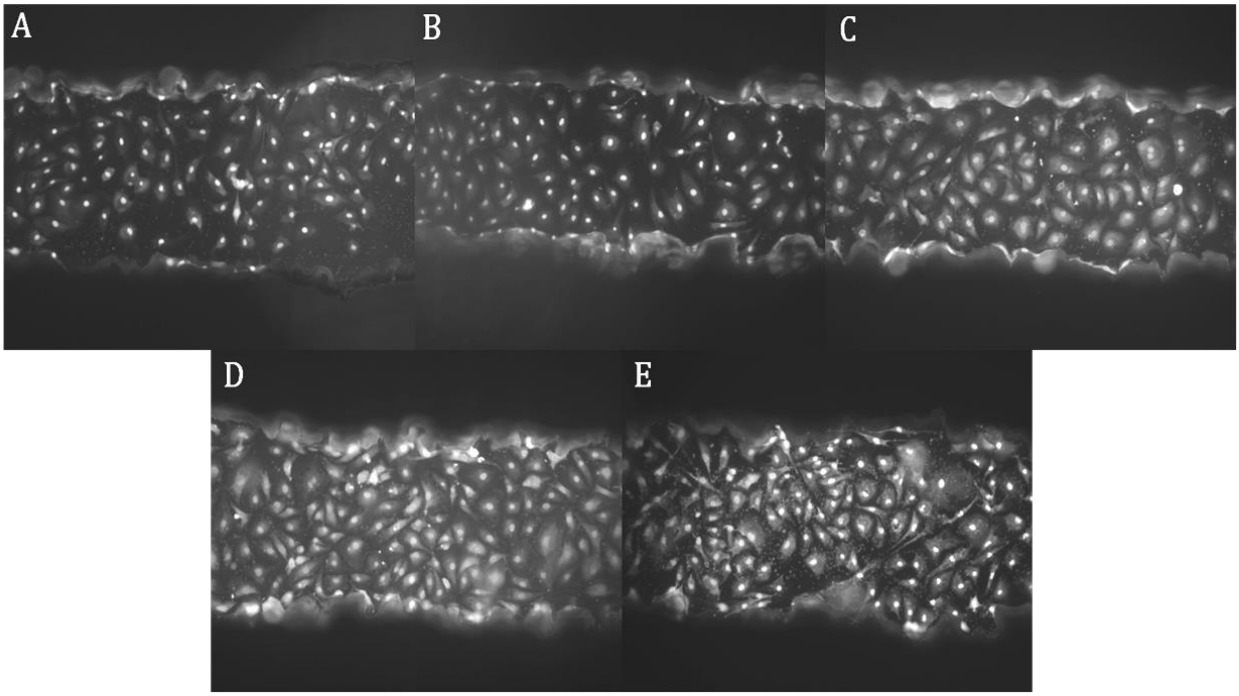

Figure 2.13 CMFDA-labeled platelet adhesion to an endothelium injured by laser irradiation of rose bengal. Either 50 μg per mL of FN (A-C) or 100 μg per mL of CN (D-E) were used as adhesive proteins for cell immobilization. Platelet adhesion (white dots) to an uninjured endothelium (A). Platelet adhesion after 3 shots (63 mJ) of irradiation (B). Platelet adhesion after 4 shots (84 mJ) of irradiation (C) Adhesion after 2 shots (42 mJ) of irradiation (D). Observed platelet adhesion after 3 shots (63 mJ) of irradiation (E).

2.3.2 Hydroxide Lysis

2.3.2.1 Y Channel Design

In order to confirm that lysis originated from hydroxide generation and not electrical lysis, the source of lysis and speed of lysis were probed. Lysis originating at the cathode (Figure 2.14, hydroxide was generated from the reduction of water) was an indicator of lysis from electrochemically generated hydroxide.

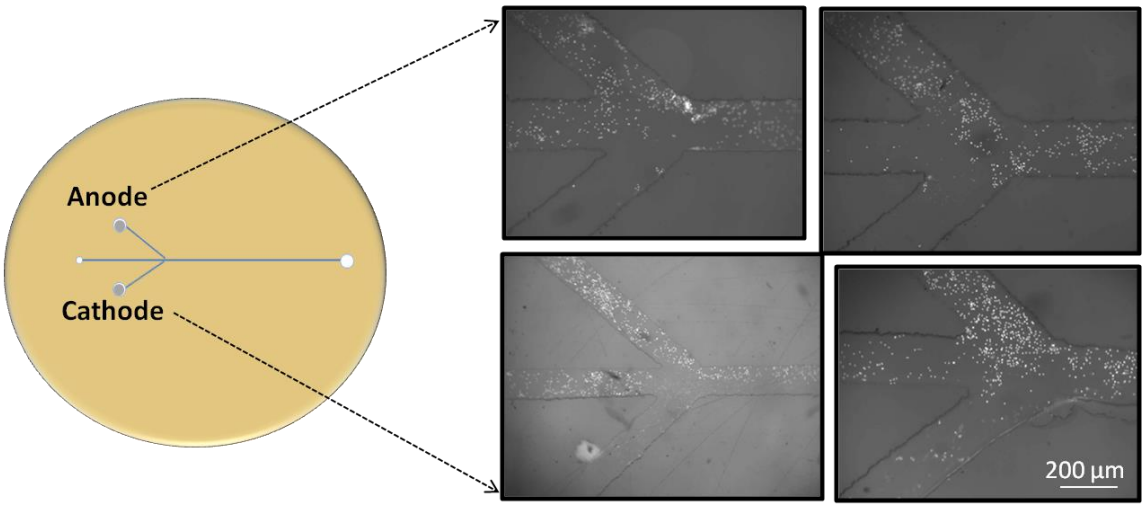

Figure 2.14 Confirming lysis via hydroxide formation by monitoring the origin of lysis. Leads of the power supply were chosen so that the cathode was positioned on the bottom. Images with Hoechst 33342 stained endothelial cells highlighted, all show lysis originating from the bottom channel oriented towards the cathode.

As seen in Figure 2.6, the region where the electrode channels intersect with the main channel was the area of desired cell lysis. The desired lysis region was monitored before and after lysis to determine lysis efficiency. For the data presented, a variety of potentials were used for one minute periods (100, 80, 60, and 40 V) or with optimized lysis times (100, 80, and 60 V). Results pertaining to lysis efficiency when potentials were applied for one minute can be seen in Figure 2.15. These results show that for applied potentials of 100 and 80 V for one minute, the lysis efficiency was nearly 100% (98 ± 1% and 97 ± 2%, respectively). Figure 2.16 shows several images of Hoechst 33342 stained bPAECs in various stages of the lysis process. In order to optimize the time needed to achieve cell clearance of the channel intersection, 100, 80, and 60 V potentials were applied until such clearance was observed. Figure 2.17 shows the results of the time optimization study.

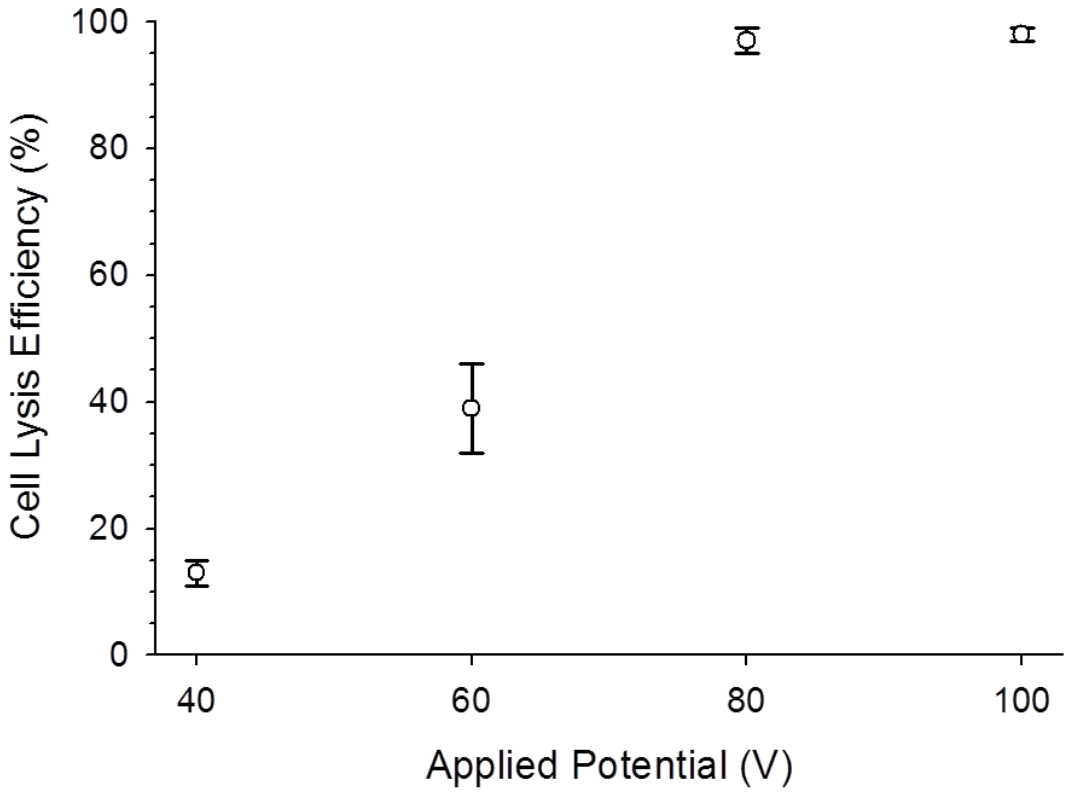

Figure 2.15 Cell lysis efficiency results pertaining to the channel intersection of the Y channel microfluidic device. Potentials of 40, 60, 80, and 100 V were applied for 1 minute with cell lysis efficiencies of 13 ± 2, 39 ± 7, 97 ± 2, and 98 ± 1 %, respectively. Data represent mean ± s.e.m.; n ≥ 3.

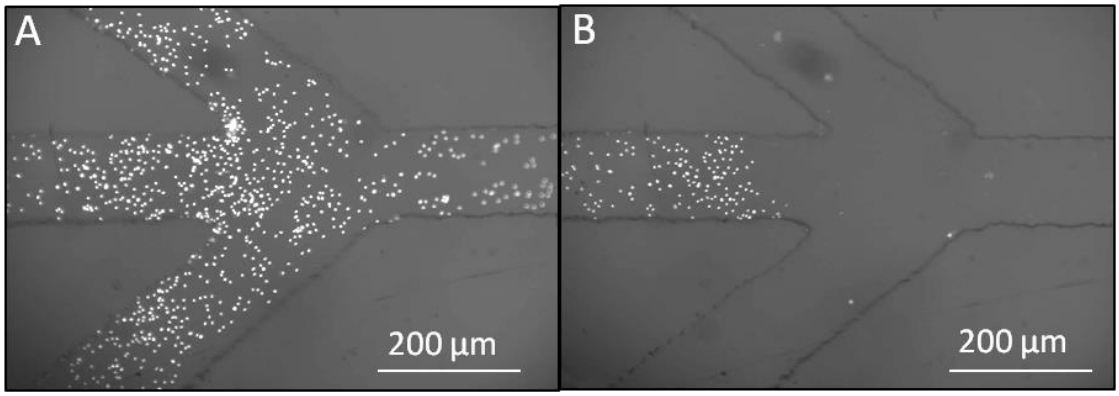

Figure 2.16 Images of Hoechst 33342 labeled bPAECs in the microfluidic Y channel before and after lysis when 80 V was applied to the device for 1 minute. bPAECs in the channel intersection before lysis (A). Rinsed channel after lysis (B).

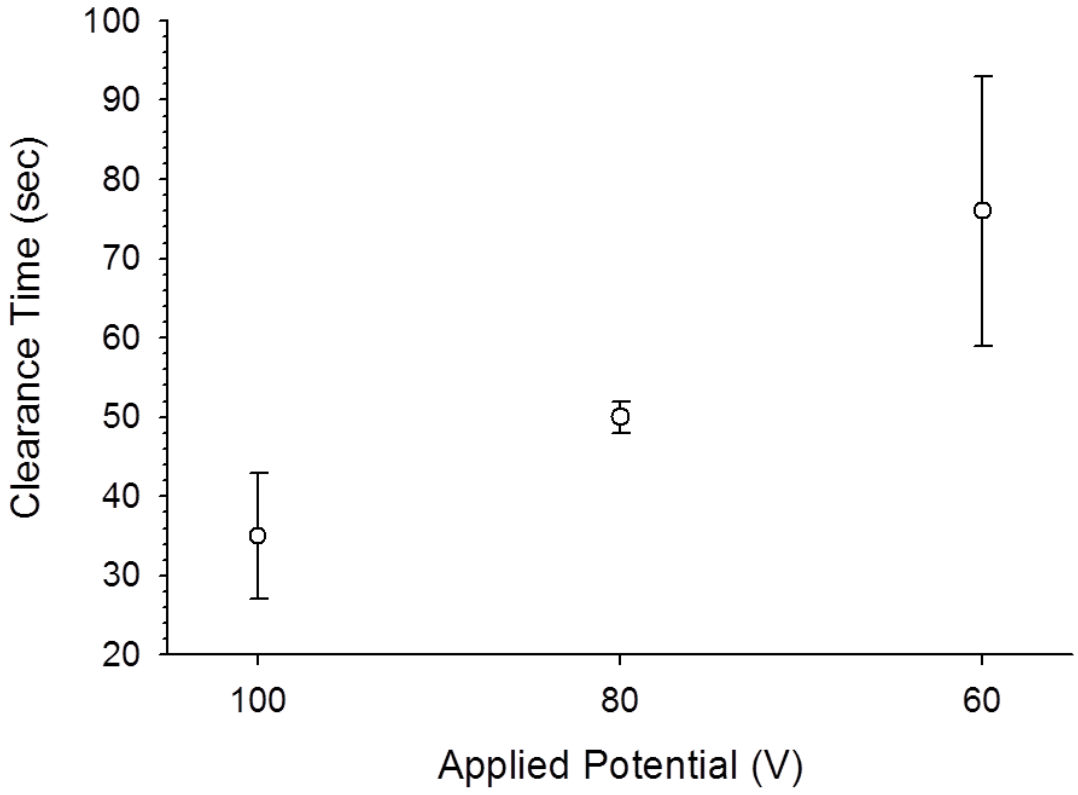

Figure 2.17 Timed lysis optimization results pertaining to the channel intersection of the microfluidic device where electrical potentials were applied until cells in the intersection were lysed. Potentials of 100, 80, and 60 V were applied for an average time of 35 ± 8, 50 ± 2, and 76 ± 17 seconds with cell lysis rates of 87 ± 1, 89 ± 3, and 80 ± 3%, respectively. Cell lysis rate data represent mean ± s.e.m.; n = 3. Clearance time data represent mean ± standard deviation; n = 3.

Application of increasing potentials resulted in less time to achieve cell lysis; the average time to reach cell clearance (as defined by visually confirming with microscopy the removal of cells from the microfluidic channel intersection by lysis) for 100, 80, and 60 V potentials was 35 ± 8, 50 ± 2, and 76 ± 17 seconds, respectively. Figure 2.18 shows representative fluorescent images taken from a time optimization experiment corresponding to a 60 V potential applied for 78 seconds.

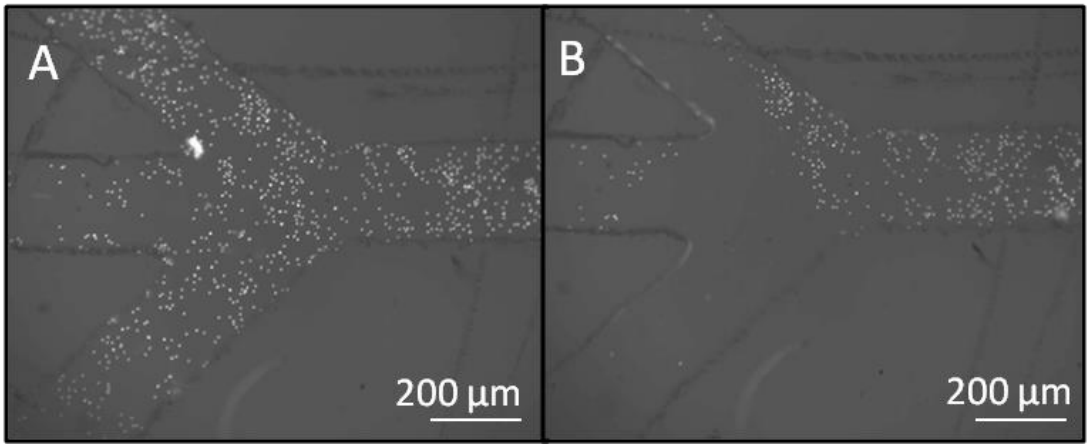

Figure 2.18 Images of Hoechst 33342 labeled bPAECs in microfluidic channels before and after the lysis process when 60 V was applied to the device for 78 seconds. bPAECs in the channel before lysis (A). Rinsed channel after lysis (B).

Hydroxide generation was further probed using fluorescein fluorescence as a pH indicator as fluorescein fluorescence intensity is sensitive to changes in pH from 5-9.[36] To confirm that increasing hydroxide concentrations result in increased intensity of fluorescein fluorescence, the microfluidic device outlined in Figure 2.19 was utilized and the fluorescent intensity of fluorescein was monitored as an indicator of pH change after flowing NaOH as a hydroxide donor.

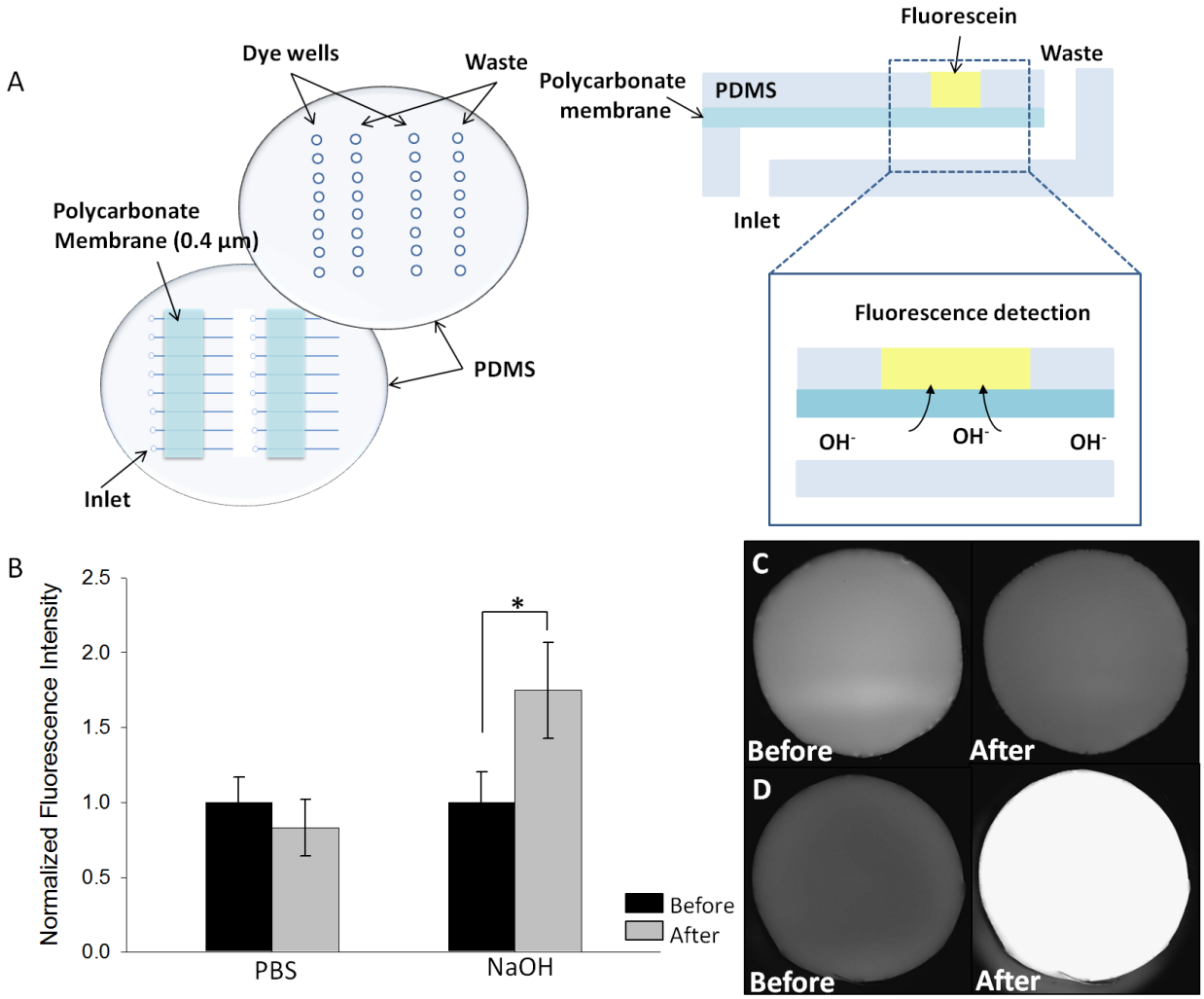

Figure 2.19 Confirmation that increased hydroxide results in an increase in fluorescein fluorescence intensity. The microfluidic device was comprised of a bottom piece of PDMS featuring parallel channels with inlet holes for sample introduction. Polycarbonate membrane with 0.4 µm diameter pores was positioned on top of the channel and lined up with dye wells punched on the top piece of PDMS. The dye well was loaded with 10 µL of 10 ppm fluorescein (A). The intensity of fluorescein in the dye well was measured before and after flowing either PBS (1X; pH 7.29) or a 5 M solution of NaOH (pH 13.56) for 30 seconds at a flow rate of 3µL/min. Data represent mean ± standard deviation; n ≥ 6; $p < 0.001$ (B). Images corresponding to intensity changes of fluorescein in the dye well before and after flowing PBS (C). Intensity changes of fluorescein before and after flowing 5 M NaOH (D).

To confirm electrolyzed buffer generated during cell lysis would also show an increase in fluorescein fluorescence intensity just as the control using NaOH as a hydroxide donor had, a 100 V potential was applied to electrodes of the Y channel device and the electrolyzed buffer generated at the cathode was collected and flowed in the device shown in Figure 2.20.

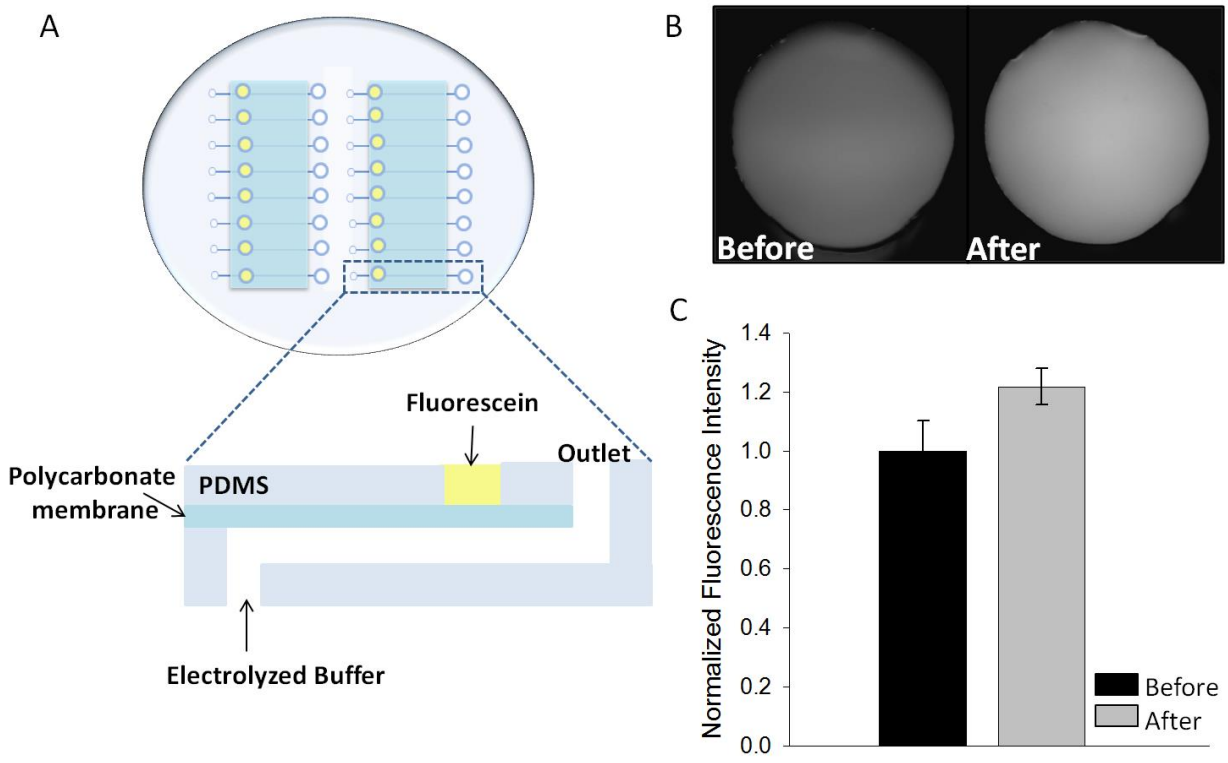

Figure 2.20 Use of fluorescein to evaluate pH change of electrolyzed buffer. The microfluidic device was comprised of two pieces of PDMS. From the bottom, a featureless slab of PDMS ontop of which a piece of polycarbonate membrane with 0.4 μm diameter pores was positioned, followed by a top piece of PDMS with a channel containing inlet and waste wells and a well containing 10 μL of 10 ppm fluorescein. Electrolyzed buffer was collected from the vent above the cathode of a microfluidic device with embedded electrodes and flowed through the channel. Any hydroxide present in the buffer could then diffuse into the fluorescein well and the pH change noted by measuring the change in fluorescence intensity (A). Images of the fluorescein containing well before and after electrolyzed buffer was flowed through the channel (B). A comparison of the normalized fluorescent intensities between the two wells showing a significant increase in intensity after flowing. Data represent mean ± standard deviation; n = 5; $p < 0.05$ (C).

2.3.2.2 Polycarbonate Membrane Design

Figure 2.21 shows results pertaining to cell lysis carried out on the polycarbonate membrane-based device featured in Figure 2.9. Lysis was confirmed both microscopically by labeling cells with Hoechst 33342 and via comparison of fluorescence intensity of the channel region exposed to hydroxide diffusion from the cathode, before and after the lysis process.

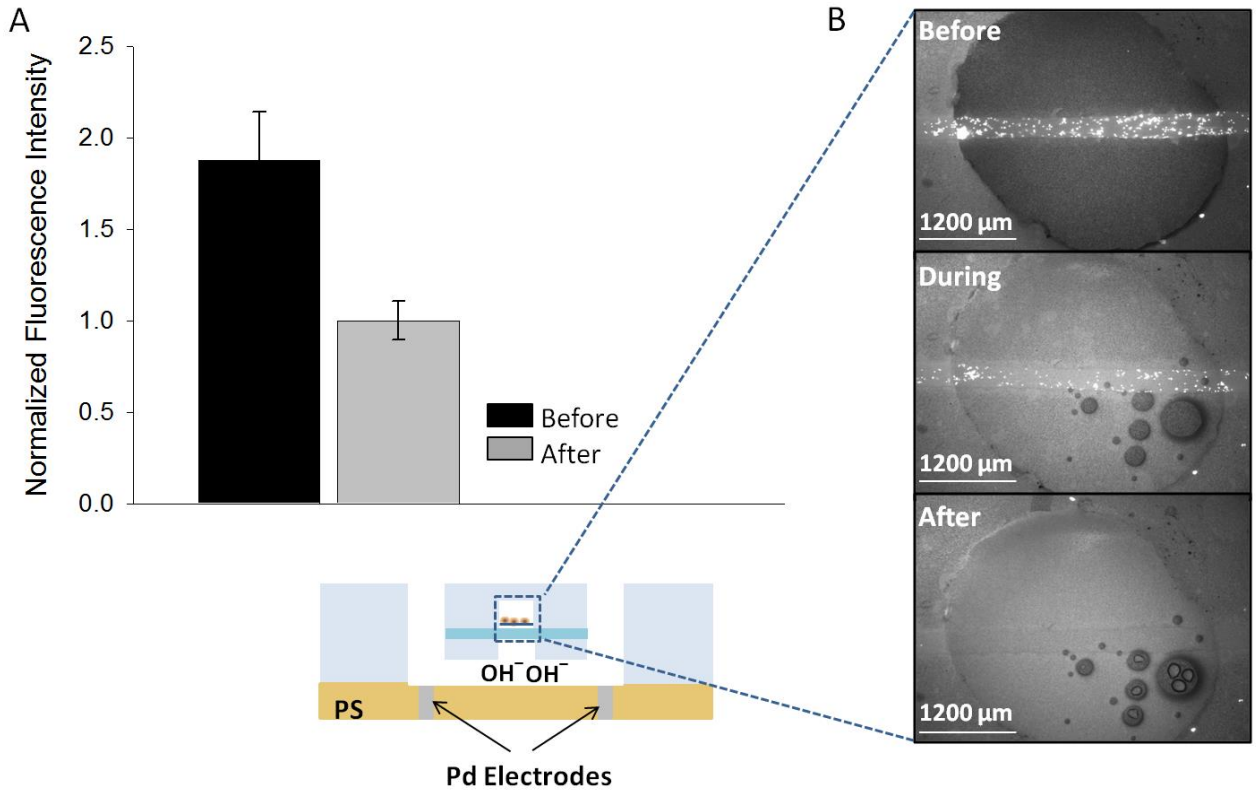

Figure 2.21 Cell lysis on a polycarbonate based microfluidic device via hydroxide. Normalized fluorescence intensity corresponding the cells over the well for hydroxide diffusion. Data represent mean ± s.e.m.; n = 4; $p < 0.05$. (A). Images corresponding to Hoechst 33342 stained cells lining the microfluidic channel before, during, and after lysis (B).

2.4 Discussion

2.4.1 Photochemical Injury Method

Cell damage resulting from irradiation of cells incubated with a photochemical dye (Figure 2.12) was more accurately characterized as cell deformation compared to cell lysis. Figure 2.12 A shows an image of non-irradiated bPAECs labeled with 0.005 mM rose bengal. 2.12 B shows the complete area of irradiation (0.0114 cm^2) with one second (210 mJ) of laser exposure. Figure 2.12 C shows the complete area as well, with two seconds (420 mJ) of exposure. From these two images it was evident that complete cell destruction was occurring as evident from the disappearance of cells from the center of the irradiated area. Furthermore, upon examination of the microfluidic devices after irradiation, the plastic component of the petri dish was burned. Figures 2.12 D and E (2 shots, 42 mJ; 3 shots 64 mJ, respectively) highlight attempts at using shorter durations of laser irradiation. These efforts were closer to the intended outcome, and show similar cellular damage seen from literature examples (Figure 2.1). For example, the magnified images of cell damage from irradiation with two and three shots from the laser show cell membrane deformation consistent with expected results and differed in appearance from non-injured control cells. Increased platelet adhesion to an injured endothelium was seen with more powerful irradiation to the endothelium when both collagen and fibronectin were used as adhesive proteins for cell immobilization in the channel (Figure 2.13).

Microfluidic devices (Figure 2.5) relying on photochemical injury of cells were riddled with complications that made them non-viable options for further development. Firstly, controlling the exact location of irradiation on the microfluidic channel was extremely difficult. Even when mounting the device on a platform for stability, it was only

through marking the back of the petri dish with permanent marker that the irradiation spot was able to be easily visualized. Secondly, the type of cell injury was cell deformation (cell swelling and surface blebbing), in lieu of cell lysis as seen in Figure 2.12. These results compared with literature examples of observed cell damage via photochemical injury.[4,3] Even after rinsing the channels after cell irradiation several times, cells remained attached to the channel. This type of cellular injury would have applications in studies aimed at endothelial cell damage, without the exposure of subendothelial collagen. However, this methodology was lacking for the purposes of fabricating a thrombosis mimic that would have allowed for the formation of a blood clot.

2.4.2 Lysis via Hydroxide Formation

2.4.2.1 Y Channel Design

Hydroxide lyses cells by cleaving membrane phospholipids, leading to cell permeabilization and eventual lysis.[12] The source of lysis was confirmed as originating from the cathode by imaging the spread of cell lysis. Figure 2.14 shows four trials where in each case lysis spreads from the electrode designated as the cathode based on lead application. PBS was used as the lysis buffer for each device, and the predominant electrolyte present was NaCl. The electrolysis of aqueous NaCl does produce hypochlorite, a chemical with bleaching action that could lead to cell lysis. However, hypoclorous acid and hypochlorite were disregarded as the electrolyzed species leading to lysis based on the spread of lysis originating at the cathode.

A crucial aspect in characterizing the device involved determining the strength and duration of the potential applied to the electrodes required for cell lysis in the desired lysis region. This proved to be a challenge because depending on these two variables (potential

duration and strength) lysis could occur across the entirety of the channel, with higher potentials applied for longer periods leading to more of the channel being cleared. The data in Figure 2.15 show that the extent of cell lysis depends on the strength of the applied potential when potential durations are one minute. Applied potentials of 60 and 40 V for one minute did result in less cell clearance (39 ± 7 and 13 ± 2%, respectively) from the channel than 80 and 100 V potentials applied for the same time (cell clearance of 97 ± 2 and 98 ± 1%, respectively). The high lysis efficiencies associated with 100 and 80 V potentials can be misleading within the context of having a device capable of targeted cell lysis, as most of the cells in the channel are lysed at these potentials, and the extent of cell clearance in the channel intersection for 60 and 40 V was not ideal. Figure 2.16 shows an example of cell clearance from a Y channel device when 80 V was applied for one minute. It was clear from these images that potential duration optimization was necessary to determine the appropriate parameters to achieve lysis selectively in the channel intersection.

Optimal lysis times were found by applying a set potential until cell clearance from the lysis region was achieved. Figure 2.17 shows the average time to achieve clearance from the lysis region in seconds for 100, 80, and 60 V applied potentials (35 ± 8, 50 ± 2, and 76 ± 17 seconds, respectively). As expected, with decreasing applied potentials, a longer time was required for hydroxide diffusion to induce cell lysis. From the calculated cell lysis efficiencies for 100 V (87 ± 1%), 80 V (89 ± 3%), and 60 V (80 ± 3%), it can be concluded that even with optimization of the time variable, clearance from Y channel devices based on hydroxide generation and diffusion for complete cell lysis isolated to the lysis region was lacking. This was further exemplified through examination of the images in Figure 2.18

where bPAECs are displayed before and after application of a 60 V potential for 78 seconds. While this protocol resulted in more selective cell clearance from the channel, cells in the desired lysis region were still evident.

Figure 2.19 showcases a proof of principle experiment designed to validate the use of fluorescein as a means of detecting hydroxide presence through an increased fluorescence intensity resulting from a decrease in pH. As shown in Figure 2.19 B and C, when PBS was flowed as a control under a well containing 10 ppm fluorescein, no significant increase in intensity was recorded. However, when a 5 M concentrated solution of NaOH used as a hydroxide donor was used, a significant increase in fluorescence intensity was found quantitatively (Figure 2.19 B) and qualitatively (Figure 2.19 D). Once the protocol had been established as a viable means of evaluating hydroxide presence, electrolyzed buffer was collected from above the cathode during a 100 V potential application. The device used to evaluate the electrolyzed buffer (Figure 2.20 A) featured a microfluidic channel under a well separated by a 0.4 μm polycarbonate membrane. The well was loaded with 10 μL of 10 ppm fluorescein and the electrolyzed buffer was flown at 3 $\mu L \cdot min^{-1}$. Intensity measurements corresponding to fluorescein were acquired before and after electrolyzed buffer was flowed under the well. Qualitative (Figure 2.20 B) and quantitative (Figure 2.20 C) data show a slight, though statistically significant ($p < 0.05$) increase in fluorescence intensity indicative of hydroxide presence.

2.4.2.2 Polycarbonate Membrane Design

In order to achieve more selective clearance of cells based on electrochemically generated hydroxide, a polycarbonate membrane was integrated with a microfluidic device as shown in Figure 2.9. Ideally, control of lysis from hydroxide diffusion would be easier to

manage with such an arrangement. Figure 2.21 summarizes efforts to selectively lyse Hoechst 33342 labeled cells. Figure 2.21 B shows a series of images taken during the lysis process where clearance of cells from the region above the well for hydroxide diffusion was seen. Gas bubbles were seen under the polycarbonate membrane during the lysis process indicating not all gas produced at electrodes was removed through the electrode vents. Overall, this design did offer an improvement in selective lysis compared to Y channel devices. However, the more complicated design made the fabrication process more time intensive. The fact that the PDMS components were discarded after one use imposed further limitations on this design.

Microfluidic devices comprised of either PDMS or PDMS/PS with embedded electrodes were fabricated and successfully used to lyse cells by chemical means. In theory, the advantages of lysis via irradiation of a photochemical dye lies in the ability to irradiate a specific region with great accuracy in a short period of time. Pinpointing the exact location of irradiation was much more difficult to manage in reality. The short time scale for initiating cell damage was an advantage compared to hydroxide lysis, but the nature of cell damage could be characterized more as a surface injury compared to cell rupture. Lysis via hydroxide diffusion was time consuming, and the scope of lysis was much more difficult to control compared to photochemical lysis. However, cells were actually lysed using this technique and so lysis via hydroxide generation was the preferred method.

Table 2.1 Comparison of chemical lysis by laser irradiation of rose bengal and electrochemically generated hydroxide with respect to mechanisms of cell damage, lysis evaluation, time scales, device designs and reusability, and lysis selectivity.

Device Characteristic	Laser Irradiation of Rose Bengal	Electrochemically Generated Hydroxide
Mechanism of Cell Damage	Membrane breakdown via radical presence	Cleavage of membrane phospholipids leading to membrane poration
Observed Cell Damage	Surface damage; membrane deformation	Cell lysis
Time Scale	< 3 seconds	< 2 minutes
Simplicity of Device Design	PDMS/petri dish reversible sealed together	PDMS/PS base with embedded electrodes; multiple PDMS components; polycarbonate membrane integration
Selectivity of Lysed Area	Damaged area corresponds to the irradiated area (0.0114 cm^2)	Difficult to control; based on hydroxide diffusion so undefined borders
Device Reusability	PDMS component discarded after use; petri dish cleaned and reused	PDMS components discarded; PS base reusable
Method to Evaluate Lysis	Optical imaging	Optical imaging

Table 2.1 gives a summary of the advantages and disadvantages of the two chemical lysis techniques. Comparing the two techniques, it became apparent both could be improved upon when the purpose was eventual thrombus formation on a microfluidic device after injury simulation. Both required introduction of non-native components to the blood stream and therefore further remove the system from *in vivo* conditions. In addition, the process leading to cell lysis on each device was labor intensive and the extent of the observed lysis was often variable. For these reasons a new avenue was explored that would allow for a simpler means of fabricating a device for cell lysis – 3D printing.

REFERENCES

REFERENCES

(1) Westrick, R. J.; Winn, M. E.; Eitzman, D. T. *Arteriosclerosis, Thrombosis, and Vascular Biology* **2007**, *27*, 2079-2093.

(2) Lee, P. C. C.; Rodgers, M. A. J. *Photochemistry and Photobiology* **1987**, *45*, 79-86.

(3) Dougherty, T. J.; Gomer, C. J.; Henderson, B. W.; Jori, G.; Kessel, D.; Korbelik, M.; Moan, J.; Peng, Q. *Journal of the National Cancer Institute* **1998**, *90*, 889-905.

(4) Yoon, I.; Li, J. Z.; Shim, Y. K. *Clinical Endoscopy* **2013**, *46*, 7-23.

(5) Mousavi, S. H.; Tavokkol-Afshari, J.; Brook, A.; Jafari-Anarkooli, I. *Food and Chemical Toxicology* **2009**, *47*, 855-859.

(6) Tseng, S. C. G.; Feenstra, R. P. G.; Watson, B. D. *Investigative Ophtalmology & Visual Science* **1994**, *35*, 3295-3307.

(7) Panzarini, E.; Inguscio, V.; Dini, L. *International Journal of Photoenergy* **2011**, *2011*, 11.

(8) Matsuno, H.; Uematsu, T.; Nagashima, S.; Nakashima, M. *Journal of Pharmacological Methods* **1991**, *25*, 303-317.

(9) Saniabadi, A. R.; Umemura, K.; Matsumoto, N.; Sakuma, S.; Nakashima, M. *Thrombosis and Haemostasis* **1995**, *73*, 868-872.

(10) Feliciello, I.; Chinali, G. *Analytical Biochemistry* **1993**, *212*, 394-401.

(11) Di Carlo, D.; Ionescu-Zanetti, C.; Zhang, Y.; Hung, P.; Lee, L. P. *Lab Chip* **2005**, *5*, 171-178.

(12) Nevill, J. T.; Cooper, R.; Dueck, M.; Breslauer, D. N.; Lee, L. P. *Lab Chip* **2007**, *7*, 1689-1695.

(13) Nge, P. N.; Rogers, C. I.; Woolley, A. T. *Chemical Reviews* **2013**, *113*, 2550-2583.

(14) Terry, S. C.; Jerman, J. H.; Angell, J. B. *IEEE Transactions on Electron Devices* **1979**, *26*, 1880-1886.

(15) Ruzicka, J.; Hansen, E. H. *Analytica Chimica Acta* **1983**, *145*, 1-15.

(16) Ruzicka, J. *Analytical Chemistry* **1983**, *55*, 1040A-1053A.

(17) Manz, A.; Graber, N.; Widmer, H. M. *Sensor and Actuators B: Chemical* **1990**, *1*, 244-248.

(18) Manz, A.; Harrison, D. J.; Verpoorte, E. M. J.; Fettinger, J. C.; Paulus, A.; Ludi, H.; Widmer, H. M. *Journal of Chromatography* **1992**, *593*, 253-258.

(19) Harrison, D. J.; Manz, A.; Fan, Z.; Luedi, H.; Widmer, H. M. *Analytical Chemistry* **1992**, *64*, 1926-1932.

(20) Jacobson, S. C.; Hergenroder, R.; Koutny, L. B.; Warmack, R. J.; Ramsey, M. J. *Analytical Chemistry* **1994**, *66*, 1107-1113.

(21) Woolley, A. T.; Mathies, R. A. *PNAS* **1994**, *91*, 11348-11352.

(22) Agilent. *Lab-on-a-chip technology.* https://www.chem.agilent.com/cag/feature/8-98/feature (accessed October 28, 2015).

(23) Whitesides, G. M.; Ostuni, E.; Takayama, S.; Jiang, X.; Ingber, D. E. *Annual Review of Biomedical Engineering* **2001**, *3*, 335-373.

(24) Xia, Y.; Whitesides, G. M. *Annual Review of Materials Science* **1998**, *28*, 153-184.

(25) Genes, L. I.; N, V. T.; Hulvey, M. K.; Martin, R. S.; Spence, D. M. *Lab Chip* **2007**, *7*, 1256-9.

(26) Martin, R. S.; Root, P. D.; Spence, D. M. *Analyst* **2006**, *131*, 1197-1206.

(27) Kane, R. S.; Takayama, S.; Ostuni, E.; Ingber, D. E.; Whitesides, G. M. *Biomaterials* **1999**, *20*, 2363-2376.

(28) McDonald, J. C.; Whitesides, G. M. *Accounts of Chemical Research* **2002**, *35*, 491-499.

(29) Tehranirokh, M.; Kouzani, A. Z.; Francis, P. S.; Kanwar, J. R. *Biomicrofluidics* **2013**, *7*.

(30) Meyvantsson, I.; Beebe, D. J. *Annual Review of Analytical Chemistry* **2008**, *1*, 423-449.

(31) Anderson, K. B.; S.Y., L.; Martin, R. S.; Spence, D. M. *Analytical Chemistry* **2013**, *85*, 5622-5626.

(32) Johnson, A. S.; Anderson, K. B.; Halpin, S. T.; Kirkpatrick, D. C.; Spence, D. M.; Martin, R. S. *Analyst* **2013**, *138*, 129-136.

(33) Duffy, D. C.; McDonald, J. C.; Schueller, O. J. A.; Whitesides, G. M. *Analytical Chemistry* **1998**, *70*, 4974-4984.

(34) Anderson, K. B.; Karunarathne, W.; Spence, D. M. *Analytical Methods* **2012**, *4*, 101-105.

(35) Ku, C.; D'Amico Oblak, T.; Spence, D. M. *Anaytical Chemistry* **2008**, *80*, 7543-7548.

(36) Klitzing, R. V.; Mohwald, H. *Langmuir* **1995**, *11*, 3554-3559.

CHAPTER 3

3D PRINTED DEVICES FEATURING REMOVABLE ELECTRODES FOR ELECTRICAL LYSIS OF ADHERED ENDOTHELIAL CELLS

3.1 Introduction

The polyjet 3D printed devices discussed below serve as *in vitro* platforms for mimicking injury to a resistance vessel through electrical lysis of endothelial cells adhered to adhesive proteins serving as components of the extra cellular matrix (ECM). Surface modification to the channel of the devices with either PDMS or PS was undertaken to facilitate endothelial cell adherence. Devices were designed using computer-aided software and converted into .STL files before printing. The transparent, rigid material (Vero Clear) used in the printing process provides an optically transparent path to visualize endothelial cell adherence and supports integration of removable electrodes for electrical cell lysis in a desired region of the channel. Through manipulation of channel geometry, a low-voltage power source was used to selectively lyse adhered endothelial cells in a narrow region of the channel.

3.1.1 Device Design

Figure 3.1 shows the channel geometry of the 3D-printed devices that were used, and Table 3.1 outlines the specific device dimensions of the channels used for lysis studies. Electrical cell lysis requires the transmembrane potential ($\Delta\gamma$) of the cell to be greater than 1 V, as potentials less than or equal to this lead to poration of the cell membrane as demonstrated in Figure 3.2.

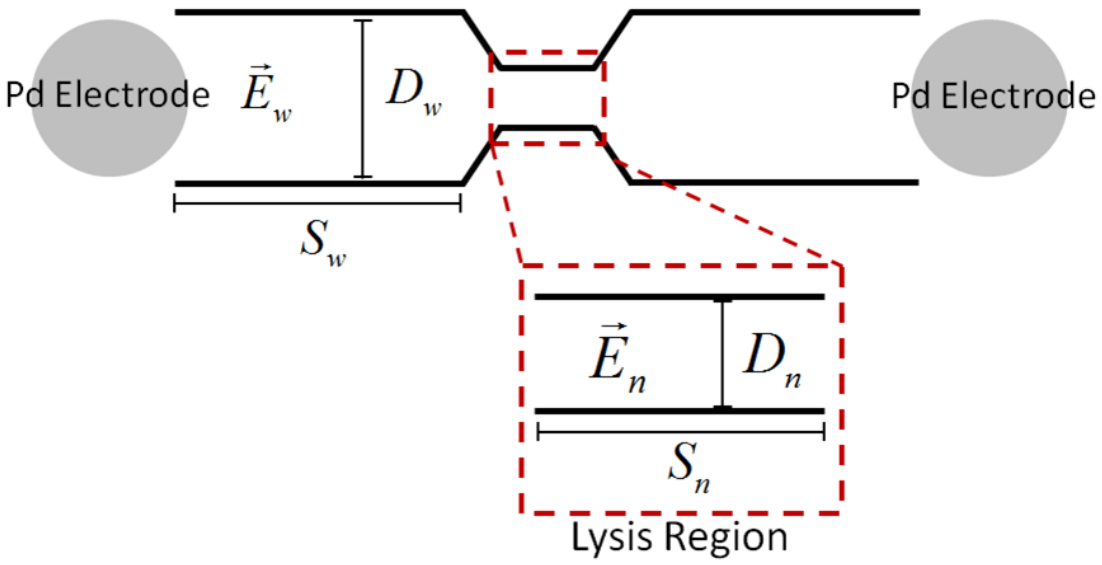

Figure 3.1 Schematic of the channel geometry of the 3D printed fluidic device highlighting the desired lysis region. Constriction of the channel mimics natural vessel stenosis and allows for electric fields of sufficient magnitude to cause cell lysis to be selectively generated in E_n while leaving cells in E_w regions unaffected.

Table 3.1 Device channel dimensions used in cell lysis optimization studies. Channel geometries for devices 1 and 2 are highlighted alongside calculated electric fields experienced in different regions of the channel when a 500 V potential was applied.

Model	D_w (mm)	D_n (mm)	S_w (mm)	S_n (mm)	Voltage (V)	E_w (V·cm^{-1})	E_n (V·cm^{-1})
Device 1	5	1	5	2	500	250	1250
Device 2	3.8	1	5	2	500	283	1084

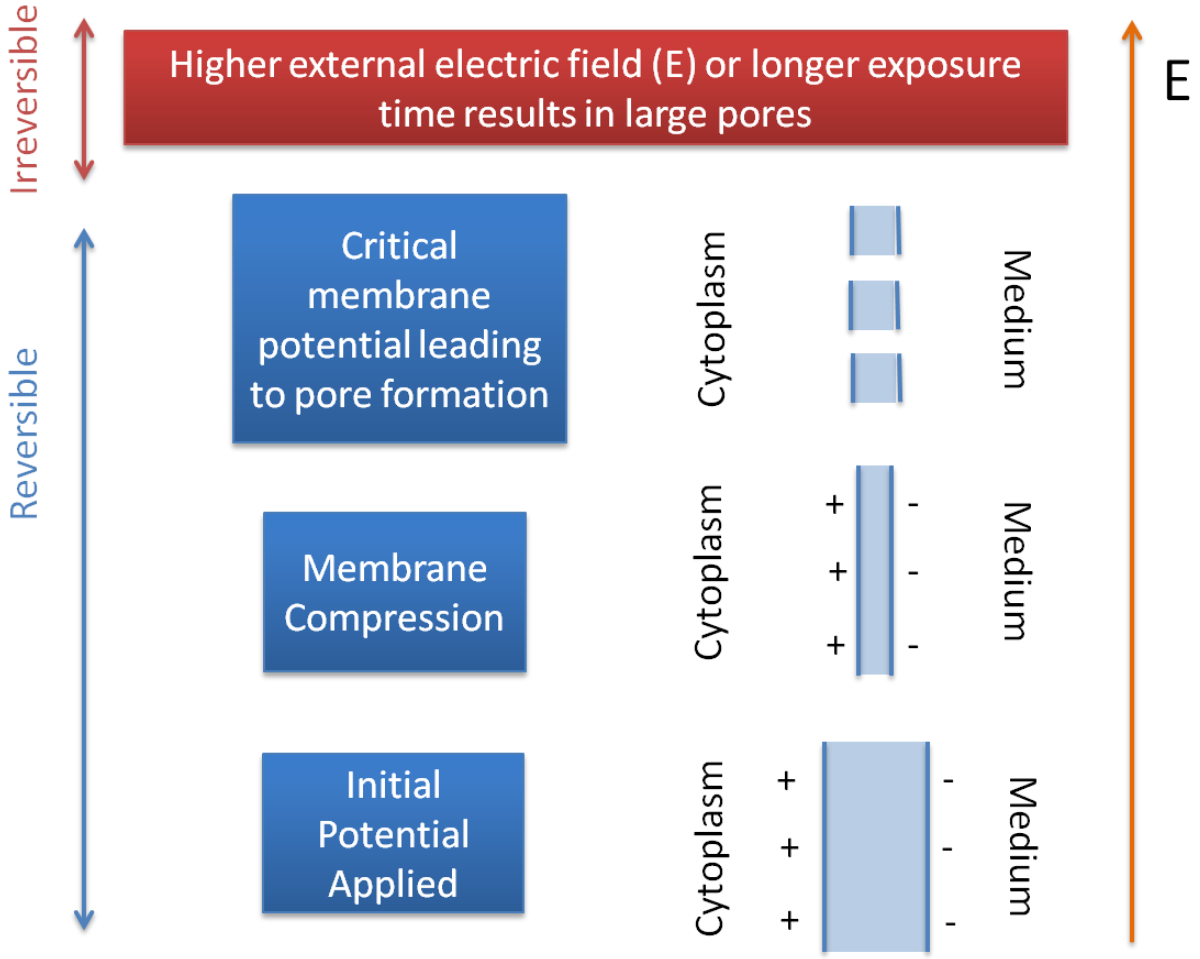

Figure 3.2 Process of cell membrane pore formation under the influence of an external electric field. Upon introduction to an external electric field, charge distribution between the intracellular and extracellular components develops. This leads to compression of the membrane. Transient pore formation occurs when the critical membrane potential is reached. If the strength of the electric field is high enough and the applied duration long enough, the membrane potential increases above 1 V, and pore formation becomes irreversible and the cell lyses.

This transient pore formation is reversible if the external electric field is removed and allows for cell fusion or delivery of drugs or DNA into a cell, but will not lead to cell lysis.[1]

The following equation outlines the external electric field necessary to achieve a $\Delta\gamma$ of 1 V,

where $\vec{E}$ is the external electric field strength, 1.5 is a weighing factor that quantifies the

effect the cell has on the external field, a is the radius of the cell, and cosθ is the polar angle of the cell in relation to the electric field (Figure 3.3):[2-4]

$$\vec{E} = \frac{\Delta\gamma}{1.5a\cos\theta} \qquad \text{Equation 3.1}$$

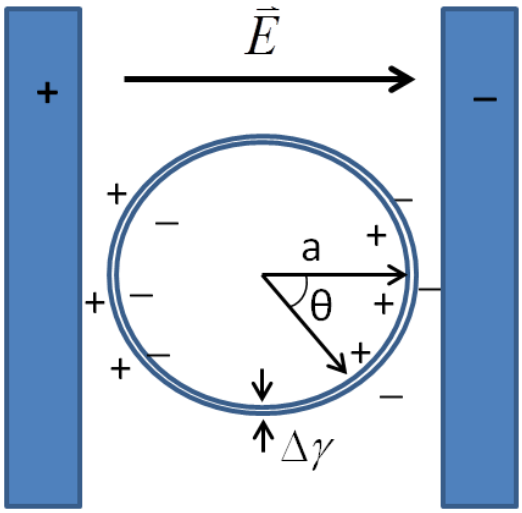

Figure 3.3 Parameters for electrical lysis of a cell under the influence of an electric field. Highlighted features include charge distribution along the cell bilayer leading to pore formation and subsequent lysis if Δγ ≥ 1 V. $\vec{E}$ is the external electric field strength, a is the radius of the cell, and cosθ is the polar angle of the cell in relation to the electric field. (Reprinted with permission from reference 5. Copyright Elsevier.)

For an endothelial cell with a diameter between 10-15 μm, the minimum electric field needed to achieve the necessary 1 V transmembrane potential for cell lysis is approximately 1000 V·cm^{-1}.

The most common methodology for electrical lysis of cells utilizes pulsed electric field strengths ranging from one to several hundred kV·cm^{-1} with microsecond to millisecond potential durations.[6] In order for a low voltage power supply (500 V_{max}) to be utilized, the geometry of the internal channel was augmented in areas so that an electric

field greater than 1000 V·cm^{-1} could be generated. Wang et al. and Lee et al. have shown that for a channel with uniform depth but varying width, a higher electric field can be generated in a narrow region, and the electric fields in the wide and narrow regions can be calculated with the following equations:[2,5]

$$\vec{E}_w = \frac{Voltage}{2S_w + S_n(D_w / D_n)} \qquad \text{Equation 3.2}$$

$$\vec{E}_n = \frac{Voltage}{2S_w(D_n / D_w) + S_n} \qquad \text{Equation 3.3}$$

Where $\vec{E}$ represents the electric field in the wide (w) or narrow (n) region, S is the segment length, D is the diameter of the channel, and voltage is the applied potential. Devices with different channel dimensions (Table 3.1) were fabricated to see which would provide more selective lysis isolated to the tapered region of the channel. Electric fields greater than 1000 V·cm^{-1} were calculated for the lysis region while in the wide regions electric fields were 250 V·cm^{-1} and 283 V·cm^{-1} for device 1 and 2, respectively, when a 500 V potential was used for cell lysis.

3.1.2 Design Iterations

Several iterations of devices were fabricated and optimized in order to better visualize and lyse cells (Figure 3.4). A limitation of using Vero Clear for cell culture is that it is not gas permeable, which is necessary for cell survival. Initial studies of cell viability carried out on slabs of Vero Clear supported cell survival up to several days, however cell adherence within channels was unsuccessful in early iterations (Figure 3.5 A-C) and so efforts were made to modify the surface of the channels with a substrate that would enable cellular adhesion and growth.

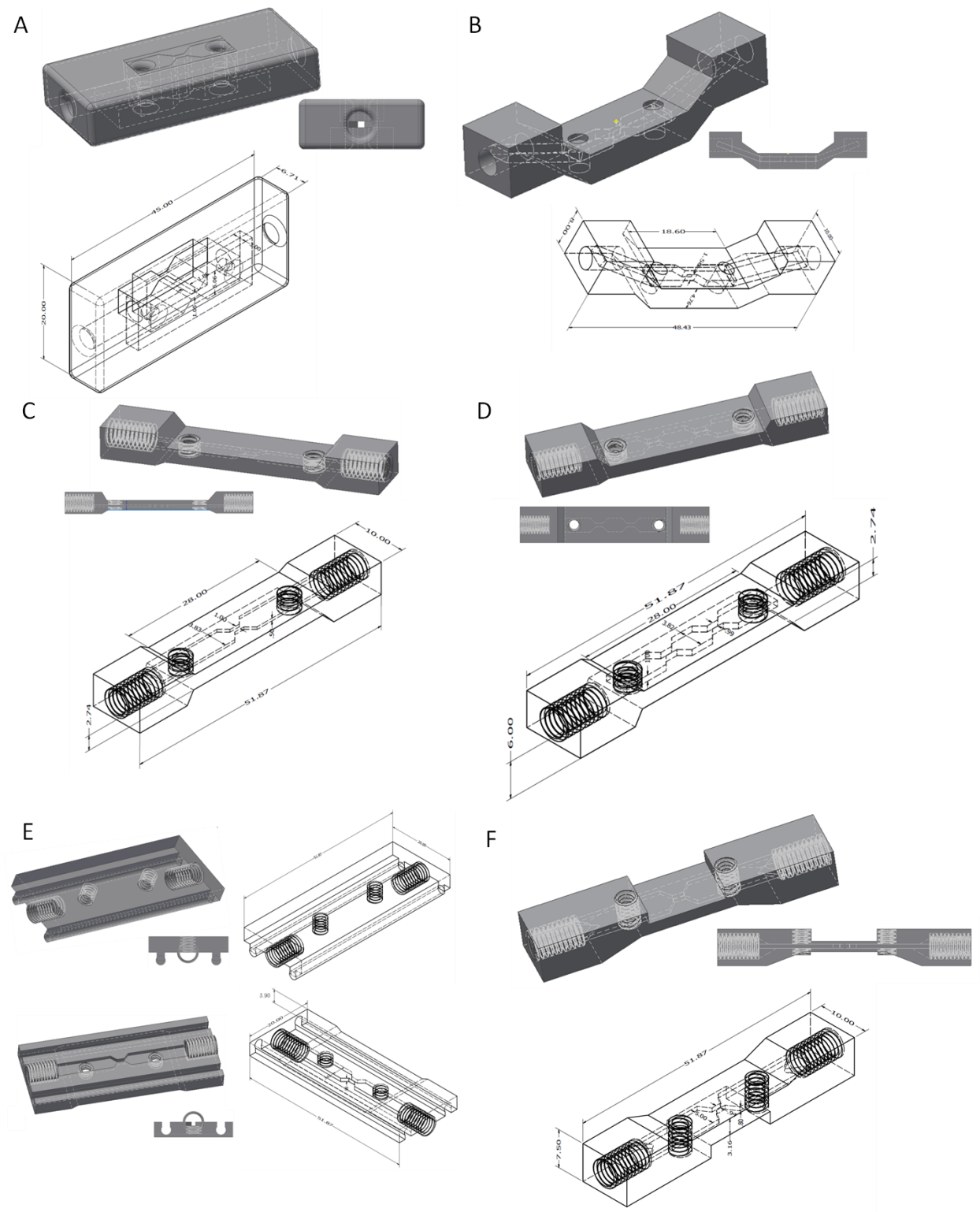

Figure 3.4 CAD images listing object dimensions for the various design iterations of 3D printed devices used for electrical lysis of adhered bPAECs. Starting with the first design (A) and ending with a more recent device that most closely resembles the final device used for electrical lysis of adhered cells (F). Dimensions are in mm.

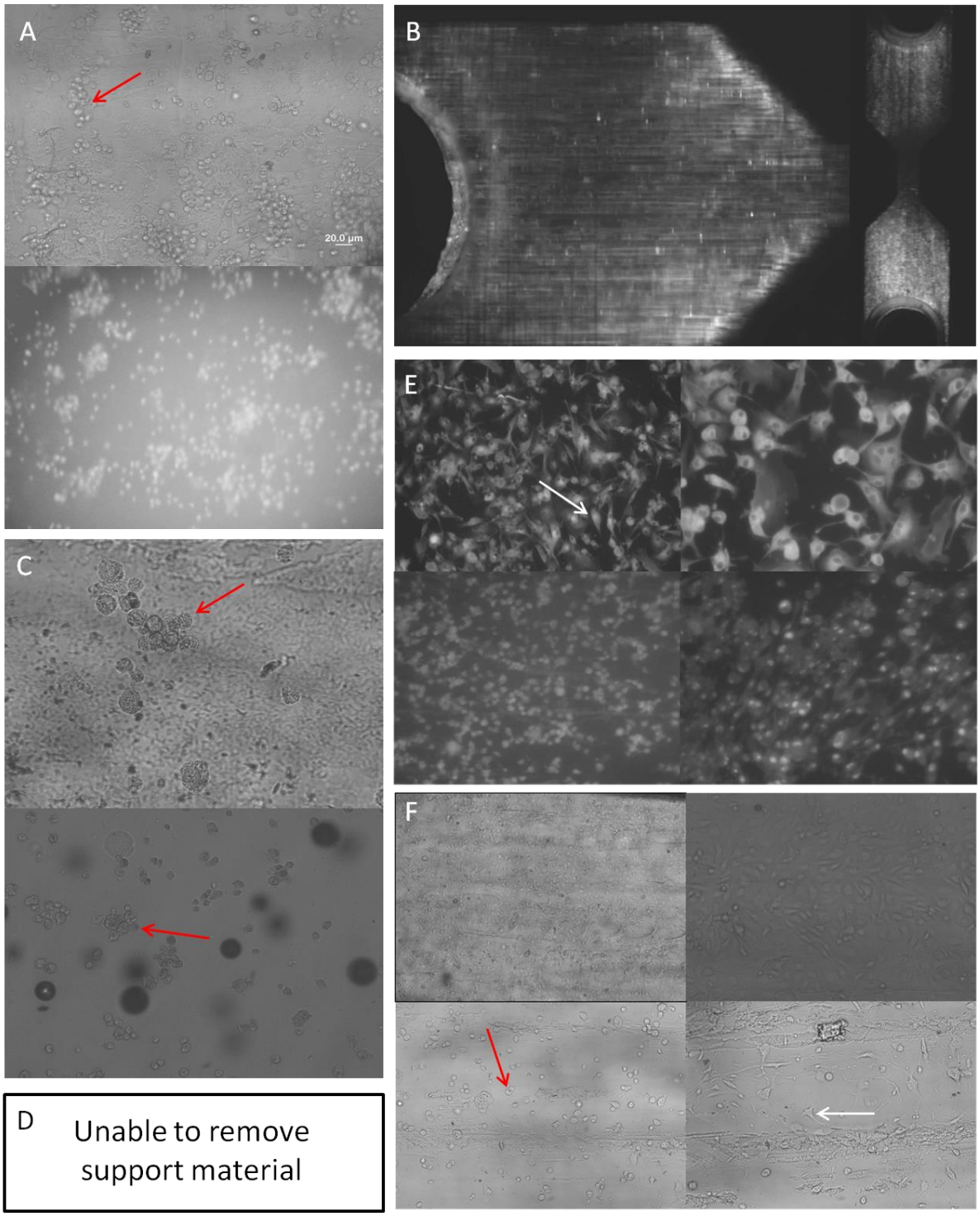

Figure 3.5 Images of bPAEC seeding attempts within fluidic channels of corresponding (alphabetical) device iterations introduced in Figure 3.4. Non-adhered cells (red arrows) in brightfield (top) and stained with Hoechst (bottom) (A). Rose bengal and Hoechst labeled cells (B). bPAECs on C-7 Armstrong epoxy coated devices (top panel) and medical grade epoxy (bottom panel) (C). Adhered (white arrows) Rose bengal stained bPAECs on a slab of Vero Clear (top panel) and on the device shown in Figure 3.4 E (bottom panel) (E). Cells on a PDMS coated channel (top panel) and on a PS coated channel (bottom panel) (F).

Support material could not be removed from the channel of the device shown in Figure 3.4 D and so no cell seeding was possible. Failed cell adhesion was characterized by cells remaining spherical, as indicated by the red arrows seen in Figure 3.5, and can be compared to adhered cells shown with white arrows. At first C-7 Armstrong epoxy (100:6 m/m, Ellsworth Adhesives, Germantown, WI) was tested with poor results since cells failed to adhere to the coated channel. A medical grade epoxy (Henkel loctite hysol M-121HP medical device adhesive, Ellsworth Adhesives, Germantown, WI) was also tested with similar negative results. Going forward, substrates that were already proven in their ability to support cell survival were tested. Specifically, PDMS and PS were used; of the two, only with PDMS was cell adhesion and growth observed. Cell seeding attempts with PS coated devices (Figure 3.5 F bottom panel) resulted in some cell adhesion, however, these cells never grew to confluency.

3.2 Methods

3.2.1 3D Printed Device Fabrication

The 3D printed devices utilized for cell lysis were designed using computer aided design software (CAD) using Autodesk Inventor 2014 Student Edition (Autodesk, San Rafael, CA), and exporting this file in the .STL format. An Objet350 Connex printer in the Department of Electrical and Computer Engineering at Michigan State University was used to print devices from Objet Vero Clear (Stratasys, Eden Prairie, MN). This is a transparent material, chosen to ensure adhered cells could be visualized on the device, and is approximately comprised of: isobornyl acrylate (15-30%), acrylic monomer (15-30%), urethane acrylate (10-30%), acrylic monomer (5-10; 10-15%), epoxy acrylate (5-10; 10-15%), acrylate oligomer (5-10; 10-15%), and photoinitiator (0.1-1;1-2%).[7] Devices were

printed with a matte or glossy finish, the difference being that devices with a matte finish have an outermost layer of support material on all printed surfaces. The CAD design of the final device and images of the actual 3D printed device complete with removable electrodes are shown in Figures 3.6 and 3.7, respectively.

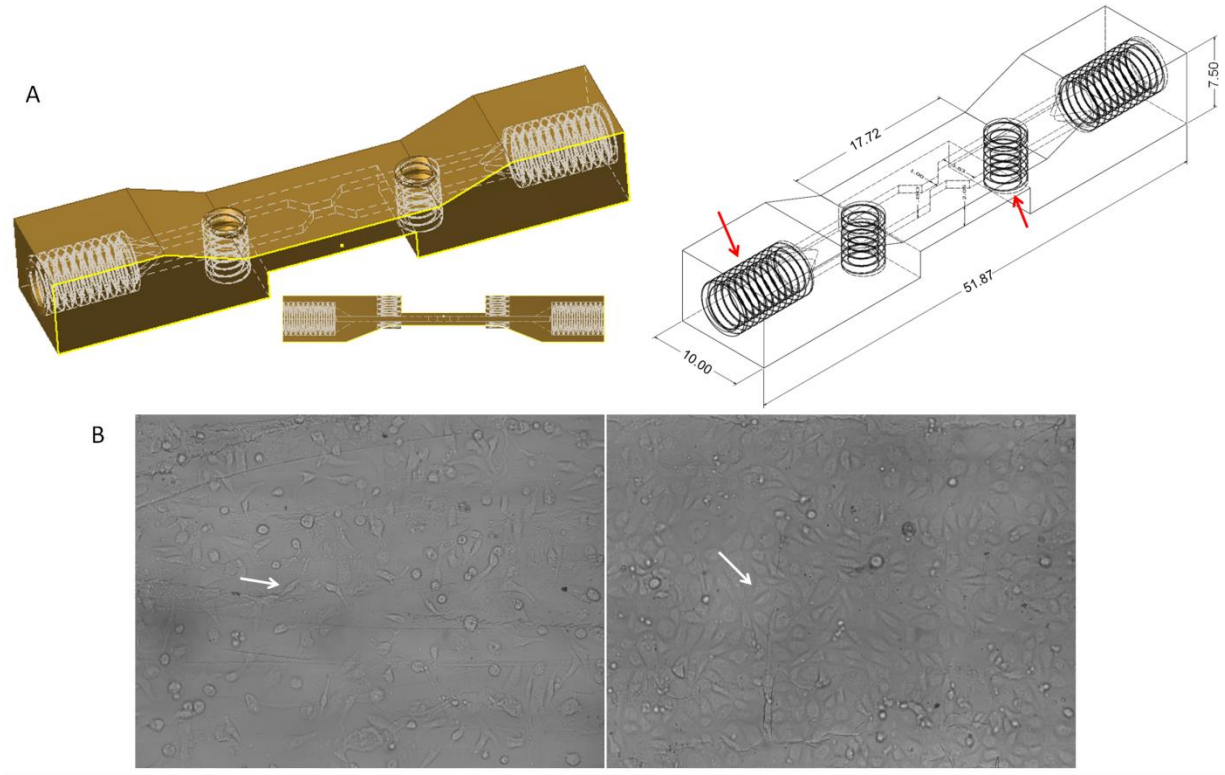

Figure 3.6 CAD images of the final iteration of the 3D printed device capable of supporting cell growth. Detailed CAD images of the final device highlighting four threaded ports at the sides and base of the device (red arrows) for integration with commercial fittings for sample delivery and removable electrode incorporation, respectively. Device dimensions are shown in mm (A). Brightfield images taken on an inverted microscope showing bPAECs displaying the characteristic cobblestone pattern (white arrows) and grown to confluency (right image) on a PDMS coated channel of the 3D printed device (B).

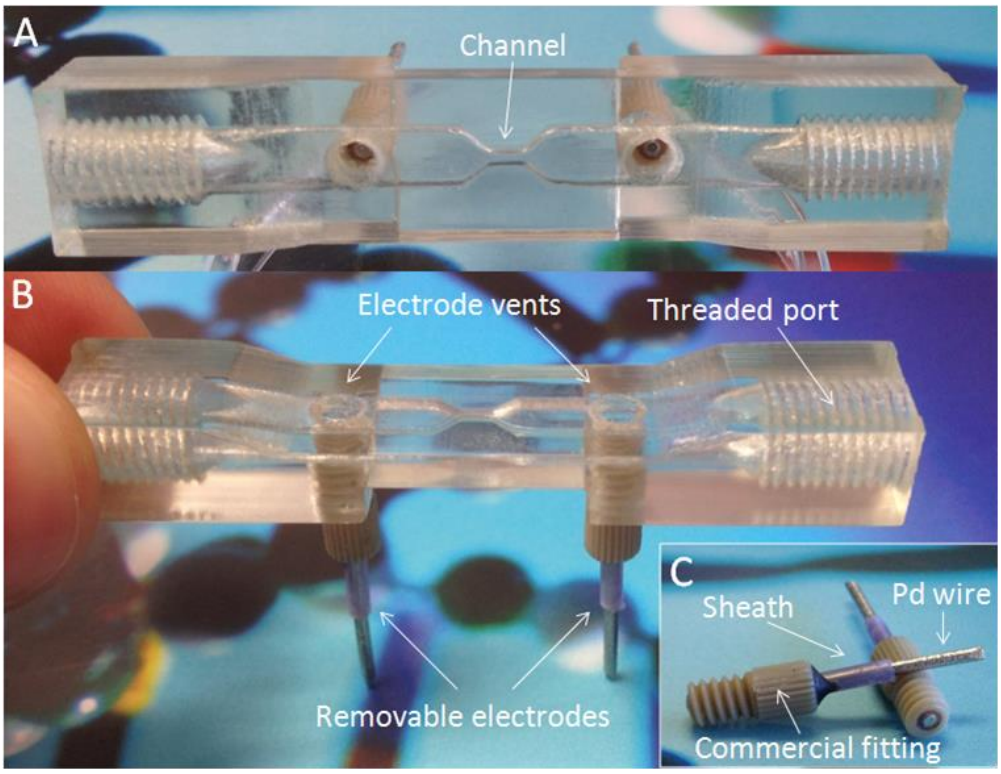

Figure 3.7 3D printed device images. Top view of the device showing the geometry of the channel between the two electrodes (A). Side view of the device highlighting the electrode vents, removable electrodes at the base of the device, and threaded ports for sample incorporation. Commercial plugs are integrated into the top of the electrode vents to facilitate sample flow through the channel (B). Profiles of the removable electrodes showing the 1 mm diameter palladium wire inserted into a commercial sheath that is fixed into a commercial fitting using epoxy and quick weld adhesive (C).

3.2.2 Post Print Processing

When printed with a matte finish, the outermost surfaces are coated with a layer of support material, which after removal gives the surface a matte appearance. Devices printed with a glossy finish lack this outer layer of support material. To remove the support material in areas with threaded inlets and channels, pressurized water, nylon brushes, and tip cleaners were first used to remove bulk material. Any remaining material was removed by sonicating the devices in a 50% isopropyl alcohol (IPA) and water solution containing polystyrene powder (250 μm particle size, Goodfellow, Oakdale, PA). The completed printed device was rigid, but not completely transparent until sanding and polishing of the outer surface and surface modification of the channel (which could not be accessed by surface polishing techniques and so remains opaque) were completed. Sanding was carried out using 1500 and 2000 grit sandpaper, and then the device was polished using blue polishing compound for plastic on a buffing wheel (Eastwood, Pottstown, PA).

3.2.3 Surface Modifications with PDMS or PS

Vero Clear material supports adhesion and growth of endothelial cells, but incorporation of cells into a fluidic channel yielded minimal cell adherence and poor cell viability over a 24 hour period. After removing support material, the internal channel is opaque, and cell visualization is compromised. In order to facilitate cell adherence and improve device clarity, PDMS or PS was incorporated into the channel. For PDMS; a 5 g mixture of an uncured 10:1 ratio of bulk polymer to curing agent of Sylgard 184 (Ellsworth Adhesives, Germantown, WI) was used, and the device was subsequently rinsed with IPA and placed inside a plasma cleaner/sterilizer (PDC-32G, Harrick, Ithaca, NY). Under vacuum, both the device and uncured PDMS in the sterilization chamber were exposed to

oxygen plasma for 7 minutes (3 min on/20 sec off/ 4 min on). After this time, the channel was immediately filled with treated PDMS and put into an oven at 75 °C for 11 minutes. The semi-cured PDMS was then promptly removed from the channel using pressurized gas, and the device was placed back into the oven for several days to aid in the curing process. The duration of oxygen plasma exposure and time in the oven following exposure were optimized for the device dimensions used in this study. Times greater or less than those reported here yielded devices with PDMS completely cured or unable to cure, respectively, within the channel. Specifically, prolonged or continuous exposure to plasma resulted in PDMS that was too cured to be incorporated into the device without plugging the channel, instead of just coating the sides of the channel. PDMS possesses a dielectric strength of 500 $V \cdot mL^{-1}$, and has a refractive index of 1.42 (632.8 nm),[8] while the refractive index of Vero Clear is 1.47 (650 nm).[9]

For PS; 1 g of polystyrene powder (250 μm particle size, Goodfellow, Oakdale, PA) was dissolved in 4 mL of solvent thinner (isophorone, Ercon, Wareham, MA). Upon degassing under vacuum, the mixture was incorporated into the channel of the 3D printed device and pressurized gas was used to remove excess PS, leaving internal channel surfaces coated with PS. The device was then placed inside an oven at 75 °C for 3 hours to cure. Prior to cell immobilization, PS coated devices were exposed to oxygen plasma for 4 minutes to facilitate cell adherence.

3.2.4 Electrode Fabrication

Removable and reusable electrodes were assembled using two 1 mm diameter palladium electrodes (Alfa Aesar, Ward Hill, MA). Palladium wire was cut to 2 cm length segments, inserted into a 1.07 mm I.D. tubing sleeve (IDEX, Health and Science, Oak Harbor,

WA) coated with C-7 Armstrong epoxy (100:6 m/m, Ellsworth Adhesives, Germantown, WI), and secured with epoxy into a female luer adapter (M-660, IDEX, Health and Science, Oak Harbor, WA). The finished electrode component could be removed from the printed device, facilitating electrode polishing using 0.05 μm alumina powder (CH instruments, Austin, TX) on a microcloth polishing pad after each use. The threaded inlets/outlets on the device were interfaced with female luer adapters (P-629, IDEX, Health and Science, Oak Harbor, WA) for sample delivery. Electrode vents were included in the device design directly above the electrodes, effectively allowing gas evolved from the electrolysis of water to be removed from the system and to prevent occlusion of the channel.

3.2.5 Confirming Lysis Mechanism

The method of lysis was determined to be electrical based on the time scale to achieve lysis and by monitoring the pH at the cathode. PBS containing 10 ppm fluorescein was made into pH standards ranging from pH 5-8. The 3D printed device was loaded with PBS containing 10 ppm fluorescein and 50 μL of electrolyzed buffer was collected at one second intervals up to ten seconds during application of 100 V. Electrolyzed buffer samples were loaded into wells of a 384 well plate and the fluorescence intensity was measured using a plate reader (Ex: 491 nm/ Em: 522 nm; Molecular Devices, Sunnyvale, CA) and a macroscope fitted with a FITC (fluorescein isothiocyanate) filter cube (ChromaTechnology Corp., Bellows Falls, VT) containing the excitation (460-500 nm) and emission (505-560 nm) filters. The pH generated at the cathode for each sample interval was calculated using the equation of the line generated from the calibration curve pertaining to pH standards.

3.2.6 Optical Characterization

The effect of coating with PDMS and PS on the optical transparency of the devices printed with either a matte or glossy finish was characterized. Transmittance information (200-800 nm) for PDMS coated, PS coated, and solely Vero Clear material (no treatment and polished) was collected employing a UV-Vis spectrophotometer (ATI Unicam UV2, Thermo Spectronic, Rochester, NY) with a scan rate of 240 nm/min and 0.5 nm sample interval, each with a 3 mm path length. Polished samples simply went through the physical means for support material removal as mentioned above.

3.2.7 Scanning Electron Microscopy Determination of PDMS and PS Coating Thickness

Thicknesses of PDMS and PS layers coating internal channels were characterized using scanning electron microscopy (SEM) by imaging cross sections of the channel. Devices were scored and submerged in liquid nitrogen to form a clean break across the channel in the narrow region. All imaged devices were coated with 5 nm of tungsten, and observed using a Carl Zeiss Evo L525 Variable Pressure SEM from the College of Engineering at Michigan State University. The microscope was operated in high vacuum mode (base pressure 4×10^{-5} Torr), with either 15 or 20 kV beam energy, and 50 pA beam current.

3.2.8 Cell Viability

Live/dead cell stains were used to determine cell viability over a five day period. Propidium iodide (30 μM, Ex: 538 nm/Em: 617 nm, Invitrogen, Carlsbad, CA) was used to permeate cells with compromised membranes and Syto 9 (5 μM, Ex: 485 nm/Em: 498 nm, Invitrogen, Carlsbad, CA) was used as the live/dead cell stain for comparison. Stains were

introduced into the fluidic channel and incubated for 15 minutes, and cells subsequently imaged on the inverted microscope detailed above.

3.2.9 Collagen Retention on the Device After Lysis

3D devices of both geometries (refer to Table 3.1 for device details) were coated with fluorescent collagen (collagen-fluorescein, bovine, Sigma-Aldrich, St. Louis, MO) prepared by dissolving lyophilized product in acetic acid and water (3:1 v/v). Collagen was allowed to dry onto the device over the course of a week, after which, PBS was incorporated into the channel and the lysis protocol was carried out without adhered cells present. Optimal lysis potentials and durations were used for both device geometries.

3.2.10 Temperature Change During Lysis

Temperature changes within the fluidic channel during electrical lysis were monitored using a thermocouple that was placed over various regions along the channel on the outside of devices. Optimal lysis conditions were used (device 1: 100 V; device 2: 150 V), potential duration was 5 seconds to mimic sufficient time for electrical lysis, and PBS was used to fill the fluidic channel.

3.2.11 Preparation of Reagents

All reagents were used as received without further purification unless otherwise noted.

Phosphate Buffered Saline

Phosphate buffered saline (PBS) was prepared by dissolving 137 mM NaCl, 10 mM Na_2HPO_4, 2 mM KH_2PO_4, and 2.7 mM KCl in 1 L of distilled deionized water. The pH was adjusted to 7.4 with HCl and sterile filtered once.

Hoechst 33342

The nuclear cell stain Hoechst 33342 (Ex: 350 nm/Ex: 461 nm, Invitrogen, Carlsbad, CA) was prepared as a 10 $mg \cdot mL^{-1}$ solution in PBS buffer.

Endothelial Growth media

Endothelial growth media (EGM) was prepared under sterile conditions from Dulbecco's Modified Eagle's Medium (DMEM, Caisson, North Logan, UT) containing 7.5% fetal bovine serum, 2.5% adult bovine serum, and 2.5% penicillin as an antibiotic solution.

Acid Citrate Dextrose

Acid citrate dextrose (ACD) was prepared in distilled deionized water and contained 38 mM $C_6H_8O_7$ (citric acid), 75 mM $C_6H_5O_7 \cdot 2H_2O \cdot 3Na$ (sodium citrate dihydrate), and 124 mM $C_6H_{12}O_6 \cdot H_2O$ (dextrose monohydrate). The resulting solution was sterile filtered once.

Modified Tyrode's Buffer

Modified Tyrode's buffer (MTB) was prepared in distilled deionized water with the following composition: 12 mM $NaHCO_3$, 0.32 mM NaH_2PO_4, 10 mM HEPES, 137 mM NaCl, 2.7 mM KCl, 0.5 mM $MgCl_2 \cdot 6H_2O$, 5.5 mM glucose, 2 mM $CaCl_2$ (for MTB with calcium, for calcium free this is omitted). The pH of the buffer was adjusted to 7.5 and filtered once.

Fluorescent Collagen

Lyophilized fluorescent collagen (collagen-fluorescein, bovine, Sigma Aldrich, St. Louis, MO, USA) was dissolved in an acetic acid: distilled deionized water mixture (3:1 v/v, 6 $mg \cdot mL^{-1}$).

3.2.12 Cell Immobilization on the 3D Printed Device

After surface modification with PDMS or PS, the 3D device was sterilized for cell immobilization by rinsing with IPA and then dried in a 75 °C oven. Prior to seeding bovine

pulmonary artery endothelial cells (bPAECs), channels were loaded with a solution containing 100 μg·mL^{-1} of collagen (Advanced BioMatrix, Poway, CA) and 50 μg·mL^{-1} of fibronectin (Sigma-Aldrich, St. Louis, MO) prepared in distilled deionized water and incubated at 37 °C for 2 hours. The adhesive proteins were then dried onto the device which was exposed to UV light for 15 minutes for sterilization. A 10 mg·mL^{-1} solution of a nuclear cell stain (Hoechst 33342, Ex: 350 nm/Ex: 461 nm, Invitrogen, Carlsbad, CA) was added to confluent endothelial cells in a T-75 culture flask 30 minutes before harvesting to facilitate visualization of cells during the immobilization and lysis process. Endothelial cells were harvested from a tissue culture flask by 1 minute incubation with 0.25% trypsin-EDTA (Life Technologies, Grand Island, NY). The cells were reconstituted in cell media, centrifuged at 1500*g* for 5 min, isolated, and reconstituted in phenol red free cell media (Dulbecco's Modified Eagle's Medium (DMEM, Caisson, North Logan, UT) containing 7.5% fetal bovine serum, 2.5% adult bovine serum, and 2.5% antibiotic solution). This concentrated cell solution was loaded into the channel of the device using a pipette. The cells were incubated at 37 °C for 1.5 hours. After this time, cell adhesion was monitored and if needed, more cells were added to the channel. Cell media was changed every 1.5 hours after cell attachment to the device was confirmed and cells were incubated with media overnight.

3.2.13 Lysis of Adhered Endothelial Cells

Cell lysis studies were carried out on devices coated with PDMS. Following the immobilization process, cell media was removed from the device by rinsing with PBS. A PowerPac Universal Power Supply (Bio-Rad, Hercules, CA) was used as the voltage source for cell lysis. Optimal cell lysis for both device geometries was determined by testing a

range of potentials and monitoring the extent of cell lysis. For the wide device (device 1), a range of 50-150 V with 25 V increments was tested; potentials ranging from 100-200 V in 25 V increments were tested for the narrow device (device 2). Before lysis, bPAECs were imaged using an Olympus IX71 inverted microscope (Olympus America, Melville, NY) with an electrothermally cooled charge-coupled device camera (Orca, Hamamatsu) and Microsuite software (Olympus America, Melville, NY). The microscope was fitted with a DAPI filter cube (ChromaTechnology Corp., Bellows Falls, VT) containing the excitation (325-375 nm) and emission (435-485 nm) filters. After electrical lysis, the channels were rinsed with PBS to remove any lysis debris from the channel. The channel was imaged again so that lysis efficiency could be determined by comparing the number of cells present in the narrow region before and after lysis using the following equations:

$$Cell\ Lysis\,\% = \frac{cells\,lysed}{cells\,before} * 100 \qquad \text{Equation 3.4}$$

Where cells lysed was defined as the difference in cells remaining in the cell lysis region compared to the total number of cells present before lysis. After lysis, the devices were cleaned by rinsing with a dilute bleach solution, distilled water, and lastly IPA. After drying devices were reused.

3.3 Results

3.3.1 Confirming Lysis Mechanism

Using PBS containing 10 ppm fluorescein, the pH generated at the cathode during potential application within (and beyond) the time scale needed to achieve lysis was calculated from fluorescence intensity measurements taken with both a macroscope and a plate reader. Calculated pH values are shown in Figure 3.8.

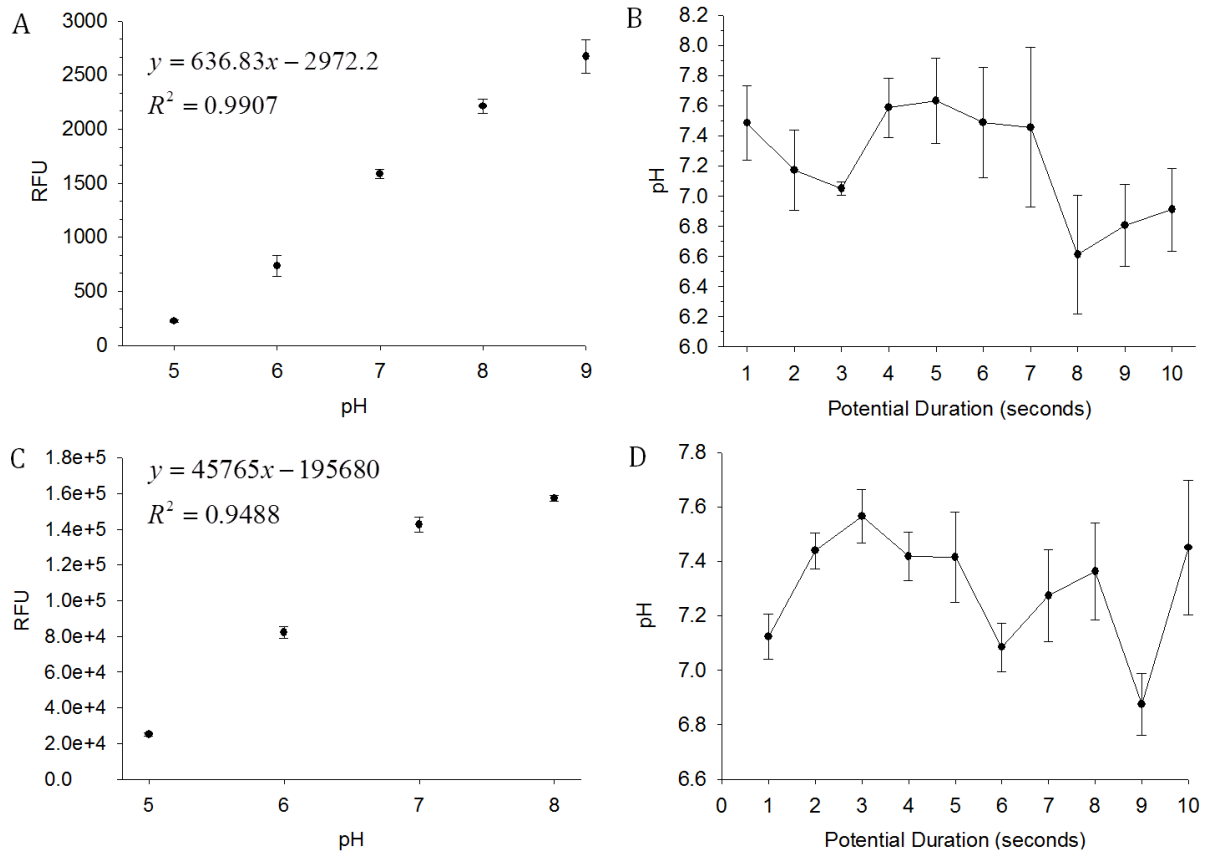

Figure 3.8 pH values generated at the cathode during cell lysis as calculated using a macroscope (A and B) and plate reader (C and D). Calibration curve for pH 5-9 standards made from a 10 ppm solution of fluorescein in PBS (A). Calculated pH of electrolyzed buffer collected from the cathode at various time points (B). Calibration curve showing relative fluorescence units (RFU) for pH standards 5-8 measured using a plate reader (C). Calculated pH values for cathode-based electrolyzed buffer (D). The starting pH of the buffer at time zero was 7.36 for both detection schemes. Data represent mean ± standard deviation; n = 3 for all.

3.3.2 Optical Characterization of the Device

Figure 3.9 shows SEM images corresponding to cross sections of the lysis region for untreated devices, before and after removal of support material.

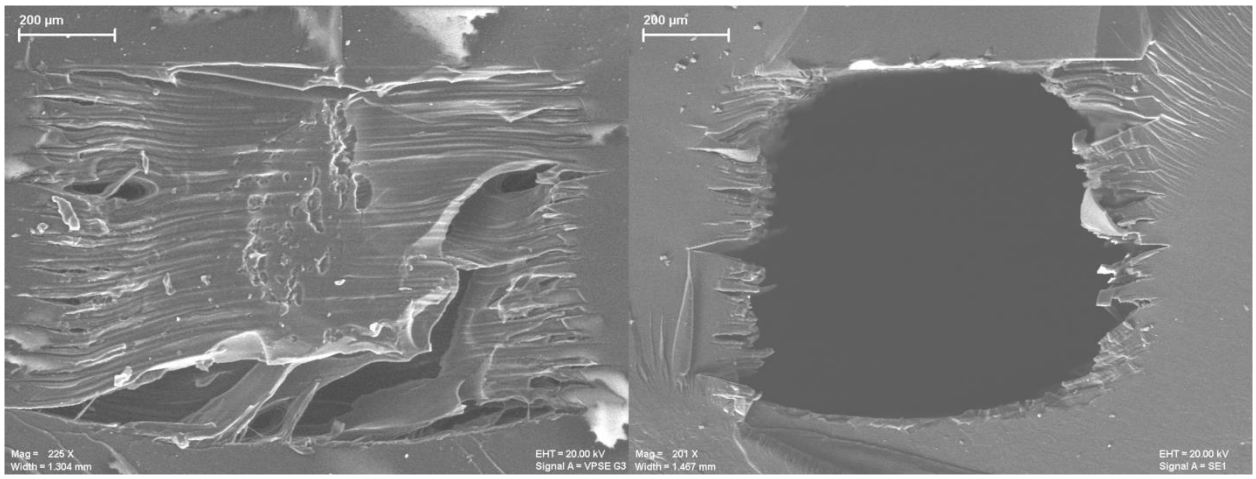

Figure 3.9 SEM images of cross sections of an untreated 1 mm x 0.8 mm channel. Cross section of a channel after printing with support material still present (left). Cross section of a channel after removal of support material (right).

Uncoated Vero Clear (no treatment and polished), PDMS coated, and PS coated Vero Clear samples were analyzed for percent transmittance using a UV-Vis spectrophotometer to determine the extent to which incorporation of PDMS and PS affected optical clarity. Furthermore, a comparison of the optical clarity between matte and glossy finish for polyjet 3D printed parts was made. Each sample prepared was 3 mm thick and transmittance data were collected from 200-800 nm. Figure 3.10 shows the percent transmittance data for each sample. For SEM analysis, cross-sections of bare channels and those coated with PS or PDMS were imaged to determine coating thickness (Figure 3.11).

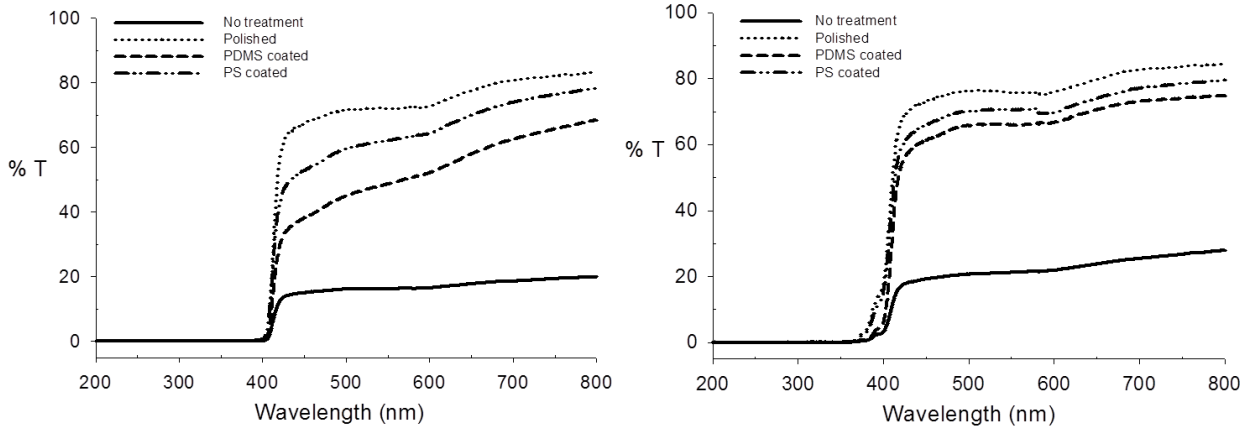

Figure 3.10 Percent transmittance of the 3D printed material. Vero Clear (no treatment and polished), PDMS coated, and PS coated slabs when printed in standard format (left) and printed with a glossy finish (right).

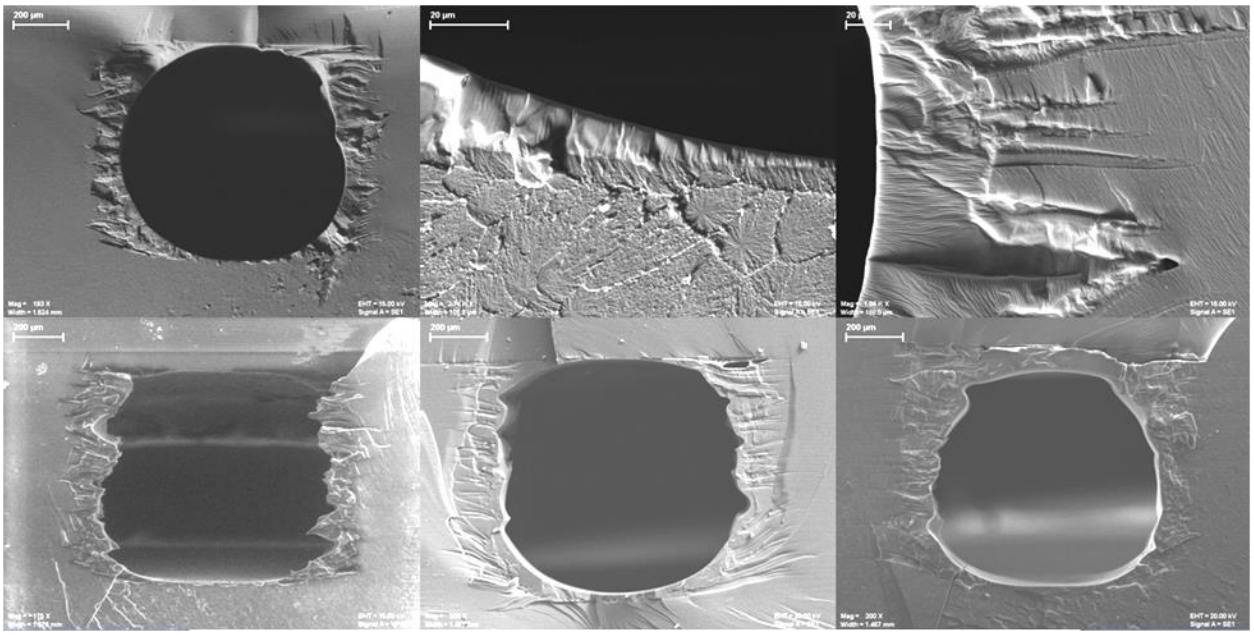

Figure 3.11 SEM images of channels coated with PDMS (top panel) or PS (bottom panel). Top panel: PDMS coated channel (left), contrast between Vero Clear printed material and PDMS coating at bottom of channel (center), and PMDS integrating into printed contours (right). Bottom panel: Channel coated with 1 layer of PS (left), 2 layers of PS (center), and 3 layers of PS (right). Scale bars for complete channel views are 200 μm and 20 μm for PDMS/Vero Clear boundary images.

3.3.3 Cell Viability

Figure 3.12 shows viability of cells on the 3D printed device through five days with static or non-flow-based media delivery. Viability remained high throughout the five day period; however, a decrease in the number of adhered cells or cell coverage was seen after day four.

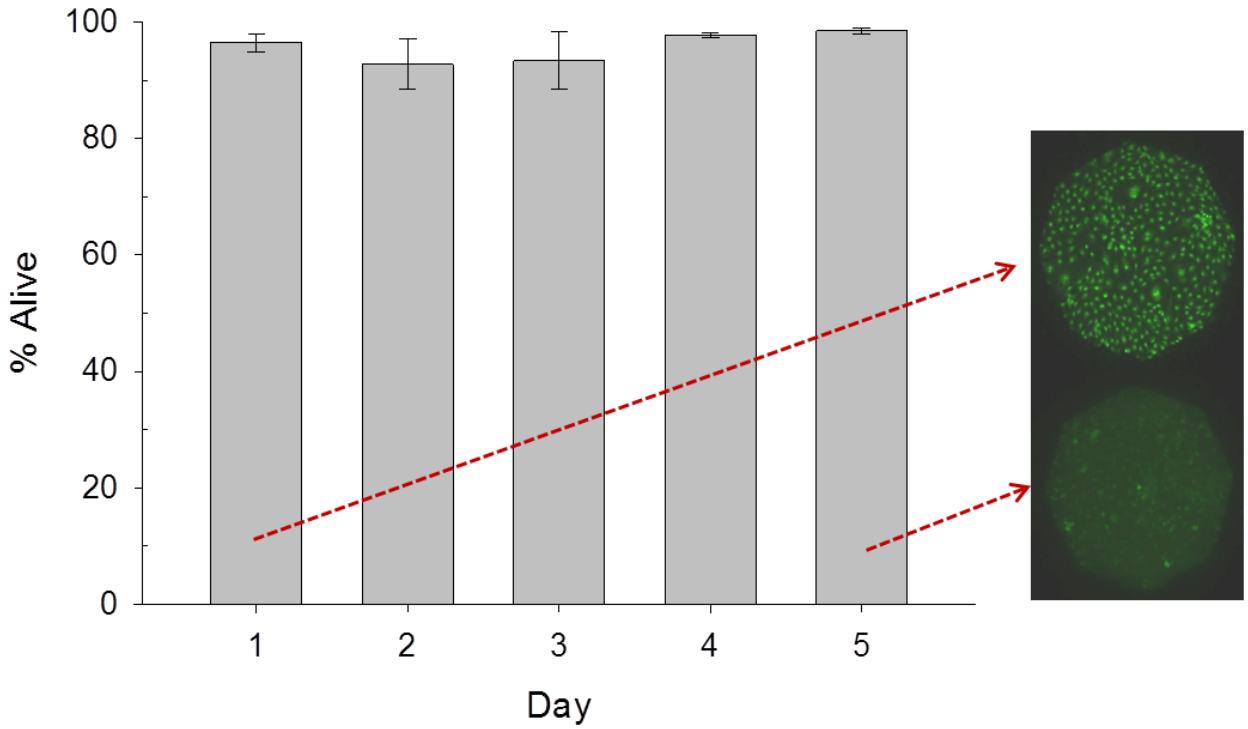

Figure 3.12 Viability of cells on the device when media delivery was static. Propidium iodide (Ex 493/ Em 636 nm) and Syto 9 (Ex 485/ Em 498nm) were used to determine viability. Data represent mean ± standard error of the mean; n ≥ 4 (left). Cell coverage on the device through day 5 (right).

3.3.4 Lysis of Adhered Endothelial Cells

Figure 3.13 shows cell lysis efficiencies for devices 1 and 2 with corresponding images of cells remaining on the device from the tapered region when insufficient (50 and 100 V) and optimal (100 and 150 V) potentials were applied.

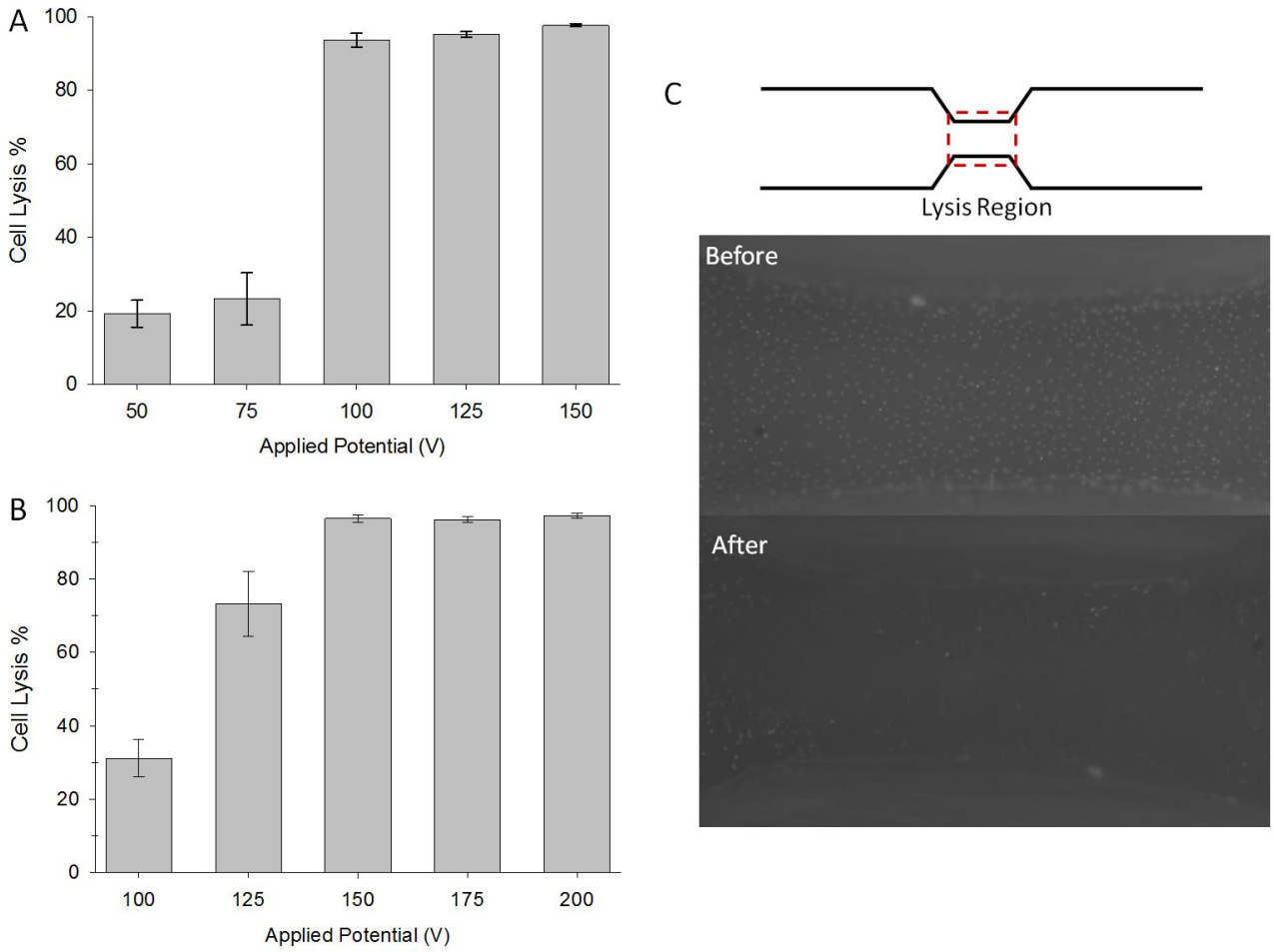

Figure 3.13 Cell lysis efficiencies (%) for devices 1 and 2 with representative images of cells in the desired lysis region before and after lysis. Device 1: Potentials ranged from 50-150 V. Incomplete lysis was seen with applied potentials of 50 and 75 V, while nearly complete clearance of cells was seen for 100-150 V. 50 V (potential duration 4±1 s, n=10); 75 V (3.5±1 s, n=8); 100 V (3±1 s, n=9); 125 V (2±1 s, n=6), 150 V (2±1 s, n=6) (A). Device 2: Applied potentials ranged from 100-200 V. Incomplete lysis was seen with applied potentials of 100 and 125 V, while nearly complete clearance of cells was seen for 175-200 V. 100 V (potential duration 3±1 s, n=7); 125 V (3±1 s, n=9); 150 V (2.5±1 s, n=6); 175 V (2±0.5 s, n=5), 200 V (2±1 s, n=6) (B). Representative images of Hoechst stained cells before and after lysis in the desired lysis region of a fluidic 3D printed channel (C). Cell lysis efficiency data represent mean ± standard error of the mean; Potential duration data represent mean ± standard deviation.

3.3.5 Collagen Retention on the Device After Lysis

Figure 3.14 shows collagen retention in the desired lysis region of 3D printed devices after potential application mirroring the optimal lysis conditions for device 1 and 2 (Figure 3.13). Specifically, for device 1 a 100 V electrical potential was applied for 3 seconds, and for device 2 a 150 V potential was applied for 2.5 seconds.

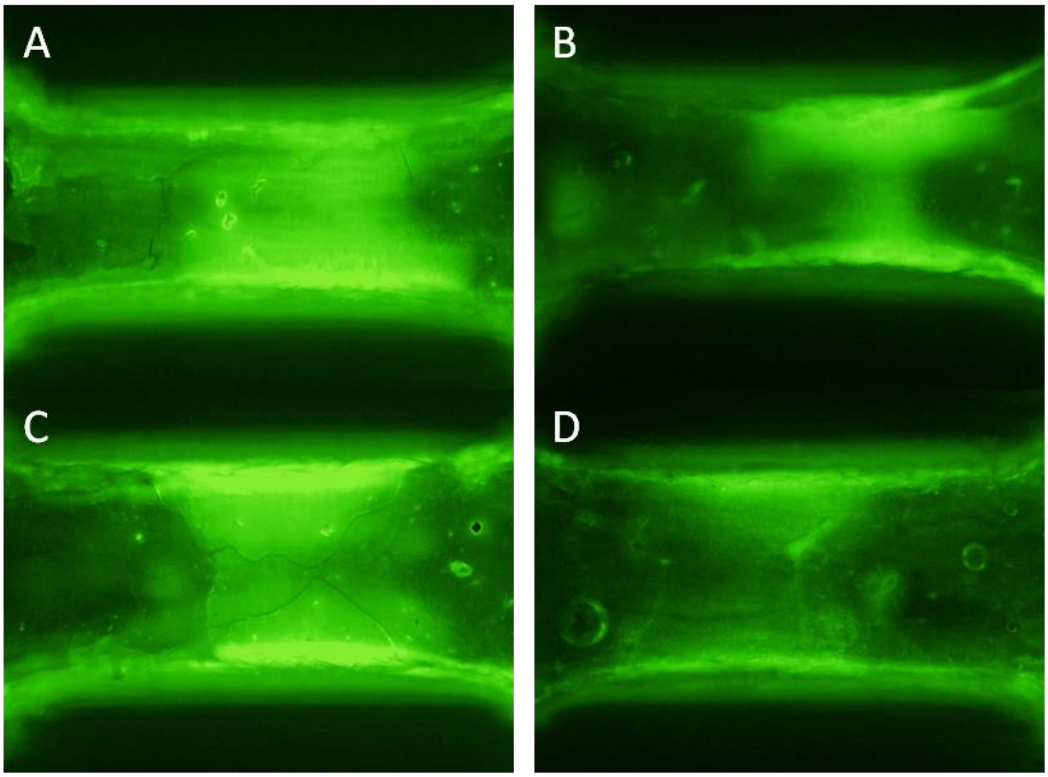

Figure 3.14 Collagen retention in the 3D printed fluidic channel after lysis. Fluorescent collagen deposited onto the channel and imaged before (A and C) and after (B and D) application of potential mimicking lysis conditions device 1 (100 V applied for 3 s; A and B) and device 2 (150 V applied for 2.5 s; C and D).

3.3.6 Joule Heating Considerations

A thermocouple was used to determine temperature change when applying optimal lysis potentials for both models over a five second application in both wide and narrow sections. For both models, no significant change in temperature occurred in the wide

sections. For device 1, there was a 2°C increase in the middle section, and no change in the middle section of device 2. The current generated during cell lysis generally ranged from 1-8 mA for device 1 and 8-20 mA for device 2.

3.4 Discussion

3.4.1 Confirming Lysis Mechanism

pH results pertaining to data acquired using a macroscope are shown in Figures 3.8 A and B, and those from a plate reader Figures 3.8 C and D. Figures 3.8 A and C show the relative fluorescence units pertaining to pH standards and the resulting calibration curves. Figures 3.8 B and D show the calculated pH values at various sampling times when a 100 V potential was applied. From this data it was noted that the pH in the region around the cathode does not dramatically change on the timescale (milliseconds) necessary for electrical lysis to occur.

3.4.2 Optical Characterization of the Device

Employing a polyjet 3D printed device for studies where optical measurements are desired poses a challenge due to the inability to polish internal surfaces that remain rough and opaque after clearance of support material. The printer manufacturer (Stratasys) suggests NaOH vapor as a chemical means for polishing Vero Clear, but this degrades the integrity of printed features such as threading. SEM images (Figure 3.9) revealed that the top and bottom of channels in the devices were smooth after printing, while the sides were rough and integrate more with support material indicating a limitation in accuracy for this dimension. Even after removal of support material the rough sides remain, posing a possible limitation of fabricating channels with this type of printer. For visualization

purposes, it becomes necessary to orient the device during printing so that the optical path aligns with the smooth edges.

A majority of 3D printed materials are proprietary in nature. Being able to incorporate well-characterized materials will expand the utility of 3D printing beyond what is currently possible. PDMS has a refractive index (1.43) close to that of Vero Clear (1.47), limiting the effect incorporation will have on optical measurements. Due to its viscous nature before curing, PDMS makes an ideal candidate for coating the surface of channels, making them visually clear. Furthermore, PDMS is well established as a non-toxic, oxygen permeable substrate onto which cells can adhere and grow.[10] Various ratios of PDMS to curing agent (5:1, 10:1, and 20:1) were tested to examine the ability to cure on a flat piece of printed Vero Clear material. Of the three ratios tested, 10:1 was the best able to cure to the printed material (fastest cure time at room temperature). PDMS would not cure inside the channel of the device unless both the uncured PDMS mixture and the device were exposed to oxygen plasma. While a flat piece of printed Vero Clear material (3 cm x 3 cm x 3 mm) was amenable to visualization of cell adherence and growth over a 48 hour period (data not shown), the same cannot be said of cells growing within a channel of a device, making PDMS or PS coating necessary.

Devices printed with a glossy finish and coated with PS had the highest percent transmittance of any coated device, while polished devices with a glossy finish reported the overall highest transmittance. Future studies carrying out optical measurements on polyjet 3D printed parts would be best suited to utilize a glossy finish (Figure 3.10). PDMS coating varied in thickness from about 3 μm near the bottom of the channel to over 100 μm at the sides and formed a more circular channel by integrating into the various contours along the

sides of the channel, as seen in Figure 3.11 top panel. The PS coated device required multiple coatings to completely fill in the sides of the channel, and the thickness after three coatings extended beyond 100 μm in some areas (Figure 3.11 bottom panel).

3.4.3 Cell Viability

After five days 94% of the cells remaining on the device were viable, as confirmed by live and dead cell stains. However, there was an overall decrease in cell coverage on the device after day four (Figure 3.12). This observed decrease in cell coverage was likely due to non-viable cells being rinsed away with media changes. The media delivery in this study was static in nature, meaning the media in the channel was flushed and replaced with new media every 1.5-2 hours. In order to extend the life of cells on the device for potential long-term studies, continuous media delivery is preferential. Growing cells in the channel under continuous flow has several benefits, namely, the cell morphologies will more closely resemble those seen *in vivo* where cells are elongated. Furthermore, cells will not have to remain in the presence of waste products.

3.4.4 Lysis of Adhered Endothelial Cells

For lysis optimization studies employing the two device designs outlined in Table 3.1, lower end potentials (device 1: 50 and 75 V; device 2: 100 and 125 V) led to incomplete lysis as evidenced by the presence of cells in the lysis region, while higher end potentials (device 1: 125 and 150 V; device 2: 175 and 200 V) led to lysis that was not confined to the desired lysis region. However, for both geometries an optimal potential (device 1: 100 V; device 2: 150 V) was found that allowed for selective lysis in the desired region while maintaining cell integrity in the surrounding areas. Figures 3.13 A and B show the cell lysis efficiencies represented as percent cell lysis for devices 1 and 2, respectively.

For device 1, the following are the calculated electric fields in the lysis region according to equation 3.3 and the corresponding applied potentials: 50 V (125 $V \cdot cm^{-1}$); 75 V (187.5 $V \cdot cm^{-1}$); 100 V (250 $V \cdot cm^{-1}$); 125 V (312.5 $V \cdot cm^{-1}$); 150 V (375 $V \cdot cm^{-1}$). For device 2 these values are: 100 V (217 $V \cdot cm^{-1}$); 125 V (271 $V \cdot cm^{-1}$); 150 V (325 $V \cdot cm^{-1}$); 175 V (380 $V \cdot cm^{-1}$); 200 V (434 $V \cdot cm^{-1}$). The lower end applied potentials resulted in more variable cell lysis efficiencies, which can be attributed to the reduced electric fields that cells experience at these potentials.

The electric fields that cells were exposed to in this study did not reach the calculated theoretical value needed for cell lysis (1000 $V \cdot cm^{-1}$). One explanation for why much lower electric fields led to cell lysis could be due to PDMS incorporation decreasing the true geometry of the internal channel and skewing the calculated electric fields. Furthermore, accounts of lower electric fields (< 1000 $V \cdot cm^{-1}$) leading to cell lysis with extended field duration (millisecond) or decreased distance between electrodes have been reported.[3,11] The PDMS coated device interfaced with removable electrodes used in this study exhibited electrical cell lysis specific to a desired region of the fluidic channel.

3.4.5 Collagen Retention on the Device After Lysis

A major concern using electrical lysis as an injury mimic was whether or not components of the extracellular matrix (collagen and fibronectin) are retained after lysis occurs. In order to determine what effect the lysis process has on collagen retention, 6 $mg \cdot mL^{-1}$ fluorescent collagen was deposited into the fluidic channels of both device geometries and allowed to dry. Several coatings were administered to ensure proper visualization. PBS buffer was incorporated into the devices and optimal potentials (100 V for device 1, 150 V for device 2) were applied for 3 seconds by connecting the leads of the

universal power supply to the removable palladium electrodes at the base of the device. An inverted microscope was used to image devices before and after potential application (Figure 3.14). The decrease in intensity in the after images indicates that some of the collagen was being cleared away from the desired lysis region. This will most likely contribute to a decrease in platelet adhesion after lysis in future studies employing biological samples.

3.4.6 Joule Heating Considerations

In order to rule out cell degradation from joule heating during potential application, a thermocouple was used to determine the temperature change that occurred when using the optimal potentials for both models over a five second application in both wide and narrow sections. The thermocouple was applied to the outside of the device, directly over the narrow and wide regions. For both models, no significant change in temperature occurred in the wide sections. For device 1, there was a 2 °C increase in the middle section, and no change in the middle section of device 2. The current generated during cell lysis generally ranged from 1-8 mA for device 1 and 8-20 mA for device 2. Generation of hydroxide from the electrolysis of water has previously been used to lyse cells on microfluidic platforms,[12] though was ruled out as the lysis source here as cells remained viable outside the lysis region (in the region close to the cathode) as confirmed by microscopy.

Applying this protocol towards the development of a vascular injury mimic offers more realistic *in vivo* conditions by omitting the addition of non-native circulation components to lyse cells. This methodology can also be applied to studies striving to dictate cell patterning within a 3D printed device, carry out *in vitro* experiments involving live cells

on platforms not inherently cell-amenable, or provide a well-characterized surface material for non-cell based studies (electrophoresis, etc.). While the channel dimensions reported here are on a millimeter scale, the Objet350 Connex 3D printer used in this study has a Z resolution (height of each layer) of 16 μm, and an X/Y resolution of 100 μm, and accuracy of 20-85 μm for features below 50 mm.[7] Removal of support material in channels less than 250 μm in diameter is often incomplete, limiting channel features with this type of printer.

Through repeated coatings of PDMS or PS, current limitations associated with 3D printer resolution or support material removal could be avoided and channels of sub-100 μm diameter could plausibly be fabricated. Furthermore, incorporation of PDMS or PS creates a semi-circular channel, avoiding low-flow regions inherent in rectangular channels formed through conventional soft lithography techniques.[13] This fabrication method could also be applied towards the recreation of larger blood vessels (veins and arteries) which experience much lower Reynold's numbers (100-300) compared to those produced in traditional microfluidic channels, and therefore differing fluid dynamics. This is critical as it is well established that fluid dynamics such as shear rate can have a profound effects on the formed thrombus.[13] In addition, the ability to lyse cells on a microfluidic platform is desirable for developing portable point of care devices to perform DNA analysis, a heavily researched area for lab-on-chip, micro-total-analysis-system (μTAS), and biomedical microelectromechanical systems (bioMEMS).[6,14]

REFERENCES

REFERENCES

(1) Zimmermann, U. *Trends in Biotechnology* **1983**, *1*, 149-155.

(2) Wang, H.; Bhunia, A. K.; Lu, C. *Biosensors and Bioelectronics* **2006**, *22*, 582-588.

(3) Wang, H.; Lu, C. *Analytical Chemistry* **2006**, *78*, 5158-5164.

(4) Wang, H.; Lu, C. *Biotechnology and Bioengineering* **2006**, *95*, 1116-1125.

(5) Lee, D. W.; Cho, Y. *Sensors and Actuators B: Chemical* **2007**, *124*, 84-89.

(6) Morshed, B. I.; Shams, M.; Mussivand, T. *Critical Reviews in Biomedical Engineering* **2013**, *41*, 37-50.

(7) Stratasys. *Polyjet materials data sheet*. http://www.stratasys.com/materials/polyjet/transparent (accessed March 20, 2014).

(8) DOW Corning. *Sylgard 184 Silicone Elastomer*. http://www.dowcorning.com (accessed March 20, 2014).

(9) Willis, K.; Brockmeyer, E.; Hudson, S.; Poupyrev, I. In *Proceedings of the 25th annual ACM symposium on user interface software and technology*; ACM New York, NY, USA, 2012, pp 589-598.

(10) Chiu, D. T.; Jeon, N. L.; Huang, S.; Kane, R. S.; Wargo, C. J.; Choi, I. S.; Ingber, D. E.; Whitesides, G. M. *PNAS* **2000**, *97*, 2408-2413; McDonald, J. C.; Whitesides, G. M. *Accounts of Chemical Research* **2002**, *35*, 491-499.

(11) Lee, S.; Tai, Y. *Sensors and Actuators A: Physical* **1999**, *73*, 74-79; McClain, M. A.; Culbertson, C. T.; Jacobson, S. C.; Albritton, N. L.; Sims, C. E.; Ramsey, M. J. *Analytical Chemistry* **2003**, *75*, 5646-5655.

(12) Di Carlo, D.; Ionescu-Zanetti, C.; Zhang, Y.; Hung, P.; Lee, L. P. *Lab Chip* **2005**, *5*, 171-178; Nevill, J. T.; Cooper, R.; Dueck, M.; Breslauer, D. N.; Lee, L. P. *Lab Chip* **2007**, *7*, 1689-1695.

(13) Neeves, K. B.; Onasoga, A. A.; Wufsus, A. R. *Current Opinion In Hematology* **2013**, *20*, 417-423.

(14) Morshed, B. I.; Shams, M.; Mussivand, T. *Micromachines* **2013**, *4*, 243-256.

CHAPTER 4

3D PRINTED *IN VITRO* THROMBOSIS MIMIC

4.1 Introduction

Thrombus formation that leads to vessel occlusion, causing heart attack or stroke, is the leading cause of death in developed countries.[1] There are a number of diseases where platelets are hyperactive,[2,3,4,5,6] putting individuals suffering from these diseases at increased risk for developing life threatening vessel occlusions during clot formation. Furthermore, stored red blood cells (RBCs) display decreased adenosine triphosphate (ATP) release which results in deleterious effects on the vasculature.[7,8,9] Specifically ATP regulates vascular tone less effectively and RBC derived ATP activation of platelets diminishes.

Microfluidic devices are ideal platforms to replicate *in vivo* thrombus conditions including the small dimensions of resistance vessels and normal physiological flow (< 10-1500 sec^{-1}) or flow under injury conditions (up to 13000 sec^{-1}).[10,11] Because rheological conditions can be recreated on microfluidic platforms, a multitude of devices aiming to recreate vascular events such as cell-to-cell communication and clot formation have been investigated. However, as will be discussed in this chapter, these devices tend to replicate only a small portion of the vasculature and leave out many key components. Chapter 3 focused on the fabrication and characterization of a 3D printed device functionalized with polydimethylsiloxane (PDMS) for cell adherence, and Chapter 4 will explain how this device can be applied to probing *in vitro* thrombus formation in a biologically relevant scheme.

4.2 Whole Blood and the Vascular System

The total volume of blood in the human body ranges from 4.5-5 liters.[12,13] Blood volume components can be broken down into the following: plasma (55%), RBCs (45%), white blood cells and platelets (1% combined). Hematocrit represents the volume of whole blood occupied by RBCs and ranges from 42-52% for men and 37-46% for women.[14] Within the body the hematocrit varies based on the size of the vessel through which blood traverses. In smaller resistance vessels (< 100 μm diameter) the hematocrit can be in the single digits, an event known as the Fahraeus-Lindquist phenomenon; occurring due to the tendency of RBCs to flow in the center of a vessel causing a decreased number of RBCs in smaller vessels as well as a decrease in blood viscosity. [11,15,16]

4.3 Introduction to Blood Banking

4.3.1 History

Transfusion medicine has roots that date back to 1492 when debatably the first transfusion was attempted on Pope Innocent VIII. As the story goes, the pope had fallen ill and the blood from three young boys was drained and administered orally, with all four participants dying in the end.[17,18] Major advancements to the field occurred when it was realized that a non-toxic anticoagulant was needed to prevent blood from clotting before transfusion, and in 1916 a citrate-dextrose solution was implemented for such purposes. World Wars I and II brought a demand for blood preservation and transfusion research. It was during this period that the first Red Cross blood bank in the United States was started. In 1957 citrate phosphate dextrose (CPD) was introduced as an improved storage solution and still finds acceptance as the standard blood storage preservative.[19] The addition of CPD allowed the donor to be separated from the recipient in space, and once glucose was added

to the storage solution as a means to maintain the metabolic function of RBCs, the two could be separated in time as well.

4.3.2 Storage Conditions

Blood donations are collected in units, where one unit represents a pint or 450 mL ± 10% of whole blood. Of these total volumes, 63 mL of anticoagulant/preservative solution (CPD) is also present. Specifically, whole blood is collected from a vein in the arm into a collection bag containing CPD as an anticoagulant. This bag is then centrifuged to separate the RBCs, which sediment to the bottom of the bag, from the platelet rich plasma (PRP). At this point further processing of PRP for platelet storage occurs and the buffy coat containing white blood cells is removed. Remaining RBCs are then added to an additive solution (AS) for preservation during storage. Additive solutions are added to the stored blood to stimulate glycolysis and maintain normal RBC metabolism. There are three different FDA approved blood storage solutions; CPD/AS-1, CP2D (citrate phosphate double dextrose) /AS-3; and CPD/AS-5 each with a 42 day storage limit.[20] The components of these additive solutions can be seen in Table 4.1.

Table 4.1 Storage component properties of the additive solutions AS-1, AS-3, and AS-5. CPD is the anti-coagulant solution for AS-1 and AS-5 while CP2D is used for AS-3. Concentrations are given in mM.

Components (mM)	CPD	CP2D	AS-1	AS-3	AS-5
Sodium citrate	89.4	89.4	/	/	/
Citric acid	15.6	15.6	/	/	/
NaH_2PO_4	16.1	16.1	/	/	/
Glucose	129	258	111	5.5	45
NaCl	/	/	154	154	150
Adenine	/	/	2	2	2.2
Mannitol	/	/	41	41	29
pH	5.6	5.6	5.8	5.8	5.8

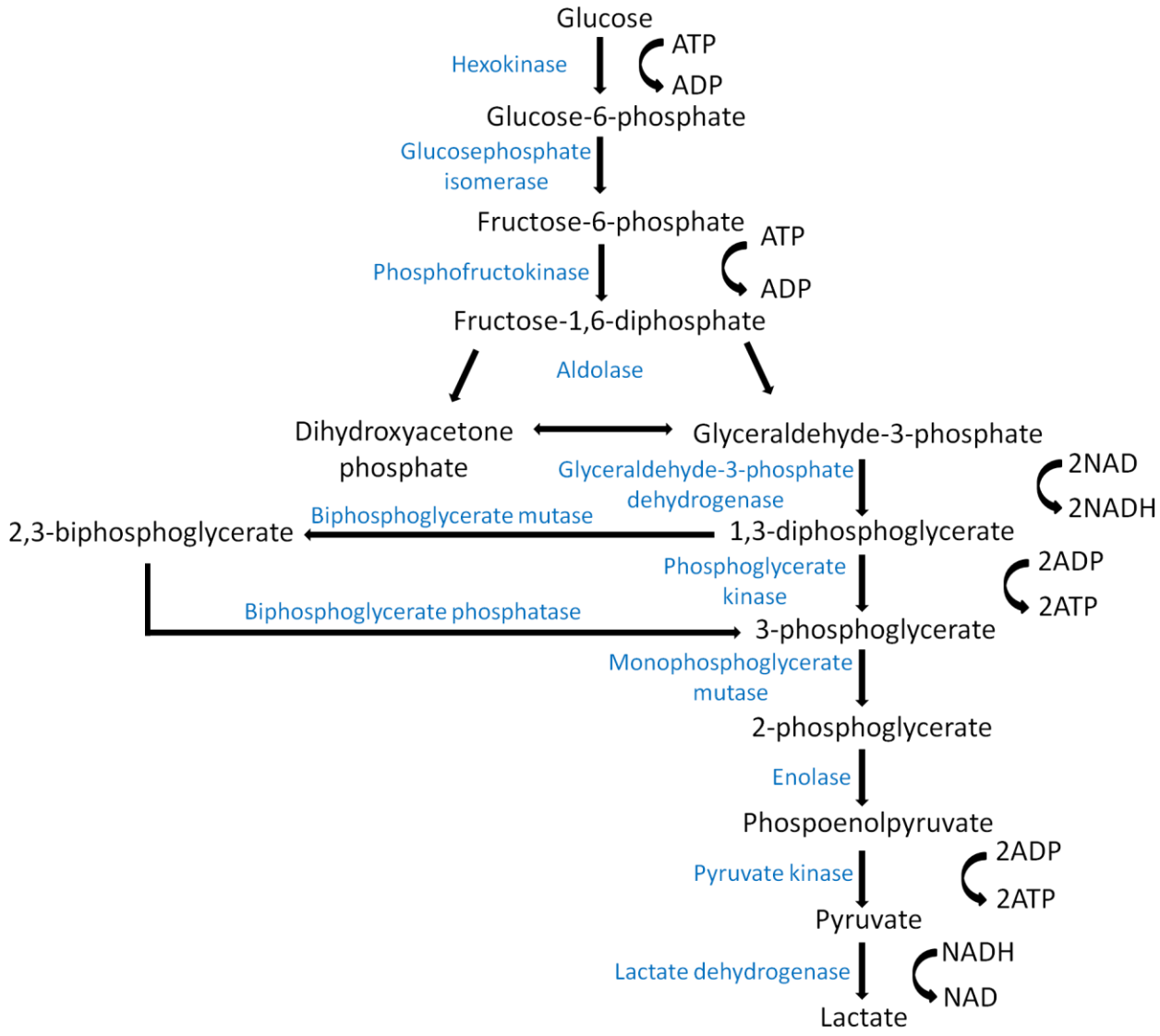

Figure 4.1 Anaerobic glycolysis in the RBC. The RBC has no expendable oxygen and lacks mitochondria; therefore the majority of ATP is produced via anaerobic glycolysis, leading to the production of lactate from glucose with a net gain of 2 ATP molecules. Lactic acid and proton buildup in stored blood decreases the pH to levels that prohibit enzyme function and continued ATP metabolism and therefore RBC viability. Glycolytic enzymes are shown in blue. NAD: nicotinamide adenine dinucleotide.

The pH of additive solutions ranges from 5.6-5.8, and upon the addition of blood (pH 7.35), the resulting pH of the banked blood is 7.2. Buffering action of the additive solutions can slow down the drop in pH and maintain the metabolic state of RBCs, namely ATP production, in the banked blood for several weeks. Storage duration constraints correlate to the amount of time it takes for lactic acid and proton production from anaerobic glycolysis by RBCs to lower the pH to 6.5, at which time glycolytic enzymes are inhibited and the ATP production is too low to support cell viability.[20,21] The flux of glucose into the RBC is controlled by glucose transporter protein 1 (GLUT1) found on the cell membrane.[22] Figure 4.1 highlights the process of anaerobic glycolysis in the RBC to produce two moles of ATP per one mole of glucose.[23]

The Food and Drug Administration (FDA) sets standards concerning RBC integrity and post-transfusion RBC viability. In the United States, free hemoglobin, a measure of RBC lysis, must be less than 1% of total hemoglobin over the duration of storage and 24 hour post-transfusion RBC viability must be at least 75%.[24,25] Blood can be stored for up to 42 days (between 1°C and 6°C) when mixed with one of the three FDA approved additive solutions.

The container in which RBCs are stored is an important component for prolonging shelf life. The container must be permeable to CO_2 for the maintenance of higher pH levels during storage. Currently, polyvinyl chloride (PVC) bags are most commonly utilized, and they contain a plasticizer (di(ethylhexyl)-phthalate or DEHP) that leaches from the bag into the storage solution and the membrane of RBCs and lipids of plasma medium. DEHP was found to stabilize the RBC membrane, extending the possible storage period as compared

to other containers including glass, polyolefin (non-DEHP containing), and latex-free containers (latex allergy considerations).[21]

Platelet storage is limited to five days due to bacterial contamination (platelets are stored at 22 °C) and loss of cell quality from platelets becoming activated and forming aggregates. Platelets were originally stored at the same temperature as RBCs (1°C to 6°C), but it was later found that cold-induced activation occurred and *in vivo* platelet viability was decreased after transfusion due to a structural change of the cells to spherical, indicating microtubule disassembly. Platelets can be cryo-preserved using dimethyl sulfoxide (DMSO) for a period of up to two years, however post-transfusion recovery of frozen platelets is only 33%.[26]

According to the World Health Organization, more than 81 million units of blood were collected globally in 2009, and a maximum of 80 million units of RBCs were transfused, of which 30 million transfusions occurred in the United States.[27,28] This indicates that overall there was a greater supply of stored blood than demand, though seasonal local shortages do occur.[29] For the Spence group, the necessity to improve storage conditions is driven by remedying maladies in RBC metabolism related to high glucose levels. In addition to improving storage conditions for metabolic function and prolonged viability, research focusing on converting various blood types to the universal donor (type O), blood pharming (converting hematopoietic stem cells into type O RBCs), and RBC substitutes that could function as oxygen carriers are underway.[30,31,32]

4.3.3 Complications Associated with Stored Blood Transfusions

4.3.3.1 RBC Storage Lesion

Physical and chemical changes experienced by the RBC as a consequence of storage are known as the RBC storage lesion.[33] These changes (loss of ATP and 2,3-diphosphoglycerate or 2,3-DPG, loss of membrane and shape, decreased deformability and oxygen delivery) pose an increased risk of mortality to patients receiving blood transfusions.[34] 2,3-DPG stabilizes deoxygenated hemoglobin, making it less efficient at binding oxygen, and allows for oxygen to be unloaded at a higher O_2 partial pressure. Glucose in the additive solution is consumed during storage, leading to a decrease in 2,3-DPG and ATP. The RBC membrane loses integrity and therefore cell lysis becomes possible.[33]

RBCs play a role in blood flow, and several deleterious effects of the RBC storage lesion (decreased deformability and ATP release) hinder the ability of RBCs to regulate blood flow.[34,7] RBCs contain millimolar concentrations of ATP,[35] and exposure of RBCs to mechanical deformation or shear stress (as well as reduced oxygen tension and pharmacological stimuli) can cause the cell to release nanomolar to micromolar concentrations of ATP, which results in the generation of vasodilators in the local endothelium.[36,37] Specifically, RBC derived ATP stimulates nitric oxide synthase (NOS) in endothelial cells lining the blood vessel.[8,38] Nitric oxide (NO) diffuses to surrounding smooth muscle cells (SMCs) and activates guanylate cyclase, which facilitates conversion of guanosine triphosphate (GTP) to cyclic guanosine monophosphate (cGMP). cGMP activates a protein kinase that phosphorylates ion channels and pumps causing a decrease in intracellular Ca^{2+} concentrations which inhibits myosin light chain kinase, resulting in

muscle relaxation and increased local blood flow through vasodilation.[39,40,41] Figure 4.2 shows how RBC derived ATP release leads to vasodilation through smooth muscle cell relaxation.

Examining the components of the additive solutions used in blood storage, the glucose levels of the three FDA approved solutions (CPD/AS-1: 45 mM, CP2D/AS-3: 35 mM, CPD/AS-5: 30 mM extracellular glucose) are much higher than the 4-6 mM *in vivo* blood glucose level of healthy individuals and even the diabetic blood glucose range of 7-9 mM.[42] Addition of RBCs to the storage solution brings the final glucose level close to 40 mM, still exorbitant compared to healthy blood glucose levels.[43]

Recent efforts by the Spence group towards improving blood storage conditions include storing RBCs in normoglycemic conditions. ATP release from RBCs stored in normoglycemic storage solutions, maintained with periodic glucose feeding, containing CPD-N (5.5 mM glucose compared to 129 mM) and AS-1N (5.5 mM glucose compared to 111 mM) was compared to the release from RBCs stored in CPN/AS-1 as seen in Figure 4.3.[7]

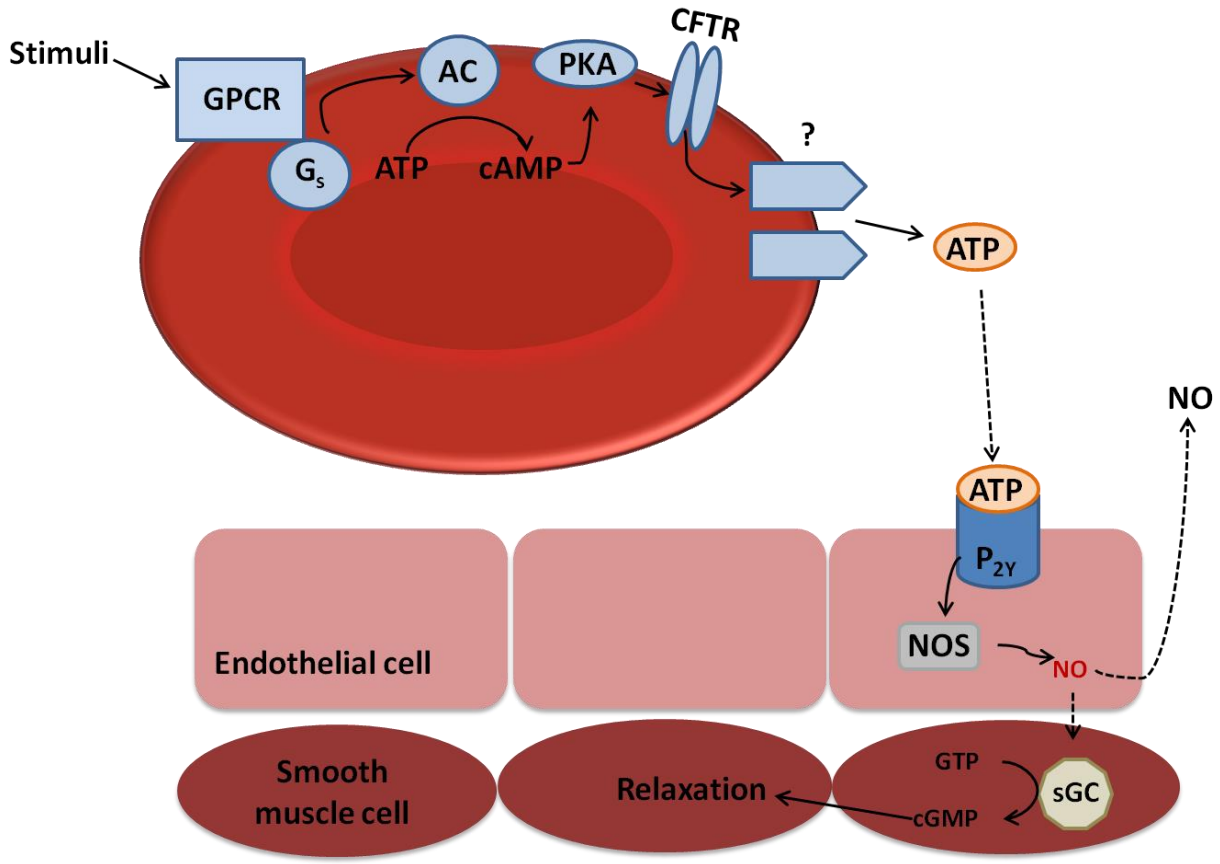

Figure 4.2 Proposed mechanism of ATP release from the RBC leading to NO production and eventual vasodilation from smooth muscle cell relaxation. The release of ATP from the RBC due to various stimuli including mechanical deformation, hypoxia, and chemical stimuli has been proposed to rely on a stimuli induced conformational change in a G-protein coupled receptor (GPCR) that activates adenyl cyclase (AC) which catalyzes the conversion of ATP into cyclic adenosine monophosphate (cAMP). cAMP activates protein kinase A which phosphorylates the cystic fibrosis transmembrane conductance regulator (CFTR). The exact mechanism of ATP release is not known,[44] but it diffuses to the endothelium where it binds with the purinergic receptor P2Y, which allows an influx of calcium ions into the cell that facilitate nitric oxide synthase (NOS) production of NO from the conversion of L-arginine to L-citruline. NO then diffuses into the blood stream and the surrounding smooth muscle tissue where it activates the enzyme soluble guanylyl cyclase (sGC). Activated sGC converts guanosine triphosphate (GTP) to cyclic guanosine monophosphate (cGMP) which causes smooth muscle cells to relax and blood vessels to dilate.

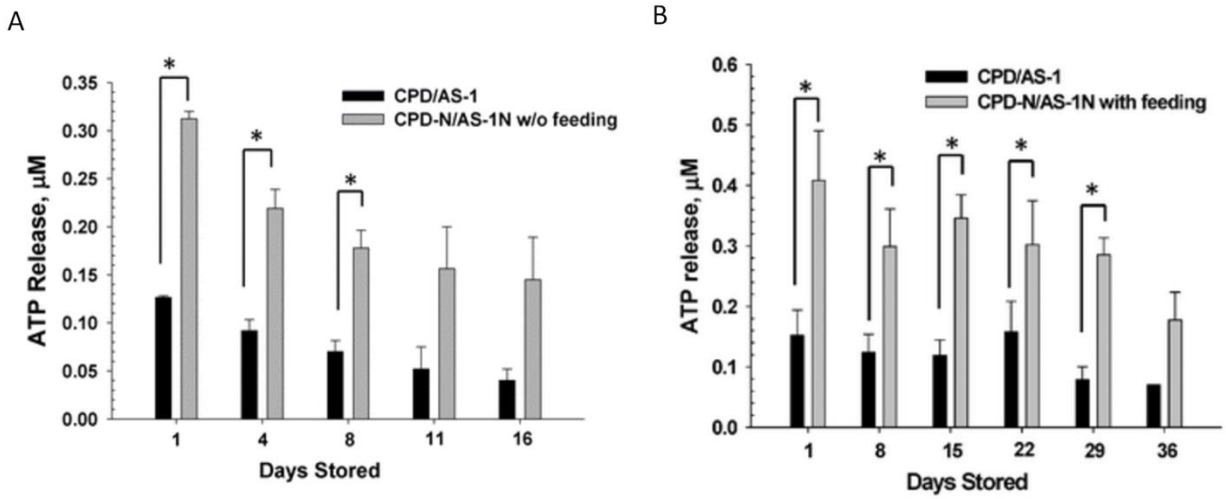

Figure 4.3 Comparison of ATP release from RBCs under hyperglycemic (AS-1) and normoglycemic (AS-1N with and without feeding) storage conditions. RBCs stored in AS-1N (gray bars) displayed significantly higher ATP release that those stored in AS-1 (black bars) for the first 8 days (*$p < 0.005$) with a gradual decrease in release as storage time increased (A). ATP release for AS-1N where the glucose level was maintained around 5 mM through weekly glucose feeding was significantly higher through 29 days of storage (*$p < 0.05$) compared to AS-1 stored RBCs (B). Data represents mean ± standard error of the mean, n=4. (Reprinted with permission from reference 7. Copyright The Royal Society of Chemistry.)

Flow-induced ATP release was measured by chemiluminescence using the luciferin-luciferase reaction. Figure 4.3 shows that RBCs stored in normoglycemic conditions released higher levels of ATP than those stored under standard hyperglycemic conditions. Periodic feeding of normoglycemic stored cells further enhanced ATP release, which was attributed to providing appropriate levels of glucose to enable continued glycolytic processes. Intracellular levels of ATP for CPD/AS-1 were slightly higher during the storage period compared to CPD-N/AS-1N, meaning that the reason for increased ATP release from RBCs stored in normoglycemic conditions is not due to intracellular ATP levels during storage.[7] Because stored RBCs are less deformable, they exhibit decreased ATP release compared to RBCs stored in normoglycemic conditions, confirmed in recent unpublished results from the Spence group.

4.3.3.2 Insufficient NO Bioavailability

Patients receiving transfusions with older stored blood experienced increased rates of mortality, sepsis, and kidney failure.[45,46] Older RBCs are those stored between 14-42 days, and the deleterious effects that manifest after transfusion are believed to be due in some part to insufficient NO bioavailability (INOBA). Deleterious effects of storage manifesting as the RBC storage lesion impair the RBC's ability to regulate vascular tone. Specifically, a number of studies have shown that stored RBCs release lower than normal levels of ATP and subsequently decrease NO release from the endothelium.[43,7] Lowered levels of NO in the blood stream result in decreased blood flow and insufficient oxygen delivery to demanding tissues. Further compounding the seriousness of the issue, individuals who suffer from cardio vascular disease (CVD) often have poor vascular tone regulation as a result of defective vascular endothelium that releases less NO. For cases like

CVD, where individuals present decreased endothelial function, paired with decreased stored RBC function (lowered ATP release), NO bioavailability is insufficient to regulate perfusion.[47,48]

4.3.3.3 Transfusion-Related Acute Lung Injury

Oxidative damage from hydroxyl radical formation, which results from oxygen removing an electron from a ferrous atom to form a superoxide radical and ferric methemoglobin, damages lipids and proteins of the RBC membrane. During high volume transfusions, the oxidative burden is often damaging to the patient. Transfusion-related acute lung injury (TRALI) arises from oxidative damage resulting in active lipid surfaces that are possible sites for thrombotic events.[34]

4.3.3.4 Sepsis

Sepsis, or bacterial infection from contamination of stored blood components, is often life threatening to transfusion recipients. Contaminations occur approximately every one in two thousand donated units, mostly due to bacteria present on donor skin or blood-borne bacteria, however most bacteria do not survive cold storage and in 2008 only one death from transfusion-related bacterial sepsis was reported.[34] Platelets stored around room temperature are the most at risk component for bacterial contamination, with sepsis occurring in donated platelets in 1 in 2,000-3,000 units.[49,50] Sepsis develops in up to 40% of individuals post-transfusion with contaminated platelets, prompting stricter screening before transfusion.[50]

4.3.4 Effect of Reduced RBC Derived ATP Release on Platelet Activation and Function

In addition to decreases in RBC deformability and the ability to regulate vascular tone in hypoxic (low O_2) conditions, stored RBCs have shown increased adherence to the

endothelium *in vitro*.[43,7,51,52] RBC derived ATP release also serves to amplify the activation of platelets through the purinergic P2X1 receptor on the platelet surface, prompting a shape change making platelets prone to aggregation with one another, and stimulates NOS in platelets leading to NO production.[53,54] Moreover, activated platelets release ATP, and other pro-thrombotic molecules, further serving to aid in local regulation of vascular tone.[55] Aside from its function as the endothelium derived relaxing factor (EDRF), NO derived from platelets and the endothelium, also serves to inhibit platelet activation and aggregation potentially preventing a thrombus that can detrimentally occlude a resistance vessel.[56,57] NO decreases platelet intracellular Ca^{2+} which leads to decreased aggregation, shape change, and granule secretion of pro-thrombotic agonists; though the exact cellular mechanism leading to this decrease is not known.[57] RBC adherence to the endothelium, decreased NO presence to inhibit platelet activation, and an impaired ability to initiate vessel dilation poses a risk for potential occlusive thrombus formation.

4.4 *In Vitro* Thrombus Formation

4.4.1 Devices to Study Thrombus Formation

The advent of parallel channel flow chambers (commonly petri dishes coated with endothelial cells featuring a gasket allowing contact of fluid flow over a specified region via syringe pump) were work horses for shear rate studies on adhesion, but failed to mimic dimensions seen *in vivo* and required copious reagent use.[58,59] Microfluidics are well suited to overcome limitations seen with flow chambers, and most microfluidic applications applied towards hemostasis focus on flow assays wherein various shear rate and stress-dependent coagulation studies can be performed on parallel channels. Such considerations are paramount as platelet adhesion and aggregation are known to be shear stress

dependent, and coagulation and fibrin formation are shear rate dependent.[60] The first microfluidic device featuring fluid flow and incorporation of cell-cell interactions in the form of cell adhesion (leukocyte adhesion to endothelial cells) came from Chang et al in 2000. In this work interactions between the two cell types, including dissociation rates and bond lengths of interacting molecules were probed.[61] Commercial microfluidic devices for cell adhesion studies are available from Ibidi, Cellix, and Fluxion Biosciences. Most of these devices are simple in nature and the majority feature parallel channels with either an adhesive protein or cell type as a substrate. However, channels featuring bifurcations, regions of stenosis, and an endothelium to more accurately mimic human vasculature have been fabricated.[62,63,64]

4.4.2 Methods to Evaluate Thrombus Formation

There are a number of established techniques for the evaluation of a formed thrombus in animal models as well as on *in vitro* platforms. These techniques range in design from simple surface area coverage measurements and enumeration of platelets within a specific region, to microscopy relying on either brightfield imaging or the use of fluorescent stains that label specific components of the clot.[65,66] Studies aimed at isolating location and overall contribution to the clot by a specific blood component focus on RBCs, platelets, thrombin, and fibrin.[67] Thromboelastography is a less common *in vitro* technique primarily used to monitor blood clot size so that coagulation can be controlled during surgical procedures. Thromboelastography measures thrombus size by taking a small volume of whole blood from the patient and placing it into a cup that rotates the blood. A pin connected to a computer inserted into the blood monitors clot formation on the pin as coagulation proceeds. Changes in the magnitude of pin motion correlate to the strength of

the clot and increases in the amplitude of pin motion indicates clot formation and eventually clot lysis with a decrease in amplitude. From thromboelastography parameters such as the time for clotting to commence (reaction time), the maximum amplitude (maximum clot strength), and clot lysis (a measure of amplitude reduction thirty minutes after the maximum amplitude was measured) are recorded.[68]

Studies that measure thrombus formation as a function of adhered platelets rely on enumeration of adhered cells after incubation and numerous washing steps. Often with such studies the strength of adhesion is measured with relation to the shear stress necessary for detachment and less commonly, the bond strength between platelet and substrate which entails finding the number of bonds and cell contact area.[69,70] Optical measurements relying on transmitted light through a portion of a channel with a formed thrombus have also been utilized to evaluate clot formation. Specifically, light transmittance through a channel increased as flowing whole blood was replaced by platelet aggregates that are less scattering and absorb less visible light than RBCs as they lack hemoglobin.[10] More simply, microscopy has been used in conjunction with varying shear rates to qualitatively measure formed thrombi in microfluidic channels featuring stenosis regions.[71] Histological staining can be used to determine the volume of a thrombus if it can be removed from the originating platform. However, this process involves multiple preservation, washing, and fixing steps.[10]

4.5 Experimental Design and Rationale

The 3D printed device introduced in Chapter 3 was utilized in studies striving for *in vitro* thrombus formation, with the exception that a version of the device lacking the electrode ports was used. For the studies that follow, the desired outcome was the

determination of the extent of thrombus formation to an intact endothelium when stored RBCs were present. The source of collagen used to represent subendothelial extra cellular matrix (ECM) was type 1 bovine collagen, as it has been reported in the literature that type I fibrillar collagen yields the best response through the glycoprotein receptors on the platelet surface that interact with collagen (GPVI) and is generally accepted as a better physiological mimic compared to other reconstituted collagens.[72]

Between existing thrombosis mimics, standardization of the collagen substrate (source, concentration, and composition) used to form the thrombus is lacking and thus variability between various platforms concerning the formed thrombus exists.[73] The stenosis feature is key as it has been shown that incorporation of a stenosis model affects platelet aggregation without agonists of platelet activation.[74] Incorporation of PDMS into the channel of the 3D printed device serves two purposes. First, it facilitates endothelial cell adhesion in the channel. Second, it represents the elasticity of blood vessels (PDMS Young's Modulus: 0.38-0.75 MPa; human resistance vessel at physiological blood pressure: 0.5-2 MPa).[10,75]

4.6 Methods

4.6.1 Preparation of Reagents

Heparin

Custom doses of heparin were prepared and added to vacutainer tubes for use as an anticoagulant during whole blood collection. A 1060 USP stock solution of heparin was prepared from heparin sodium salt (212 USP·mg^{-1}, Sigma Aldrich, St. Louis, MO, USA) by adding 5 mg of heparin into 1 mL of PBS. Working solutions of 1, 2, 3, 4, 5, 10, 20, 50, and

100 USP were made by diluting the 1060 USP stock solution with the appropriate volume of phosphate buffered saline (PBS).

Drabkin's Solution

Drabkin's solution was prepared by mixing 1 vial of Drabkin's reagent (contains sodium bicarbonate, potassium ferricyanide, and potassium cyanide; Sigma-Aldrich, St. Louis, MO, USA) into 1 L of deionized and distilled water. A detergent was added to the solution to facilitate cell lysis, releasing hemoglobin. Specifically, 0.5 mL of 30% Brij solution was added (Sigma-Aldrich, St. Louis, MO, USA).

4.6.2 Determination of Optimal Heparin Concentration

Heparin, when bound to a plasma cofactor anti-heparin, acts as an anticoagulant by inactivating proteases necessary for blood clotting (thrombin, factors XIIa, XIa, IXa, and Xa). Thrombin inactivation prevents formation of fibrin, the protein involved in stabilizing platelet aggregates.[76] Standard heparinized tubes come coated with 157 USP heparin and will stave off coagulation of whole blood for several days. Using such high doses of heparin for studies aimed at thrombosis development becomes problematic, as the coagulation cascade is inhibited. Ideally, untreated whole blood would be used; unfortunately, the working time until complete coagulation is often less than 5 minutes, not enough to allow for sample handling after venous blood draw and completion of a flow based experiment. In order to determine the optimal heparin dose that would prevent coagulation for the duration of the time necessary to complete experiments, a range of heparin concentrations were prepared. Whole blood was collected in vacutainer tubes (BD, Franklin Lakes, NJ, USA) containing 1 mL of 1, 2, 3, 4, 5, 10, 20, 50, or 100 USP heparin prepared in PBS buffer that was injected prior to collection. Tubes were inverted upon collection and monitored

for 7 hours to determine the time required to reach complete blood coagulation. Table 4.2 shows the observed clotting times for the above mentioned heparin doses. Based on this information, a dose of 10 USP heparin was added to untreated vacutainer tubes prior to blood collection.

Table 4.2 Observed clotting stages for whole blood dosed with heparin up to 100 USP. From the information contained in this table, a minimal dose of heparin was determined that could be used to stave off coagulation in the time needed to carry out experiments utilizing whole blood.

Heparin USP	1-5 min	5-10	10-15	15-20	30	40	50	60	420
1	No change	Increased viscosity	Increased viscosity	Clots present	Complete coagulation	-	-	-	-
2	No change	Increased viscosity	Increased viscosity	Clots present	Complete coagulation	-	-	-	-
3	No change	Increased viscosity	Increased viscosity	No change	Severe coagulation	Complete coagulation	-	-	-
4	No change	Increased viscosity	Increased viscosity	No change	Severe coagulation	Complete coagulation	-	-	-
5	No change	Increased viscosity	Increased viscosity	No change	Small clot present	Clots present	Complete coagulation	-	-
10	No change	No change	No change	No change	No change	Clots present	Clots present	Complete coagulation	-
20	No change	No change	No change	No change	No change	No change	No change	No change	No change
50	No change	No change	No change	No change	No change	No change	No change	No change	No change
100	No change	No change	No change	No change	No change	No change	No change	No change	No change

4.6.3 Cell Immobilization on the 3D Printed Device

The device channel was sterilized for cell immobilization by rinsing with isopropyl alcohol (IPA) and then dried in a 75 °C oven. Prior to seeding bovine pulmonary artery endothelial cells (bPAECs), channels were incubated with a solution containing 100 $\mu g \cdot mL^{-1}$ of collagen (Advanced BioMatrix, Poway, CA) and 50 $\mu g \cdot mL^{-1}$ of fibronectin (Sigma-Aldrich, St. Louis, MO) prepared in distilled deionized water at 37 °C for 2 hours. The adhesive proteins were then dried onto the device which was exposed to UV light for 15 minutes for sterilization. Endothelial cells were harvested from a tissue culture flask after a one minute incubation with 0.25% trypsin-EDTA (Life Technologies, Grand Island, NY). The cells were

reconstituted in cell media, centrifuged at 1500*g* for 5 min, isolated, and reconstituted in phenol red free cell media (Dulbecco's Modified Eagle's Medium (DMEM) Caisson, North Logan, UT) containing 7.5% fetal bovine serum, 2.5% adult bovine serum, and 2.5% antibiotic solution. This concentrated cell solution was loaded into the channel of the device using a pipette. The cells were incubated at 37 °C for 1.5 hours. After this time, cell adhesion was monitored and if needed, more cells were added to the channel. Cell media was changed every 1.5 hours for 6 hours after cell attachment to the device was confirmed and cells were incubated with media overnight.

4.6.4 Collection and Preparation of Whole Blood

Whole blood was collected via venipuncture into vacutainer tubes containing 10 USP of heparin from consenting donors and used the same day for experiments (flow rate studies or stored via the protocol detailed in the following section). Other anticoagulants such as citrate are available, however, use of citrate (ACD) as an anti-coagulant often requires the addition of ADP to re-activate platelets and so was avoided.[10] Handling of the whole blood was kept to a minimum aside from loading into syringes for delivery to the 3D printed device to avoid unwanted activation of platelets.

4.6.5 Flow Rate Study

A series of different flow rates were evaluated to determine the optimal flow rate necessary for thrombus formation within the fluidic device containing a confluent endothelium. Whole blood was collected into vacutainer tubes containing 10 USP heparin. Thrombus coverage on the device was monitored using brightfield imaging with an Olympus IX71 inverted microscope (Olympus America, Melville, NY) when flow rates of 5, 10, 20, 25, and 30 $\mu L \cdot min^{-1}$ were applied. Specifically, 500 µL of whole blood was loaded

into a syringe (Hamilton, Franklin, MA) and delivered with a syringe pump (Pump 11 Plus, Harvard Apparatus, Holliston, MA). Shear rates were determined by first calculating the volumetric flow rate (Q; $cm^3 \cdot sec^{-1}$) from the applied flow rate with the following equation:

$$Q = u \cdot A \qquad \text{Equation 4.1}$$

where u is the average linear velocity ($cm \cdot sec^{-1}$) and A represents the cross sectional area (cm^2) of the stenosed channel which was assumed to be circular after PDMS incorporation. Once the linear velocity was know, shear rates (γ; sec^{-1}) for the narrow regions of the channel were calculated using equation 4.2 where d is the channel diameter.

$$\gamma = 32 \frac{Q}{\pi \cdot d^3} \qquad \text{Equation 4.2}$$

This variation of the Haagen-Poisseuille equation can be applied to determine the shear rate, assuming that blood is a Newtonian fluid with constant viscosity, the flow remains laminar throughout, and that the channel is both cylindrical and inelastic.[11]

Shear stress (τ; $dyn \cdot cm^{-2}$) was calculated using equation 4.3:

$$\tau = 8 \cdot \mu \cdot \frac{u}{d} \qquad \text{Equation 4.3}$$

Here μ represents the blood viscosity which was assumed to be 10 cP for calculations which is appropriate for blood in vessels with shear rates around 5 sec^{-1} and a hematocrit

of 45%.[11] The Reynold's number can be used to describe the type of flow profile, either laminar or turbulent, by comparing inertial forces to viscous forces.

$$R_e = \frac{\rho \cdot u \cdot d}{\eta} \qquad \text{Equation 4.4}$$

Reynold's number is dependent upon solvent density (ρ; g·cm^{-3}), solvent linear velocity (*u*; cm·sec^{-1}), tube diameter (*d*; cm) and solvent viscosity (η; gcm^{-1}·sec^{-1}). Reynold's numbers less than 2100 indicate laminar flow where fluid mixing is diffusion controlled compared to turbulent mixing at higher Reynold's numbers.

4.6.6 Evaluating Thrombus Formation on the Fluidic Device

Whole blood samples were loaded into 500 µL syringes (Hamilton, Franklin, MA) fitted with luer lock adapters (IDEX Health & Science LLC, Oak Harbor, WA) connected to 20 cm pieces of 1/8" Tygon tubing (Saint-Gobain PPL Corp, Jackson, MI). Sample delivery was achieved using a syringe pump (Pump 11 Plus, Harvard Apparatus, Holliston, MA) programmed with the inner diameter of the syringes (3.26 mm) and flow rates of 30 µL·min^{-1}. Blood was flowed into channels of 3D printed devices containing a confluent layer of endothelial cells for 20 minutes. Channel dimensions for the 3D printed devices can be seen in Table 3.1 from Chapter 3. Devices were then incubated for 20 minutes in a cell incubator set at 37 °C. After the incubation period, devices were gently rinsed to remove any non adherent cells.

Thrombus formation was evaluated using a plate reader (Spectramax M4, Molecular Devices, Sunnyvale, CA) to take absorbance measurements of the channel portion of the device after flowing whole blood samples. Devices were positioned so that the lysis region was directly over a well of a 96 well plate. The absorbance of the devices in this region was

measured from 400 nm to 700 nm with 5 nm steps. The corresponding absorbance measurements were converted to percent transmittance. This protocol allowed thrombus formation to be monitored through changes in percent transmittance, as decreases in percent transmittance corresponded to an increase in thrombus coverage on the device. Figure 4.4 shows the experimental setup for taking fluorescence measurements by pairing the 3D printed devices with commercial 96 well plates and a plate reader.

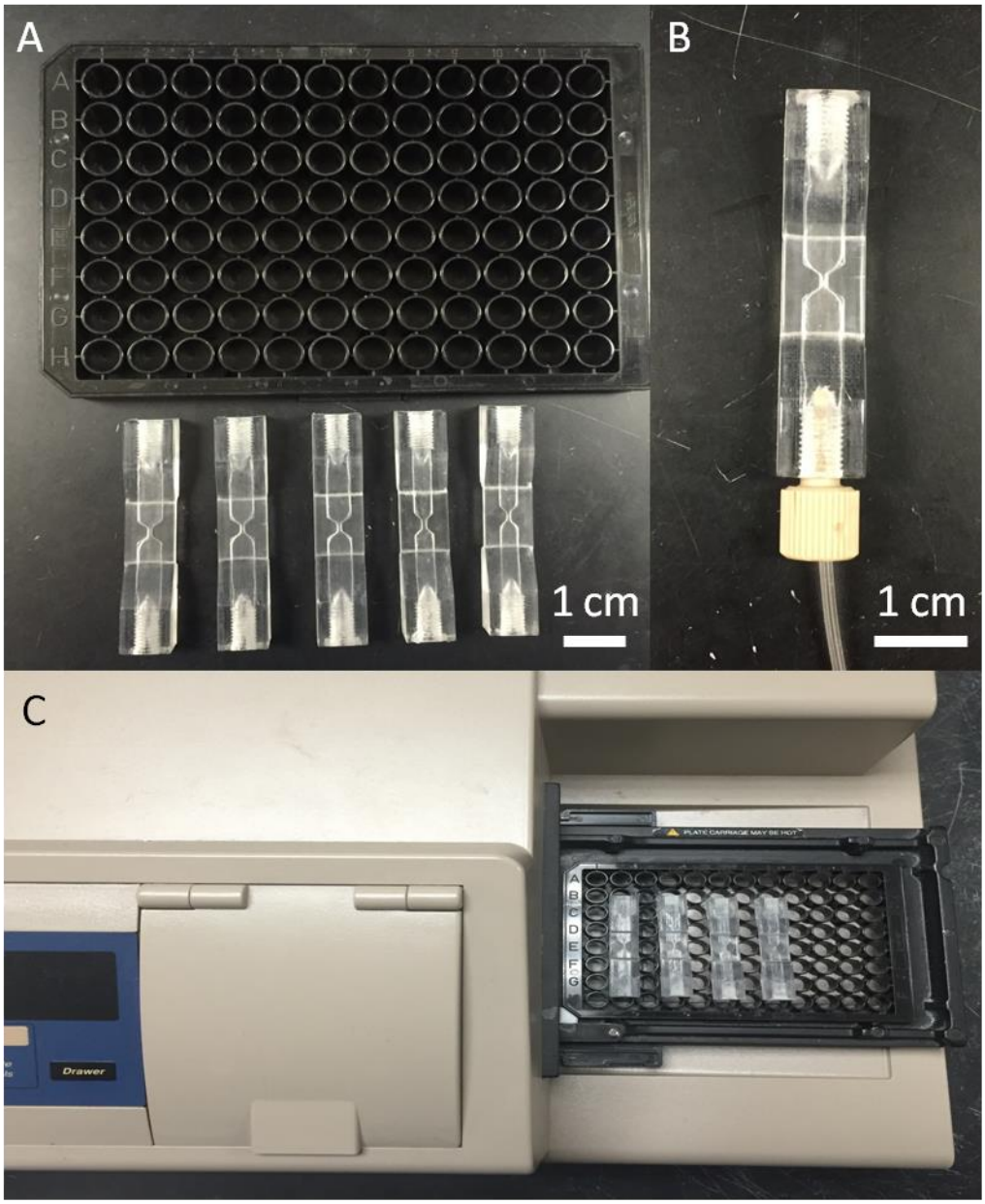

Figure 4.4 Interfacing 3D printed devices and a commercial plate reader for easy and rapid absorbance measurements of formed thrombi. The 3D printed fluidic devices used to monitor thrombus formation can be paired with a clear bottom 96 well plate to facilitate absorbance measurements of the stenosed region (A). Printed threads connect with a male luer lock adaptor fitted with Tygon tubing and attach to a syringe pump for controlled sample delivery (B). Devices can be placed over a well of a 96 well plate and absorbance measurements taken by a commercial plate reader.

4.6.7 Storage Conditions for RBCs

Storage solutions were prepared as depicted in Table 4.3. CPD was used as an anticoagulant solution for whole blood and additive solution was used to facilitate storage.

Table 4.3 Components of the RBC storage solutions used to evaluate thrombus formation when stored RBCs were reincorporated into freshly drawn platelets. Normoglycemic storage solutions (CPD-N/AS-1N) and hyperglycemic storage solutions (CPD/AS-1) contained identical component concentrations with the exception of glucose. Concentrations are given in mM.

Component	CPD/mM	CPD-N/mM	AS-1/mM	AS-1N/mM
Sodium citrate	89.4	89.4	/	/
Citric acid	15.6	15.6	/	/
NaH_2PO_4	16.1	16.1	/	/
Glucose	129	5.5	111	5.5
NaCl	/	/	154	154
Adenine	/	/	2	2
Mannitol	/	/	41	41
pH	5.6	5.6	5.8	5.8

Hyperglycemic and normoglycemic (denoted with the suffix -N) solutions were prepared. Whole blood was drawn into non-heparinized tubes containing CPD or CPD-N. After 30 minutes, tubes were centrifuged at 2000*g* for 10 minutes and plasma and buffy coat were removed. Packed RBCs were stored in a 2:1 ratio with AS-1 in PVC bags. Bags were heat sealed and stored at 4 °C. Glucose levels for AS-1N stored RBCs were maintained through dosing with a 200 mM glucose saline solution every 4 days of storage.[7] Figure 4.5 shows the process of collecting whole blood and storing RBCs.

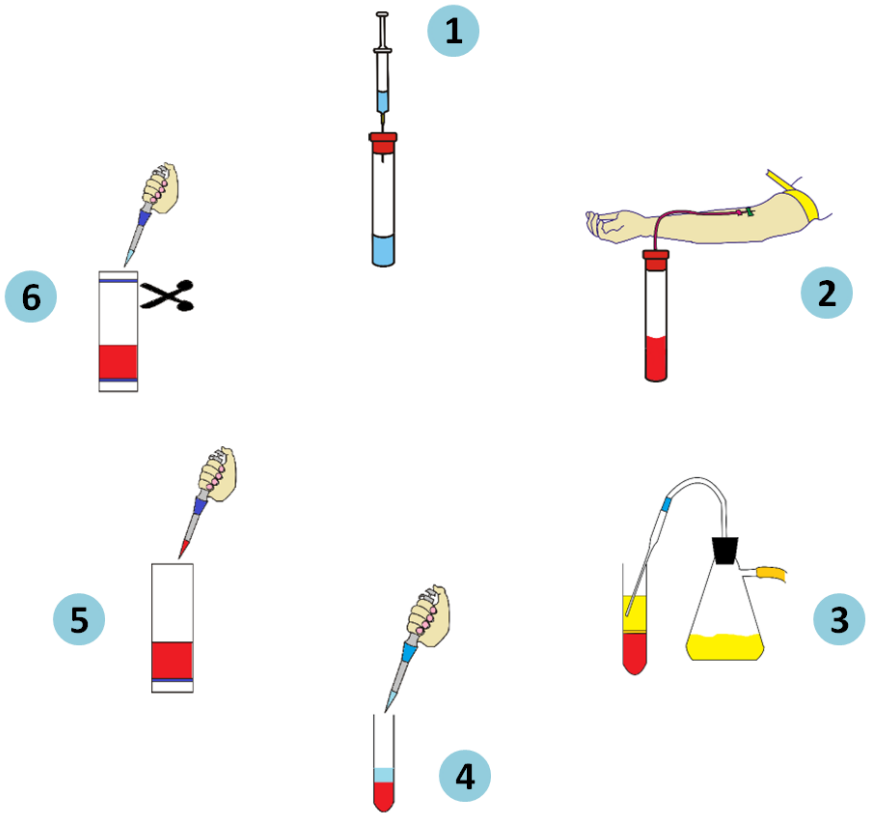

Figure 4.5 RBC storage protocol. 1 mL of anticoagulant solution (CPD) was added into a non-heparinized vacutainer tube. Around 7 mL of whole blood was collected from a consenting donor via venipuncture and allowed to rest for 30 min. Blood was then centrifuged at 2000*g* for 10 minutes to facilitate removal of the buffy coat and plasma. AS-1 or AS-1N was added to the vacutainer tube at a volume ratio of 2:1 (packed RBCs: AS). RBCs were stored in polyvinyl chloride (PVC) bags at 4 °C. AS-1N stored RBCs were fed every 4 days with a 200 mM glucose saline solution.

4.6.8 Determining Hemolysis of Stored RBCs via Hemoglobin Quantification

The percentage of stored RBCs that had lysed (percent hemolysis) was determined by taking the ratio of free hemoglobin (Hbf) released into the additive solution to the total hemoglobin (Hbt) in the sample. Hemoglobin standards were prepared from a 7.2 $g \cdot L^{-1}$ stock hemoglobin solution made by dissolving 0.036 g of adult hemoglobin (Sigma-Aldrich, St. Louis, MO, USA) in 5 mL of Drabkin's solution. From this stock solution, standards (0-0.8 $g \cdot L^{-1}$) were prepared by diluting in appropriate volumes of Drabkin's solution. Before determining hemolysis, the hematocrit of each stored sample was calculated. Total hemoglobin (Hbt) was found by making a 1:1000 dilution of stored RBCs into Drabkin's solution, specifically by diluting 10 µL of the mixed RBC sample into 990 µL of Drabkin's solution and mixing; then taking 100 µL of that solution into 900 µL of Drabkin's solution. Free hemoglobin in the supernatant (Hbf) was found by centrifuging 500 µL of stored RBCs at 15,000*g* for 10 minutes and adding 100 µL of the resulting supernatant to 900 µL Drabkin's solution (1:10 dilution). Samples and standards were thoroughly mixed by vortex before being loaded into wells of a clear bottom 96 well plate (200 µL per well), and the absorbance measured in triplicate at 542 nm using a plate reader (Spectramax M4, Molecular Devices, USA).[7] Percent hemolysis was calculated using the following equation:

$$\%\ Hemolysis = \frac{(Supernatant\ Hb\ (g\ L^{-1})\ [100 - hematocrit\ (\%)])}{Total\ Hb\ (g\ L^{-1})} \qquad \text{Equation 4.5}$$

4.6.9 Platelets Reconstituted in Stored Blood for Thrombus Formation Evaluation

The protocol for the preparation of reconstituted stored blood samples containing freshly drawn platelets is shown in Figure 4.6. Whole blood was collected via venipuncture into heparinized vacutainer tubes (157 USP) from consenting donors and allowed to sit for 15 minutes to avoid excessive agitation of platelets leading to unwanted activation. Samples were then centrifuged at 100*g* for 15 minutes to ensure that platelets would remain in the plasma instead of settling in the buffy coat, making isolation easier. The platelet rich plasma (PRP) was carefully removed and centrifuged at 1000*g* for 12 minutes. This resulted in a platelet pellet at the bottom of the centrifuge tube with platelet poor plasma (PPP) in the supernatant. Platelets were reconstituted in 2 mL of PPP, and excess plasma was retained. Platelet concentrations were determined by counting with a hemacytometer (Bright-line Reichert, Sigma-Aldrich, St. Louis, MO, USA), 10 µL of concentrated platelet solution was added to 990 µL of phosphate buffered saline. From this solution, 10 µL was loaded into the hemacytometer and the total number of platelets determined as per manufacturer recommended calculations. Platelets were reconstituted in PPP and adjusted to a concentration of 4.0×10^8 platelets mL^{-1} in stored blood for thrombosis studies.

The PVC bags containing stored blood samples (AS-1 and AS-1N) were cut open and mixed by pipetting. The hematocrit of each stored blood solution was acquired by sampling blood from each storage solution into micro-hematocrit tubes, sealed to prevent leaking during centrifugation with a micro-hematocrit centrifuge. After centrifugation, the hematocrit was determined using a digital hematocrit reader. Hematocrit tubes, sealant, centrifuge, and reader were purchased from Iris Sample Processing, Chatsworth, CA, USA.

The final hematocrit of stored blood samples containing platelets was adjusted to 45%, a value within the physiological range of whole blood.[14]

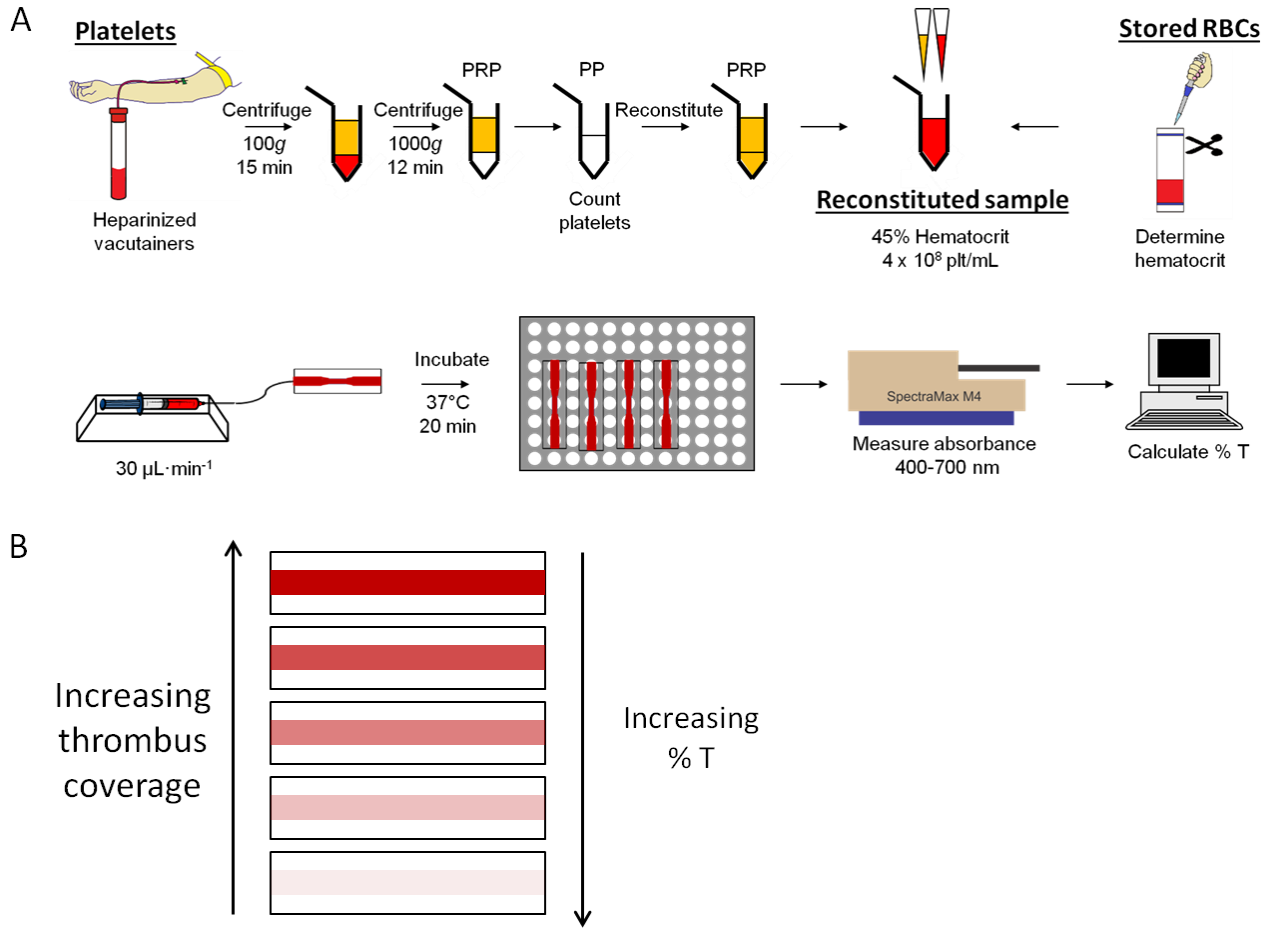

Figure 4.6 Preparation of reconstituted stored blood samples containing freshly drawn platelets (4 x 10^8 per mL). Stored RBC samples were added to platelets so that the final sample contained 45% RBCs and platelets at a concentration of 4 x 10^8 platelets mL^{-1}. Samples were then loaded into syringes and flowed over 3D printed devices containing a confluent endothelial layer at 30 µL·min^{-1} for 20 minutes. Devices were then incubated at 37 °C for 20 min and gently rinsed in PBS to remove any non-adherent cells. Afterwards, the stenosed region of devices was aligned over a well on a clear bottom 96 well plate and absorbance from 400-700 nm measured in 5 nm steps so that the percent transmittance could be calculated (A). Interpretation of percent transmittance data. Increasing thrombus coverage on the 3D printed device correlates to a decrease in percent transmittance (B).

Combined RBCs and platelets were flowed over a confluent endothelium at a flow rate of 30 μL·min^{-1} for 20 minutes then incubated for 20 minutes. Following the incubation period devices were submerged in PBS and gently agitated to remove any non-adhered cells. The stenosed region of devices was aligned over a well of a 96 well plate and the absorbance was measured from 400 – 700 nm with 5 nm steps using a plate reader (Molecular Devices, Sunnyvale, CA). Percent transmittance was calculated from the measured absorbance values.

4.7 Results

4.7.1 Flow Rate Study

Figure 4.7 shows the observed thrombus coverage of the stenosis region in the middle of the channel and representative brightfield images of a surrounding wide region with varying applied flow rates.

Flow Rate	5 μL·min^{-1}	10 μL·min^{-1}	20 μL·min^{-1}	25 μL·min^{-1}	30 μL·min^{-1}
Stenosis Region (brightfield)		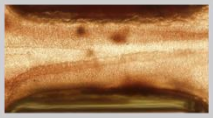	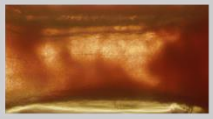	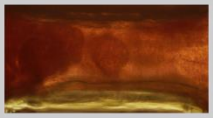	
Wide Region (brightfield)	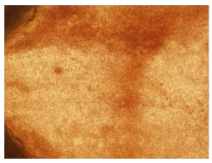	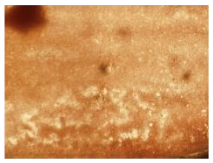	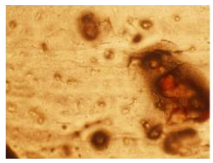	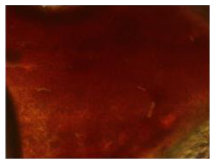	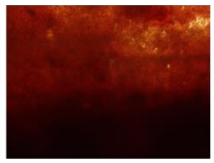
Flow Duration	30 min	30 min	25 min	20 min	20 min
Shear Rate	1.66 sec^{-1}	3.32 sec^{-1}	6.63 sec^{-1}	8.29 sec^{-1}	9.95 sec^{-1}
Shear Stress	0.166 dyn·cm^{-2}	0.332 dyn·cm^{-2}	0.663 dyn·cm^{-2}	0.829 dyn·cm^{-2}	0.995 dyn·cm^{-2}

Figure 4.7 Qualitative Evaluation of Flow Rates on the 3D Printed Fluidic Device with accompanying Shear and Stress Rates. Increasing flow rates resulted in higher shear rates and stresses. The effect of which manifested as increased cell coverage in both stenosed and wide regions of the 3D printed devices as confirmed by brightfield imaging on an inverted microscope.

No discernible difference could be seen between 5 and 10 μL·min^{-1} flow rates. In both cases minimal clotting was observed and only a few areas of coagulated blood were observed. Higher flow rates were attempted since minimal clotting was observed at these low flow rates. Increased thrombus coverage and increased incidence of individual clot aggregates were witnessed for 20 μL·min^{-1} flow rates. Near complete stenosis and wide region coverage was observed with a 25 μL·min^{-1} flow rate, and complete occlusion of the stenosis region with a 30 μL·min^{-1} flow rate. Increasing the flow rate resulted in increased thrombus coverage within the fluidic channel as expected since higher shear rates were produced. The Reynold's number for each flow rate was less than 1, indicating a parabolic flow profile from laminar flow. It is of note that the shear rates that were calculated are indicative of blood vessels such as veins (approximately 5 sec^{-1}).[11] Higher shear rates and stresses could be mimicked with this device if the diameter of the channel was made smaller and if higher flow rates were applied. For example halving the diameter to 400 μm would result in a shear rate of 132 sec^{-1} for a 50 μL·min^{-1} flow rate. In order to achieve such a small channel diameter, multiple coatings of PDMS would need to be applied, and while it is possible to do so, the optical clarity of the device suffers with repeated coatings. Unless utilizing a 3D printer with higher resolution capabilities, making it possible to print channels with smaller dimensions, the present device is limited to mimicking larger resistance vessels.

4.7.2 Evaluating Thrombus Formation on the Fluidic Device with Whole Blood

Unlike conventional transmittance data used to correlate platelet activity, where the percent transmittance increases with increasing platelet aggregation, the methodology followed for thrombus evaluation on the 3D printed devices outlined here correlates to a decrease in transmittance with an increase in thrombus coverage on the device. The main

difference being that the sample used for these studies was whole blood so with increased coverage, decreased light transmittance was expected. Figure 4.8 shows the percent transmittance and absorbance value at 540 nm when the final 3D printed devices (introduced in Chapter 3) had cultured endothelial cells on the channels in the absence of blood, and after flowing 10 USP heparinized whole blood over a cultured endothelium.

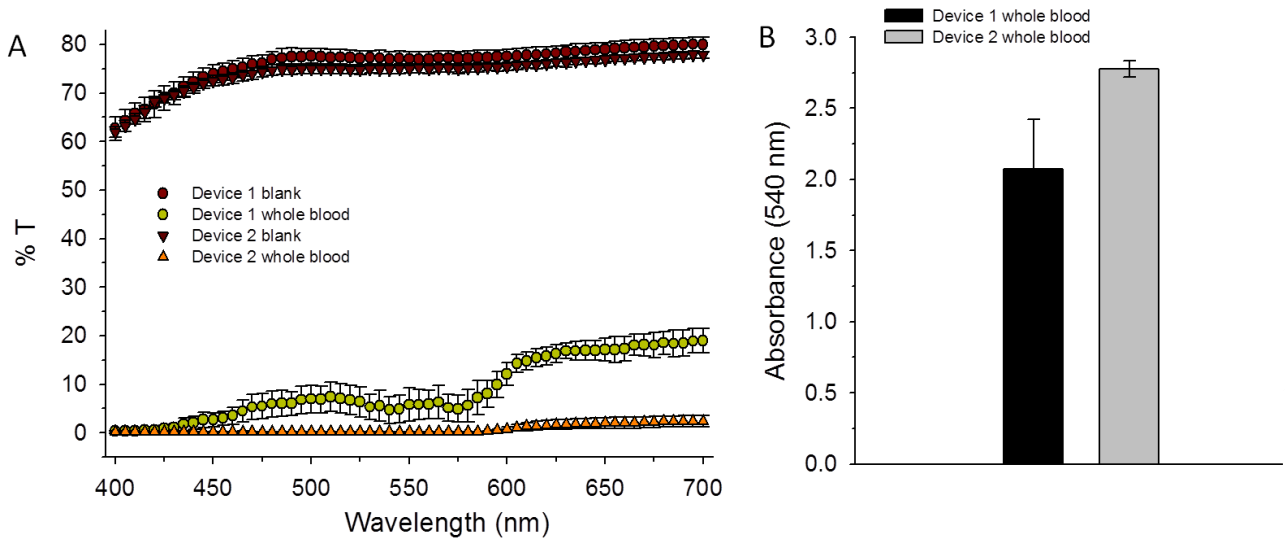

Figure 4.8 Evaluating thrombus coverage on 3D printed devices using percent transmittance (%T) and absorbance measurements for hemoglobin at 540 nm. Percent transmittance values measured with only a cultured endothelium and in the absence of whole blood for device 1 (red circles) and device 2 (red triangles), and percent transmittance values after flowing whole blood over an endothelium at 30 $\mu L \cdot min^{-1}$ for 20 minutes for device 1 (green circle) and device 2 (orange triangle) (A). Absorbance measurements for device 1 (black bar) and 2 (gray bar) at 540 nm after flowing whole blood over a confluent endothelium (B). Data represent mean ± standard error of the mean, $n \geq 3$.

Absorbance measurements (converted to percent transmittance, Figure 4.8 B) were acquired in the presence of a confluent endothelium and compared to when blood was present. The absorbance value at 540 nm was selected to show a comparison between hemoglobin absorbance on the two devices (Figure 4.8 B). The scanned range between 400-700 nm was chosen because Vero Clear material absorbs strongly between 200 – 400 nm (as shown in Chapter 3), and hemoglobin absorbs strongly between 300-600 nm, with the highest molar extinction coefficient coinciding with 390 nm followed by 542 nm.[77,78,79] This in part explains the decrease in transmittance observed over the range scanned in the presence of whole blood for both devices. The transmittance through the devices with only the cultured endothelium present, were similar to the transmittance measurements of Vero Clear material reported in Chapter 3.

4.7.3 Determining Hemolysis of Stored RBCs

RBC hemolysis leads to an emptying of intracellular stores of ATP, making further use of lysed RBCs ineffective when evaluating thrombus formation. To ensure stored RBCs had not exceeded lysis limitations set by the FDA, hemolysis of stored RBCs was determined the same day RBCs were used for thrombus formation studies. Figure 4.9 shows the hemolysis percentage of stored blood samples through twenty one days of storage for RBCs stored in AS-1N and AS-1.

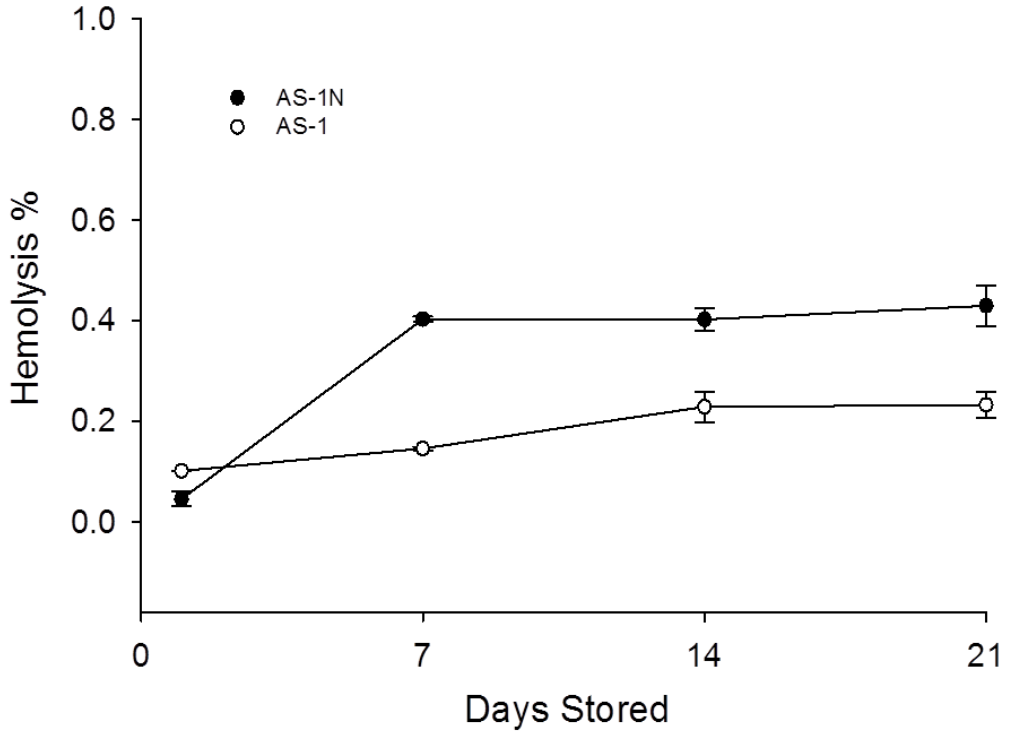

Figure 4.9 Lysis percentage of RBCs stored in CPD-N/AS-1N (black circles) and CPD/AS-1(white circles). CPD-N/AS-1N stored RBCs were periodically fed with glucose to maintain a normoglycemic glucose level. Both storage solutions successfully maintained lysis levels below the 1% FDA recommended threshold. Data represent mean ± standard error of the mean, n=4.

As observed in Figure 4.9, hemolysis of the stored RBCs was maintained below the 1% threshold required by the FDA for stored blood samples through the 3 week storage period.[24] RBCs stored in AS-1N storage solution exhibited increased lysis compared to AS-1 stored RBCs. This increased lysis may be due to agitation of the AS-1N stored RBCs when storage bags were opened and RBCs mixed during weekly glucose feedings. This study ensured that viable RBCs were used in thrombosis formation studies.

4.7.4 Evaluating Thrombus Formation Using Stored RBCs

Figure 4.10 shows percent transmittance data correlating to cell adherence on 3D printed devices with endothelial cells lining the channels when stored RBCs (day 1, 7, 14, and 21) were reconstituted with a physiologically relevant number of freshly drawn platelets as per the protocol outlined in Figure 4.6.

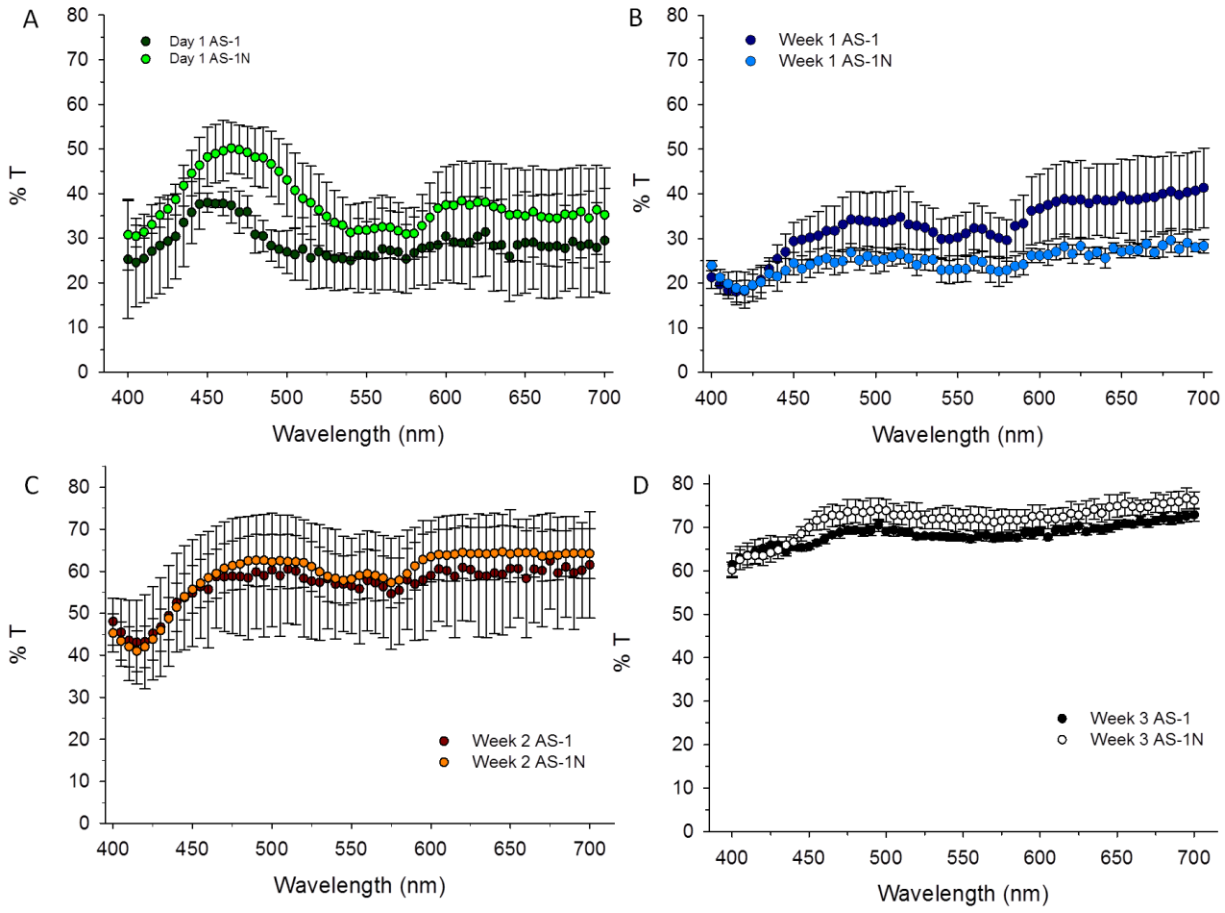

Figure 4.10 Percent Transmittance values relating to thrombus coverage on 3D printed devices when RBCs stored in AS-1N or AS-1 were reconstituted with freshly drawn platelets. Increasing percent transmittance indicative of decreasing cell coverage was observed with increasing storage duration for both AS-1 and AS-1N stored RBCs. Data represent mean ± standard error of the mean, n ≥ 3.

As seen in Figure 4.10, the degree of cell adherence on the fluidic devices decreased with increasing storage durations for RBCs stored in both AS-1N and AS-1.

To further evaluate cell adherence, hemoglobin absorbance at 540 nm was measured throughout the storage period as this wavelength corresponds to a peak in hemoglobin absorption. Experimental conditions shown in Figure 4.6 were followed. Figure 4.11 shows absorbance measurements at 540 nm after flowing stored blood samples over a confluent endothelium on a 3D printed device.

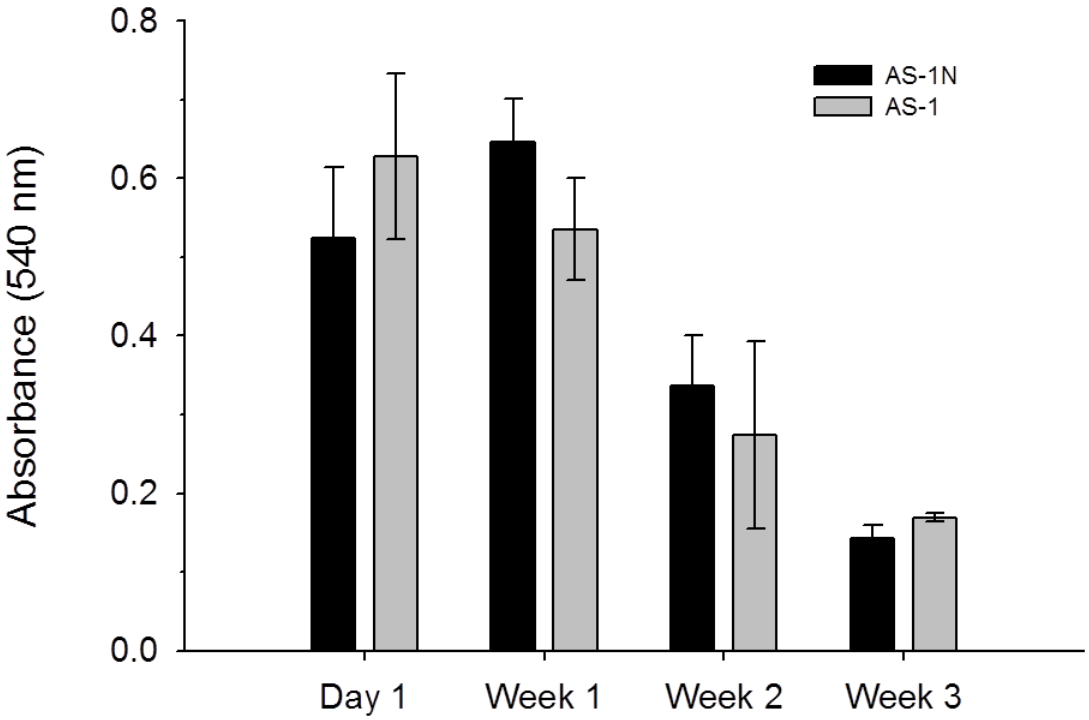

Figure 4.11 Absorbance of hemoglobin at 540 nm for reconstituted stored blood samples. Absorbance values for AS-1 and AS-1N stored RBC samples were statistically equivalent for equivalent storage periods. Day 1: $p = 0.493$, n = 3; week 1: $p = 0.257$, n = 3; week 2: $p = 0.672$, n = 3; week 3: $p = 0.184$, n = 4. Significant decreases in absorbance at 540 nm were seen for Day 1 AS-1N and AS-1 samples compared to their respective week 3 storage solutions (AS-1N: $p = 0.005$, $n \geq 3$; AS-1: $p < 0.003$, $n \geq 3$). Data represent mean ± standard error of the mean.

Within the same storage period, AS-1N and AS-1 stored RBCs samples showed no significant difference in hemoglobin absorption indicative of cell adherence. However, a

significant decrease in cell adherence between day 1 and week 3 in AS-1N and AS-1 samples was observed.

4.8 Discussion

In vitro studies probing cell-to-cell and cell-to-substrate interactions, such as platelet adhesion to an endothelium, typically rely on static incubations of the two components. After washing away any non-adherent cells, adhesion can be measured. While this methodology has proven useful in gleaning information on optimal conditions for cell adhesion processes, it neglects the impact fluid flow has on these complex biological processes.[62] The protocol outlined in this chapter for evaluating thrombus formation incorporates flow conditions as observed in resistance vessels. Specifically, shear rates of larger blood vessels such as veins were recreated.

The methodology described in this chapter was successful in showing a decrease in light transmitted through the device as an effect of increasing thrombus coverage when the sample was whole blood (Figure 4.8). Measurement of thrombus formation using whole blood is a major advancement in the area of *in vitro* thrombus formation, as many platforms require diluted whole blood or purified platelet solutions.[67] Studies involving the flow of whole blood often require diluted samples with decreased hematocrit to prevent clogging in tubing used for sample delivery.[8,80,81] Yet the channel dimensions of the 3D printed fluidic devices utilized in these studies were sufficiently sized to allow for high enough flow rates to be implemented, recreating physiological flow conditions without channel clogging. It was only when samples were platelets mixed with stored RBCs that a decrease in thrombus coverage was observed (Figures 4.10 and 4.11).

ATP release from hyperglycemic (AS-1) stored RBCs is significantly less than from RBCs stored in normoglycemic conditions (AS-1N) and progressively decreases over the storage period (evaluated through 36 days).[7] Specifically, control RBCs release 300 nM ATP (7% hematocrit), but stored RBCs release less than half that amount, even after only one day of storage.[7,43] We hypothesized that this decreased ATP release would hamper platelet activation through the ATP gated P2X1 receptor on the platelet surface and decrease cell adherence or thrombus coverage with increasing storage durations for RBCs stored in AS-1. As expected, a progressive decrease in cell adhesion for AS-1 stored RBCs was observed (Figures 4.10 and 4.11), however RBCs stored in normoglycemic levels (AS-1N), that were periodically fed with glucose to maintain a 5 mM glucose storage level, release normal amounts of ATP. Therefore, increased cell coverage was expected to be seen with AS-1N stored samples compared to AS-1 samples but comparable coverage was observed for both storage conditions.

The half maximal effective concentration (EC_{50}) of ATP for P2X1 is around 1 μM, and less than 100 nM of ATP may evoke a Ca^{2+} influx into platelets through P2X1 purinergic receptors on the platelet surface within several seconds.[82] The Tygon tubing utilized in these studies can elicit RBC derived ATP release via mechanical deformation of the RBC,[43] therefore physiologically necessary levels of ATP should have been present in AS-1N stored samples considering RBCs were adjusted to a 45% hematocrit. The inability to observe this hypothesized trend (decreased cell adherence for AS-1 stored RBC containing solutions and increased adherence for AS-1N stored RBC containing samples in comparison) may indicate a fault of this particular method to evaluate thrombus coverage when reconstituted blood samples in lieu of whole blood samples are utilized. While occlusive

blood clots *in vivo* are primarily composed of RBCs due to their higher prevalence in the bloodstream,[83] and monitoring RBCs through hemoglobin is physiologically relevant, the reconstituted samples did not result in an occluded channel even before rinsing away non adherent cells and the protocol used was not suited for identifying individual adhered cells.

Additionally, it was expected that decreased ATP release from the RBC would result in a lowered amount of NO production from the endothelial cells lining the fluidic channel as well as from flowing platelets (Figure 4.2). When activated, platelets can release up to 5 x 10^{-17} mol NO per platelet (through NOS), and this NO inhibits the extent of platelet aggregation compared to activated platelets unable to release NO.[84] NO inhibits platelet activation and aggregation in three ways. First, it results in activation of sGC leading to an increase in intracellular cGMP which enhances refilling of intracellular Ca^{2+} stores thereby inhibiting platelet shape change through myosin light chain kinase activation and the release of platelet activation agonists stored in α and dense granules. Second, the decreased intracellular Ca^{2+} level suppresses conformational changes of GPIIb/IIIa (binds to vWF on endothelial cell surface and fibrin between activated platelets) to its active form and suppresses the expression of P-selectin, an adhesion molecule found on activated endothelial cells and platelets. Third, NO inhibits enzyme conversion of arachidonic acid found in the platelet lipid membrane to thromboxane A2 (increases GPIIb/IIIa expression).[85,86,84] A decrease in NO production from endothelial cells and platelets themselves would be expected to result in less inhibition of platelet activation and aggregation, however in these studies NO release was not probed but represents an area of future study. As seen in Figure 4.9, even though lysis levels of AS-1N stored RBC samples were well below the FDA limit of 1% before being mixed with platelets, they were still

elevated compared to AS-1 stored RBCs. It is possible that increased lysis resulted in elevated ATP presence, and thus more NO production from the endothelium that was employed as a substrate for these studies. In this case, the platelets were likely activated and forming aggregates, but were inhibited from adhering to the endothelium.

During platelet isolation from freshly drawn whole blood, every effort was made to prevent platelet activation via agitation by carefully performing centrifugation and isolation steps. Any platelets that had activated during handling resulting in observable aggregation were not used in thrombus evaluation studies. However, in most cases some platelet aggregates were observed in the purified platelet solutions, meaning that some portion of platelets had already released intracellular stores of pro-thrombotic molecules and were therefore less able to initiate thrombus formation. Though these samples were only used if a majority of the cells remained in suspension as visually confirmed. Means of improving platelet handling to ensure platelets do not become desensitized include adding chemicals that prevent platelet activation. However, this methodology would require adding an agonist to initiate platelet activation before mixing with stored blood, and was avoided to keep platelet treatment to a minimum.

Purified platelets were reconstituted in plasma prior to mixing with stored RBCs to ensure that plasma proteins necessary for the coagulation cascade to progress were present. Yet, in order to maintain a 45% hematocrit, the volume of plasma for each sample was not maintained constant. Furthermore, after the incubation period non-adherent cells were manually rinsed away from the channel. This process involved submerging the devices into PBS and gently agitating. While efforts were made to maintain consistency between different experiments, the manual nature of the rinsing step may have led to an

increased number of weakly adhered cells being dislodged from the device. The rigidity of the 3D printed material was ideal for having rugged and reusable devices, but the inherent inelasticity would fail to allow a mimic of vessel dilation and incorporation of smooth muscle cells. Furthermore, the manner in which blood was introduced to the device was via a syringe pump providing a continuous pressure and flow rate. A better means of mimicking the pulsating nature of blood flow would be to implement a peristaltic pump or a variable pressure pump that could account for increasing pressures due to thrombus formation.

Since the hypothesized results for thrombus coverage comparing AS-1N and AS-1 stored RBCs were not observed, additional tests are warranted to ensure repeatability of results reported here. To better mimic a transfusion, the protocol for thrombus evaluation could be applied to whole blood (drawn into non-heparinized tubes) mixed with stored RBC samples. This would ensure a physiological level of plasma proteins and platelets were present, and would forego the need for platelet handling so that unwanted activation does not occur. Specifically, this transfusion mimic could be used to compare cell adhesion between AS-1 and AS-1N stored RBCs in the presence of an uninjured endothelium, the extra cellular matrix, or after an injury to the endothelium. Additionally, cell specific fluorescent probes should be employed to identify individual cell type involvement in the formed thrombus.

REFERENCES

REFERENCES

(1) Nieswandt, B.; Watson, S. P. *Blood* **2003**, *102*, 449-461.

(2) Wright, H. P.; Thompson, R. H.; Zilkha, K. J. *Lancet* **1965**, *2*, 1109-1110.

(3) Ataga, K. I.; Orringer, E. P. *The American Journal of Medicine* **2003**, *115*, 721-728.

(4) O'Sullivan, B. P.; Linden, M. D.; Frelinger, A. L.; Barnard, M. R.; Spencer-Manzon, M.; Morris, J. E.; Salem, R. O.; Laposata, M.; Michelson, A. D. *Blood* **2005**, *12*, 4635-4641.

(5) Somova, L.; Mufunda, J. *Clinical and Experimental Hypertension* **1993**, *15*, 781-796.

(6) Tchoepe, D.; Roesen, P.; Esser, J.; Schwippert, B.; Nieuwenhuis, H. K.; Kehrel, B.; Gries, F. A. *Seminars in Thrombosis and Hemostasis* **1991**, *17*, 433-438.

(7) Wang, Y.; Giebink, A.; Spence, D. M. *Integrative Biology* **2014**, *6*, 65-75.

(8) Sprague, R. S.; Ellsworth, M. L.; Stephenson, A. H. *American Journal of Physiology* **1996**, *271*, 2717-2722.

(9) Sprague, R. S.; Olearczyk, J. J.; Spence, D. M.; Stephenson, A. H.; Sprung, R. W.; Lonigro, A. J. *American Journal of Physiology Heart and Circulatory Physiology* **2003**, *285*, H693-700.

(10) Li, M.; Ku, D. N.; Forest, C. R. *Lab Chip* **2012**, *12*, 1355-1362.

(11) Papaioannou, T. G.; Stefanadis, C. *Hellenic Journal of Cardiology* **2005**, *46*, 9-15.

(12) Lemmens, H. J. M.; Bernstein, D. P.; Brodsky, J. B. *Obesity Surgery* **2006**, *16*, 773-776.

(13) Singbartl, K.; Innerhofer, P.; Radvan, J.; Westphalen, B.; Fries, D.; Stogbauer, R.; Van Aken, H. *Anesthesia & Analgesia* **2003**, *96*, 929-935.

(14) Ditzel, J.; Kampmann, J. *Acta Physiologica* **1971**, *81*, 264-268.

(15) Barbee, J. H.; Cokelet, G. R. *Microvascular Research* **1971**, *3*, 6-16.

(16) Mchedlishvili, G.; Varazashvili, M. *Journal of Cerebral Blood Flow and Metabolism* **1987**, *7*, 739-744.

(17) Lindeboom, G. A. *Journal of the History of Medicine and Allied Sciences* **1954**, *9*, 455-459.

(18) Greenwalt, T. J. *Transfusion* **2003**, *37*, 550-563.

(19) Harmening, D. M. *Modern Blood Banking & Transfusion Practices*, 6 ed.; F.A. Davis Philadelphia, PA, 2012.

(20) Sparrow, R. L. *Blood Transfusion* **2012**, *10*, s7-s11.

(21) Hess, J. R. *Vox Sanguinis* **2006**, *91*, 13-19.

(22) Levine, M.; Oxender, D. L.; Stein, W. D. *Diochimica et Biophysica Acta (BBA) - Biophysics including Photosyntesis* **1965**, *109*, 151-163.

(23) van Wijk, R.; van Solinge, W. W. *Blood* **2005**, *106*, 4034-4042.

(24) Dumont, L. J.; AuBuchon, J. P. *Transfusion* **2008**, *48*, 1053-1060.

(25) Hod, E. A.; Zhang, N.; Sokol, S. A.; Wojczy, B. S.; Francis, R. O.; Ansaldi, D.; Francis, K. P.; Della-Latta, P.; Whittier, S.; Sheth, S.; Hendrickson, J. E.; Simring, J. C.; Brittenham, G. M.; Spitalnik, S. L. *Blood* **2010**, *115*, 4284-4292.

(26) Roback, J.; Combs, M.; Grossman, B.; Hillyer, C. *Technical Manual*, 16 ed.; American Association of Blood Banks: Bethesda, MD, 2009.

(27) Seifried, E.; Klueter, H.; Weidmann, C.; Staudenmaier, T.; Schrezenmeier, H.; Henschler, R.; Greinacher, A.; Mueller, M. M. *Vox Sanguinis* **2011**, *100*, 10-21.

(28) American Red Cross. *Blood facts and statistics.* http://www.redcrossblood.org (accessed October 30, 2015).

(29) Gilcher, R. O.; McCombs, S. *Current Opinion in Hematology* **2005**, *12*, 503-508.

(30) Garratty, G. *Vox Sanguinis* **2008**, *94*, 87-95.

(31) Timmins, N. E.; Nielsen, L. K. *Trends in Biotechnology* **2009**, *27*, 415-422.

(32) Kim, H. W.; Greenburg, A. G. *Artificial Organs* **2004**, *28*, 813-828.

(33) Kim-Shapiro, D. B.; Lee, J.; Gladwin, M. T. *Transfusion* **2011**, *51*, 844-851.

(34) Hess, J. R. *Transfusion and Apheresis Science* **2010**, *43*, 51-59.

(35) Olearczyk, J. J.; Stephenson, A. H.; Lonigro, A. J.; Sprague, R. S. *American Journal of Physiology Heart and Circulatory Physiology* **2004**, *286*, 940-945.

(36) Sprague, R. S.; Ellsworth, M. L. *Microcirculation* **2012**, *19*, 430-439.

(37) Sridharan, M.; Adderley, S. P.; Bowles, E. A.; Egan, T. M.; Stephenson, A. H.; Ellsworth, M. L.; Sprague, R. S. *American Journal of Physiology Heart and Circulatory Physiology* **2010**, *299*, 1146-1152.

(38) Sprague, R. S.; Stephenson, A. H.; Bowles, E.; Stumpf, M.; Ricketts, G.; Lonigro, A. *Hypoxia and Exercise* **2006**, 207-216.

(39) Villar, I. C.; Francis, S.; Webb, A.; Hobbs, A. J.; Ahluwalia, A. *Kidney International* **2006**, *70*, 840-853.

(40) Walford, G.; Loscalzo, J. *Journal of Thrombosis and Haemostasis* **2003**, *10*, 2112-2118.

(41) Dietrich, H. H.; Ellsworth, M. L.; Sprague, R. S.; Dacey, R. G., Jr. *American Journal of Physiology Heart and Circulatory Physiolology* **2000**, *278*, H1294-8.

(42) Engelgau, M. M.; KNarayan, K. M.; Herman, W. H. *Diabetes Care* **2000**, *23*, 1563-1580.

(43) Chen, C.; Wang, Y.; Lockwood, S. Y.; Spence, D. M. *Analyst* **2014**, *139*, 3219-3226.

(44) Sprague, R. S.; Ellsworth, M. L.; Stephenson, A. H.; Kleinhenz, M. E.; Lonigro, A. J. *American Journal of Physiology* **1998**, *275*, H1726-32.

(45) Wang, D.; Sun, J.; Solomon, S. B.; Klein, H. G.; Natanson, C. *Transfusion* **2012**, *52*, 1184-1195.

(46) Tinmouth, A.; Fergusson, D.; Yee, I. C. *Transfusion* **2006**, *46*, 2014-2027.

(47) Roback, J. D. *Hematology* **2011**, *2011*, 475-479.

(48) Roback, J. D.; Neuman, R. B.; Quyyumi, A.; Sutliff, R. *Transfusion* **2011**, *51*, 859-866.

(49) Yomtovian, R. A.; Palavecino, E. L.; Dysktra, A. H.; Downes, K. A.; Morrissey, A. M.; Bajakzouzian, S.; Pokorny, M. A.; Lazarus, H. M.; Jacobs, M. R. *Transfusion* **2006**, *46*, 719-730.

(50) Eder, A. F.; Kennedy, J. M.; Dy, B. A.; Notari, E. P.; Weiss, J. W.; Fang, C. T.; Wagner, S.; Dodd, R. Y.; Benjamin, R. J. *Transfusion* **2007**, *47*, 1134-1142.

(51) Zhu, H.; Zennadi, R.; Xu, B. X.; Eu, J. P.; Torok, J. A.; Telen, M. J.; McMahon, T. J. *Critical Care Medicine* **2011**, *39*, 2478-2486.

(52) Wan, J.; Ristenpart, W. D.; Stone, H. A. *PNAS* **2008**, *105*, 16432-7.

(53) Ku, C.; Karunarathne, W.; Kenyon, S.; Root, P.; D., S. *Analytical Chemistry* **2007**, *79*, 2421-2426.

(54) Valles, J.; Santos, M. T.; Aznar, J.; Marcus, A. J.; Martinez-Sales, V.; Portoles, M.; Broekman, M. J.; Safier, L. B. *Blood* **1991**, *78*, 154-162.

(55) Harrison, P. *Blood Reviews* **2005**, *19*, 111-123.

(56) Kotsis, D. H.; Spence, D. M. *Anal Chem* **2003**, *75*, 145-151; Morrel, C. N.; Matsushita, K.; Chiles, K.; Scharpf, R. B.; Yamakuchi, M.; Mason, R. J. A.; Bergmeier, W.; Mankowski, J. L.; Baldwin III, W. M.; Faraday, N.; Lowenstein, C. J. *PNAS* **2005**, *102*, 3782-3787.

(57) Busse, R.; Lackhoff, A.; Bassenge, E. *Naunyn-Schmiedeberg's Archives of Pharmacology* **1987**, *336*, 566-571.

(58) Lawrence, M. B.; McIntire, L. V.; Eskin, S. G. *Blood* **1987**, *70*.

(59) Sprague, E. A.; Steinbach, B. L.; Nerem, R. M.; Schwartz, C. J. *Circulation* **1987**, *76*, 648-656.

(60) Neeves, K. B.; Onasoga, A. A.; Wufsus, A. R. *Current Opinion In Hematology* **2013**, *20*, 417-423.

(61) Chang, K.; Tees, D. F. J.; Hammer, D. A. *PNAS* **2000**, *97*, 11262-11267.

(62) Prabhakarpandian, B.; Shen, M.; Pant, K.; Kiani, M. F. *Microvascular Research* **2011**, *82*, 210-220.

(63) Tovar-Lopez, F. J.; Rosengarten, G.; Westein, E.; Khoshmanesh, K.; Jackson, S.; Mitchell, A.; Nesbitt, W. S. *Lab Chip* **2010**, *10*, 291-302.

(64) Ku, C.; Oblack, T.; Spence, D. *Analytical Chemistry* **2008**, *80*, 7543-7548.

(65) Philipose, S.; Konya, V.; Sreckovic, I.; Marsche, G.; Lippe, I. T.; Peskar, B. A.; Heinemann, A.; Schuligoi, R. *Arteriosclerosis, Thrombosis, and Vascular Biology* **2010**, *30*, 2416-2423.

(66) Gutierrez, E.; Petrich, B. G.; Shattil, S. J.; Ginsberg, M. H.; Groisman, A.; Kasirer-Friede, A. *Lab Chip* **2010**, *8*, 1486-1495.

(67) Westein, E.; de Witt, S.; Lamers, M.; Cosemans, J.; Heemskerk, J. *Platelets* **2012**, *23*, 501-509.

(68) Rivard, G. E.; Brummel-Ziedins, K. E.; Mann, K. G.; Fan, L.; Hofer, A.; Cohen, E. *Journal of Thrombosis and Haemostasis* **2005**, *3*, 2039-2043.

(69) Gutierrez, E.; Groisman, A. *Analytical Chemistry* **2007**, *79*, 2249-2258.

(70) Young, E. W. K.; Simmons, C. A. *Lab Chip* **2010**, *10*, 143-160.

(71) Li, M.; Hotaling, N. A.; Ku, D. N.; Forest, C. R. *Plosone* **2014**, *9*, e82493.

(72) Savage, B.; Ginsberg, M. H.; Ruggeri, Z. M. *Blood* **1999**, *94*, 2704-2715.

(73) Heemskerk, J. W. M.; Sakariassen, K. S.; Zwaginga, K. S.; Brass, L. F.; Jackson, S. P.; Farndale, R. W. *Journal of Thrombosis and Haemostasis* **2011**, *9*, 856-858.

(74) Fransisco, J. T.; Rosengarten, G.; Westein, E.; Khoshmanesh, K.; Jackson, S. P.; Mitchell, A.; Nesbitt, W. S. *Lab Chip* **2009**, *10*, 291-302.

(75) Peter, R. H. *Ultrasound in Medicine & Biology* **2007**, *33*, 1527-1539.

(76) Hirsh, J.; Anand, S. S.; Halperin, J. L.; Fuster, V. *Arteriosclerosis, Thrombosis, and Vascular Biology* **2001**, *103*, 2994-3018.

(77) Robles, F. E.; Chowdhury, S.; Wax, A. *Biomedical Optics Express* **2010**, *1*, 310-317.

(78) Raththagala, M.; Root, P. D.; Spence, D. M. *Analytical Chemistry* **2006**, *78*, 8556-8560.

(79) Vo-Dinh, T. *Biomedical Photonics Handbook: Biomedical Diagnostics*; CRC press, 2014; Vol. 2.

(80) Halpin, S. T.; Spence, D. M. *Analytical Chemistry* **2010**, *82*, 7492-7497.

(81) Erkal, J. L.; Selimovic, A.; Gross, B. C.; Lockwood, S. Y.; Walton, E. L.; McNamara, S.; Martin, R. S.; Spence, D. M. *Lab Chip* **2014**, *14*, 2023-2032.

(82) Mahaut-Smith, M. P.; Jones, S.; Evans, R. J. *Purinergic Signalling* **2011**, *7*, 341-356.

(83) Davies, M. J. *Criculation* **1996**, *94*, 2013-2020.

(84) Freedman, J. E.; Loscalzo, J.; Barnard, M. R.; Alpert, C.; Keaney, J. F.; Michelson, A. D. *Journal of Clinical Investigation* **1997**, *100*, 350-356.

(85) Wang, G.; Zhu, Y.; Halushka, P. V.; Lincoln, T. M.; Mendelsohn, M. E. *PNAS* **1998**, *95*, 4888-4893.

(86) Mellion, B. T.; Ignarro, L. J.; Ohlstein, E. H.; Pontecorvo, E. G.; Hyman, A. L.; Kadowitz, P. J. *Blood* **1981**, *57*, 946-955.

CHAPTER 5

CONCLUSIONS AND FUTURE DIRECTIONS

5.1 Errant Platelet Function

The main function of platelets is to regulate blood flow via vessel repair in the event of an injury to arrest blood loss. This is achieved through platelet activation via interaction with components of the sub-endothelium and through exposure to agonists, released from RBCs or endothelial cells, that act on purinergic receptors (P2Y12 and P2X1) on the platelet surface. The activated platelet goes from a spherical 2-4 μm in diameter cell, to one with filopodial membrane extensions allowing it to better adhere to other platelets and the site of injury.[1,2,3,4]

For a number of diseases, including diabetes, cystic fibrosis, multiple sclerosis, sickle cell anemia, and hypertension, platelets are hyperactive and are more easily activated by agonists.[5,6,7,8,9] RBCs from individuals with multiple sclerosis[9,10] and sickle cell anemia[8,11] release higher than normal levels of ATP and those with diabetes[12,13], cystic fibrosis[6,14], and hypertension[7,15] display decreased ATP release. There is also a decrease in RBC-derived ATP release from RBCs stored in hyperglycemic conditions.[16] The Spence group hypothesizes that the lowered ATP release in these stored cells will have detrimental effects for recipients of transfusions not only because of diminished RBC regulation of blood flow through vasodilation, but also because this decreased ATP release could hinder platelet activation. Exploring the extent of thrombus formation and platelet function as it pertains to the above diseases and to stored blood provided the motivation to design and fabricate the microfluidic devices outlined in this dissertation. *In vitro* microfluidic devices comprised of polydimethylsiloxane (PDMS) and polystyrene (PS) offered an ideal platform to model *in vivo* conditions through incorporation of vascular components such as the extra

cellular matrix and endothelium, facilitating interactions of multiple cell types, recreation of flow conditions, and *in vivo* dimensions.[17,18,19,20,21,22] Unique to this device from other thrombosis mimics in the literature was the ability to induce injury on-chip through either chemical or electrical lysis.

5.2 Cell Lysis on Microfluidic Devices Using Chemical Lysis Techniques

Chapter 2 introduced devices that rely on chemical lysis techniques. Initially microfluidic devices were fabricated using either PDMS or a combination of PDMS and PS as these materials were amenable to replica molding fabrication techniques. PDMS offers a gas permeable material that supports cell culture and could be fabricated using soft lithography. PS was also shown to support cell adhesion and facilitated the embedding of electrodes for cell lysis. PDMS based devices fabricated for chemical lysis via radical generation from irradiation of a photochemical dye showed promise as injury mimics, but the injury to the cells could best be described as cell deformation rather than lysis. Failure to remove the cells after irradiation resulted in studies relying on platelet adherence to a damaged endothelium without exposure of collagen. Of all the iterations of thrombosis mimics attempted, these were the easiest on which to visualize cells. This technique was inherently amendable to selective and localized cell damage, but devices were not reusable and channel seals often failed causing leakage. Also, the steps needed to achieve lysis were tedious, and specificity in lysing cells in a desired region was lacking due to the distance of the laser from the device.

Further attempts at chemical lysis of cells utilized a device with a PS base containing embedded electrodes positioned under a channel engrained in PDMS. The channel was designed to allow electrochemically generated hydroxide to diffuse to a channel

intersection. Lysis was often difficult to isolate to the desired region, even with the incorporation of polycarbonate membranes to control the diffusion of hydroxide on the device. An advantage of this design was that the PS base was reusable, and after discarding the PDMS component the electrodes could be easily accessed and polished for continued use. Unlike the device made solely from PDMS, imaging on these devices was limited to a macroscope as cells could not be visualized through the PS using an inverted microscope. However, an improvement with this platform was that cell lysis occurred using these PDMS-PS devices rather than cell deformation.

5.3 3D Printed Devices Featuring Removable Electrodes for Electrical Lysis

3D printing the thrombosis mimic streamlined the fabrication process and offered an easier means of integrating electrodes and interfacing with sample delivery systems. Minute changes to the design were easily achieved through alterations of the CAD file as opposed to remaking a master for replica molding using photolithography. 3D printing completely removes the user from the actual fabrication of the device, limiting possible human error. The finished devices were durable and able to be reused for months at a time. Integrating threaded inlets and electrode ports meant that commercial fittings could be used to house electrodes and interface the device with syringe pumps. This increased the versatility of the device and ensured that various modules (sample delivery, electrodes, or the device itself) could be individually addressed.

Initial attempts at culturing endothelial cells on Vero Clear material were performed on slabs so that cells were not enclosed in a channel. This was done to validate cell visibility and confirm adhesion to the proprietary material. The cells adhered and survived on the slabs for 48 hours, but failed to do so once they were immobilized in a 3D printed channel.

Failure of cells to survive may stem from insufficient gas permeability of Vero Clear, but this property of the printed material was not evaluated.

To overcome cell adhesion and survival limitations, numerous surface modifications were attempted. To begin, several different epoxies spanning standard industrial grade to medical grade epoxies used for adhesion of artificial implants were evaluated. Modifications with epoxy were advantageous due to the ease in which channels could be coated, however, all efforts with epoxies failed to support cell adhesion. Only materials that could be cited as supporting cell adhesion were studied moving forward, with an emphasis on PDMS and PS. The preparation and coating process for PS was straightforward and not as time consuming as PDMS. A single PS coating was thinner compared to a single coating of PDMS, and multiple PS coatings were required to achieve a comparable coating to PDMS. PS facilitates better adhesion for certain cell types over PDMS and lacks several issues inherent to PDMS use including partioning of hydrophobic materials into PDMS and leaching of uncured or cross-linked oligomers from bulk PDMS.[23] However, the majority of attempts at culturing an endothelium onto 3D printed channels coated with PS failed. This was likely due to decreased levels of dissolved oxygen present in PS coated channels compared to those coated with PDMS.

Previous efforts by the Spence group to use PDMS as an adhesive for 3D printed device components failed because the PDMS would not cure while in contact with Vero Clear. These studies sought to use cured PDMS to secure transwell culture inserts above device channels, but even after several days in a 75 °C oven, the PDMS would not cure. To evaluate the potential of Vero Clear modified with PDMS to support cell adhesion, slabs of printed material were coated with films of either 5:1, 10:1, or 20:1 bulk PDMS polymer:

curing agent and left at room temperature. Over the course of several days, the 10:1 ratio was the most cured. Simply coating 10:1 uncured PDMS onto the 3D printed channel (either at room temperature or 75 °C) failed to promote curing. Only after optimizing exposure of both the device and uncured PDMS to oxygen plasma did the PDMS cure inside the channel. Endothelial cell immobilization and culture was successful with PDMS modification, and marked the first account of incorporation of cells on a 3D printed platform. The versatility of this technique expands beyond developing a thrombosis mimic, and increases the use of 3D printing for studies relying on cell scaffolding and pattering.

This work also represents the first use of electrodes to electrically lyse adherent cells on a 3D printed platform, as electrical lysis typically finds utility for single cell lysis and analysis. The removable electrodes housed in commercial luer fittings offered an advantage over conventional means of integration with microfluidics as both the platform and electrodes themselves were reusable. The device introduced in Chapter 3 provided more specificity and reproducibility in lysing cells compared to previous design attempts using chemical lysis techniques. Furthermore, because electrical lysis depends on pore formation in the lipid membrane for lysis to commence, introduction of non-native circulation components was avoided and thus a more accurate mimic of the vasculature was achieved.

5.4 3D Printed Thrombosis Mimic

Thrombus coverage or cell adherence on an immobilized endothelium in a channel of a 3D printed device was evaluated by measuring light transmittance through the device introduced in Chapter 3 and by monitoring hemoglobin absorbance at 540 nm. These studies used samples containing hyperglycemic or normoglycemic stored RBCs combined

with platelets. The protocol detailed in Chapter 4 offered a straight forward means of probing thrombus formation under physiologically relevant flow conditions. This simplicity did impose limitations however, as individual cell types involved in the clot could not be evaluated. We hypothesized that samples containing AS-1N stored RBCs would display increased thrombus coverage compared to AS-1 RBCs due to an increased presence of RBC-derived ATP to promote platelet activation. Yet no statistical difference in cell adhesion was found between AS-1N and AS-1 stored RBC samples within equivalent storage periods. There was however, a statistically significant decrease in thrombus coverage between samples of both storage solutions from day 1 to day 21.

Faults in the protocol included unwanted platelet activation during isolation steps, and while no observably aggregated platelets were used for thrombus studies, a portion of the platelets had likely been exposed to pro-thrombotic agonists released from the activated platelets. To ensure that any non-adherent cells were removed from the device prior to measurements, devices were submerged in PBS and gently agitated. While efforts were made to maintain consistency between different devices, the manual nature of this step may have led to an increased number of weakly adhered cells being dislodged from the device.

Additional experiments using this protocol include diluting freshly drawn, non-heparinized whole blood with AS-1N and AS-1 stored RBCs to more accurately mimic a transfusion. This sample preparation would ensure physiologically relevant levels of plasma proteins and platelets without requiring platelet handling, and could be used to measure cell adherence to an endothelium, extracellular matrix proteins, or an injured

endothelium. It would also be prudent to include cell specific fluorescent probes so that individual cell types participating in thrombus formation could be monitored.

5.5 Fluorescence-Based Detection of Platelets

5.5.1 Preparation of Reagents

CD31

Alexa Fluor 594 anti-human CD31 (Ex: 590 nm, Em: 617 nm; Biolegend, San Diego, CA), a fluorescently labeled antibody, was received as a 0.5 $mg \cdot mL^{-1}$ stock solution. The manufacturer-recommended immunofluorescence concentration range was 5-10 $\mu g \cdot mL^{-1}$ so 16 µL of CD31 was added to 984 µL of whole blood for an 8 $\mu g \cdot mL^{-1}$ concentration. Before addition of CD31 to whole blood, the stock vial was spun down as per manufacturer recommendations.

Cell Tracker Green CMFDA

Cell tracker green CMFDA (5-chloromethylfluorescein diacetate ($C_{25}H_{17}ClO_7$); MW: 464.9 $g \cdot mol^{-1}$; Ex: 492 nm, Em: 517 nm; Invitrogen, Waltham, MA) was dissolved in 20 µL of anhydrous dimethylsulfoxide (DMSO) to a final concentration of 5.4 mM. The stock solution was diluted into a final working concentration of 10.8 µM when 2 µL of the stock solution was added to a total volume of 1 mL of purified platelet suspensions or whole blood.

Cell Tracker Red CMTPX

Cell tracker red CMTPX ($C_{42}H_{40}ClN_3O_4$; MW: 686.3 $g \cdot mol^{-1}$; Ex: 577 nm, Em: 602 nm; Invitrogen, Waltham, MA) was prepared in a similar fashion to cell tracker green. The provided 50 µg of powder was dissolved in 20 µL of anhydrous dimethylsulfoxide (DMSO) to give a final stock concentration of 3.6 mM. Working solutions of 7.2 µM were made by

adding 2 µL from stock solutions to form a total volume of 1 mL purified platelet or whole blood.

5.5.2 Collection and Preparation of Whole Blood

Whole blood was collected via venipuncture into heparinized (standard 157 USP) vacutainer tubes from consenting donors and used the same day for experiments. Handling of the whole blood was kept to a minimum aside from loading into syringes for delivery to the 3D printed device to avoid unwanted activation of platelets.

5.5.3 Collection and Purification of Platelets from Whole Blood

Whole blood was collected via venipuncture into heparinized vacutainer tubes (157 USP) from consenting donors and used the same day as experiments. Samples were centrifuged at 100*g* for 15 minutes to ensure that platelets would remain in the plasma instead of the buffy coat, making isolation easier. For studies relying on the use of platelets in platelet rich plasma (PRP), the PRP was separated from packed RBCs. For studies requiring purified platelets, the PRP was carefully removed and 1 mL of acid citrate dextrose (ACD) was added for every 9 mL of isolated PRP. Then the PRP was spun at 1500*g* for 12 minutes. This resulted in a platelet pellet at the bottom of the centrifuge tube with platelet poor plasma (PPP) in the supernatant. PPP was removed and discarded and 1 mL of a 10% ACD solution was used to put platelets into solution, avoiding any RBCs. Reconstituted platelets were spun down at 1500*g* for 12 min and washed twice.

5.5.4 Towards Fluorescence Detection of Platelets in a Formed Thrombus

To identify platelets in a formed thrombus, platelets adhered to collagen were imaged in brightfield and various cell stains were attempted to visually isolate platelets in whole blood. Figure 5.1 displays platelet adherence to collagen on the 3D printed devices

as purified platelet solutions or as platelet rich plasma. The cell trackers used (green and red) are permeable to the cell membrane, but once inside are transformed into cell-impermeant products by esterases as seen in Figure 5.2 (for CMFDA), and display cytosplasmic staining. Cell tracker green contains a chloromethyl group that reacts with thiol groups on intracellular glutathione.

Cell tracker red also contains a chloromethyl group that reacts with thiols, likely in a glutathione S-transferase-mediated reaction.[24] Fluorescence is retained in the cell through several generations, transferred to daughter cells, and labeled cells can retain fluorescence for up to three days. Platelets were purified following protocols outlined in Chapter 4, and incubated with either cell tracker green or red for 45 minutes. After this time cells were centrifuged and excess cell tracker discarded from the supernatant. The washing process was performed three times in PBS to ensure removal of excess stain. Labeled platelets were imaged using an Olympus IX71 inverted microscope (Olympus America, Melville, NY) with an electrothermally cooled charge-coupled device camera (Orca, Hamamatsu) and Microsuite software (Olympus America, Melville, NY).

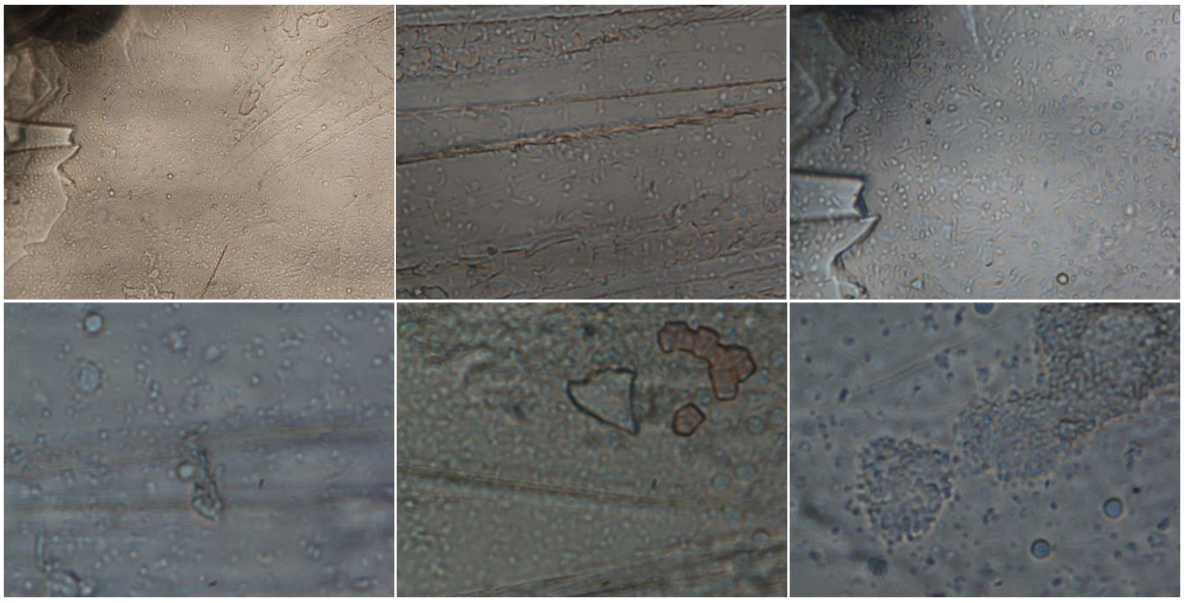

Figure 5.1 Images of platelet adherence on 3D printed devices with collagen as an adhesive protein. Samples were flowed for 20 minutes at a flow rate of 20 µL per minute, and were allowed to incubate for 20 minutes before gently rinsing away of any non-adhered cells. Platelets in a purified platelet solution comprised of platelets resuspended in buffer (top panel). Platelets resuspended in blood plasma to form a platelet rich plasma where more platelet aggregates were formed (bottom panel). Images acquired with an inverted microscope.

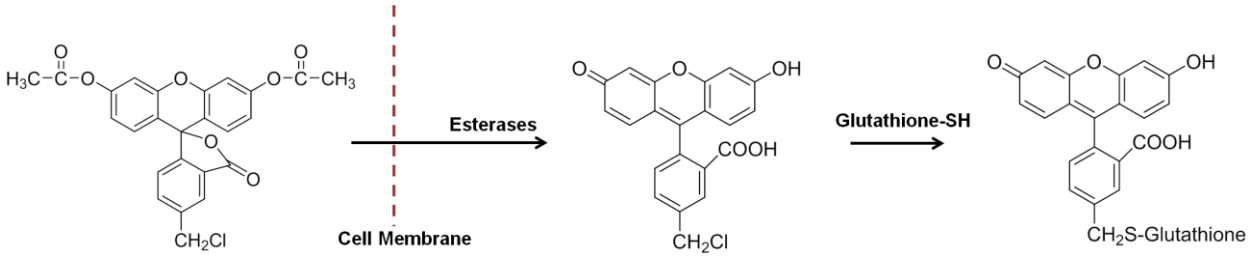

Figure 5.2 Intracellular reactions of cell tracker green CMFDA (5-chloromethylfluorescein diacetate). CMFDA is able to freely pass through the cell membrane, but once inside esterases convert CMFDA to cell-impermeant products and activation of fluorescence after enzymatic removal of acetate groups. The chloromethyl group reacts with the thiol groups on glutathione through S-transferase-mediated reaction. This forms a stable reaction end product that remains fluorescent beyond 72 hours and has an excitation maximum at 492 nm and emission maximum at 517 nm.

CD31 (cluster of differentiation 31), also referred to as the platelet endothelial cell adhesion molecule, is found on the surface of platelets, endothelial cells, and white blood

cells (neutrophils and monocytes).[25] Alexa Fluor 594 anti-human CD31 is an antibody conjugated with a fluorescent probe. Upon addition of fluorescently labeled CD31 antibody with whole blood, the mixture was allowed to incubate for 30 minutes after which time the blood was imaged using fluorescence microscopy and intensity measured using a plate reader. Fluorescence intensity measurements of CD31 labeled whole blood compared to unlabeled whole blood was measured with a plate reader and the results showed a significant difference in relative fluorescence units between the two samples, indicating this would also be a viable detection scheme. Figure 5.3 shows platelets labeled with various cell stains and a fluorescently labeled CD31 antibody.

Neutrophils (12-15 μm diameter; 1800-7700 cells per microliter) and monocytes (10-30 μm diameter; 0-800 cells per microliter) exist in the blood at much lower concentrations than platelets and are significantly larger than platelets, so it stands to reason that the majority of cells imaged using CD31 were platelets due to their size.[26] Of the three methods to label platelets, CD31 was the most promising for platelet visualization and excess platelet handling was avoided. As seen in Figure 5.3, cell tracker red labeled platelets were not as readily visualized compared to cell tracker green and CD31 labeled platelets. Future studies include measuring thrombus formation using the protocol outlined in Chapter 4, when flowing whole blood containing CD31 labeled platelets on a device with fibronectin and collagen as components of the extracellular matrix and with an injured endothelium. To increase platelet isolation specificity, monoclonal antibodies specific to platelets could be purchased at an increased cost. However, the ability to single out platelets without having to remove unwanted possible targets, as would be necessary moving forward with CD31, offers a great advantage. Determining the contribution of

various blood cells to formed thrombi represents the next major undertaking to validate this thrombosis mimic.

Cell Stain	Cell Tracker Green	Cell Tracker Red	CD31
Purified Platelets	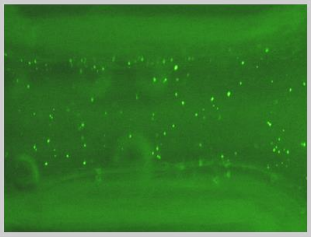	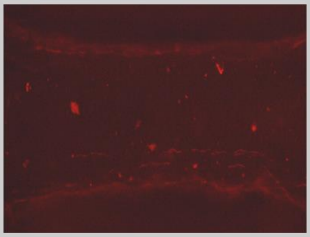	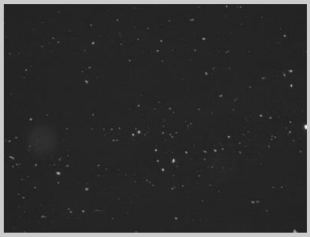
Whole Blood	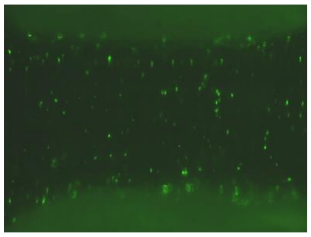	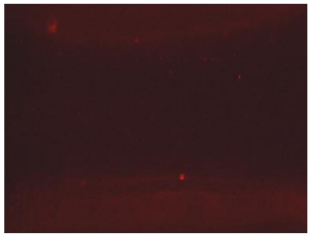	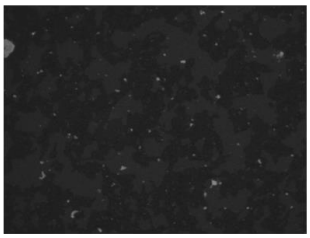
Incubation	45 min	45 min	30 min
Washed	3xs	3xs	None
Platform	3D Printed Device	3D Printed Device	Glass Slide

Figure 5.3 Fluorescence microscopy evaluation of platelets labeled with fluorescent probes. After 45 minute incubations and three washing steps, labeled platelets (cell tracker green or red) were reincorporated with whole blood or as purified platelets over 3D printed channels containing collagen as an adhesive protein for 20 minutes and incubated for an additional 20 minutes at 37 °C and 5% CO_2. After incubation, non-adherent platelets were rinsed from the channels and resultant platelets in the lysis regions were imaged. CD31 labeled platelets were imaged on glass slides directly after a 30 minute incubation without any washing steps.

5.6 Dynamic Media Delivery

In an attempt to grow an endothelium within the channel of the fluidic device that more accurately mimicked *in vivo* cell conditions, continuous media delivery during the cell immobilization process was carried out. Sterilized devices with adhered adhesive proteins (100 $\mu g \cdot mL^{-1}$ of collagen and 50 $\mu g \cdot mL^{-1}$ of fibronectin) were seeded with a concentrated solution of endothelial cells and incubated at 37 °C for 1.5 hours. After this time, initial cell

adhesion was monitored and if needed, more cells were added to the channel. Once initial immobilization was confirmed via microscopy, the fluidic device was attached to tubing feeding through a 3D printed peristaltic pump. An image depicting the experimental setup of the peristaltic pump and continuous media delivery setup can be seen in Figure 5.4 A and B. Figure 5.4 C shows the difference in cell morphology between cells grown under static versus dynamic conditions.

Continuous media delivery to cells provides fresh nutrients while expediting the removal of cell waste products from the device channel. The printed peristaltic pump was compact enough to be placed into a cell incubator so that cells could grow in 37 °C and 5% CO_2 conditions. Available flow rates were evaluated by measuring the time necessary to draw 1 milliliter from a graduated cylinder. From such studies a flow rate range of 155-215 µL per minute was found. These flow rates equate to shear rates from 51 sec^{-1} to 71 sec^{-1} and shear stress values of 5.14 and 7.13 $dyn \cdot cm^{-2}$, which resembles shear stress values of aortas and veins.[27] To mimic the shear rates seen in arterioles and capillaries (1250-1500 sec^{-1})[27,28] the dimensions of the device channel would need to be reduced, and with current limitations in polyjet 3D printing the only way to reach smaller dimensions is through surface modifications. Towards this end, multiple coatings of PDMS and PS have been attempted, but at an increased cost to visibility of adhered cells. Recreation of cell morphology is critical because it has been linked to proper cellular signal transduction, for example, during immune cell chemotaxis.[29,30]

The 3D printed peristaltic pump suffered from numerous mechanical problems, including tubing becoming dislodged from the track above the motor and rollers lifting off of their supportive posts over 24 hours of continuous media delivery. For these reasons,

cells were never able to grow to confluence on the device. Improvements to the pump design addressing these issues need to be carried out before moving forward with these experiments.

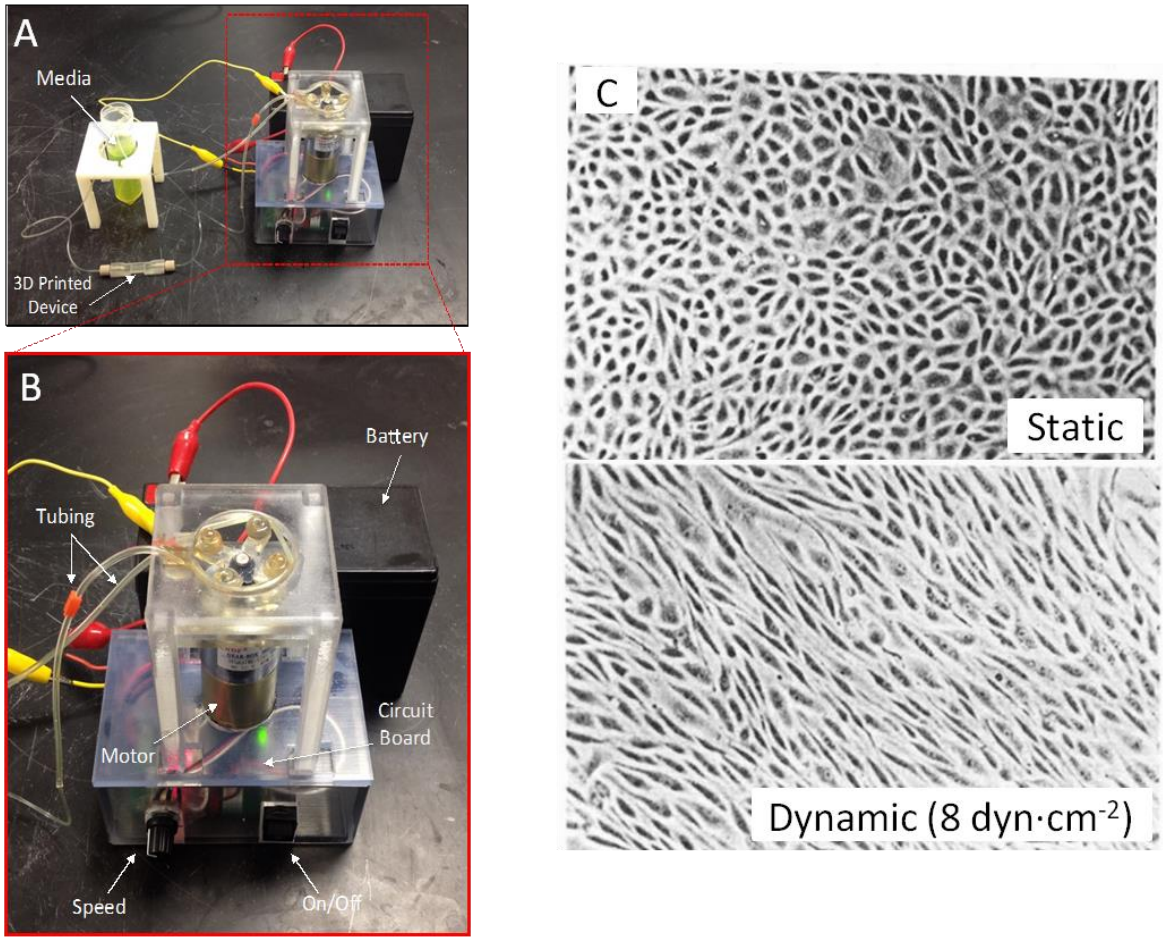

Figure 5.4 3D printed peristaltic pump for continuous media delivery. The pump and moving parts were printed in Vero Clear and house the motor and circuit board. The 3D printed fluidic device was connected to tubing of the peristaltic pump and a media reservoir (A). A battery connected to the circuit board through openings in the back of the printed casing accommodated components of the motor, circuitry, and peristaltic pump parts. Flow rates of 155-215 µL per minute were possible, corresponding to shear rates between 51 sec^{-1}-71 sec^{-1} and shear stresses between 5.14 and 7.13 $dyn \cdot cm^{-2}$. The entire setup (battery, 3D pump, media, and 3D printed device with adhered cells) fit inside a cell incubator (B). Comparison of cell morphology when cells were cultured in static conditions and under dynamic flow for 48 hours (shear stress of 8 $dyn \cdot cm^{-2}$) (C). (Reprinted with permission from reference 31. Copyright ASME.)

5.7 Anti-Platelet Therapy

The International Society on Thrombosis and Hemostasis (ISTH) has put forth criteria for instrumentation meant to evaluate thrombosis before and after the onset of anti-platelet therapies. The criteria included evaluation of thrombosis under flow conditions where a stenosis was featured, reproducible thrombus formation by thrombogenic surfaces and defined shear rates, continuous monitoring of thrombus formation and dissociation, and low sample volume requirements (whole blood).[32,33,34] The 3D printed device outlined in this dissertation can meet all these criterion with slight changes to the protocol and device design, and has the potential to be widely utilized in thrombosis studies aimed not only at anti-platelet therapies, but also towards monitoring thrombus formation for diseases with errant platelet function. Beyond arresting blood loss through thrombus formation the platelet has several other integral functions including hemostasis, wound repair, and maintaining vessel integrity as seen in Figure 5.5. Platelets play a role in maintaining normal blood flow as deficient platelet counts in circulation (thrombocytopenia) have been linked to bleeding into neighboring tissues, thinning of the vasculature, and increased clotting times. Platelets release growth factors that draw smooth muscle cells, fibroblasts, and macrophages to the site of injury via chemotaxis. Fibroblasts aid in tissue regeneration by depositing new extracellular matrix and macrophages aid in removing damaged tissues.[35,36]

The advantages of an *in vitro* device that can probe multiple platelet functions are numerous and span multiple disciplines. The built in advantage of standardization inherent in 3D printing fabrication encourages reproducible results between labs. Improvements to the 3D printed device to make it more relevant for probing cell-to-cell interactions include

integration with membrane inserts for measuring downstream molecule of interest released from vascular components. For example, these devices could be used to probe NO and ATP release from RBCs and endothelial cells exclusively and together, before and after injury to the endothelium to gain insight on the extent ATP release from RBCs and the endothelium impact platelet activation and thrombus formation. Figure 5.6 outlines the design of such a device and shows an example of parallelization via printing devices with multiple channels. ATP and NO released from RBCs and endothelial cells would diffuse through the polycarbonate membrane base of the membrane inserts (filled with the fluorescent probe DAF-FM (4-amino-5-methylamino-2', 7'-difluorescein) or luciferin-luciferase for NO and ATP detection, respectively). These membrane inserts could be designed to align with a 96 well plate for fluorescence detection using a commercial plate reader. [16,37]

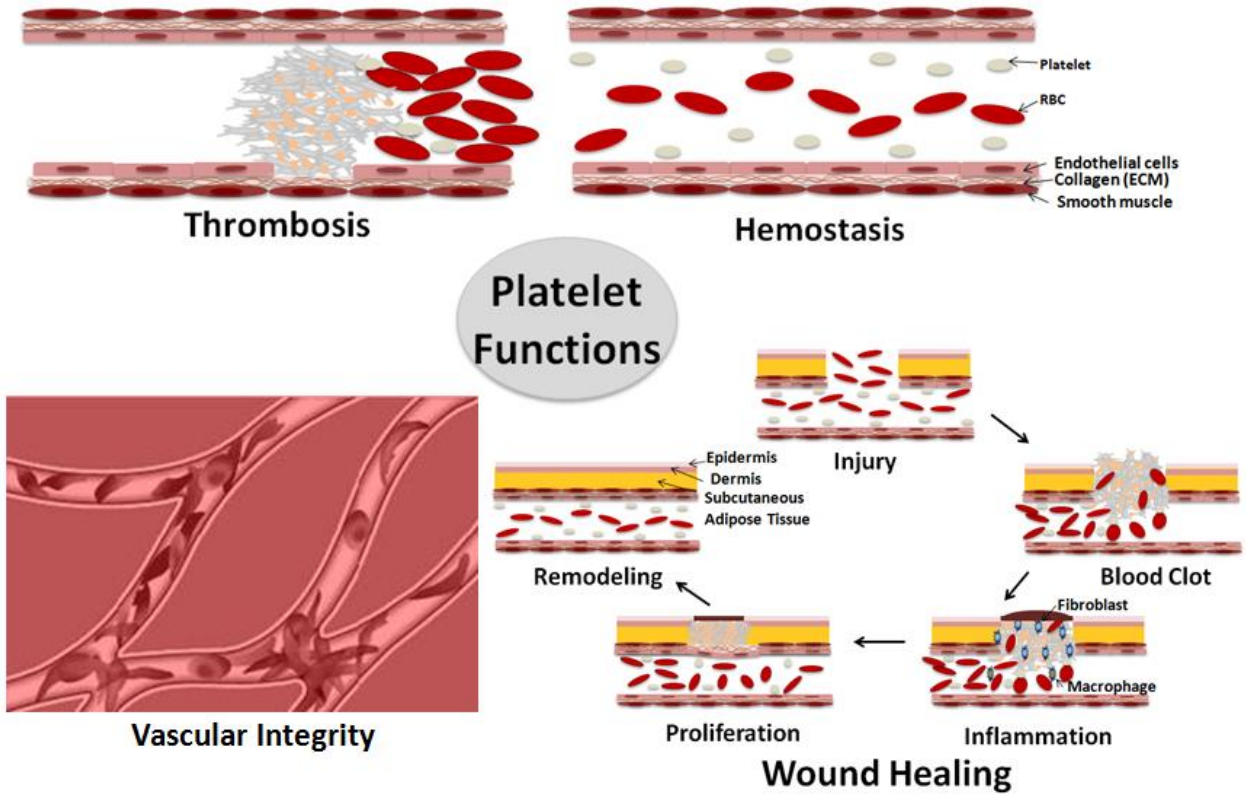

Figure 5.5 Physiological platelet functions include thrombosis, hemostasis, wound healing, and maintaining vessel integrity. Platelets form a platelet plug at the site of vessel injury to arrest blood loss in a process referred to as thrombosis or blood clot formation. Platelets regulate normal blood flow through hemostasis by ameliorating damages to the vascular wall. During wound healing platelets release a number of growth factors and chemicals that facilitate chemotaxis of fibroblasts and macrophages, which are necessary cells for tissue regeneration and remodeling. Platelets play a role in maintaining vascular integrity as thrombocytopenia (lowered platelet count) has been linked with thinning of the vascular wall.

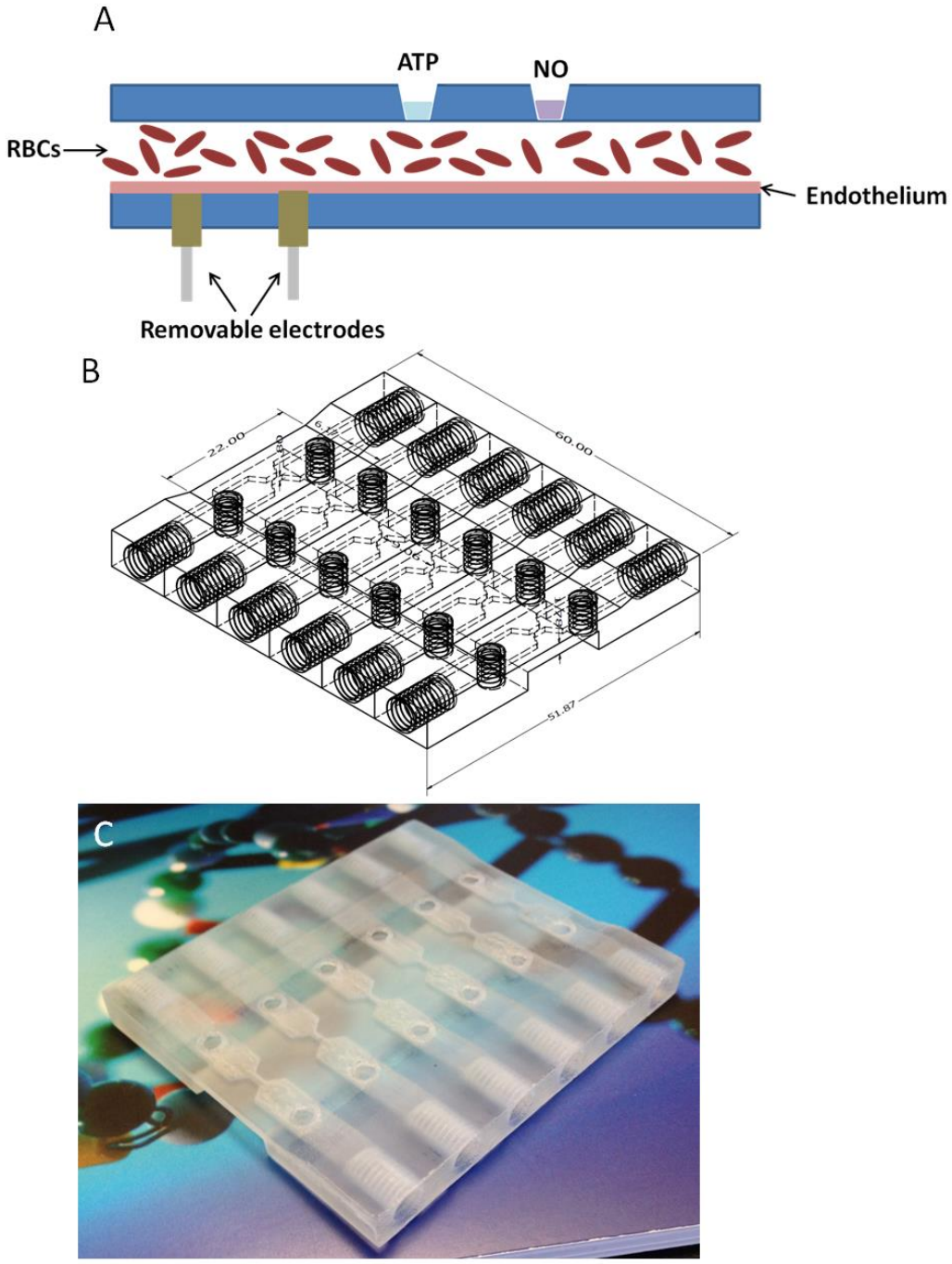

Figure 5.6 3D printed thrombosis mimic with integrated well inserts for the fluorescent detection of RBC-derived ATP and ATP-stimulated NO release from endothelial cells using a commercial plate reader. RBC-derived ATP can diffuse through the polycarbonate membrane at the base of inserts and also stimulate NO production from endothelial cells. Inserts for ATP detection contain luciferin-luciferase and those for NO detection contain the fluorescent probe DAF-FM (4-amino-5-methylamino-2', 7'-difluorescein). The extent of thrombus formation can be evaluated using the protocol introduced in Chapter 4.

5.8 Assessment of 3D Printing for Microfluidic Device Fabrication

3D printing has already had an impact on the field of microfluidics and lab on a chip technology, and it stands to reason that this technology will find further use in these disciplines as a means to fabricate biomedical and point of care devices for use in under resourced areas. Compared to the lithographic techniques typically employed by many educational labs, 3D printing offers a much simpler fabrication process by foregoing the need to use a master for replica molding.[38] What has made soft lithography-based PDMS microfluidic devices attractive as a rapid prototyping tool lies in the user's ability to fine tune the device easily until the desired effect is achieved, all within a short period of time. While conventional techniques have their value, 3D printing may be the answer to some of the troubles that have plagued traditional replica molding techniques, such as soft lithography-based microfluidics, including a lack of standardization between labs and the labor-intensive fabrication processes. Furthermore, geometries that traditional fabrication and rapid prototyping techniques (milling and injection molding) would be unable to reproduce are not a challenge for 3D printers. Examples in the literature of 3D printing used towards microfluidic device fabrication showcase diverse applications. Examples include 3D printed organic reaction-ware,[39,40] 3D printed complex microvascular networks,[41] or integration with commercial fittings, membrane inserts, and removable electrodes for easy sample delivery and analyte detection via spectroscopy or electrochemical means. [16,37,42,43,44]

5.8.1 Materials

As the cost of 3D printers continues to decline, it is probable that the prevalence of 3D printers will increase. Decreasing printer costs make it feasible for laboratories to

purchase their own 3D printer, and material costs may also decrease as demand and variety of materials increases. Areas of improvement to 3D printed materials include variety, composition, strength, and finishing procedures. Material variety is currently limited by the ability of the material to be powder-based or to have a low enough viscosity to be extruded from the printing head. Many of the commercial printers require that only the provided proprietary resins be used with the printer, or risk voiding the warranty. This limits material experimentation and drives the use of custom 3D printers for material expansion.

For 3D printing to find continued use outside of initial prototyping, advances in material diversity and strength, print resolution, and print speed must be made so that 3D printing becomes more competitive with conventional methods. Advancements in these areas are already progressing, and in the spring of 2015 a 3D printing technique relying on continuous liquid interface production (CLIP) via UV irradiation of a photocurable polymer was introduced with build speeds of five hundred millimeters per hour (25 to 100 times faster than traditional 3D printers), and a build resolution of 50 μm. Build speeds in excess of 1000 millimeters per hour are possible, but at a severe cost to resolution. The available materials would include elastics, ceramics, and biological materials. By comparison, print speeds of a few millimeters per hours are typical of conventional stereolithography 3D printers, but higher resolutions are achievable with methods such as stereolithography (SLA; 70-250 in XY plane and 1-10 μm in the Z plane)[45], selective laser sintering (SLS; 50 μm XY plane; 1-2 μm Z),[46,47] laminated object manufacturing (LOM; 10 μm XY plane; 100 μm Z),[48] inkjet printing (20-50 μm XY plane; 50 μm Z),[49] and polyjet printing (100 μm XY direction; 16 μm Z).[50] The only 3D printing technique over which CLIP offers a clear

advantage in terms of resolution is fused deposition modeling (FDM; 250 μm XY; 50 μm Z).[51] CLIP does offer an advantage in structural soundness over conventional 3D printing techniques, as the finished product is one continuous structure instead of a series of 2D layers.[52] A schematic of the continuous 3D printer can be seen in Figure 5.7.

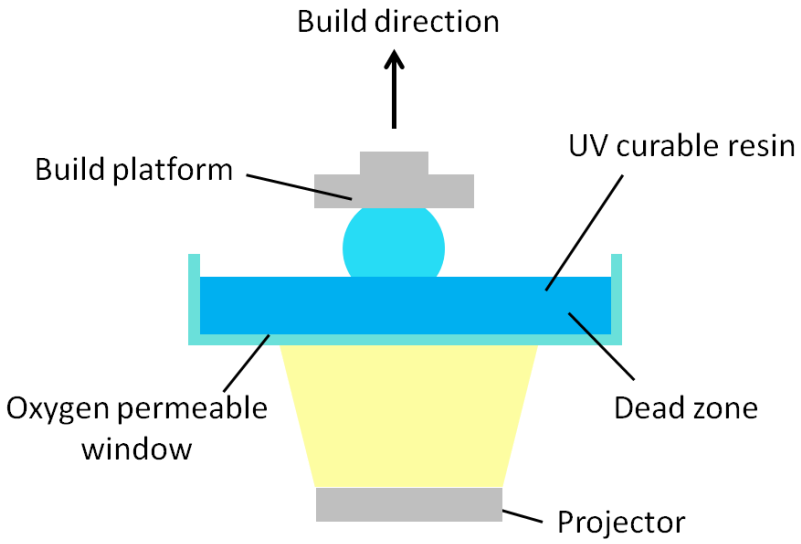

Figure 5.7 Schematic of a continuous liquid interface production (CLIP) 3D printer. In this method, a sequence of UV images are projected and passed through an oxygen permeable window into a vat containing photocurable resin. The oxygen permeable window allows enough oxygen into the resin vat to create a dead zone where no material is being polymerized between the window and object, making continuous printing possible. The thickness of the dead zone can be controlled to regulate print speed, but with increasing speed, resolution suffers. The build platform continuously raises the object up from the resin vat until the printing process is complete.

Post-print processing of objects also requires improvement. Polyjet 3D printing and other techniques that employ support material are at a disadvantage to selective laser sintering and stereolithography for the fabrication of transparent devices that forego the use of support material and offer higher resolution. For the devices outlined in this dissertation, support material removal was oftentimes incomplete or the process of removal damaged the channel leaving visible marks. More efficient ways to remove support

material would prove beneficial, specifically in microfluidics, by allowing smaller features to be printed. For all the improvements the fabrication process of 3D printing offers over soft lithography, the transparency and optical clarity of the finished product remains inferior to PDMS devices. The development of a chemical polish for clear materials would be advantageous for developing optically clear devices, especially for designs with areas that are difficult to access by conventional means. Any chemical finish would have to be specific to the support material however, or object dimensions could be skewed by unwanted chemical etching. The ability to print materials amenable to cell culture without surface modification would also have a substantial impact on biomedical device development.

5.8.2 File Sharing

3D printing offers a unique means of collaboration and information sharing not available with conventional techniques due to the nature of the digital data files (.STL files) generated from CAD software during object development. Dissemination of fabrication protocols via publications can result in variability of the final product between different laboratories. However, printing objects from the same .STL file will result in an exact replica even if fabrication is separated in time and space. One caveat is that the same type of 3D printer must be used to ensure uniformity with material and resolution.

5.8.3 Outlook

The creation of virtually any geometry can be realized and made tangible using CAD software capable of formatting .STL files that can be read by a 3D printer. Choosing the appropriate printer type, SLA, inkjet printer, SLS, FDM, LOM, or CLIP depends on the design, materials, and purpose of the device. 3D printing has become a valuable tool for a

variety of disciplines. As printer performance, resolution, and available materials have increased, so too have the number of applications. Applying 3D printing to microfluidics, and what will surely be nanofluidics with time, has resulted in devices that can more closely achieve the true meaning of lab-on-a-chip devices. With ongoing research focused on improvement of printer performance, applications of 3D printing can be predicted to increase and find use in a variety of disciplines. With the recent advent of CLIP 3D printing, increased print speeds beyond any other 3D printing technique have been achieved without the use of support material. This type of work exemplifies the direction 3D printing is heading and the possibilities of devices fabricated from such methods are growing. The increased utility of 3D printing marks a particularly exciting time for biomedical device development.

The work detailed in this dissertation represents the beginnings of research dedicated to developing a fully working thrombosis mimic, complete with components of the vasculature, and amenable to straight-forward thrombosis evaluation. In an ideal version, the mimic would be self-contained, lacking the need for external sample delivery. Re-imagining the design of the 3D printed peristaltic pump and fluidic device to one where the two components are joined, forms a device that is inherently more true to the original premise of lab-on-a-chip devices. Advances in 3D printing may eventually forego the need for surface modifications and post-print processing procedures to facilitate cell adhesion and visualization, respectively. A fully operational *in vitro* thrombosis mimic has the potential to evaluate diseased blood cell interactions during injury and to impact the early stages of anti-thrombotic drug discovery.

REFERENCES

REFERENCES

(1) Furie, B.; Furie, B. C. *New England Journal of Medicine* **2008**, *359*, 938-949.

(2) Nieswandt, B.; Watson, S. P. *Blood* **2003**, *102*, 449-461.

(3) Wootton, D. M.; Ku, D. N. *Annual Review of Biomedical Engineering* **1999**, *1*, 299-329.

(4) Escolar, G.; Krumwiede, M.; White, J. G. *The American Journal of Pathology* **1986**, *123*, 86-94.

(5) Tchoepe, D.; Roesen, P.; Esser, J.; Schwippert, B.; Nieuwenhuis, H. K.; Kehrel, B.; Gries, F. A. *Seminars in Thrombosis and Hemostasis* **1991**, *17*, 433-438.

(6) O'Sullivan, B. P.; Linden, M. D.; Frelinger, A. L.; Barnard, M. R.; Spencer-Manzon, M.; Morris, J. E.; Salem, R. O.; Laposata, M.; Michelson, A. D. *Blood* **2005**, *12*, 4635-4641.

(7) Somova, L.; Mufunda, J. *Clinical and Experimental Hypertension* **1993**, *15*, 781-796.

(8) Ataga, K. I.; Orringer, E. P. *The American Journal of Medicine* **2003**, *115*, 721-728.

(9) Wright, H. P.; Thompson, R. H.; Zilkha, K. J. *Lancet* **1965**, *2*, 1109-1110.

(10) Letourneau, S.; Hernandez, L.; Faris, A. N.; Spence, D. M. *Analytical and Bioanalytical Chemistry* **2010**, *397*, 3369-3375.

(11) Francis, R. B. J. *Blood Coagulation & Fibrinolysis* **1991**, *2*, 341-353.

(12) Vinik, A. I.; Erbas, T.; Park, T. S.; Nolan, R.; Pittenger, G. L. *Diabetes Care* **2001**, *24*, 1476-1485.

(13) Carroll, J.; Raththagala, M.; Subasinghe, W.; Baguzis, S.; D'Amico Oblak, T.; Root, P.; Spence, D. *Molecular BioSystems* **2006**, *2*, 305-311.

(14) Sprague, R. S.; Ellsworth, M. L.; Stephenson, A. H.; Kleinhenz, M. E.; Lonigro, A. J. *American Journal of Physiology* **1998**, *275*, H1726-32.

(15) Sprague, R. S.; Stephenson, A. H.; Ellsworth, M. L.; Keller, C.; Lonigro, A. J. *Experimental Biology and Medicine* **2001**, *226*, 434-439.

(16) Chen, C.; Wang, Y.; Lockwood, S. Y.; Spence, D. M. *Analyst* **2014**, *139*, 3219-3226.

(17) Genes, L. I.; N, V. T.; Hulvey, M. K.; Martin, R. S.; Spence, D. M. *Lab Chip* **2007**, *7*, 1256-9.

(18) Tolan, N. V.; Genes, L. I.; Subasinghe, W.; Raththagala, M.; Spence, D. M. *Analytical Chemistry* **2009**, *81*, 3102-3108.

(19) McDonald, J. C.; Duffy, D. C.; Anderson, J. R.; Chiu, D. T.; Wu, H.; Schueller, O. J.; Whitesides, G. M. *Electrophoresis* **2000**, *21*, 27-40.

(20) Duffy, D. C.; McDonald, J. C.; Schueller, O. J.; Whitesides, G. M. *Analytical Chemistry* **1998**, *70*, 4974-84.

(21) Detwiler, D. A.; Dobes, N. C.; Sims, C. E.; Kornegay, J. N.; Allbritton, N. L. *Analytical and Bioanalytical Chemistry* **2012**, *402*, 1083-1091.

(22) Johnson, A. S.; Anderson, K. B.; Halpin, S. T.; Kirkpatrick, D. C.; Spence, D. M.; Martin, R. S. *Analyst* **2013**, *138*, 129-136.

(23) Regehr, K. J.; Domenech, M.; Koepsel, J. T.; Carver, K. C.; Ellison-Zelski, S. J.; Murphy, W. L.; Schuler, L. A.; Alarid, E. T.; Beebe, D. J. *Lab Chip* **2009**, *9*, 2132-2139.

(24) Mogoa, E.; Bodet, C.; Legube, B.; Hechard, Y. *Experimental Parasitololgy* **2010**, *126*, 97-102.

(25) Albelda, S. M.; W.A., M.; Buck, C. A.; Newman, P. J. *Journal of Cell Biology* **1991**, *114*, 1059-1068.

(26) Abbas, A. *Elsevier* **2012**.

(27) Papaioannou, T. G.; Stefanadis, C. *Hellenic Journal of Cardiology* **2005**, *46*, 9-15.

(28) Li, M.; Ku, D. N.; Forest, C. R. *Lab Chip* **2012**, *12*, 1355-1362.

(29) Neves, S. R.; Tsokas, P.; Sarkar, A.; Grace, E. A.; Rangamani, P.; Taubenfeld, S. M.; Alberini, C. M.; Schaff, J. C.; Blitzer, R. D.; Moraru, I. I.; Iyengar, R. *Cell* **2008**, *133*, 666-680.

(30) Onsum, M. D.; Wong, K.; Herzmark, P.; Bourne, H. R.; Arkin, A. P. *Physical Biology* **2006**, *3*, 190-199.

(31) Dewey, C. F.; Bussolari, S. R.; Gimbrone, M. A.; Davies, P. F. *Journal of Biomechanical Engineering* **1981**, *103*, 177-185.

(32) Zwaginga, J. J.; Nash, G.; King, M. R.; Heemskerk, J. W.; Frojmovic, M.; Hoylaerts, M. F.; Sakariassen, K. S.; ISTH, B. s. o. t. S. o. t. *Journal of Thrombosis and Haemostasis* **2006**, *4*, 2486-2487.

(33) Zwaginga, J. J.; Sakariassen, K. S.; Nash, G.; King, M. R.; Heemskerk, J. W.; Frojmovic, M.; Hoylaerts, M. F.; ISTH, B. S. o. t. S. o. t. *Journal of Thrombosis and Haemostasis* **2006**, *4*, 2716-2717.

(34) Li, M.; Hotaling, N. A.; Ku, D. N.; Forest, C. R. *Plosone* **2014**, *9*, e82493.

(35) Smyth, S. S.; Mcever, R. P.; Weyrich, A. S.; Morrell, C. N.; Hoffman, M. R.; Arepally, G. M.; French, P. A.; Dauerman, H. L.; Becker, R. C. *Journal of Thrombosis and Haemostasis* **2009**, *7*, 1759-1766.

(36) Gimbrone, M. A.; Aster, R. H.; Cotran, R. S.; Corkery, J.; Jandl, J. H.; Folkman, J. *Nature Biotechnology* **1969**, *222*, 33-36.

(37) Liu, Y.; Chen, C.; Summers, S.; Medawala, W.; Spence, D. M. *Integrative Biology* **2015**, *7*, 534-543.

(38) Waldbaur, A.; Rapp, H.; Lange, K.; Rapp, B. E. *Analytical Methods* **2011**, *3*, 2681-2716.

(39) Mathieson, J. S.; Rosnes, M. H.; Sans, V.; Kitson, P. J.; Cronin, L. *Beilstein Journal of Organic Chemistry* **2013**, *4*, 285-291.

(40) Kitson, P. J.; Rosnes, M. H.; Sans, V.; Dragone, V.; Cronin, L. *Lab Chip* **2012**, *12*, 3267-3271.

(41) Therriault, D.; White, S. R.; Lewis, J. A. *Nature Materials* **2003**, *2*, 265-271.

(42) Anderson, K. B.; S.Y., L.; Martin, R. S.; Spence, D. M. *Analytical Chemistry* **2013**, *85*, 5622-5626.

(43) Erkal, J. L.; Selimovic, A.; Gross, B. C.; Lockwood, S. Y.; Walton, E. L.; McNamara, S.; Martin, R. S.; Spence, D. M. *Lab Chip* **2014**, *14*, 2023-2032.

(44) Gross, B. C.; Anderson, K. B.; Meisel, J. E.; McNitt, M. I.; Spence, D. M. *Analytical Chemistry* **2015**, *87*, 6335-6341.

(45) FormLabs. *Formlabs-high resolution desktop 3D Printer*. http://www.formlabs.com (accessed November 30, 2015).

(46) Ko, S. H.; Pan, H.; Grigoropoulos, C. P.; Luscombe, C. K.; Fréchet, J. M. J.; Poulikakos, D. *Nanotechnology* **2007**, *18*, 345202.

(47) Chung, J.; Bieri, N. R.; Ko, S.; Grigoropoulos, C. P.; Poulikakos, D. *Applied Physics A* **2004**, *79*.

(48) Pham, D. T.; Gault, R. S. *International Journal of Machine Tools and Manufacture* **1998**, *38*, 1257-1287.

(49) Calvert, P. *Chemistry of Materials* **2001**, *13*, 3299-3305.

(50) 3DSystems. *Polyjet technology.* http://www.stratasys.com/3d-printers/technology/polyjet-technology (September 30, 2015).

(51) Van Weeren, R.; Agarwala, M.; Jamalabad, V.; Bandyophadyay, A.; Vaidyanathan, R.; Langrana, N.; Safari, A.; Whalen, P.; Danforth, S.; Ballard, C. In *Proceedings of the Solid Freeform Fabrication Symposium*; ASME, 1995, pp 314-21.

(52) Tumbleston, J. R.; Shirvanyants, D.; Ermoshikin, N.; Janusziewics, R.; Johnson, A. R.; Kelly, D.; Chen, K.; Pinschmidt, R.; Rolland, J. P.; Ermoshkin, A.; Samulski, E. T.; DeSimone, J. M. *Science* **2015**, *347*, 1349-1352.